Self-assemblies of Cobalt (II) and Zinc (II) Complexes of Amide, Urea-Based Ligands and Their Ions, Molecular Recognitions

A Dissertation

Submitted in partial fulfillment for the degree of

Doctor of Philosophy

Rinki Brahma

(Roll No. 186122029)

Thesis Supervisor: Prof. Jubaraj Bikash Baruah

Department of Chemistry

Indian Institute of Technology Guwahati

Assam-781039, India

Dedicated to the loving memory of my father...
and
To my family members...

INDIAN INSTITUTE OF TECHNOLOGY GUWAHATI

Department of Chemistry

STATEMENT

I hereby declare that this thesis entitled "***Self-assemblies of Cobalt (II) and Zinc (II) Complexes of Amide, Urea-Based Ligands and Their Ions, Molecular Recognitions***" is the outcome of research work carried out by me under the supervision of Prof. Jubaraj Bikash Baruah in the Department of Chemistry, Indian Institute of Technology Guwahati, India.

In keeping with the general practice of reporting scientific observations, due acknowledgments have been made wherever this work is based on the findings of other investigators.

IIT Guwahati (Rinki Brahma)

February, 2024

INDIAN INSTITUTE OF TECHNOLOGY GUWAHATI

Department of Chemistry

CERTIFICATE

This is to certify that **Mrs. Rinki Brahma** (Roll No. 186122029) has been working under my supervision since July 2018 as a regular registered Ph.D. student. Her thesis entitled ***"Self-assemblies of Cobalt (II) and Zinc (II) Complexes of Amide, Urea-Based Ligands and Their Ions, Molecular Recognitions"*** is an authentic record of the results obtained from the research work carried out under my supervision in the Department of Chemistry, Indian Institute of Technology Guwahati, India. I am forwarding her thesis to submit for the award of degree of Doctor of Philosophy, from this institute. I hereby certify that she has fulfilled all the requirements, according to the rules of this institute regarding the investigations represented in her thesis and this work has not been submitted elsewhere for a degree.

IIT Guwahati

February, 2024

Prof. Jubaraj Bikash Baruah
(Thesis supervisor)
Professor, Department of Chemistry
Indian Institute of Technology Guwahati
Assam (India)

Acknowledgments

" I walk in a space of gratitude..." – *Jurnee Smollett-Bell*

I am overwhelmed while writing this section of my thesis.

Foremost, I am gratified by the unwavering love, encouragement, and resilience that I received from my parents, Late Haren Chandra Brahma and Mrs. Champabati Brahma. I express my heartfelt gratitude to Nabanita Brahma (sister), Sunraj Brahma (brother), and my beloved husband, Karanjeet Narzary, Bhaskar Jyoti Brahma (brother-in-law), and Paarthiv Brahma (nephew) for their unwavering support throughout my journey. Their constant presence by my side has been a source of immense strength and encouragement, for which I am truly grateful. Furthermore, I am beholden to the constant support of my parents-in-law in my pursuit of higher education. I am also grateful to my cousins- Thajim Brahma and Bilash Brahma, my sister-in-law, Sheena Narzary, Prasenjit Boro (brother-in-law), and Shlok Boro (nephew), for their consistent support during my Ph.D. journey.

In this journey towards attaining my Ph.D. degree, I deeply express my gratitude to my supervisor, Prof. Jubaraj Bikash Baruah, for consistently supporting and motivating me. His timely help during this crucial phase of my career has made it possible to achieve this target. The enlightening experience of doing science under his guidance can hardly be described in words. The numerous discussions and interactions I had with him expanded my horizons to hitherto unknown frontiers of science and knowledge. I am in debt to this wonderful person for all that he has given me and, above all, for motivating me towards scientific research. My everlasting gratitude goes towards him.

I would like to acknowledge my sincere gratitude to all my doctoral committee members, Prof. Bhubaneswar Mandal, Dr. Kalyan Raidongia, and Dr. Shyam Biswas, for their insightful advice and valuable suggestions. I am also grateful to the entire faculty and staff in the Department of Chemistry, Indian Institute of Technology Guwahati, for providing a wonderful work atmosphere throughout this period.

Lab CHL101 was a nice place to work with these people with whom I had the opportunity to work with Dr. Babulal Das, Dr. Prithviraj Khakhlary, Dr. Arup Tarai, Dr. Munendra Pal

Singh, Jitendra Nath, Abhay Pratap Singh, and Satyendra Verma. No words can express my thankfulness for giving me their time and companionship, which made the time spent in the laboratory pleasant and memorable.

I would like to give my special thanks to my friends from July 2018 batch of IIT Guwahati, Bittu Lama, Sabina Yashmin, Sandeep Kumar, Sagnik Dey, Pran Gobindo Nandi, Bikoshita Porashar, Vinay Arora, Priyanka Adhikari, Surabhi Paul, Monuranjan Konwar, Tanumoy Sarkar, Debjyoti Pal, Chanreingam Long, Indraneel Debnath, Aritra Mitra, Tirupati Roy, Mrinmoy Roy and Somnath Paik.

I am grateful to Maitery Yadav, Tamanna Khandelia, Ravinder Chahal, and Arisha Arora for their unstinting help during my research work.

I would like to acknowledge IIT Guwahati for the fellowship, Microsoft Corporation for presenting MS Word, MS Excel, MS PowerPoint, and Adobe computer software company for providing AI software.

The thesis entitled **"Self-assemblies of Cobalt (II) and Zinc (II) Complexes of Amide, Urea-Based Ligands and Their Ions, Molecular Recognitions"**, describes synthetic and physico-chemical studies based on the self-assemblies of a series of pyridyl group containing amide, and urea derivatives as well as their salts, cobalt (II) and zinc (II) complexes. Those complexes and coordination polymers provided scope to understand their photo-physical properties and effects on the intrinsic supramolecular aspects. The content of the thesis is divided into five chapters which are elaborated below.

Chapter 1. Introduction

Pyridyl amide and pyridyl urea derivatives find applications in various fields, such as molecular recognition,[1-2] anion recognition[3,4] catalysis,[5,6] medicine,[7] and molecular devices.[8,9] Both amide and urea-based complexes have high value in separating anions.[9,10] In pyridyl amide derivatives, the carboxamide functional group and pyridyl N-atom are available for hydrogen-donating and hydrogen-accepting, respectively. Also, the urea functional group can assemble via N-H···O tape utilizing the N-H as a hydrogen bond donor to hydrogen bond acceptor oxygen atom of another urea molecule.[11] Urea derivatives have large structural variations due to *syn-syn* or *syn-anti* orientation of the NH-groups of the urea derivative participating in hydrogen-bonded assemblies.[12] The ionic cocrystals of urea derivatives act as urease inhibitors by controlling nutrients in soil.[13] Urea-based molecules also form anion-guided non-covalent assemblies.[14] Pyridyl amides and urea-based ligands are interesting due to the formation of varieties of transition metal clusters, metal-organic frameworks,[15,16] and the ability to recognize anions.[17,18] The NH-groups of amide and urea derivatives form hydrogen bonds, providing a means for anion detection. The introduction section is presented to lay the foundation for utilizing the supramolecular sites on metal complexes or the free binding sites of those ligands for self-assembling. The examples of the secondary coordination sphere complexes of amide and urea functionalized ligands are elaborated.[19,20] Accordingly, the diverse supramolecular aspects of amide and urea derivatives having scopes to further understand the role of these functional groups in ion recognitions and for developing new supramolecular assemblies are described.

Chapter 2. Zinc (II) nitrobenzoate complexes of isonicotinamide and nicotinamide

(R. Brahma and J. B. Baruah, *ACS Omega*, 2020, **5**, 3774–3785)

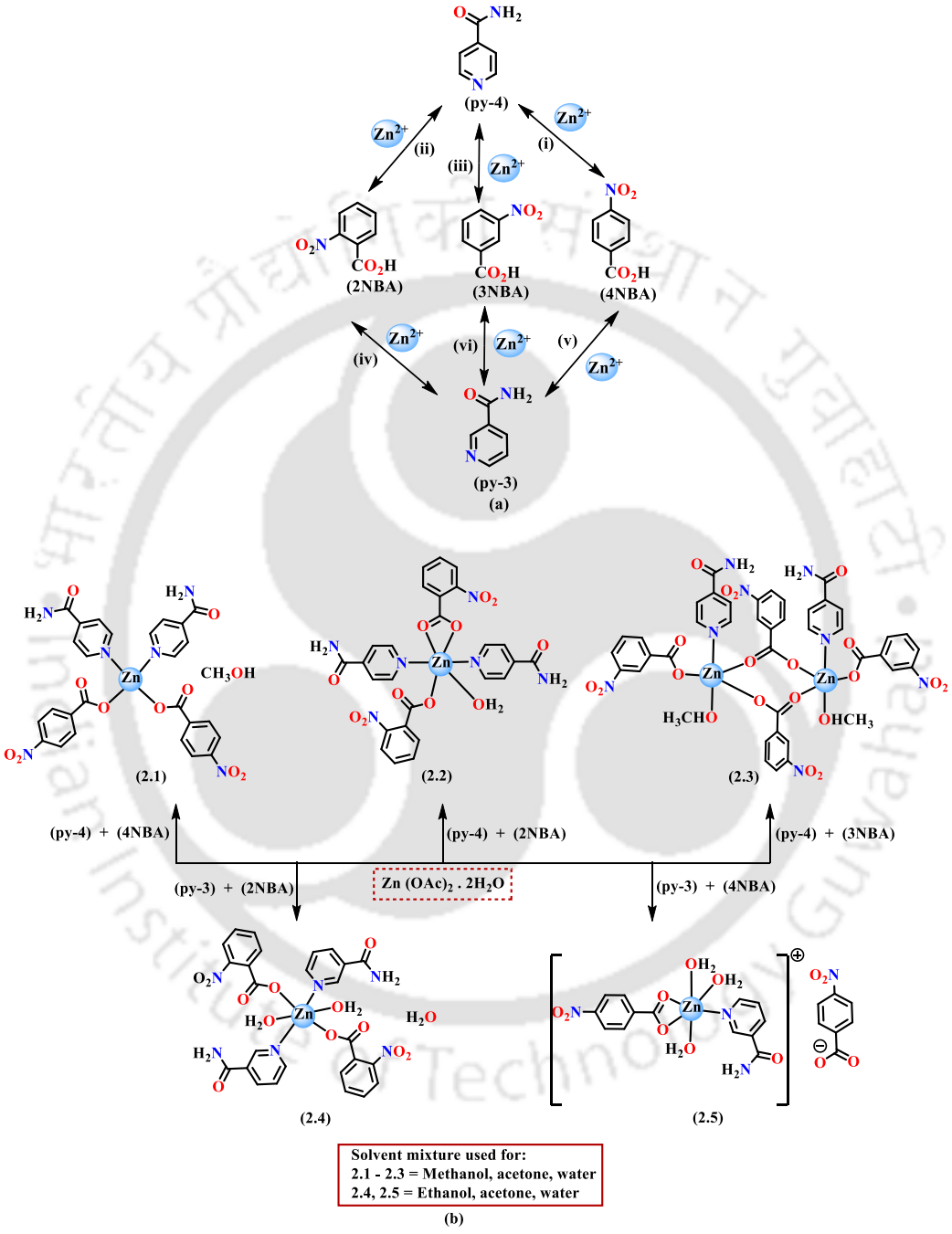

Scheme 2.1. (a) Different combinations of nitrobenzoic acids with pyridine -3-(or 4-) carboxamide. (b) Synthesis of zinc (II) complexes of pyridine -3-(or-4-) carboxamide and nitrobenzoic acids

In this chapter, we report the synthesis and characterization of zinc(II) complexes from positional isomers of nitrobenzoic acid **(2.1–2.5)** with pyridine -3-(or 4-) carboxamide listed

in Scheme 2.1a. Among these, all three combinations with pyridine-4-carboxamide (or isonicotinamide) gave crystalline zinc (II) complexes, but in the case of pyridine-3-carboxamide (or, nicotinamide), only the zinc (II) complexes with 2-nitrobenzoic and 4-nitrobenzoic acid were obtained (Scheme 2.1b). Besides crystal structure determination, the complexes were characterized by spectroscopic tools in both solid and solution.

All the complexes have independent compositions, but in each case, the amide groups in the complexes were free; hence they participated in the formation of self-assemblies. As an example, the single crystal X-ray diffraction analysis revealed that the bis(pyridine-4-carboxamide)di(4-nitrobenzoato)zinc(II)·methanol (**2.1**) has two pyridyl amide ligands in equatorial positions and rest of the sites of the tetrahedron are completed by two monodentate 4-nitrobenzoate. The geometry index, τ_4, is 0.83, so this complex **2.1** has a pseudo tetrahedral geometry.[21] The other complexes **2.2**, **2.4**, and **2.5**, have hexacoordinated geometry, having an N_2O_4 coordination environment around zinc(II) ions. The complex di-μ^2-(3-nitrobenzoato)[(methanol)(pyridine-4-carboxamide)(3-nitrobenzoato)zinc(II)] (**2.3**) is a binuclear complex having two molecules of 3-nitrobenzoate bridging and another two monodentate molecules of 3-nitrobenzoate are coordinated to the Zn(II) ion at terminal positions. In this complex, each zinc (II) site is pentacoordinated with slightly distorted trigonal-bipyramidal geometry. The τ_5 values for the two Zn(II) metal centers are 0.92 and 0.94. Since $\tau_5 < 1$, so, **2.3** has a distorted trigonal bipyramidal geometry.[22] The two 4-pyridylamide (isonicotinamide) ligands are independently ligating two Zn(II) ions and are projected on the same side of the complex. Each Zn(II) center had a coordinated methanol molecule. All the complexes **2.1**-**2.5** were characterized by FTIR, UV-visible, photoluminescence, ^{1}H-NMR, and ^{13}C-NMR spectroscopy.

Table 2.1. Geometries of around the zinc(II) ion in the complexes **2.1**-**2.5**

Complex	Geometry
2.1	Psuedotetrahedral
2.2	Distorted octahedral
2.3	Distorted trigonal bipyramidal
2.4	Distorted octahedral
2.5	Distorted octahedral

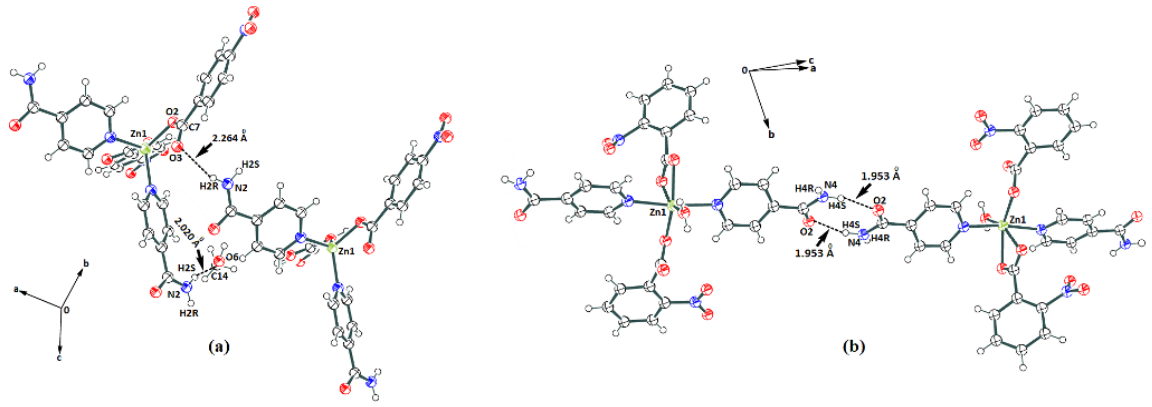

Figure 2.1. Hydrogen-bonded self-assembly of the complexes (a) **2.1** and (b) **2.2**

The hydrogen-bonded self-assembly in complexes **2.1** and **2.2** are illustrated in Fig. 2.1. Amide-amide supramolecular $R^2_2(8)$ synthon is formed due to intermolecular hydrogen bonding in complexes **2.6** (Fig. 2.1b) and **2.4**. In complexes **2.4** and **2.5**, intramolecular hydrogen bonding between the carboxylate group and aqua ligand is observed.

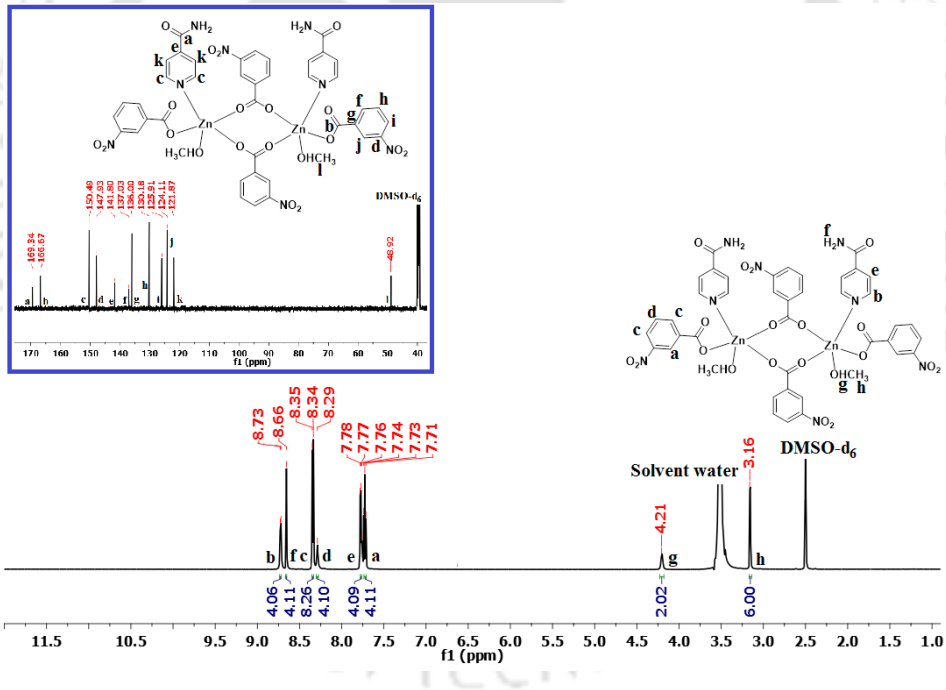

Figure 2.2. ^{1}H-NMR (600MHz) spectra of a representative example complex **2.3** [inset: ^{13}C-NMR (151 MHz, DMSO-d_6) of the same]

As a typical example, the ^{1}H-NMR spectrum of the **2.3** is shown in Fig. 2.2. There were signals for the ring protons of the pyridine-4-carboxamide as well as amide protons that are assigned in Fig. 2.2. The chemical shifts from the coordinated methanol molecules were seen at 4.21 ppm for O-H and at 3.16 ppm for methoxy protons and the integrations were as per the composition revealed from the crystal structure.

From these observations, it was clear that the structures of the complexes are ligand-dependent and not uniform to have predesigned synthesis. Moreover, there are carboxylate ligands that either acted as monodentate, chelating, or bridges, and these could have happened as a consequence of small activation energy to transform from monodentate to a chelate carboxylate which is about 6 kJ/mol.[23]

Thus, the energy of all the five complexes was optimized by taking all the possible isomers from each composition by using the B3LYP functional with LANL2DZ basis set. Each isolated (synthesized) complex was taken as a reference to form different combinations, and the energy difference between the possible geometries was calculated and are compared, as shown in Fig. 2.3. It was found that the as-synthesized complexes **2.1-2.4** did not have the lowest stable energy as compared to other theoretically formulated structures. This suggested that the isolated compounds were stabilized by their propensity to form supramolecular assemblies through second coordination sphere properties and steric adjustments during formation.

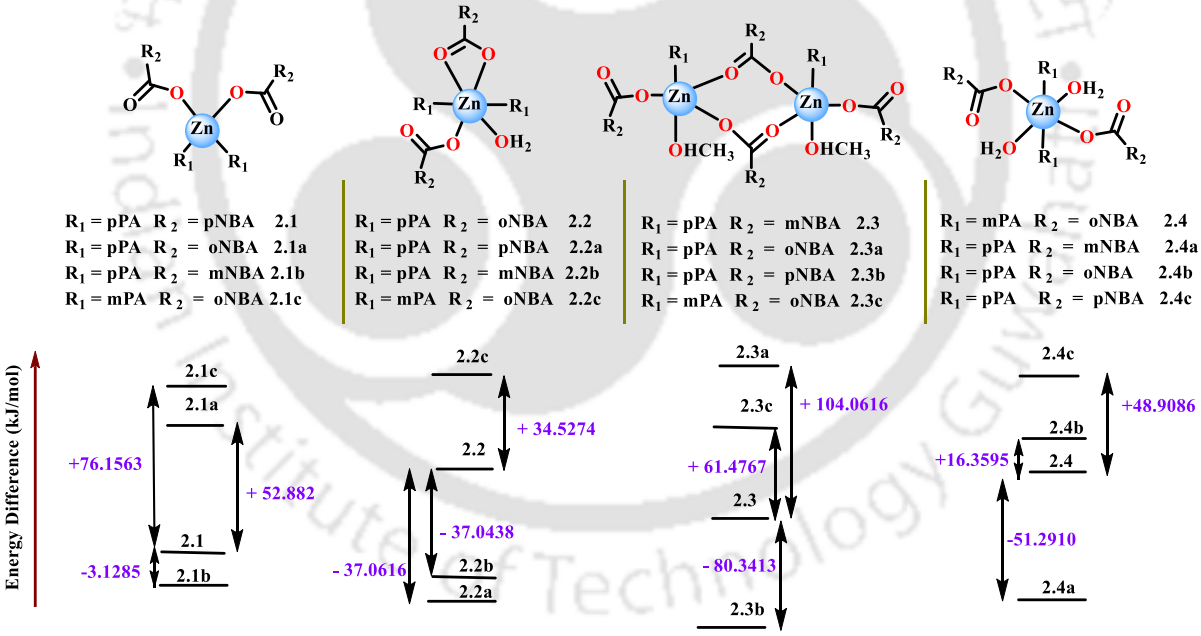

Figure 2.3. Optimized energy of different structures of all the possible combinations that were observed in (a) neutral zinc(II) complexes **2.1-2.4** (B3LYP functional and LANL2DZ basis set)

The solid-state UV-visible absorptions of the complexes **2.1-2.5** were observed at 379 nm, 347 nm, 340 nm, 265 nm, 328 nm and 256 nm, 328 nm, respectively. TD-DFT calculations have suggested the absorption (S_o to S_1 transitions) of the respective complexes be at 340 nm, 383 nm, 332 nm, 392 nm, and 326 nm, respectively. The solid-state emission spectra of the

complexes (Fig. 2.4a) were very weak emissions at a wavelength far away from theoretically expected S_1 to S_0 transitions, as listed in Table 2.2. In the present case, the ligands were non-fluorescent. Zinc(II) complexes are well known to show photoluminescence due to aggregation,[24-25] Thus, the experimentally observed emissions of these complexes **2.1**-**2.5** were aggregation-induced and originated from metal-based emission due to aggregations. The aggregation-induced emission or quenching refers to emission at a higher or lower wavelength than the regular S_1 to S_0 transitions due to aggregation.[26,27]

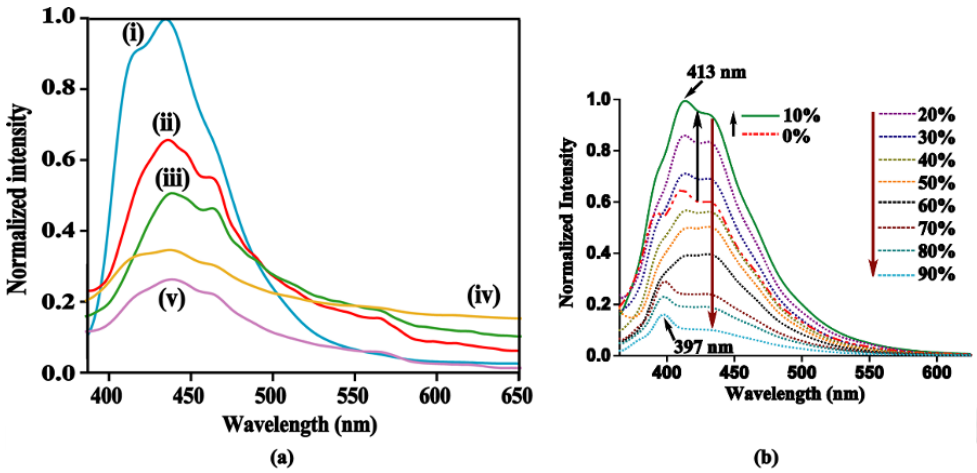

Figure 2.4. Photoluminescence spectra of the (a) solid samples of complexes **2.1**-**2.5** (λ_{ex} = 350 nm in all cases), **2.1** (10^{-4} M in DMSO) upon addition of different amounts of water λ_{ex} = 350 nm) (thick lines show an initial increase, whereas dotted lines show a decrease in emission)

Table 2.2. UV-visible and emission, quantum yields, and lifetimes of the solid samples of complexes **2.1**-**2.5**

Complex	Observed absorbance wavelength (nm)	Observed emission wavelength (nm)	Quantum Yield (Φ_F)[a] (%)	Lifetime for excited state, τ (ns)	k_{nr} (10^7 s^{-1})	k_r (10^7 s^{-1})	TD-DFT calculated	
							Wavelength (nm)	Oscillator Strength (f)
2.1	379	437	1.48	3.025	25.30	1.093	340	0.0003
2.2	347	438	4.14	3.788	27.40	0.734	383	0.0095
2.3	340	434	2.61	3.554	32.57	0.489	332	0.0002
2.4	350	439	13.56	3.506	24.65	3.867	392	0.0350
2.5	328	448	0.56	3.780	26.30	0.148	326	0.0149

[a] in each case, bi-exponential decay is observed; only the higher lifetime relating AIE is shown here.

The emission spectra of the complexes **2.1**-**2.5** in solution were {10^{-4} M in dimethyl sulphoxide (DMSO) solvent} studied, and possible aggregation-induced emissions were followed by adding different amounts of water. These experiments showed aggregation-induced emission in each case. In all cases, upon addition of water to a solution of the metal complex in DMSO, initially the emission intensity was increased, followed by quenching

(Fig. 2.4b). The enhancement in emission intensity without a shift in emission wavelength at low water concentration indicated that they retained intermolecular self-assembly among the molecules of the zinc(II) complex under consideration. As the concentration of water was increased, the water molecules participated in the formation of hydrogen bonds to reconstruct or reorganize the self-assemblies of the complexes, resulting in quenching of emissions with a shift of emission to a shorter wavelength.[28]

This chapter showed the self-assemblies of the five zinc(II) complexes starting from very closely structurally related positional isomeric ligands and successfully demonstrated the importance of the directional hydrogen bonds of the nitro and amide groups. The energetic aspects through DFT calculation were used to show that the multicomponent reactions at ambient conditions did not necessarily provide the lower energy composition of zinc complexes, and self-assemblies have influenced emission properties in both solid and solution states despite having non-fluorescent ligands in the complexes.

Chapter 3. Characterization of assemblies of semi-flexible urea and thiourea derivatives and their salts with mineral acids

(R. Brahma and J. B. Baruah, *New J. Chem.*, 2023, **47**, 6211–6223)

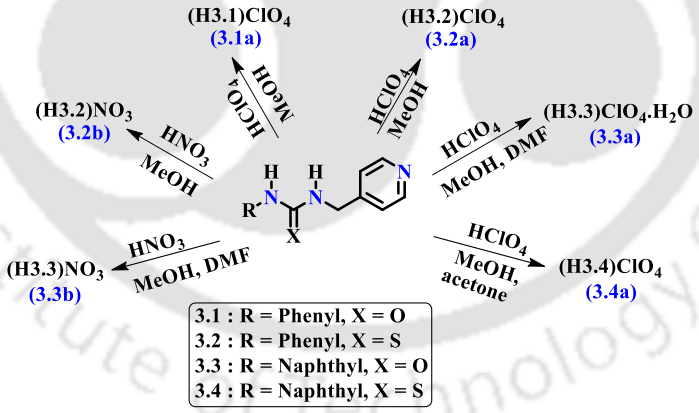

Scheme 3.1. The semi-flexible pyridine-derived urea derivatives, their nitrate and perchlorate salts

In this chapter, self-assemblies of four urea and thiourea derived compounds 1-phenyl-3-(pyridin-4-ylmethyl) urea (**3.1**), 1-phenyl-3-(pyridin-4-ylmethyl) thiourea (**3.2**), 1-(naphthalen-1-yl)-3-(pyridin-4-ylmethyl) urea (**3.3**), and 1-(naphthalen-1-yl)-3-(pyridin-4-ylmethyl) thiourea (**3.4**) and their release from salts are presented. A series of compounds and their salts were prepared by treating them with mineral acids, as shown in Scheme 3.1. The structural studies have provided the roles of the aryl groups and semi-flexible pyridylmethyl

units in the respective self-assemblies and distinguish the packing and conformations in urea and thiourea derivatives.

The self-assembly of the anhydrous form of **3.1** was reported in the literature to have intermolecular hydrogen bonding between one of the two -NH groups and the $N_{pyridyl}$ atom of **3.1** (Fig. 3.1a).[29] However, we obtained a monohydrate of **3.1** (i.e., **3.1.H$_2$O**), which consisted of hydrogen bonding interactions between O_{water} and two -NH groups of the urea part, and the H-atoms of the water of crystallization formed hydrogen bonds with both pyridyl N-atom and carbonyl O-atom. The two -NH groups are in *syn-syn* orientations. The single crystal structure of **3.2** revealed the presence of thioamide-thioamide synthon $R^2_2(8)$ formed by N-H···S hydrogen bonding with an *anti-syn* orientation of the -NH groups (Fig. 3.1a). These hydrogen-bonded dimers are self-assembled to form hydrogen-bonded hexamer (Fig. 3.1b). The urea having naphthyl group (**3.3**) crystallized with a molecule of water of crystallization, **3.3.H$_2$O**, it has a *syn-syn* orientation of the two -NH groups. It consisted of urea tape synthon $R^1_2(6)$. The water molecule is hydrogen-bonded with the $N_{pyridyl}$ atom of **3.3**. In the case of **3.4**, the *anti-syn* orientation of the -NH groups is observed.

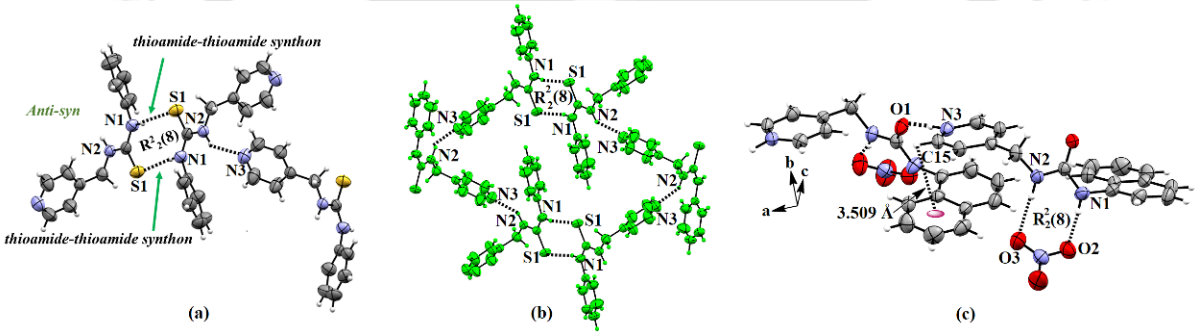

Figure 3.1. Self-assembly in (a) thioamide-thioamide synthon in **3.2**, (b) hydrogen-bonded hexamer in **3.2**, and (c) **3.3b**

We prepared salts of oxyacid having tetrahedral and planar anions, namely perchloric and nitric acid, to study their assemblies with the urea and thiourea derivatives. This study aimed to identify the distinct features of self-assemblies, such as the thiourea derivatives as analogous urea derivatives, which are known to recognize anions in distinct manners.[10, 30,31,34] The orientations of the urea (or thiourea) unit in the parent compounds **3.1**-**3.4** and their salts were guided by anions and the aromatic group on the remote site from the pyridyl group. The perchlorate salt of **3.1** (**3.1a**) had the *syn-syn* orientation; perchlorate salt of **3.2** (**3.2a**) had the *anti-syn* orientations, whereas the nitrate salt of **3.2** (**3.2b**) had *syn-syn* orientations. In the salt, (**3.4a**), that is **(H3.4)ClO$_4$**, the orientations of the -NH groups provided *anti-syn orientation*. The naphthyl group instead of phenyl made a difference in orientation in such

salts. As an illustration, the *syn-syn* orientation of the urea part of the naphthyl group containing urea derivative **3.3** in the nitrate salt, **3.3b**, is shown in Fig. 3.1c.

The solid samples of **3.3** and its corresponding salts showed interesting emission properties (Fig. 3.2). **3.3b** showed dual emissions at 386 nm and 509 nm upon excitation at 335 nm, which was a special case to show as a characteristic signature of the compound in solid state. This was due to locally-excited and twisted intramolecular charge transfer (TICT) states.[32]

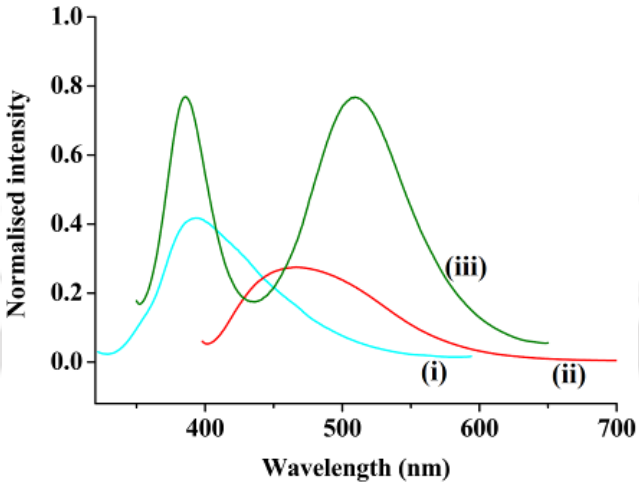

Figure 3.2. (a) Photoluminescence spectra of the solid samples of (i) **3.3.H_2O** (λ_{ex} = 307 nm, λ_{em} = 393 nm), (ii) **3.3a** (λ_{ex} = 383 nm, λ_{em} = 471 nm), (iii) **3.3b** (λ_{ex} = 335 nm, λ_{em} = 386 nm, 509 nm)

The compound **3.3** was soluble in water, and in solution, it had an emission at 385 nm (λ_{ex} = 285 nm). Fluorescence spectroscopic titration of an aqueous solution of **3.3** with different aliquots of perchloric acid showed emission quenching with increasing concentration of the perchloric acid. This was due to the protonation of the $N_{pyridyl}$ -atom of **3.3**, resulting in the reorganization of the inter-molecular hydrogen bonds. We also studied the possibility of anion exchange in **3.3a** by arsenite (As^{3+}) or arsenate (As^{5+}). Upon titration with sodium salts of As^{3+} and As^{5+}, in both cases, an identical increase in emission intensity due to the release of **3.3** was observed, same effect was observed in the fluorescence titration with a dilute solution of NaOH. Hence the emission changes in these cases were due to acid-base properties.

Based on these fluorescence titration results, the release of the parent urea from the composites of **3.3**, **3.3a**, and **3.3b** with calcium oxide in different molar ratios, 1:1, 2:1, 3:1, and 4:1 (maintaining a constant mole of calcium oxide in all the cases) was studied. These composites were prepared by grinding in a mortar pestle; pellets were prepared by pressing under a hydraulic press. The emission intensity of the aqueous solution of the respective

composite pellet dispersed in water was recorded at different time intervals. With increasing time intervals, the composite pellets released the parent urea molecule **3.3** into the solution, which was confirmed by monitoring increase in the intensity of emission of each solution at 385 nm. A representative example of the release of **3.3** from **3.3a**, pellet (1:1 molar ratio) and a comparison of **3.3** release from different molar ratio pellets of **3.3a @CaO** are shown in Fig. 3.4.

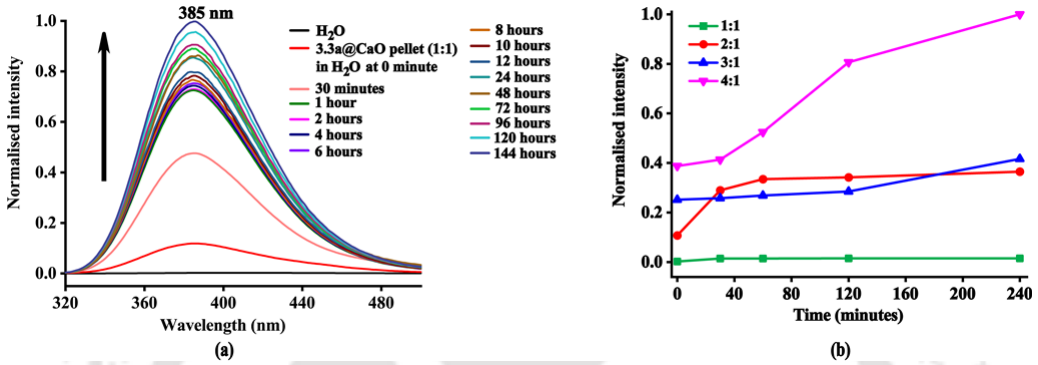

Figure 3.4. Changes in the fluorescence emission intensity during the release of **3.3** from **3.3a @CaO**, pellet (1:1 molar ratio) in water (λ_{ex} = 258 nm), (b) Plots of intensity versus time of different ratios of **3.3a @CaO** pellets in water (λ_{ex} = 258 nm, λ_{em} = 385 nm)

From the time-dependent study of different composites, anion dependency on the release of **3.3** was established. A small amount of calcium oxide was good enough to break the ionic perchlorate salt. Whereas, the less ionic composites prepared with the neutral form and nitrate salt required higher amounts of calcium oxide to show better efficiencies.

The salient points from this chapter were to reveal that the *syn-syn* or *syn-anti* forms are stabilised by weak interactions. The nitrate salt **3.3b** showed dual emission, which is, in fact a rare case in the solid state. Finally, the release of parent compound **3.3** and its protonated form from their respective composite with calcium oxide showed that salts can release parent compound **3.3** more easily that the perchlorate salt **3.3a**, releases **3.3** much easily than the nitrate salt **3.3b**.

Chapter 4: Zinc (II) and cobalt (II) dicarboxylate coordination polymers having pyridine urea-based ligand

(R. Brahma and J. B. Baruah, *CrystEngComm*, 2021, **23**, 3812–3827)

Chapter 4 deals with the synthesis, characterization, and dye adsorption properties of five dicarboxylate-based 2D-coordination polymers (CPs) **4.1-4.5** having 1-phenyl-3-((pyridin-4-yl)methyl)urea (**$L_{4.1}$**) as co-ligands. They have general formula **$[M_2(L_{4.1})_2(dicarb)(H_2O)_2]_n$** {dicarb = succinate or fumarate for M = Co (II) and Zn (II); terephthalate for M = Co (II)}. The coordination polymers were prepared at ambient conditions by mixing the appropriate amounts of the reactants in methanol (Scheme 4.1). While the attempt to prepare an analogous terephthalate coordination polymer of zinc with ligand **$L_{4.1}$**, did not result in the incorporation of the **$L_{4.1}$** to the metal site but yielded a zinc-terephthalate 2D-coordination polymer. This coordination polymer $[Zn_4(Ter)(H_2O)(DMF)_2]_n$ (**CP-4.5**) is reported in the literature.[33]

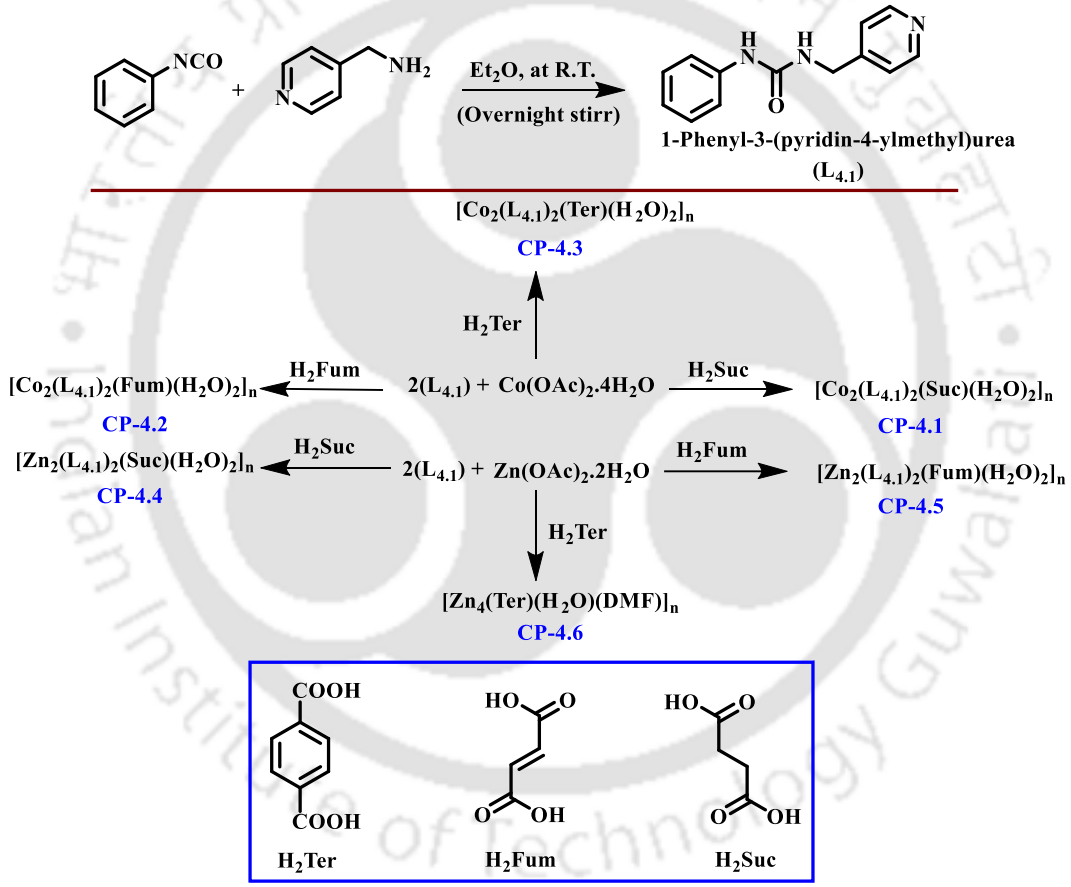

Scheme 4.1. Synthesis of different Zn(II) and Co(II) dicarboxylate coordination polymers (**4.1-4.6**) of pyridyl urea ligand **$L_{4.1}$**

Self-assemblies in the coordination polymers **4.1-4.5** involved C-H···π and hydrogen bonds of the coordinated ligands, namely, aqua or dicarboxylates. Except the coordination polymer **CP-4.3**, the isostructural coordination polymers **4.1**, **4.2**, **4.4**, and **4.5** had urea tapes with graph set-notation $R^1_2(6)$ (Fig. 4.1a). The interesting feature of the coordination polymers is

having C-H···π interactions between pyridyl ring and phenyl ring of the ligand **$L_{4.1}$** in the coordination polymers **4.1-4.5** which locks the phenyl ring (Fig. 4.5b).

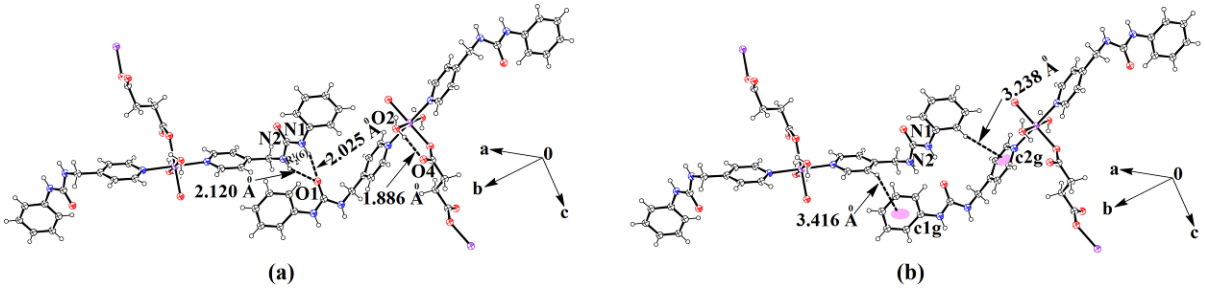

(a) (b)

Figure 4.1. (a) Urea tapes (mark on the fig) and (b) C-H···π interactions in **CP-4.1**

The solid sample of the ligand **$(L_{4.1})\cdot H_2O$** showed emission at 473 nm, 492 nm, 530 nm (λ_{ex} = 330 nm; Fig. 4.2a). The cobalt (II) coordination polymers **4.1-4.3** were non-emissive due to the paramagnetic cobalt (II) centre. Some zinc(II) complexes show dual emission due to TICT and metal-to-ligand charge transfer transition.[34-35] In the present case, the zinc(II) coordination polymers **4.4** (262 nm, 368 nm) and **4.5** (281 nm, 384 nm) showed dual emission (λ_{ex} = 330 nm; Table 4.1), of which one emission occurred due to S_1-S_0 transition, and second one due to aggregation-induced emission.

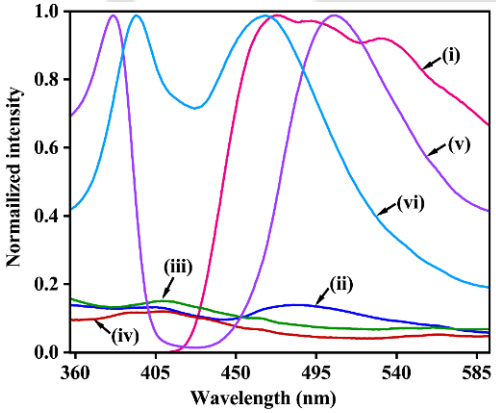

(a)

Compound	λ_{max} (nm)	λ_{em} (nm)
$(L_{4.1})\cdot H_2O$	291	473, 492, 530
CP-4.1	282, 494	Non-emissive
CP-4.2	282, 498	Non-emissive
CP-4.3	324, 498	Non-emissive
CP-4.4	262, 368	381, 506
CP-4.5	281, 384	394, 467

(b)

Figure 4.2. (a) photoluminescence spectra of the solid samples of (i) **$(L_{4.1})\cdot H_2O$**, **CPs** (ii) **4.1**, (iii) **4.2**, (iv) **4.3**, (v) **4.4**, (vi) **4.5** (for all compounds, λ_{ex} = 330 nm), (b) a table showing absorbance and emission wavelengths of the **$(L_{4.1})\cdot H_2O$**, and **CPs 4.1-4.5**

The coordination polymers, in general, have applications in dye adsorption.[36] The coordination polymers **4.1-4.5** were utilized for the adsorption of anionic dyes, namely, methyl orange, phenol red, and cationic dyes: methylene blue trihydrate, and rhodamine B (Fig. 4.3, Table 4.1). **CP-4.6**, without the pyridyl urea ligand, was also used for the dye adsorption study. Adsorptions of these dyes was studied by UV-visible absorption spectroscopy. This study showed that the methyl orange adsorption was selective by **CP-4.3**,

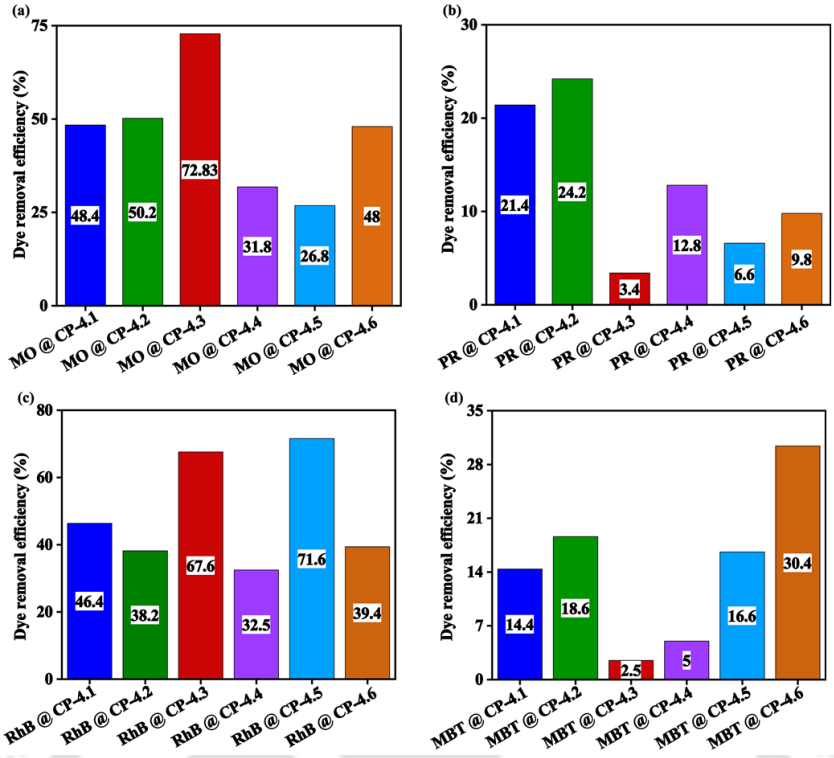

Figure 4.3. Relative removal efficiencies (a) methyl orange (MO), (b) phenol red (PR), (c) rhodamine blue (RhB), (d) methylene blue trihydrate (MBT) after treating with **CPs 4.1-4.6** (the spectra were taken after treatment of CPs with the dye for three hours)

Table 4.1. Amount and percentage of dye adsorbed by the coordination polymers **4.1**-**4.6** (a) methyl orange, (b) phenol red, (c) rhodamine B, and (d) methylene blue trihydrate

Coordination polymers	**Amount of dye adsorbed, q_e, (mg g^{-1}) and {dye removal (%)}**			
	MO	**PR**	**RhB**	**MBT**
4.1	1.320 {48.4}	0.632 {21.4}	1.852{46.4}	0.45 {14.4}
4.2	1.369 {50.2}	**0.714 {24.2}**	1.524 {38.2}	0.58 {18.6}
4.3	**1.986 {72.83}**	0.100 {3.4}	2.698 {67.6}	0.08 {2.5}
4.4	0.867 {31.8}	0.378 {12.8}	1.297 {32.5}	0.16 {5}
4.5	0.731{26.8}	0.194 {6.6}	**2.858 {71.6}**	0.54 {16.6}
4.6	1.309{48}	0.289 {9.8}	1.573{39.4}	**0.95 {30.4}**

and the same coordination polymer was not able to decolorize phenol red (PR). These occurred due to the higher hydrogen bond formation ability of the oxygen atom bearing a negative charge of the sulphonate group of methyl orange with the urea moiety of the coordination polymers. Thus, it provided a means to recognize methyl orange through decolorization affected by hydrogen bonding with the urea sidechains of the coordination polymer. The presence of terephthalate bridges in **CP-4.3** provided a different self-assembly having urea easily accessible to bind to methyl orange better than phenol red. On the other hand, the cationic dye, rhodamine B, was absorbed highest by **CP-4.5** with a removal

efficiency of 71.6%. However, **CP-4.6**, without pyridyl urea ligand **L4.1**, showed the highest adsorption for cationic dye methylene blue trihydrate.

This study revealed that the C-H···π interactions between the pyridyl and phenyl rings locked the phenyl ring, hence significantly contributed to the self-assembly of the coordination polymers. A change in the metal ion changes the hydrogen bonds in the assembly of the pyridyl urea ligand (**L4.1**). The terephthalate bridges in **CP-4.3** provided a self-assembly in which the urea -NH groups were easily accessible to bind methyl orange instead of phenol red. The Zn (II) coordination polymers **4.4** and **4.5** showed dual emission in their solid state.

Chapter 5. *Cis* and *trans* isomers of cobalt (II) nalidixate complex having 1-(4-chlorophenyl)-3-(pyridin-4-ylmethyl)urea

(Manuscript Communicated)

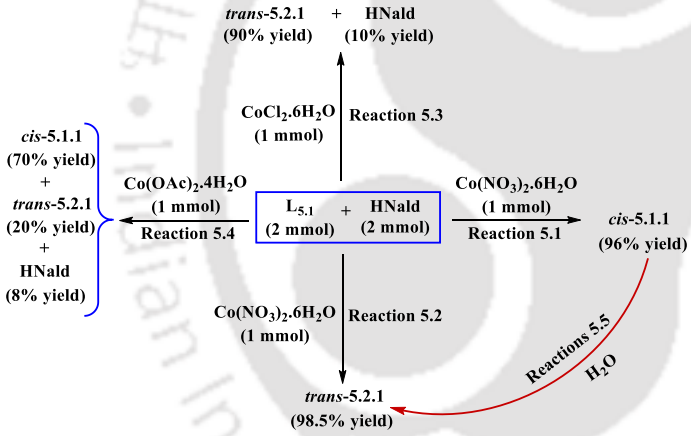

Reaction	Tetrabutylamonnium salt used	Reaction time (hours)	Solvent used, condition for all reactions
5.1	-	2	DMF Reflux, 80°C
5.2	-	1	
5.3	-	1	
5.4	-	49	
5.5	TBACl	1	

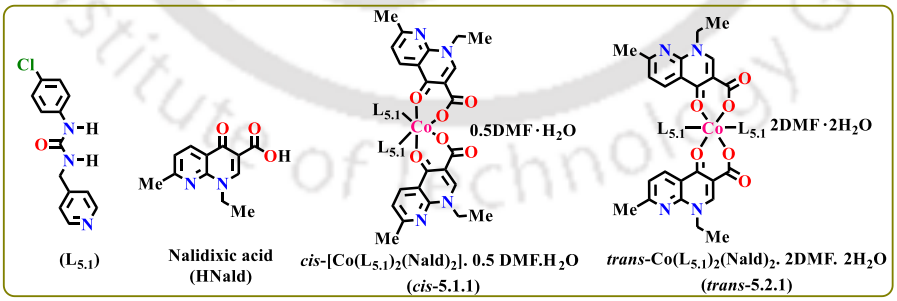

Scheme 5.2. Synthesis of *cis*- and *trans*-isomers of cobalt (II) nalidixate complexes of ligand **L5.1**

In this chapter, *cis*- and *trans*-Co (II) nalidixate complexes of 1-(4-chlorophenyl)-3-(pyridine-4-ylmethyl)urea ligand (**L5.1**) are described. The two complexes were prepared by anion-guided synthesis. The *trans*-isomer was prepared by using $CoCl_2.6H_2O$, whereas, Co (II) salt having nitrate ion yielded both *cis*- and *trans*-isomers under different reaction

conditions (Scheme 5.1). In the presence of nitrate ion in the Co (II) salt, *trans*-isomer was formed. When the same reaction mixture was heated for a longer time, the *cis*-isomer was formed. In reaction 5.4 (Scheme 5.1), the use of $Co(OAc)_2.4H_2O$ resulted in the formation of a mixture of the Co (II) isomers, *cis*- (70% yield), *trans*- (20% yield), and the starting material **HNald** (8% yield). This was confirmed by comparing the powder X-ray pattern of this crude mixture with the simulated P-XRD patterns of the *cis*-, *trans*-, and $\mathbf{L}_{5.1}$.

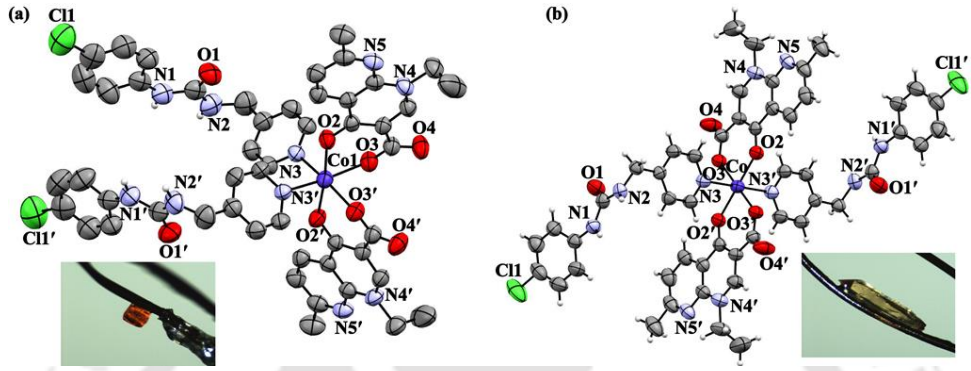

Figure 5.1. Single crystal structure of the (a) ***cis*-5.1.1**, and (b) ***trans*-5.2.1** (solvent molecules are omitted for clarity) (ORTEP diagram drawn with 50% ellipsoid probability) (inset: respective photograph of the crystals)

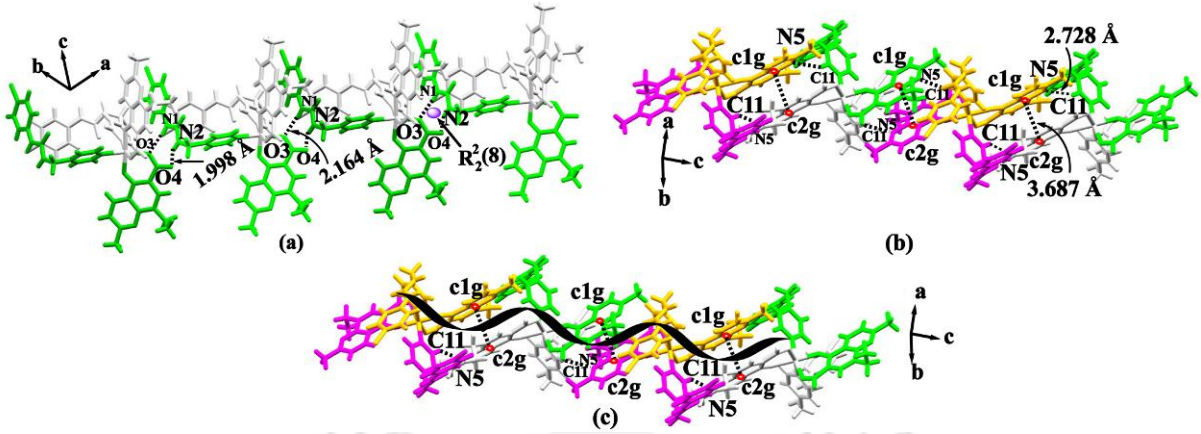

Figure 5.2. (a) Intermolecular hydrogen bonds of -NH groups of $\mathbf{L}_{5.1}$ and carboxylate groups of **Nald**, (b) π···π stacking interaction and C11-H···N5 hydrogen bond, and (c) single-stranded helical arrangement along crystallographic *b*-axis in ***cis*-5.1.1**

The isomers of the complexes were characterized by X-ray crystallography. Both the isomers have distorted octahedral geometry (Figs. 5.1a and 5.1b). The *cis*- and *trans*-geometry was confirmed by the N-M-N angle of 93.02º and 180º, respectively. The *cis*-Co (II) complex had a single-stranded hydrogen-bonded helical arrangement. ***Cis*-5.1.1** was crystallized in space group *C*2/*c*. The intermolecular hydrogen bonding interactions of two -NH groups of

5.1 with the two carboxylate oxygen atoms of the coordinated ligand **Nald** contributed to the single-stranded helical arrangement of this complex (Fig. 5.2c). This hydrogen bonds provided a hydrogen-bonded cyclic unit with $R^2_2(8)$ graph set notation (Fig. 5.2a). The assembly also showed C11-$H_{5.2}\cdots N5_{5.1}$ (≈ 2.728 Å) intermolecular hydrogen bonds (Fig. 5.2b) and π··· π stacking (≈ 3.687 Å) between two 1,8-naphthyridine units of **Nald**.

The magnetic moment of the solid samples of ***cis*-5.1.1** and ***trans*-5.2.1** were 4.49 BM and 4.69 BM, respectively, confirming the +2 oxidation state of the cobalt metal centre in respective complex. Due to the high magnetic moment of Co(II) metal ion, paramagnetic broad ^{1}H-NMR signals were observed from both the isomers of the complex in solution.

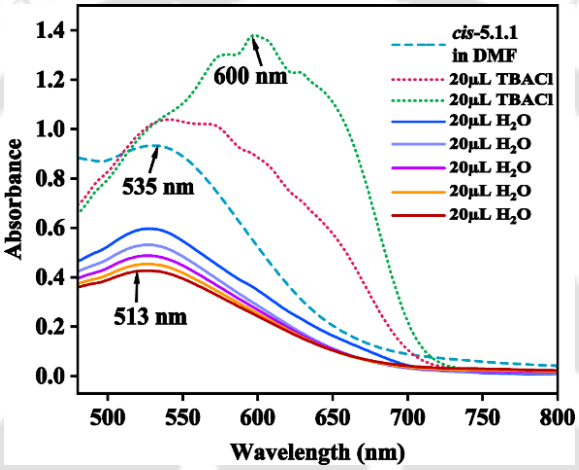

Figure 5.3. Visible spectroscopic titration of ***cis*-5.1.1** in DMF (23.0×10^{-4} M) by adding 20μL aliquot of TBACl in DMF (46.0×10^{-4} M) followed by 20 μL aliquot of water

We found that the ***cis*-5.1.1** was converted to the ***trans*-5.2.1** by treating the *cis*-isomer with TBACl or TBABr salt (Reactions 5.5 and 5.6). However, when TBAF and TBAI salts were used, no product was formed. So, to study the role of these halide ions in the *cis*-to-*trans*-conversion, ***cis*-5.1.1** was titrated with TBAX (X = Cl, Br, I, F) followed by the addition of milliQ water (Fig. 5.3). In case of TBACl, a broad peak was observed at 600 nm, to which water was added, causing a blue shift to at 513 nm, which corresponded to the absorbance of ***trans*-5.2.1**. In case of TBABr, TBAF, and TBAI, this conversion was observed by the formation of an isosbestic point at 597 nm, 618 nm, and 623 nm, respectively, which indicated the involvement of an intramolecular process in this conversion. *Cis*- and *trans*- isomers of inert and non-labile Co (III) complexes undergo interconversion through various twist mechanism.[37] Thus, the halide ions, except Cl^- do not break the chelation of the ligand **Nald**, keeping

the metal ion coordination site intact and thus, these ions Br^-, F^-, I^- prefer to bond with the -NH groups of **$L_{5.1}$**.

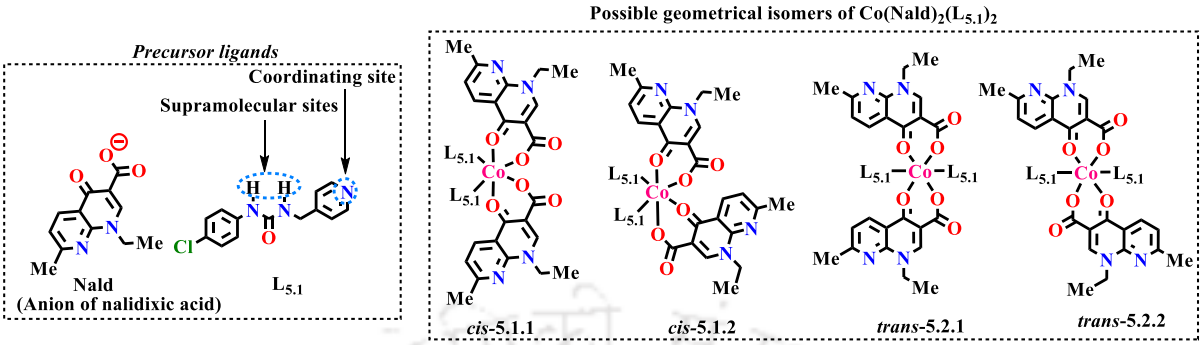

Figure 5.4. (a) The structures of the ligands, (b) The two *cis* isomers and two *trans*-isomers of a cobalt(II) complex with composition **$[Co(Nald)_2(L_{5.1})_2]$**

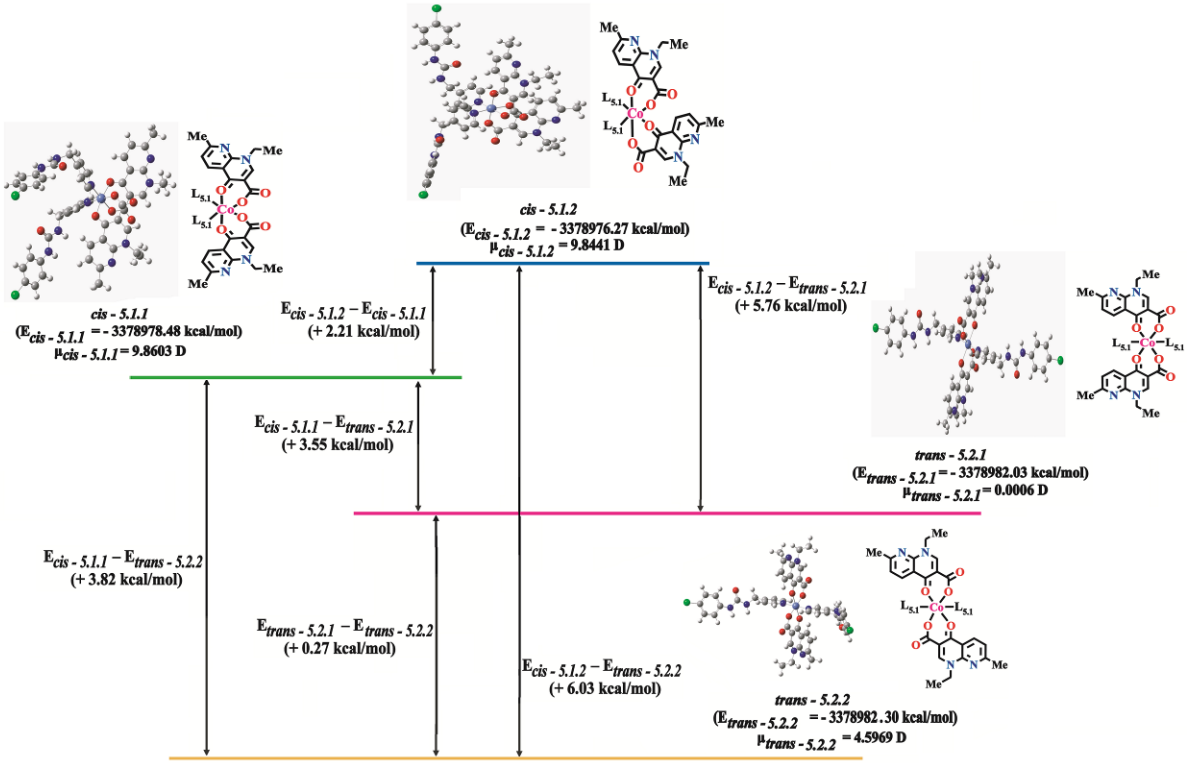

Figure 5.5. Theoretical energies of the ***cis*-5.1.1**, ***cis*-5.1.2** (i.e., ***cis*-$[Co(L_{5.1})_2(Nald)_2]$** and ***trans*-5.2.1**, ***trans*-5.2.2** {i.e., ***trans*-$[Co(L)_2(NALD)_2]$**} (DFT calculation was done with B3LYP functional using 6-31G as the basis set; ball and stick structures are the respective optimized structures of the isomers)

The respective energy the four possible isomers of the complexes shown in Fig. 5.4 and were calculated (Fig. 5.5). Among these, ***trans*-5.2.1** isomer had lower energy than ***cis*-5.1.1** by energy of 3.55 kcal/mole (Fig. 5.5). It was found that ***trans*-5.2.2** was the most stable form, followed by ***trans*-5.2.1**, and ***cis*-5.1.1** and then ***cis*-5.1.2**. The energy difference between the two *cis*-isomers was 2.21 kcal/mol, whereas the energy difference

between ***trans*-5.2.1** isomer and ***cis*-5.1.2** was 3.55 kcal/mol. These energy differences were small, yet the values were significant enough to support the experimental findings on the ***cis*-5.1.1** isomer converting to ***trans*-5.2.1** and the fact of not observing the highest energy isomer (***cis*-5.1.2**).

In this chapter, a study on anion-guided synthesis and reaction conditions influencing synthesis of geometrical isomers of Co (II) nalidixate complexes of a pyridyl urea ligand $\mathbf{L_{5.1}}$ has been demonstrated. This study threw light on the anion recognition in the synthesis of a particular isomer.

A conclusion section is given in the thesis underlying the major overall findings from the present work; this is done to complement the conclusions that are given in the discussion of each chapter. Relevant literature and experimental sections of each chapter are compiled after the results and discussion in each chapter. The crystallographic parameters and specifications of analytical instruments employed in the characterization of the compounds are given in the Appendix. The corresponding crystallographic information files are provided as soft copies attached to the thesis.

References

1 S. K. Kim, J. M. Lim, T. Pradhan, H. S. Jung, V. M. Lynch, J. S. Kim, D. Kim and J. L. Sessler, *J. Am. Chem. Soc.*, 2014, **136**, 495–505.

2 M. Yokoya, S. Kimura and M. Yamanaka, *Chem. – A Eur. J.*, 2021, **27**, 5601–5614.

3 U. Manna, R. Chutia and G. Das, *Cryst. Growth Des.*, 2016, **16**, 2893–2903.

4 M. A. Martínez-Aguirre, D. M. Otero, M. L. Álvarez-Hernández, T. Torres-Blancas, A. Dorazco-González and A. K. Yatsimirsky, 2017, **23**, 171–180.

5 P. Howlader, P. Das, E. Zangrando and P. S. Mukherjee, *J. Am. Chem. Soc.*, 2016, **138**, 1668–1676.

6 J. M. Roberts, B. M. Fini, A. A. Sarjeant, O. K. Farha, J. T. Hupp and K. A. Scheidt, *J. Am. Chem. Soc.*, 2012, **134**, 3334–3337.

7 S. Konduri, D. Bhargavi, J. Prashanth, V. S. Krishna, D. Sriram and K. P. Rao, *ACS Omega*, 2021, **6**, 1657–1667.

8 H. Chen, Y. Liu, X. Cheng, S. Fang, Y. Sun, Z. Yang, W. Zheng, X. Ji and Z. Wu, *Angew. Chemie Int. Ed.*, 2021, **60**, 10833–10841.

9 R. Custelcean, D. E. Jiang, B. P. Hay, W. Luo and B. Gu, *Cryst. Growth Des.*, 2008, **8**, 1909–1915.

10 B. Wu, X. Huang, Y. Xia, X. J. Yang and C. Janiak, *CrystEngComm*, 2007, **9**, 676–685.

11 J. P. Smith, D. S. Yufit, J. F. McCabe and J. W. Steed, *Cryst. Growth Des.*, 2022, **22**, 1914–1921.

12 N. Phukan and J. B. Baruah, *CrystEngComm*, 2016, **18**, 7753–7763.

13 L. Casali, L. Mazzei, O. Shemchuk, K. Honer, F. Grepioni, S. Ciurli, D. Braga and J. Baltrusaitis, *Chem. Commun.*, 2018, **54**, 7637–7640.

14 V. Amendola, L. Fabbrizzi and L. Mosca, *Chem. Soc. Rev.*, 2010, **39**, 3889–3915.

15 R. Custelcean, B. A. Moyer, V. S. Bryantsev and B. P. Hay, *Cryst. Growth Des.*, 2006, **6**, 555–563.

16 R. Custelcean, T. J. Haverlock and B. A. Moyer, *Inorg. Chem.*, 2006, **45**, 6446–6452.

17 D. R. Turner, M. B. Hursthouse, M. E. Light and J. W. Steed, *Chem. Commun.*, 2004, **4**, 1354–1355.

18 J. M. Russell, A. D. M. Parker, I. Radosavljevic-Evans, J. A. K. Howard and J. W. Steed, *Chem. Commun.*, 2006, **4**, 269–271.

19 D. Prabha, D. Singh, P. Kumar and R. Gupta, *Inorg. Chem.*, 2021, **60**, 17889–17899.

20 D. Bansal, G. Kumar, G. Hundal and R. Gupta, *Dalt. Trans.*, 2014, **43**, 14865–14875.

21 K. D. Karlin, R. W. Cruse, Y. Gultneh, A. Farooq, J. C. Hayes and J. Zubieta, *J. Am. Chem. Soc.*, 1987, **109**, 2668–2679.

22 A. G. Blackman, E. B. Schenk, R. E. Jelley, E. H. Krenske and L. R. Gahan, *Dalt. Trans.*, 2020, **49**, 14798–14806.

23 W. M. Singh and J. B. Baruah, *Dalt. Trans.*, 2009, 2352–2358.

24 J. Holub, A. Santoro and J. M. Lehn, *Inorganica Chim. Acta*, 2019, **494**, 223–231.

25 F. Borbone, U. Caruso, S. Concilio, S. Nabha, B. Panunzi, S. Piotto, R. Shikler and A. Tuzi, *Eur. J. Inorg. Chem.*, 2016, **2016**, 818–825.

26 G. R. Suman, M. Pandey and A. S. J. Chakravarthy, *Mater. Chem. Front.*, 2021, **5**, 1541–1584.

27 J. Mei, N. L. C. Leung, R. T. K. Kwok, J. W. Y. Lam and B. Z. Tang, *Chem. Rev.*, 2015, **115**, 11718–11940.

28 R. Brahma and J. B. Baruah, *ACS Omega*, 2020, **5**, 3774–3785.

29 K. Yamaguchi and K. Shudo, *J. Agric. Food Chem.*, 1991, **39**, 793–796.

30 N. Phukan and J. B. Baruah, *Cryst. Growth Des.*, 2014, **14**, 2640–2653.

31 N. Phukan and J. B. Baruah, *CrystEngComm*, 2016, **18**, 3877–3890.

32 H. Naito, K. Nishino, Y. Morisaki, K. Tanaka and Y. Chujo, *Angew. Chemie - Int. Ed.*, 2017, **56**, 254–259.

33 M. Nakhaei, K. Akhbari, M. Kalati and A. Phuruangrat, *Inorganica Chim. Acta*, 2021, **522**, 120353.

34 Z. R. Grabowski, K. Rotkiewicz and W. Rettig, *Chem. Rev.*, 2003, **103**, 3899–4032.

35 X. Bi and Y. Pang, *J. Phys. Chem. B*, 2016, **120**, 3311–3317.

36 Y. Rachuri, S. Subhagan, B. Parmar, K. K. Bisht and E. Suresh, *Dalt. Trans.*, 2018, **47**, 898–908.

37 K. Durka, P. Borowski, K. N. Jarzembska, R. Kamin and D. Schaniel, , DOI:10.1021/acs.cgd.3c00544.

भारतीय प्रौद्योगिकी संस्थान गुवाहाटी
Indian Institute of Technology Guwahati

Table of Contents

Chapters	Page No.
CHAPTER 1: Introduction	1
1.1. Supramolecular aspects of pyridyl amide and pyridyl-derived urea	
1.1.1. Pyridyl amide derivatives	10
1.1.2. Pyridyl urea derivatives	20
1.2. Second coordination sphere from pyridyl amide and pyridyl urea derivatives	
1.2.1. Pyridyl amides in building secondary coordination sphere	25
1.2.2. Pyridyl urea derivatives in building secondary coordination sphere	27
1.3. Pyridyl amide and pyridyl urea as anion sensors	
1.3.1. Pyridyl amide in anion sensing	29
1.3.2. Pyridyl urea in anion sensing	33
1.4. Pyridyl amide and pyridyl urea as cation sensors	
1.4.1. Pyridyl amide in cation sensing	37
1.4.2. Pyridyl urea in cation sensing	39
1.5. Coordination chemistry of pyridyl amide and pyridyl urea derivatives	
1.5.1. Coordination chemistry of pyridyl amide derivatives	42
1.5.2. Flexibility and weak interactions of pyridyl urea ligands in coordination complexes	45
1.6. Pharmaceutical applications of pyridyl amide and pyridyl urea derivatives	47
1.7. Scope of the present work	49
1.8. References	51
CHAPTER 2: Zinc (II) nitrobenzoate complexes of isonicotinamide and nicotinamide	
2.1. Structures and Self-assemblies of complexes **2.1-2.5**	68
2.2. Characterization of complexes **2.1-2.5**	74
2.3. Comparison of optimized energy of zinc(II) complexes of the four neutral combinations	80
2.4. UV-Visible, Photoluminescence and Dynamic Light Scattering study	82
2.5. HOMO-LUMO of the complexes **2.1-2.5**	86

2.6. Conclusion 88

2.7. Experimental section 88

2.8. References 91

Appendix- Chapter 2 94

CHAPTER 3: Characterization of assemblies of semi-flexible urea and thiourea derivatives and their salts with mineral acids

3.1. Synthesis and characterization of pyridylmethyl functionalized phenyl (or naphthyl) urea (or thiourea) derivatives **3.1-3.4** 102

3.2. Self-assemblies of **(3.1)·H_2O, 3.2, (3.3)·H_2O, and 3.4** 104

3.3. Self-assemblies of perchlorate and nitrate salts of **3.1- 3.4** 106

3.4. Spectroscopic characterization of the salts of **3.1-3.4** 111

3.5. Thermogravimetric analysis of hydrated compounds and their salts 114

3.6. Absorbance and photoluminescence studies of **3.1-3.4** and their salts 115

3.7. Stability of the salts of **3.3** in water 118

3.8. Conclusions 121

3.9. Experimental section 123

3.10. References 126

Appendix- Chapter 3 128

CHAPTER 4: Zinc (II) and cobalt (II) dicarboxylate coordination polymers having pyridine urea-based ligand

4.1. Synthesis of coordination polymers (**CPs**) 139

4.2. Synthesis and characterization of ligand **$L_{4.1}$** 140

4.3. Structure and self-assemblies of coordination polymers (**CPs**) **4.1-4.5** 141

4.4. Hirshfeld surface analyses of isostructural **CPs** 148

4.5. Spectroscopic characterization of the coordination polymers **CPs 4.1-4.5** 149

4.6. Aggregation-induced emission of ligand **$L_{4.1}$** 154

4.7. Dye adsorptions by the coordination polymers **CPs 4.1-4.6** 156

4.8. Conclusion 160

4.9. Experimental section 161

4.10. References 163

Appendix- Chapter 4 168

CHAPTER 5: Cis and trans isomers of Cobalt (II) nalidixate complex having 1-(4-chlorophenyl)-3-(pyridin-4-ylmethyl)urea

5.1. Synthesis and characterization of ligand **$L_{5.1}$** 172

5.2. Synthesis and characterization of ***cis*-5.1.1** and ***trans*-5.2.1** 174

5.3. Spectroscopic characterization of ***cis*-5.1.1** and ***trans*-5.2.1** 183

5.4. ***cis*-5.1.1**-to-***trans*-5.2.1** conversion study through UV-visible spectroscopy 187

5.5. Comparison of torsion angles of the urea part in ligand **$L_{5.1}$**, and two isomeric complexes 190

5.6. Circular dichroism and optical activity of ***cis*-5.1.1** 195

5.7. Conclusion 200

5.8. Experimental section 200

5.9. References 203

Appendix- Chapter 5 206

Conclusion and Future Perspective 223

List of Publications 225

Abbreviations used:

AIE: Aggregation-induced emission

AIEgens: Aggregation-induced emission luminogens

DMSO: Dimethyl sulphoxide

TICT: Twisted intramolecular charge transfer

LE: Locally excited

NMR: Nuclear Magnetic Resonance

FTIR: Fourier Transform Infrared

DFT: Density Functional Theory

MHC: Major histocompatibility complex

Cys: Cysteine

Glu: Glutamic acid

Lys: Lysine

Ile: Isoleucine

Arg: Arginine

Leu: Leucine

Asp: Aspartic acid

Thr: Threonine

MPAs: Metal-peptide assemblies

NNMT: Nicotinamide N-methyltransferase

CCE: Cycloaddition of CO_2 with epoxide

NLO: Non-linear optical

EDTAM: Ethylenediamine-N,N,N′,N′-tetraacetamide

MRI: Magnetic resonance imaging

CA: Contrast agents

CEST: Chemical exchange-dependent saturation transfer

His: Histidine

PICT: Photoinduced charge transfer

ATP: Adenosine triphosphate

ESI mass: Electrospray Ionisation mass spectrometry

DMF: Dimethylformamide

HIV: Human immunodeficiency virus

VEGFR2: Vascular endothelial growth factor receptor 2

CIF: Crystallographic Information File

MOFs: Metal-Organic Frameworks

DLS: Dynamic Light Scattering

Chapter 1

Introduction

The importance of amide-based compounds stems from their biological indispensability.[1,2] Amides are the principal linking units of a protein; their presence in biomolecules influences various aspects of life and basic sciences.[3,4] The ability to form hydrogen bonds by amides plays a key role in stabilizing the secondary structure of proteins,[5,6] and other important biological systems, such as protein-nucleic acid interactions.[7,8] The amide derivatives adopt various hydrogen-bonded synthons and have versatilities in supramolecular chemistry.[9] Due to the delocalization of the non-bonding electrons on the nitrogen atom of the amide bond with the C=O bond, the activation barriers for C-N bond rotation in different amides are between 10-35 kcal/mol, which is subjected to the effect of N-alkyl groups on the activation barrier.[10] As a result, the amide C-N bond adopts a partial double bond character, resulting in the planarity of the amide, as well as the equivalence of two identical functional groups attached to the nitrogen atom. For example, the two methyl groups of dimethylformamide are distinguishable at low temperatures. The torsion angles of O=C-C-N, O=C-C-R, and O=C-N-H planes across the carbonyl of a dipeptide unit **1.2** (in Fig. 1.1) guide the skeletal backbone adopting a particular type of secondary structures by a protein, and these geometrical dihedral angles are well known as Ramachandran angles that are used to understand and describe different forms.[11]

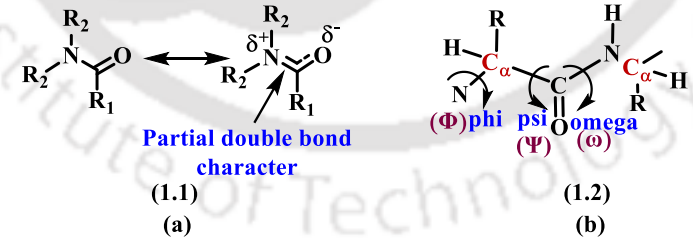

Figure 1.1. (a) Partial double bond character of amide bond; (b) the torsion angles deciding the geometry of a peptide bond

The geometrical aspect of amides has been a critical feature in regulating structures and protein assembling.[12,13] Amide bonds are common in the structures of various natural products and pharmaceutical drug molecules.[14,15] The amide groups are easily degraded under biological and chemical reactions in laboratories and yield biocompatible products, which makes them useful in bio-degradable polymers.[16–18] They also provide binding sites of

biomolecules or directional properties to self-assemblies to recognize biomolecules.[19] In this regard, the artificially designed amide-based receptors find special attention in recognizing biomolecules. For example, peptide-bound pyrene-based compound **1.3,** shown in Fig. 1.2, showed monomer emission (at 375 nm) upon binding to protein, whereas the unbound state showed excimer emission at 475 nm.[20,21] Based on this, the major histocompatibility complex (MHC) proteins or neuropeptide receptors could be easily sensed with high efficacies.[22]

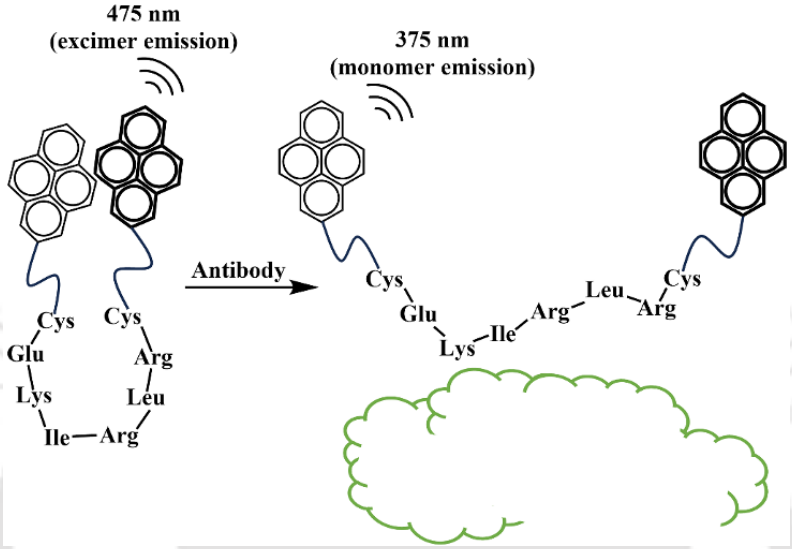

Figure 1.2. A receptor having pyrene linked to peptide (**1.3**) useful in the selective sensing of proteins

Amide-appended small molecules generate interest in optical induction and as enzyme mimics [23,24] and fluorescence-based bio-sensors.[21] Amides as constituents of artificial enzyme mimics, namely in nanoenzymes, have a pivotal role in guiding their self-assembling and reactivity. The polyamide derivatives, related polymeric compounds, and composites exhibiting adsorption properties,[25] separation ability,[26], and delivery of drugs[27,28] are well studied. Recently, squaramide derivatives have been shown to selectively extract biphosphates from solutions.[29] There are large numbers of optically active compounds possessing amide bonds; the simplest examples are proteins. Proteins in general, are optically active due to the asymmetry at the α-carbon atoms of the amino acid residues and polypeptide chains. For example, insulin, a small globular protein, is a peptide hormone produced by pancreatic cells in human beings. It consists of two types of peptide chains: chain A (21 amino acids) and chain B (30 amino acids). This hormone is optically active due to the presence of disulfide bonds, tyrosine, and phenylalanine residues. The circular dichroism spectrum confirmed its α-helical conformation.[30] Additionally, metal-peptide assemblies (MPAs) also form chiral porous materials as they contain nanometre-sized cavities. In metal coordination, the peptides can assemble and fold through non-covalent interactions, thereby

creating protein-like nanocavities. Altering the side chains and amino acid residues of the MPAs can result in enantioselective recognition, which is a guiding tool for biomaterials.[31] As biopolymers, they find applications in designing materials with diverse properties. Biopolymers are natural polymers derived from plants and animals, such as polysaccharides, polyester amides, and proteins/polypeptides. In these biopolymers, the presence of functional groups, such as ester and amide, allow them to interact with various drugs and biomolecules, yielding interesting biomaterials.[32–35] Recently, in 2022, Tachibana and coworkers developed a small peptide molecule that acted as a nicotinamide N-methyltransferase (NNMT) inhibitor. This provided a strategy for drug discovery.[36]

The coordination complexes of amide-based ligands are of great interest due to the importance of such metal complexes in biological systems.[37] Electrochemically active[38] amide-functionalized ferrocene,[39] thiophenes,[40] pyridines,[41] are used in the selective sensing of metal ions and anions.[42] Tetradentate ligands such as pyridyl-amide substituted imidazole **1.4** were utilized as precursors to form N-heterocyclic carbene metal complexes with cobalt and nickel, and these complexes are capable of causing reductions of protons in acetic acid medium. The ligand (**1.4)** and the corresponding cobalt(III) complex (**1.5**) are shown in Fig. 1.3. In the cobalt(III) complex (**1.5**), the imidazole part serves as the precursor for carbene, whereas the amide arms provide the binding sites to the metal ion through a nitrogen atom and also the pyridine binds through the nitrogen atom to the metal ion.[43] There are related ligand systems derived from amide derivatives where they serve as a part of a multidentate ligand forming a heterocyclic carbene complex, such as, with palladium ion.[44]

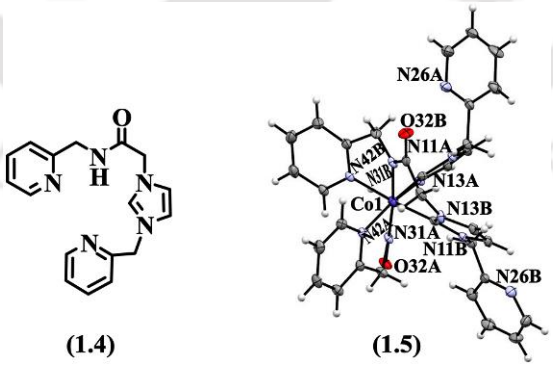

Figure 1.3. Carbene cobalt(III) complex (**1.5**) causing electrochemical proton reduction in acetic acid (ellipsoids are drawn at 50% probability for complex **1.5**)

A large number of amide-based ligands for metal complexes have been reported in the literature.[45–48] Among the amide complexes, generally two types of amide ligands get attention: one is the amide directly participating in coordinating with ligand, and the other is participating as linkers of the ligands deciding the reactivity and geometry without directly

coordinating to the metal ion. The first category includes primary amides, carboxamides, and related ligands, where the amide portion collectively binds with other binding sites serving as multidentate ligands. Examples of primary amide-based ligands based on ethylene diamine carboxylic acid-derived amides are common.[49–53] Examples of commonly used amide-based ligands are listed in Fig. 1.4.

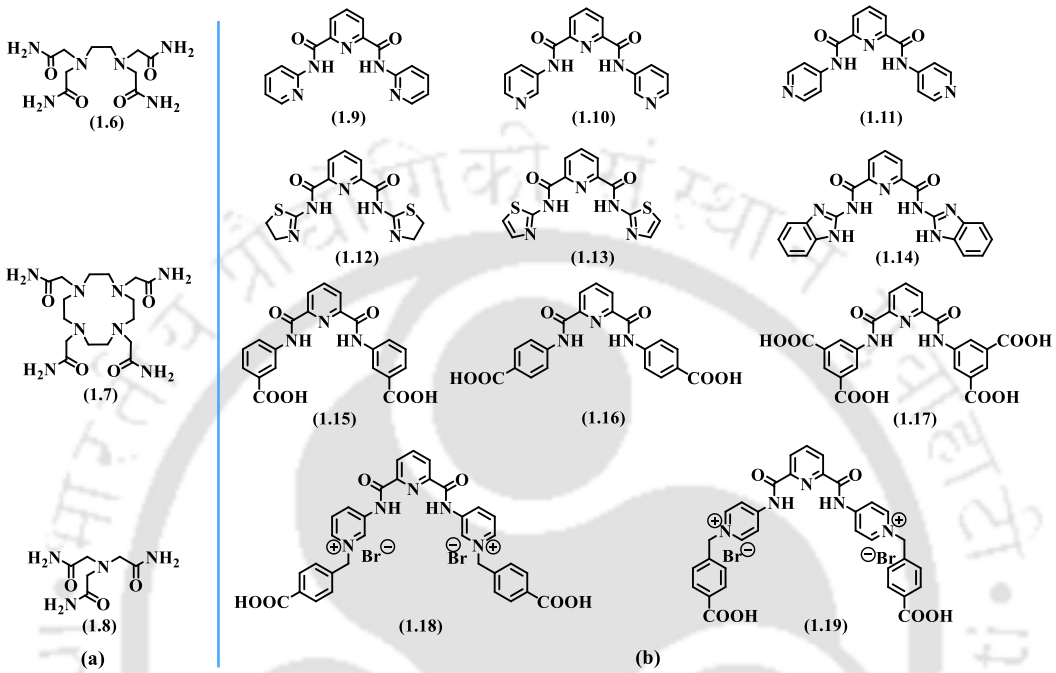

Figure 1.4. Examples of some (a) primary amide and (b) secondary amide-based ligands (adapted from ethylene diamine carboxylic acid and 2,6-pyridine dicarboxylic acid, respectively)

N, N'-diacetyl formamide is the simplest example, which forms a metal complex.[45] On the other hand, the carboxamide and malonamide ligands have drawn interest due to their selective binding towards uranium(VI), and those ligands have been proven to be important in the extraction of uranium and selective binding to thorium, too.[54–56] Secondary amide-based 2,6-pyridine dicarboxylic acid-derived ligands have been utilized in various metal complexation, and they generate interest due to their utilization as metallo-ligands to form different types of clusters, coordination polymer which has applications in sensing, catalysis etc.[57] The amide units attached with an appended group in a small molecule with additional binding sites in addition to the amide group generate interest in coordination chemistry as ligands and in biological studies.[58] Some common amide-tethered compounds designed for various found applications are listed in Table 1.1.

Table 1.1. List of amide-based ligands

Amide-tethered derivatives	Application	Reference
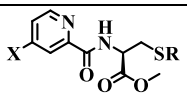 (1.20) : X = H (1.21) : X = Cl	(a) causes tumour cell death by apoptosis. (b) high cellular uptake of the compound.	47
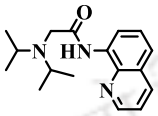 (1.22)	chemosensor of Zn^{2+}, pyrophosphate, and sulphur ions.	59
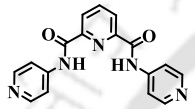 (1.23) : X = N (1.24) : X = C 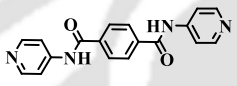 (1.25)	selective towards halides, cyanide, or acetate anions, with only moderate binding affinity toward dihydrogen phosphate.	60
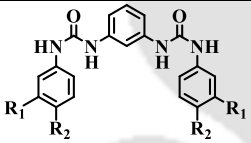 (1.26) : R_1 = -NO_2 , R_2 = -H; (1.27) : R_1 = -H, R_2 = -NO_2	strongly binds with halides, planar, and tetrahedral oxyanions.	61
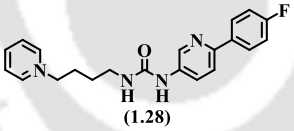 (1.28)	alpha 7 nicotinic acetylcholine receptor agonist.	62
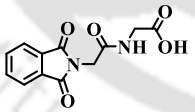 (1.29)	adopted β-pleated sheet assembly after coordinating with Cu(II) and Zn(II) metal ions.	63
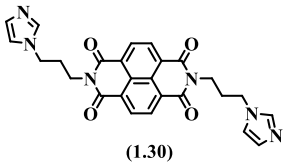 (1.30)	photoluminescence distinction between spherical anions (such as Cl^-, Br^-) (caused quenching) and trigonal planar, or tetrahedral anions (such as ClO_4^-, NO_3^-) (caused enhancement).	64

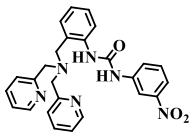 (1.31) 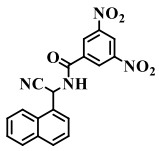 (1.32) 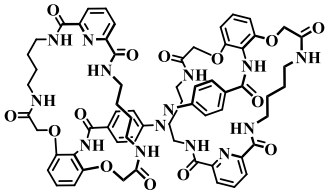 (1.33) 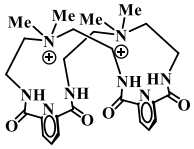 (1.34) 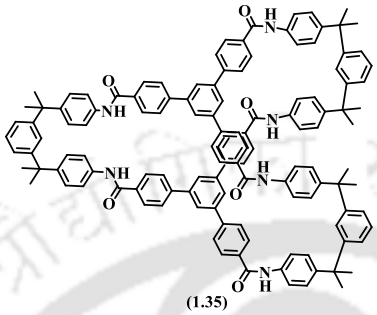 (1.35) 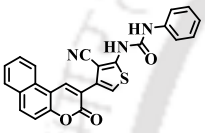 (1.36) 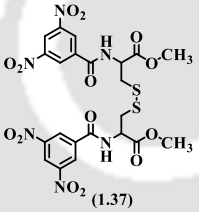 (1.37)	anion recognition.	65–71
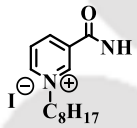 (1.38)	was used as an organocatalyst for (a) CO_2 fixation, and (b) cycloaddition of CO_2 with epoxide (CCE) reaction.	72
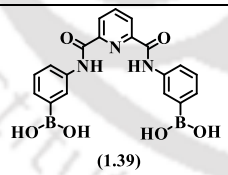 (1.39)	anion and sugar sensor	73
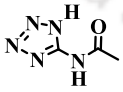 (1.40) 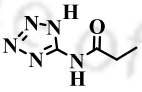 (1.41)	formed metal organic coordination polymers.	74
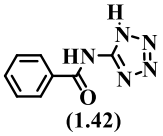 (1.42)	formed metal organic coordination polymers, which showed non-linear optical (NLO) properties.	75

In simple amide-based ligands such as ethylenediamine-N,N,N′,N′-tetraacetamide (EDTAM) (**1.6**), the amidic O-atom is a strong Lewis base in water compared to the alcoholic O-atom. Large metal ions such as Ca^{2+} formed a metal complex (**1.43**) with such ligand by strongly coordinating to the amidic O-atom of EDTAM ligand **1.6** (Fig. 1.5a).[76] These large metal ions tolerate the M-O=C bond angle distortion. Thus, these types of EDTAM-metal complexes have higher formation constant (log K_1). This selectivity of amidic O-atom by Ca^{2+} is also observed in some calcium-binding proteins such as calmodulin,[77] due to the higher affinity of Ca^{2+} for the O-donor atom present in the amide groups of such calcium-binding proteins.

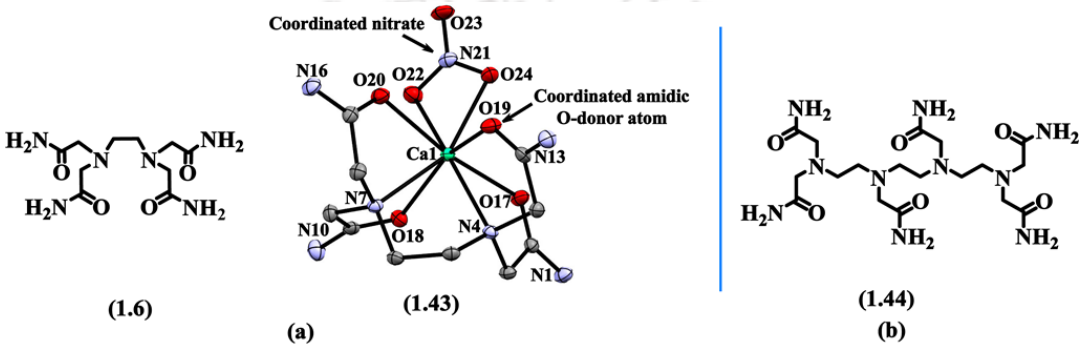

Figure 1.5. (a) Ca^{2+}-EDTAM complex (**1.43**), and (b) triethylenetetramine-N,N,N′,N″,N‴,N‴-hexa acetamide ligand (**1.44**) [ellipsoids are drawn at 50% probability for **1.43**, hydrogen atoms are removed for clarity]

Magnetic resonance imaging (MRI) contrast agents (CA) depend on the chemical exchange-dependent saturation transfer (CEST). In the presence of CEST agent, the signal intensity of water protons is altered by saturating with the strong radiofrequency pulse of mildly acidic protons of the CEST. These acidic protons are in equilibrium with the bulk water. Ochoa and coworkers synthesized triethylenetetramine-N,N,N′,N″,N‴,N‴-hexaacetamide **1.44** (Fig. 1.5b), which formed a metal complex with Yb^{3+} metal ion, with magnetically different amide groups. In solution, this complex had low symmetry and showed applicability as an MRI agent through the CEST effect. Due to the presence of magnetically different amide groups, the CEST effect was smaller than expected.[78]

A strategy based on the through-the-space strategy has also been developed for redox sensing. The probe has a modular design in which a conformationally restricted peptide with a central β-hairpin promoting sequence is flanked by a pair of cysteines. The N-terminus is labeled with a lanthanide chelate (DTPA) and the C-terminus with a carbostyril chromophore, which is a good terbium sensitizer (Fig. 1.6). Under oxidizing conditions, the cysteine residues formed a disulfide bond that tethered the ends of the peptide sequence in close proximity, allowing efficient energy transfer and high emission luminescence from the

metal ion (**1.45**). In a reductive environment, the disulfide bond is broken, and the peptide adopted an extended random coil conformation that reduces the energy transfer, resulting in reduced emission from the metal center (**1.46**). The reduction potential of the disulfide bond can be tuned by incorporating different peptide sequences between the cysteine residues; sequences with high β-turn propensities will favor the formation of the disulfide bond, resulting in a probe with a lower (more negative) reduction potential.[79]

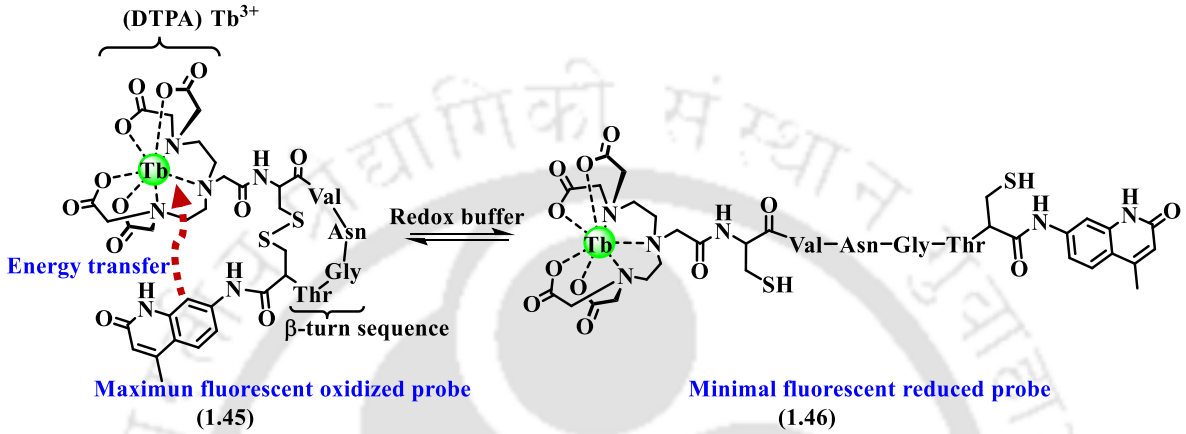

Figure 1.6. Probes based on energy transfer modulated by the conformation of a peptide scaffold. The oxidation state of a disulfide bond is coupled with the luminescence of the DTPA chelate

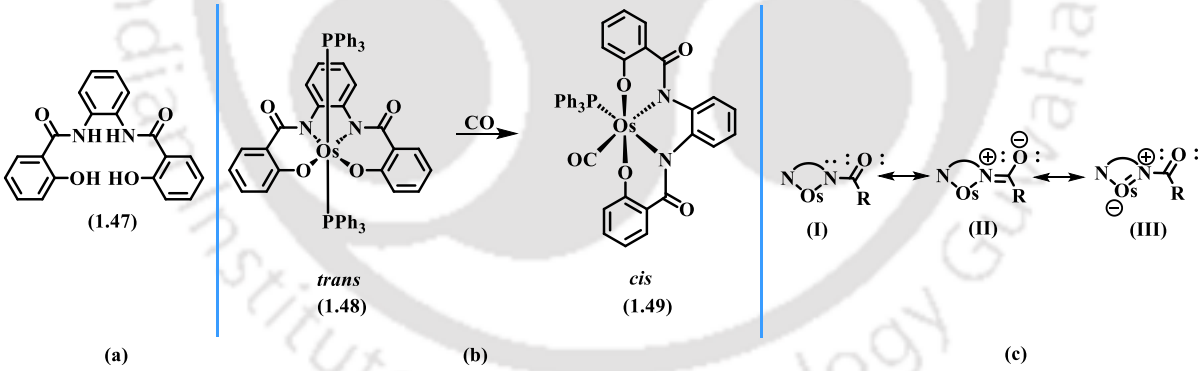

Figure 1.7. *trans* (**1.48**) and *cis* (**1.49**) Os(IV) complexes consisting of amide-based polyanionic chelating ligands (**1.47**). (c) shows the resonance structure of ligand **1.47** coordinated to Os(IV) metal ion through the N-amido atom

Amide functional groups are present in two forms, planar and non-planar. Rotation around the C-N bond of the amide group causes delocalization of amide, which results in a non-planar arrangement of this functional group in some compounds, such as formamide.[80] Earlier in 1960, Santarsiero and coworkers developed amide-based polyanionic chelating ligand (**1.47**) containing osmium(IV) complexes, namely ***trans*-Os(η⁴-1.46)(PPh₃)₂** (i.e., **1.48**) and ***cis*-Os(η⁴-1.46)(CO)(PPh₃)** (i.e., **1.49**). **1.48** consisted of the planar form of ligand **1.47**.

However, in complex **1.48**, the planar N-coordinated amide groups adopted a non-planar arrangement. When **1.48** was treated with a strong π-acid ligand carbon monoxide (CO), one of the PPh_3 ligands was replaced by a CO ligand to give **1.49**. This *trans* (**1.48**) to *cis* (**1.49**) isomerization was achieved due to the change in the amide bonding character, resulting in the delocalization of the amide group of the ligand **1.47** (Fig. 1.7).[81]

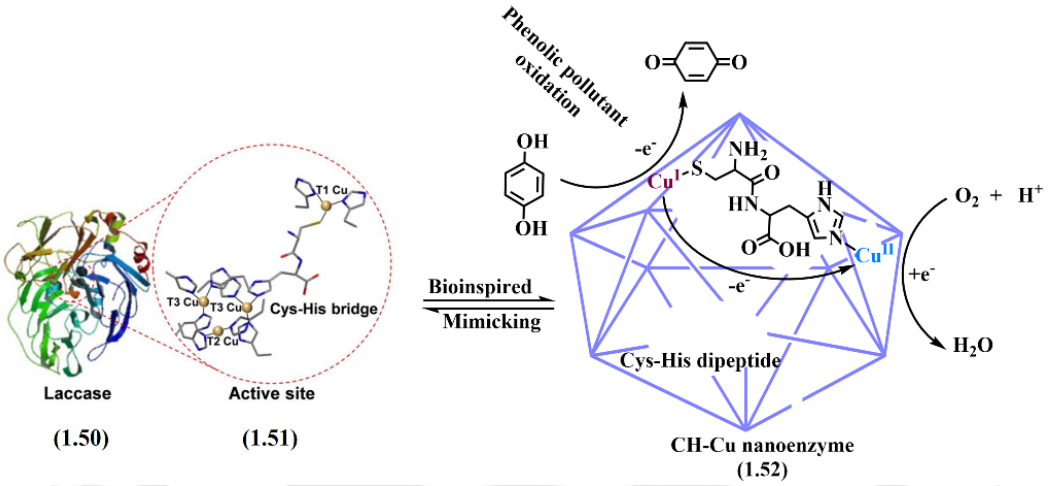

Figure 1.8. Bioinspired laccase-mimicking CH-Cu nanoenzyme **1.52** ("Reprinted from Applied Catalysis B: Environmental, Vol. 254, J. Wang, R. Huang, W. Qi, R. Su, B.P. Binks, Z. He, Construction of a bioinspired laccase-mimicking nanoenzyme for the degradation and detection of phenolic pollutants, Page No. 452-462, Copyright (2019), with permission from Elsevier")

The strategy for the preparation of a new class of nanoenzyme (denoted as CH-Cu, or **1.52**) with laccase-like activity inspired by the structure of the active site (**1.51**) and the electron transfer pathway of laccase (**1.50**) *via* the coordination of Cu^{+}/Cu^{2+} with cysteine (Cys)-histidine (His) dipeptide (Fig. 1.8). The CH-Cu nanoenzymes **1.52** exhibit excellent catalytic activity, recyclability, and substrate universality and have a similar K_m (Michaelis constant) and a higher v_{max} (maximum rate) than laccase at the same mass concentration. They are robust under a variety of conditions, such as extreme pH, high temperature, long-term storage, and high salinity, which can cause severe loss in the catalytic activity of laccase. A higher efficacy of **1.52** compared with laccase in the degradation of chlorophenols and bisphenols is also demonstrated in a batch reaction.[82]

1.1. Supramolecular aspects of pyridyl amide and pyridyl-derived urea

Organizing molecules into regular arrays by weak interactions is highly interesting in generating soft materials. On the other hand, identifying a host system for selective guest

binding or encapsulation requires a closer look at the size, shape, and complementing interactions, which are the prime factors of both the partner components.[83] Inspired by the roles of heterocycles such as imidazole, pyrrole, indole, etc., in proteins, the supramolecular features change; hence, it is necessary to know the role of such heterocycles in the self-assembling of amide-based compounds. In this context, pyridyl amide and pyridyl urea derivatives are ideal candidates for understanding their roles as component/s of non-covalent assemblies or as ligands. They have the combined effect of the amide group and N-atom of the heterocyclic ring, each having independent hydrogen bonding features. The pyridyl group is amenable to change with pH and provides scopes to modulate an assembly by varying pH. These ligands have structural flexibility and adopt different geometries to bind to a metal ion and in molecular assemblies.[84] Coordination compounds formed by pyridine amide-based ligands have innumerable utilities as materials with improved catalytic, adsorption, electronic, optical, and magnetic properties.[85,86] Depending on the directional effect of the amide units as part of ligands in metal complexes, complexes having different topologies are observed. [85,87–89] Pyridyl-derived urea-based compounds have skeletal features of a pyridyl amide derivative, but instead of having one N-H bond of the secondary amide, the urea derivative has two N-H bonds available for hydrogen bonding. Many of these complexes form supramolecular assemblies, and amide is a basis for extending the second coordination sphere of a metal complex for ion and molecular recognitions, which are discussed in the subsequent sections.

1.1.1. Pyridyl amide derivatives

The self-assemblies of the positional isomers of pyridyl-amide with carboxylic acid provide access to understanding the salient features of the commonly observed synthons in a cocrystal of an amide with carboxylic acid. Synthons are the descriptors of hydrogen-bonded repeat units found in non-covalent self-assembly.[90] These are represented by graph set notations[91] based on the number of atoms in the synthon as well as the number of hydrogen bond donors and acceptors. This notation is given as $G^n_m(l)$ differentiation on the type of hydrogen bonds by using notations (G is R for cyclic, D for discrete, and C for hydrogen-bonded chains, l = number of atoms in the unit, m and n = respective number of hydrogen bond donors and acceptors). The amide-amide synthons are generally part of a system that provides additional stability to self-assembly with other stronger synthons. For example, the energy of an acid-amide $R^2_2(8)$ heterosynthon II (Fig. 1.9) is relatively lower as compared to acid-acid

{$R^2_2(8)$}, amide-amide {$R^2_4(8)$}synthons.[92] The common homo and hetero-dimeric synthons[93,92] such as IV {$R^2_2(8)$} and II {$R^2_2(8)$} found in the cocrystals of nicotinamide and isonicotinamide independently with a carboxylic acid are shown in Fig. 1.9. In general, the amide functionality of a compound forms non-covalent assembly through cyclic hydrogen bonded synthons[94] or robust supramolecular synthon such as V {$R^2_4(8)$} of Fig. 1.9.[92,90] There are also examples where amides are involved in forming hydrogen-bonded chain-like structures.[95] There are many examples of cocrystals having acid-amide synthons as the deciding structural elements,[96–99] and several examples to understand the synthon competitions have been studied.[100] An acid-amide heterosynthon consists of one N-H···O and one O-H···O hydrogen bonds.[101] Isonicotinamide also forms cocrystals with phenol.[102]

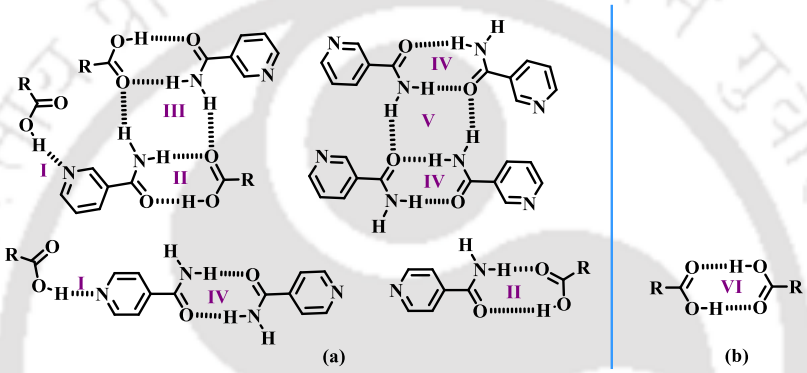

Figure 1.9. (a) Different synthons in the cocrystals of nicotinamide (**1.53**) and isonicotinamide (**1.54**) with carboxylic acid, and (b) carboxylic acid-carboxylic acid synthon

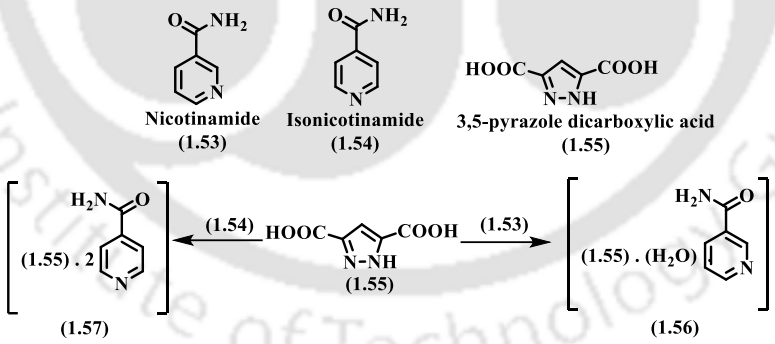

Scheme 1.1. Multicomponent cocrystal formation by 3,5-pyrazole dicarboxylic acid (**1.55**) with **1.53** and **1.54**, respectively

Nicotinamide (**1.53**) and isonicotinamide (**1.54**) formed multi-component cocrystals with N-heterocycle-based dicarboxylic acids, namely, 3,5-pyrazole dicarboxylic acid (**1.55**) (Scheme 1.1). The cocrystal of **1.53** with **1.55** was a 1:1 cocrystal in hydrated form (**1.56**). This cocrystal had acid-pyridine and acid-amide hydrogen-bonded supramolecular heterosynthons.

Synthon I was formed by hydrogen bonding between the carboxylic acid group of **1.55** and pyridine N-atom of **1.53**. The second carboxylic acid group of **1.55** formed a hydrogen-

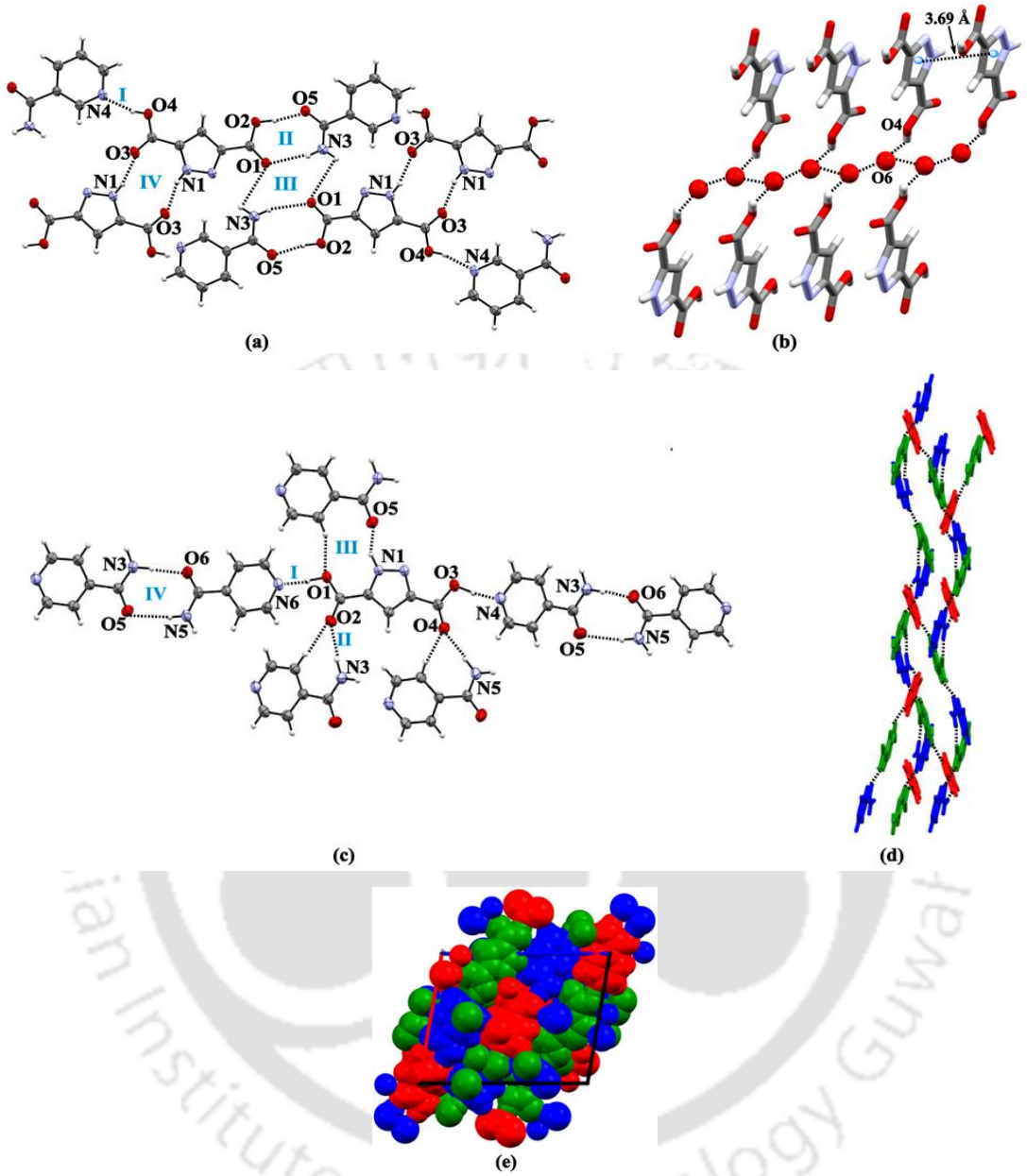

Figure 1.10. Cocrystals of **1.53** and **1.55** showing (a) hydrogen-bonded heterosynthons, (b) infinite water chain formation, and π- π stacking interaction between adjacent molecules of **1.55**; and 2:1 cocrystal of **1.54** and **1.55** showing (c) four heterosynthons, (d) infinite hydrogen-bonded helical chain, (e) packing diagram in an ABBA manner along crystallographic *b*-axis (ellipsoids are drawn at 50% probability)

bonded heterodimeric $R^2_2(8)$ synthon II. This heterodimer was further associated with another similar unit forming an $R^2_4(8)$ heterotetramer, synthon III. Homomeric dimer $R^2_2(10)$ synthon IV was formed through hydrogen bond interaction between pyrazole proton and a carboxylic

acid group of **1.55** (Fig. 1.10a). The water molecule acted as a hydrogen bond donor to the adjacent **1.55** molecule, forming an infinite chain of water molecules (Fig. 1.10b).

A 2:1 cocrystal was formed by **1.54** with **1.55** (i.e., **1.57**). Four different types of supramolecular heterosynthons (I, II, III, and IV) were formed by **1.55** by hydrogen bonding with two molecules of **1.54** (Fig. 1.10c). These heterosynthons generated an infinite 3D hydrogen-bonded helical network (Fig. 1.10d). In the self-assembly, the pyridine rings exhibited face-to-face π-π-stacking with pyrazole rings, and there were C-H···O interactions to provide an arrangement among the molecules in an ABBA manner (Fig. 1.10e).[93]

The self-assemblies of amide-based metal complexes depend on several factors. They may be directly coordinating with a metal ion or remain free. Furthermore, their binding mode may vary, such as only through the oxygen of the C=O coordinates to a metal ion, or it acts as a bidentate ligand by involving the nitrogen and oxygen atoms as the two ligating atoms to a metal ion. The amide part contributes to the self-assembling or second coordination sphere, and auxiliary ligands guide the nature of the non-covalent assemblies. The hydrogen-bonded self-assemblies of metal complexes possessing coordinated amide ligands depend on the geometry of the complex as well as the coordination mode of a ligand; for example, the self-assembly of the *cis* and *trans* complexes **1.59**, **1.60**, and **1.61** were dependent on the coordination modes of the thiocyanate auxiliary ligands as well as the directional nature conferred by the position. In the *cis*-complexes formed by cobalt(II) and nickel(II), there was N-coordination, whereas, in the copper(II) case, it was S-coordination of the thiocyanide ligand. Among the complexes, the complexes **1.59** and **1.60** were isomorphous. In both these complexes, four neighbouring molecules formed centrosymmetric supramolecular $R^2_4(8)$ synthon (Figs. 1.11a and 1.11b). The N-atom of the picolinamide **1.58** acted as a double hydrogen bond donor, while the S-atom of the thiocyanate ligand acted as a hydrogen bond acceptor. The O-atoms of the **1.58** were not involved in the formation of these synthons but were coordinated with the metal ion. On the other hand, complex **1.61** had the thiocyanate at *trans* positions, which were coordinated to the Cu(II) center by the S-atom of each thiocyanate. The free amine portion of the amide of each complex was involved in hydrogen bonding, forming a supramolecular synthon $R^2_4(8)$ (Fig. 1.11c). The difference between the two types of tetramers found in the self-assemblies of the complexes was that the S-atom was involved in the synthon of the assembly of the complexes **1.59** and **1.60**. In contrast, the N-atom of the thiocyanide was involved in complex **1.61**. All these three complexes, **1.59**-**1.61,** formed two-dimensional supramolecular framework structures.[103]

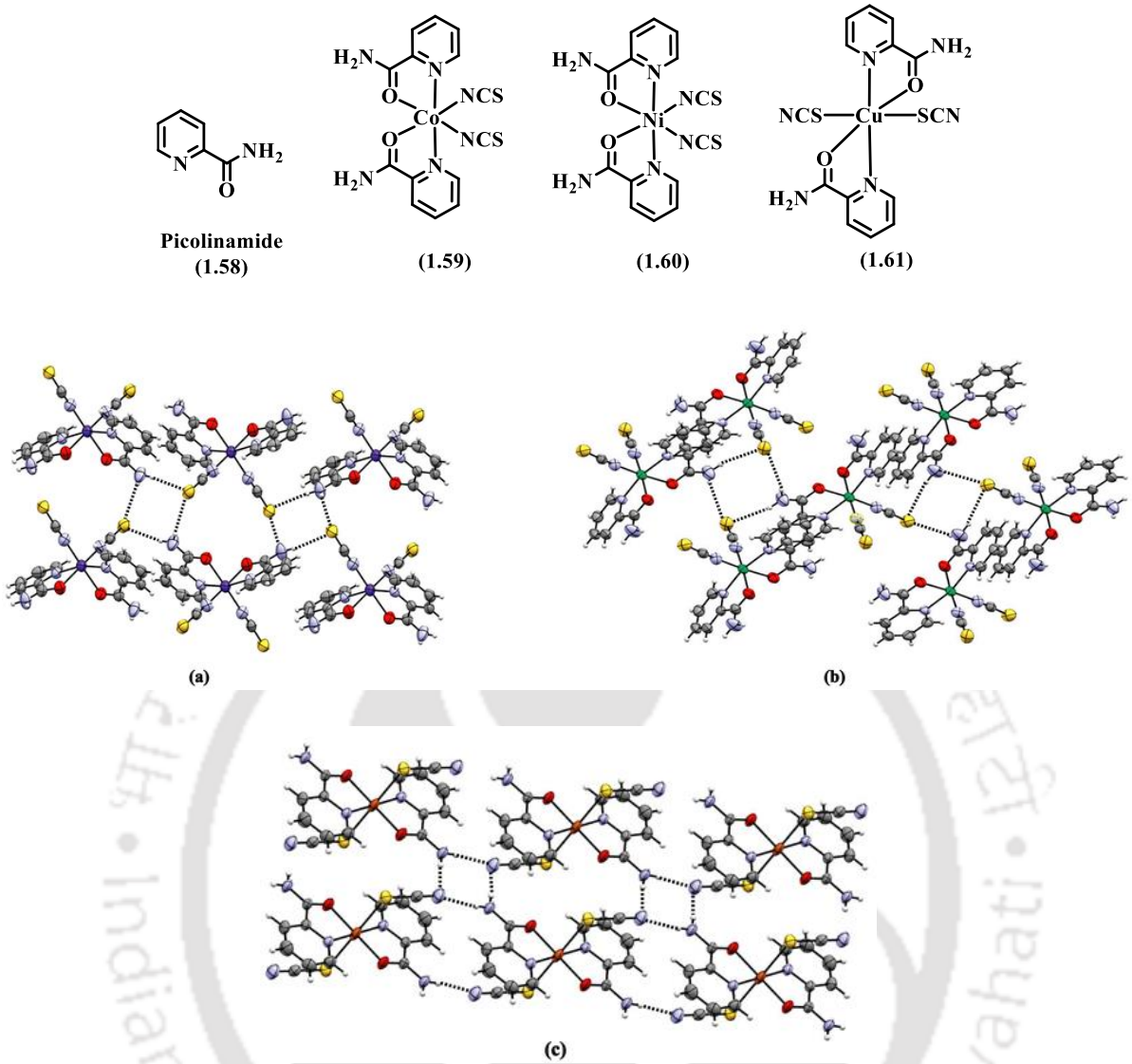

Figure 1.11. The $R^2_4(8)$ synthons in the complexes (a) **1.59**, (b) **1.60**, and (c) **1.61** (ellipsoids are drawn at 50% probability)

The amide group of a ligand remains free in many metal complexes,[86,88,104,105] and those free portions form amide-amide hydrogen bonds. For example, isonicotinamide (**1.54**) forms complexes with silver(I),[106] and Zn(II) ions[107] having such features. The Zn(II) complexes **1.62**-**1.64** had chloride (**1.62**), nitrate (**1.63**), and acetate (**1.64**) as the respective anion. Complexs **1.62** and **1.63** were tetrahedral and octahedral, respectively. Complex **1.64** was a dinuclear complex with mixed coordination geometry. One Zn(II) center had a distorted octahedral geometry, and the second Zn(II) center was pentacoordinated (square pyramid geometry). Out of four acetate ligands, three were coordinated to the two Zn(II) centers in a similar bridging mode, but the fourth one was a bis-chelating ligand for one of the metal centers. In complexes **1.62**-**1.64**, amide-amide homosynthon $R^2_2(8)$ was formed in the H-bonded network, which indicated that the presence of halide ion (chloride), nitrate and

acetate, did not interfere the formation of this homosynthons (Fig. 1.12). It may be noted that in the case of the complex having a perchlorate anion, the amide-amide homosynthons were absent.[107]

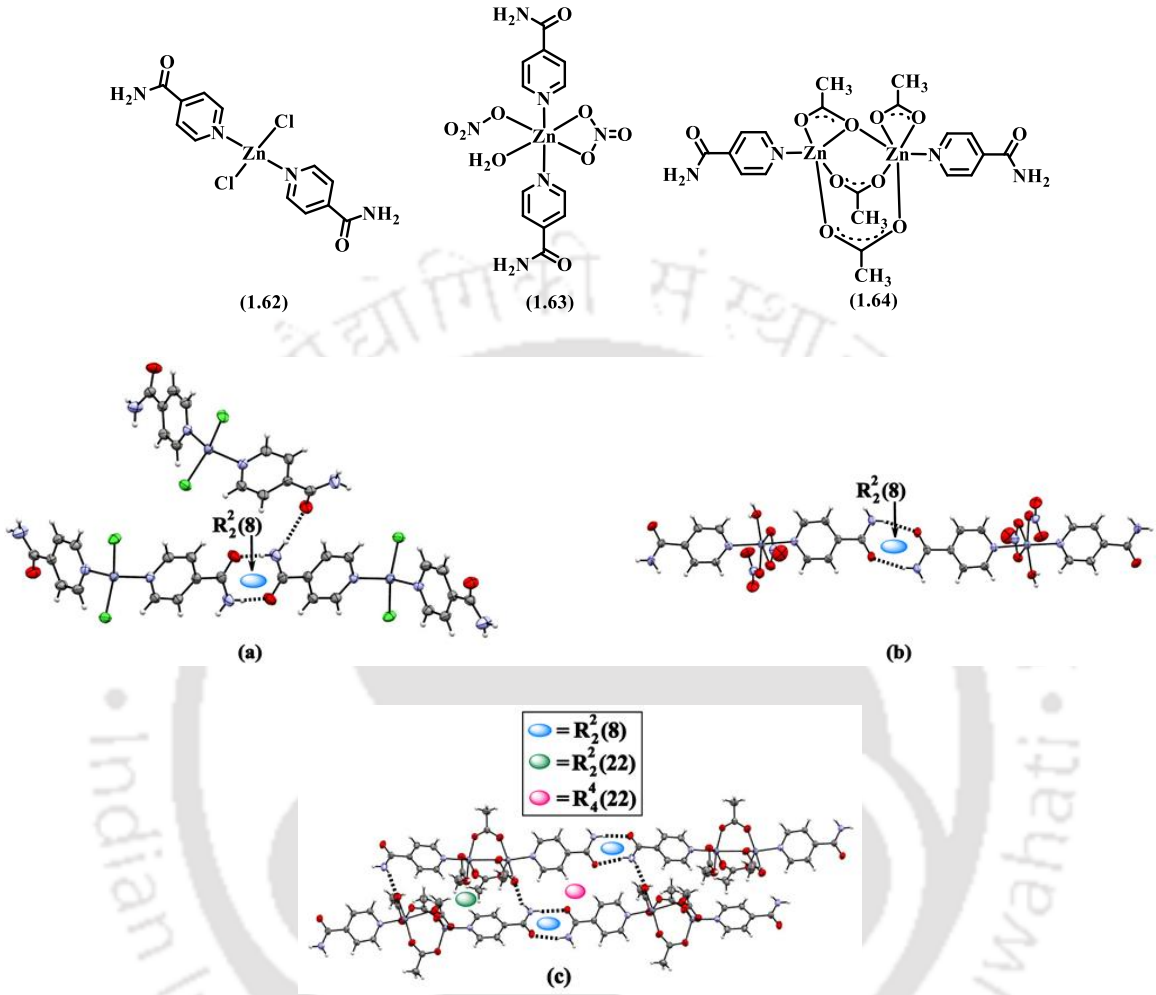

Figure 1.12. Hydrogen-bonded supramolecular synthons in complexes (a) **1.62**, (b) **1.63**, and (c) **1.64** (ellipsoids are drawn at 50% probability)

The metal binding ability of the pyridylidene amide-based ligands, such as **1.65,** depends on the polarity of the solvent,[108] electronic configuration of the metal center.[109,110] The **1.65** is a pincer-based pyridylidene amide ligand, which formed a gold (III) complex, **1.66** (Scheme 1.2), upon reaction with $K[AuCl_4]$.[111] The coordination modes of Au (III) with **1.65** were

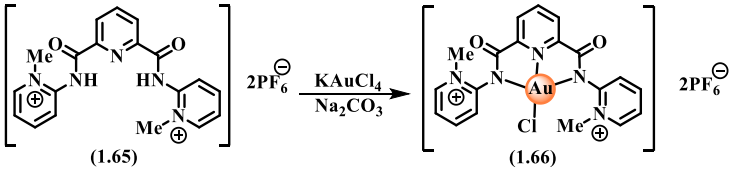

Scheme 1.2. Synthesis of complex **1.66** containing donor-flexible pyridylidene amide ligand **1.65**

found to be different in solid and solution. The solid-state structure of **1.66** showed four-coordination geometry, whereas, in solution, **1.66** showed neutral three-coordinate geometry. This effect was reflected in an electrochemical study, where the reversible reduction of Au (III) was not observed due to the abstraction of the chloride ligand in the solution. Furthermore, the coordination ability of such ligands was dependent on the orientations of the amide groups in a complex.[112,113]

Compound **1.67** is a pyridyl amide-based bisporphyrin cleft consisting of two porphyrin molecules connected to pyridine-2,6-dicarboxamide, known as a handy cleft-shaped molecular tweezer.[114] It has a cleft-shaped cavity, which is sustained by the intramolecular hydrogen bonds between the pyridyl N-atom (basic) and -NH groups (acidic) of amide. It encapsulated guest molecules **G1.1** and **G1.2,** respectively (Scheme 1.3). The single crystal structure of **G1.1@1.67**, i.e., **1.68** (Fig. 1.13a), revealed that it had an antiplanar conformation of the N=C-C=O bond, stabilized by intramolecular hydrogen bonds between the pyridyl N-atom and -NH groups. **G1.1** was present within the bisporphyrin cleft, forming a layered π-stacked donor-acceptor structure with an interlayer distance of 3.44 Å. The oxygen atom of the carbonyl group of **G1.1** was involved in weak CH···O hydrogen bonding with *ortho*-CH protons of the phenyl group of host **1.67**. Here, the amide part provided adequate geometry for encapsulation within the cleft, and those did not participate in intermolecular hydrogen bonds.

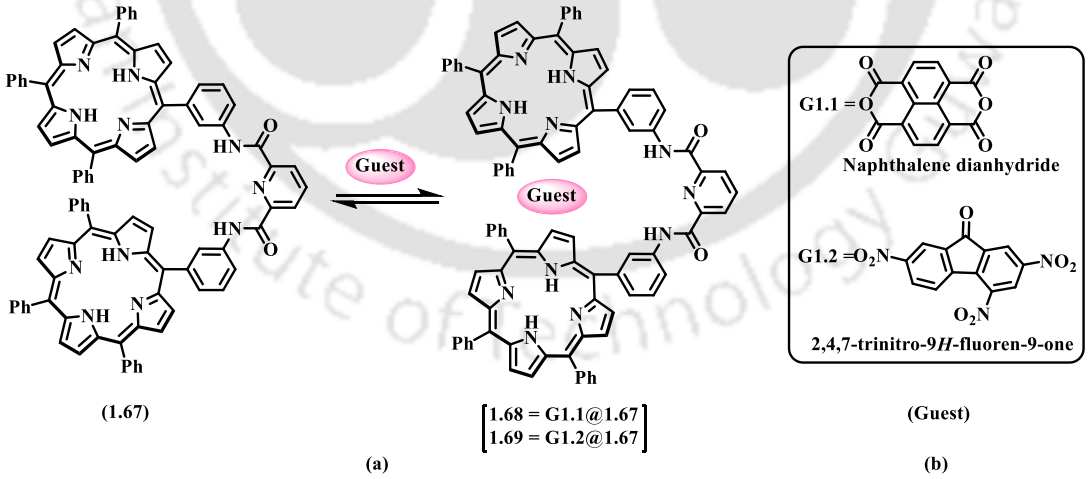

Scheme 1.3. (a) Host-guest complexation of **1.67**, (b) molecular structures of guest molecules (**G1.1** and **G1.2**)

Similarly, in the **G1.2@1.67**, i.e., **1.69**, the guest molecule was located within the cleft with interlayer distances 3.43 Å and 3.34 Å, leading to π-π stacking interactions between the host and guest molecules. The amide N-atom of the host and nitro O-atom of the guest were at a

distance of 3.32 Å and 3.11 Å, indicating weak intermolecular hydrogen bonds (Fig. 1.13b). This host-guest complexation was also guided by C-H···O interactions in addition to the other hydrogen bonds and donor-acceptor interactions present in the assembly. The 1:1 complexation of **1.69** was also confirmed by isothermal titration calorimetry in two solvents, dichloromethane and toluene.[115]

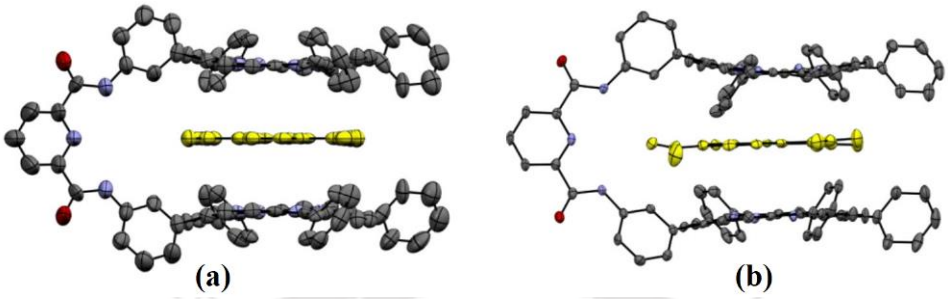

Figure 1.13. Encapsulation of guest molecules **G1.1** and **G1.2** by the host **1.67** forming (a) **1.68**, (b) **1.69** {"Reprinted (adapted) with permission from N. Hisano and T. Haino, *J. Org. Chem.*, 2022, **87**, 4001–4009. Copyright {2022} American Chemical Society. "}

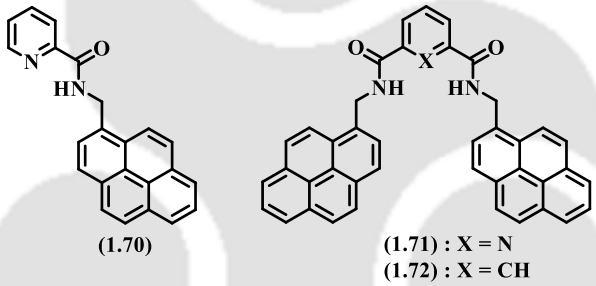

Chart 1.1. Two pyrene-tethered pyridyl amides

1.70 is a pyrene methyl amide functionalized pyridine compound, whereas **1.71** and **1.72** (Chart 1.1) are bis-pyrene methyl amide functionalized pyridine and benzene tweezers, respectively. NMR studies showed that **1.70** and **1.72** did not form self-association in $CDCl_3$ solvent. However, **1.71** was involved in self-association to form a supramolecular polymer because of (a) the preorganization of the two pyrene moieties to form a cleft, (b) the orientation of the amide carbonyl oxygen atoms towards an outward direction, which facilitated its interaction with another molecule of **1.71**, and (c) presence of two -NH groups stabilized the self-associated oligomeric or polymeric structure.

Guest molecule trinitrobenzene (**G1.3**) formed a 1:1 host-guest complex **G1.3@1.71** (i.e., **1.73**) (Scheme 1.4). This host-guest complex was confirmed by a visual colour change (colourless to red in chloroform solvent), ^{1}H-NMR, and quenching of fluorescence emission intensity. This host-guest binding was assisted by donor-acceptor hydrogen bonds between

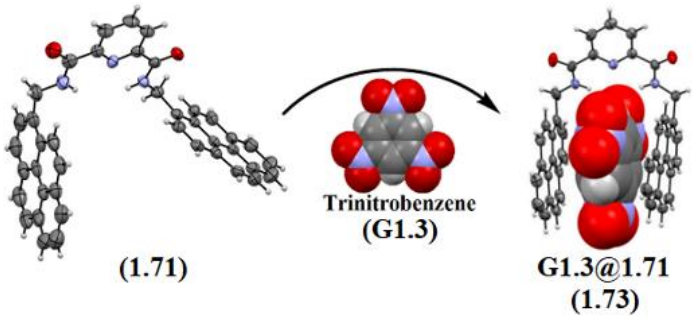

Scheme 1.4. Schematic representation of the formation of donor-acceptor complex **G1.3@1.71**, i.e., **1.73** {"Reprinted (adapted) with permission from S. K. Kim, J. M. Lim, T. Pradhan, H. S. Jung, V. M. Lynch, J. S. Kim, D. Kim and J. L. Sessler, *J. Am. Chem. Soc.*, 2014, **136**, 495–505. Copyright {2014} American Chemical Society.")

the amide -NH groups of **1.71** and one of the nitro groups of the guest **G1.3**. This guest molecule was encapsulated into the cleft of the two pyrene moieties of **1.71**. The intermolecular π-π interactions involving pyrene moieties stabilized the structure of **1.73**.

Fluorescence emission studies showed that the addition of **G1.3** to **1.71** or **1.72** caused quenching. These host-guest complexes **G1.3@1.71** (i.e., **1.73**) and **G1.3@1.72** (i.e., **1.74**) did not show significant emission due to the photoinduced charge transfer (PICT) from pyrene moieties to **G1.3**. Fluorescence emission studies of **1.71** and **1.72** with other guest molecules such as nitrobenzene, dinitrobenzene, dinitrotoluene, and trinitrotoluene caused quenching, suggesting host-guest interactions. The stability of these complexes increased with the number of electron-withdrawing nitro groups in the guest molecules. Host **1.71** was more efficient towards these nitro aromatic guest molecules such that its excimer emission switched OFF due to host-guest binding.[116]

Pyridyl amide-based compounds also possess acid-responsive properties. These derivatives switch their confirmations by solvent and pH. These environment-dependent conformational changes control the shape of large molecules. Thus, these compounds are used as external stimuli-responsive molecular devices. ^{1}H-NMR studies of **1.75** in deuterated methanol or dichloromethane solvents showed *cis*-confirmation. In acetone, the *cis*-conformer was less dominant. In tetrahydrofuran or toluene, the *trans*-conformation was observed. These studies also showed that conformational switching between *cis* and *trans* conformers could be carried out in a dichloromethane/toluene solvent mixture by changing the ratios of the two solvents. A solvent having a higher ability to hydrogen bond with the amide carbonyl group caused a reduction in the dipole interaction with the central pyridine ring. This changed the position of

amide carbonyl group *cis* to the pyridine nitrogen, resulting in the stabilization of the *cis* conformation (Scheme 1.5).[117]

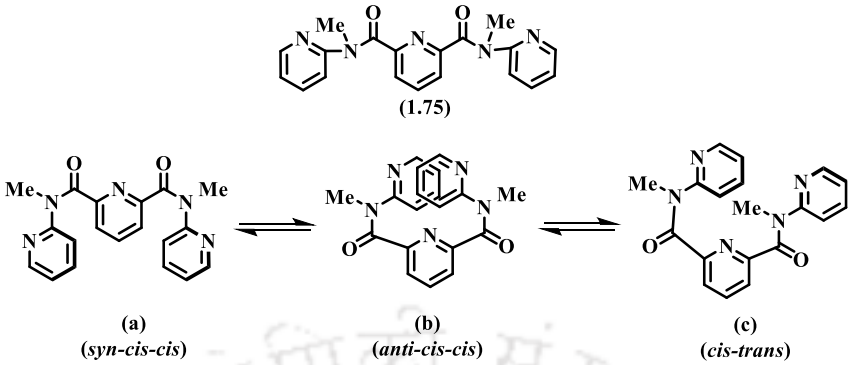

Scheme 1.5. Schematic representation of the conformational changes observed in **1.75**

The compound **1.76**, an N-methyl pyridyl amide derivative, underwent conformational transformations from layered to spiral and then flat by changing the pH. The single crystal X-ray structure of the **1.76** showed all the amide bonds in *cis* orientations. The pyridine rings were in a *syn* arrangement about the central pyridine, forming a layered arrangement (Scheme 1.6). The ^{1}H-NMR studies revealed that **1.76** changed the layered geometry to a spiral form (**1.77a**) upon adding excess $DClO_4$, which resulted in a flat structure of **1.77b**. The conformational change from layered (**1.76a**) to spiral form (**1.77a**) upon the addition of perchloric acid is due to the presence of rigid *cis*-amide building blocks and protonation of the two terminal pyridyl N-atoms, forming intramolecular hydrogen bonds with the amidic oxygen atoms (in **1.77a**). This spiral arrangement of **1.77a** was released upon further protonation, causing protonation of all the five pyridyl N-atoms and *cis-trans* switching of the N-methyl amides to give a flattened form **1.77b**. Thus, these structural conversions occurred due to the switching of amide bonds with intramolecular hydrogen bonding at different pH and solvents.[118]

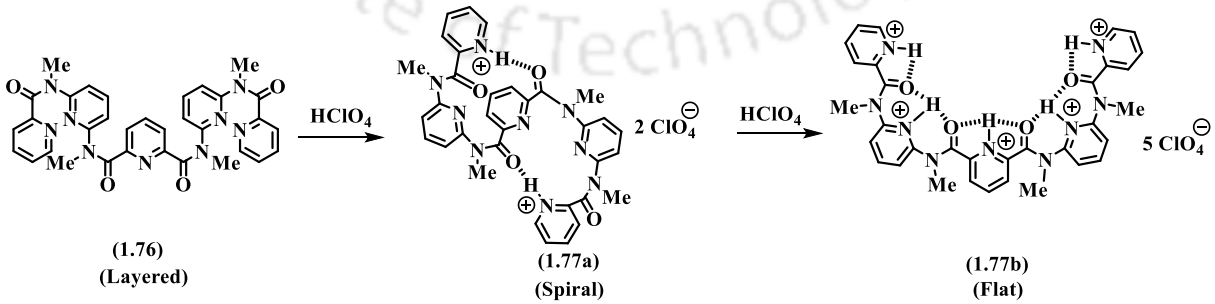

Scheme 1.6. Reaction of **1.76** with perchloric acid to give spiral **1.77a**, which on further treatment with excess perchloric acid yielded flattened **1.77b**

These examples have shown that the participation of amide groups of pyridyl-based amides in metal complexation and host-guest complexes is mainly dependent on external factors such as solvent, pH, and the nature of the guest molecule. Designed molecules can be utilized for switching binding properties to a guest or ion to modulate properties.

1.1.2. Pyridyl urea derivatives

Urea is an extensively studied compound and has drawn interest in research due to the presence of a key functional unit. It has applications in fertilizers[119,120] and medicines.[121,122] In supramolecular chemistry, the urea functional group is of primary importance due to its strong hydrogen bond donating and accepting abilities, which enables it to participate in self-association such as in molecular capsules,[123–125] bis (urea) gels,[126–128] anion guest binding.[126,129,130] The supramolecular features of urea-based compounds are utilized in catalysis,[131,132] molecular recognition,[133–135] and preparation of cocrystals.[136–139] The self-assemblies in the metal complexes,[140,141] anion-assisted assemblies,[141–143] or guest-assisted

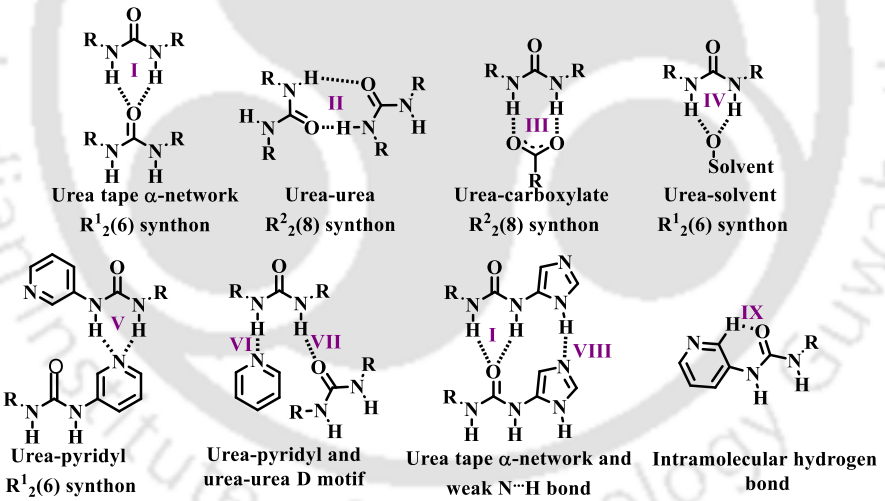

Figure 1.14. Supramolecular heterosynthons formed by urea derivatives

assemblies[144,145] of urea derivatives show different structural features. Aryl urea derivatives are sustained by urea tape synthons involving a bifurcated hydrogen bond involving carbonyl O-atom, except in cases where the aryl groups are incorporated by electron-withdrawing groups.[146] Pyridyl urea compounds act as receptors by taking advantage of the $N_{pyridine}$ atom and NH-groups of the urea part.[147] So, pyridyl urea derivatives consist of N-H···$N_{pyridine}$ hydrogen bond interactions, regardless of the low hydrogen bond basicity of pyridyl N-atom.[148] The electron-deficient pyridyl ring causes the acidic nature of the pyridyl CH

groups, which forces the carbonyl O-atom to form strong intramolecular C-H···O hydrogen bonding (synthon IX of Fig. 1.14). This hydrogen bonding leads to a planar molecular conformation. Some of the supramolecular heterosynthons formed by urea are shown in Fig. 1.14. Among several N-heterocycle urea derivatives, pyridyl urea precursors have been extensively utilized for anion recognition[149,150] and gelation.[151–154] Pyridyl urea derivatives can form interesting solid-state structures sustained by intramolecular hydrogen bonds, N-H···O urea tape synthons, N-H···$N_{pyridyl}$ interactions. In quinoline-based urea derivatives, which consist of a benzene ring fused with a pyridine ring, the N-atom of the quinoline moiety is available for metal coordination, while the urea part can bind with the anion guest molecules.[155] Urea-based monodentate pyridyl ligands form metal complexes and selectively bind anions,[140,150] some of which are anion sensors.[156,157]

The compounds **1.78**-**1.80** (Chart 1.2) are pyridyl urea derivatives, assisted by urea-$N_{pyridyl}$ hydrogen bonding due to the steric congestion of carbonyl O-atom of urea moiety by intramolecular C-H···O interactions. The pyridyl N-atom acted as a strong hydrogen bond acceptor due to steric hindrance around the urea carbonyl O-atom. The crystal structure of

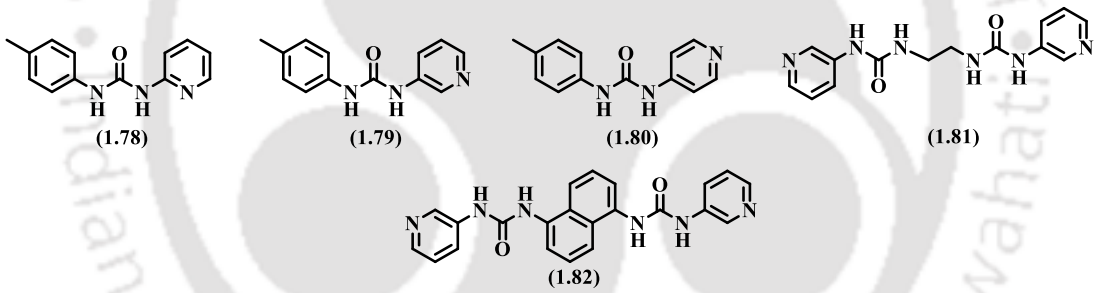

Chart 1.2. Examples of pyridyl urea-based molecules

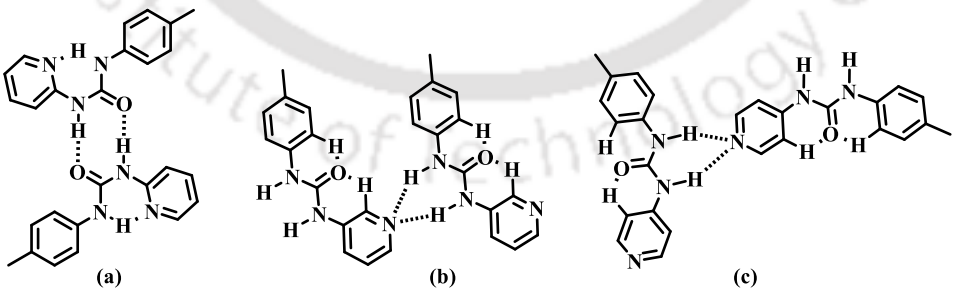

Figure 1.15. (a) Hydrogen-bonded dimer of **1.78**, (b), and (c) are part of the infinite chains of **1.79** and **1.80,** respectively

1.78 consisted of intramolecular hydrogen bonds between urea -NH groups and pyridyl N-atom, forming a six-membered hydrogen-bonded ring (Fig. 1.15a). On the other hand, the assemblies of the **1.79** and **1.80** were infinite strands held together by N-H···$N_{pyridyl}$ hydrogen

bonds forming cyclic units with $R^1_2(6)$ notation. The carbonyl O-atom was involved in intramolecular C-H···O interactions with CH protons of the acidic pyridyl and aryl rings. These interactions gave a planar conformation to **1.79** and **1.80** (Figs. 1.15b and 1.15c).[158]

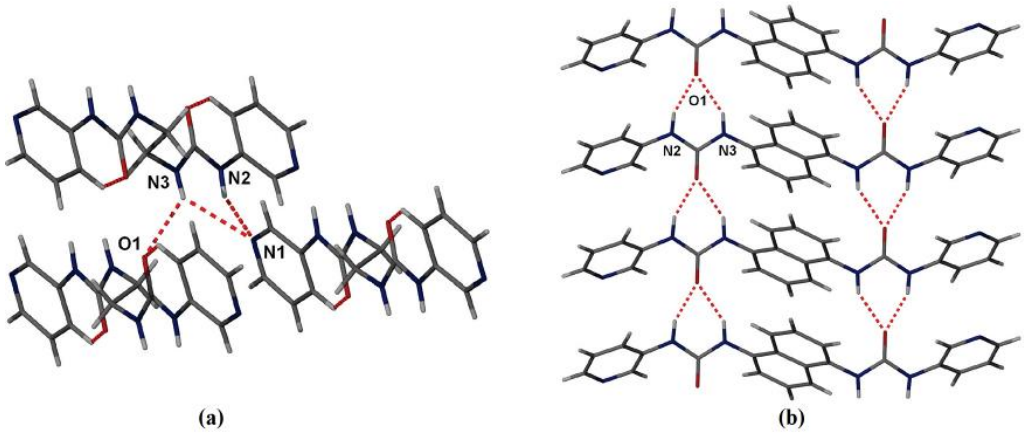

Figure 1.16. Crystal structure of (a) **1.81** showing bifurcated hydrogen bonded synthon, and (b) **1.82** showing urea tape α-network and π-π stacking of the naphthalenyl moieties { "Reprinted (adapted) with permission from P. Byrne, D. R. Turner, G. O. Lloyd, N. Clarke and J. W. Steed, *Cryst. Growth Des.*, 2008, **8**, 3335–3344. Copyright {2008} American Chemical Society."}

The bis (pyridyl urea) alkane derivative (**1.81**) had a puckered geometry, three molecules of which were hydrogen bonded through N-H···$N_{pyridyl}$ bonds. In **1.81**, one of the -NH groups of urea moiety on one side formed a strong N-H···$N_{pyridyl}$ hydrogen bond, and the second -NH group formed an intermolecular bifurcated hydrogen bond with pyridyl N-atom and carbonyl O-atom (Fig. 1.16a). In this example, the carbonyl group was involved in intramolecular C-H···O interactions. The *p*-naphthalene-bridged bis(3-pyridyl urea) **1.82** had a urea tape α-network and π-π stacking interactions between the naphthalene moieties (Fig. 1.16b).[159]

Urea is widely known to form hexagonal clathrates, where the guest molecules are encapsulated in the channels walled by urea helices. The bipyridyl bis(urea) **1.83** consists of a sterically hindering -CMe_2 group. Crystallization of **1.83** in methanol solvent yielded **methanol@1.83** (i.e., **1.84**), having a polar and chiral packing arrangement with a three-fold helix of pitch 12.50 Å. This helix consisted of an AABAAB-type repetition of the two independent molecules linked by a twisted chiral variation on the urea α-tape network (Fig. 1.17a). Unlike other pyridyl bis(urea) derivatives, the carbonyl O-atom of this compound was not blocked by intramolecular C-H···O hydrogen bond. The axes of the three-fold helices were in a distorted hexagonal arrangement. These layers were linked by C-H···$N_{pyridyl}$

interactions. The distorted methanol guest molecules were too small to fit inside the distorted hexagonal cavity (Fig. 1.17b).[160]

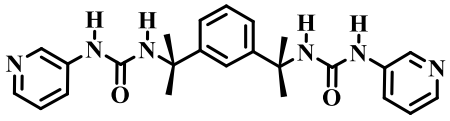

(1.83)

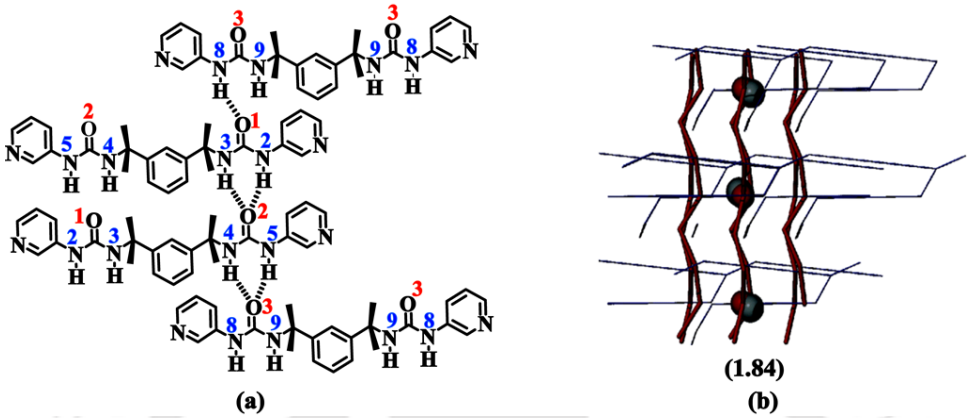

(a) **(1.84)** **(b)**

Figure 1.17. Crystal structure of **methanol@1.83** (i.e., **1.84**) showing (a) arrangement of urea moieties and (b) host network topology where methanol molecules are presented as spheres { "Reprinted (adapted) with permission from A. M. Todd, K. M. Anderson, P. Byrne, A. E. Goeta and J. W. Steed, *Cryst. Growth Des.*, 2006, **6**, 1750–1752. Copyright {2006} American Chemical Society."}

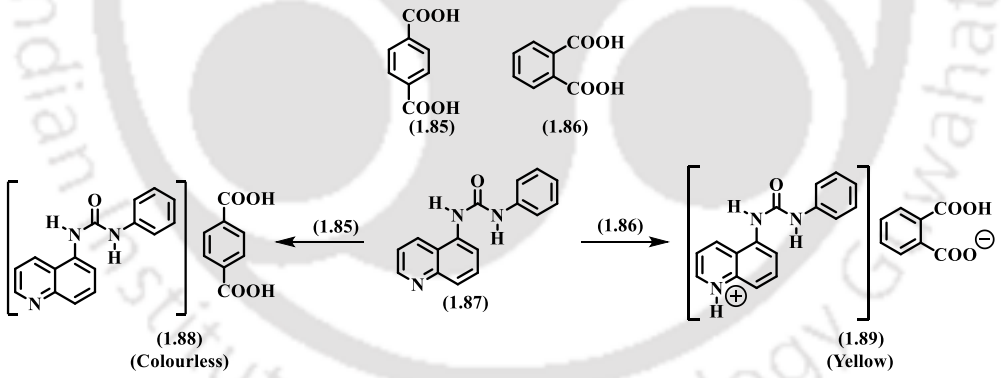

(1.85) (1.86) (1.87) (1.88) (Colourless) (1.89) (Yellow)

Scheme 1.7. Schematic representation of **1.87**, which distinguished terephthalic acid (**1.85**) and phthalic acid (**1.86**)

The quinoline-based urea derivative **1.87** showed a visual distinction between the two positional isomers of benzene dicarboxylic acid, **1.85** and **1.86** (Scheme 1.7). Guest **1.85** formed a colourless cocrystal with **1.87**, namely **1.88**, where the urea tape α-network of the host **1.87** was present and intermolecular hydrogen bonding between the quinoline N-atom of the host **1.87** and carboxylic acid of the guest **1.85** formed a bridge between the two host molecules (Fig. 1.18a). On the other hand, **1.86** formed a yellow-coloured salt with **1.87**, namely **1.89**. This salt consisted of hydrogen bonds between the anionic form of **1.86** and -

NH groups of **1.87** and intermolecular hydrogen bonds between the protonated N-atom of **1.87** and the carboxylate group of anion **1.86** (Fig. 1.18b). However, urea tapes were absent in this salt.[161]

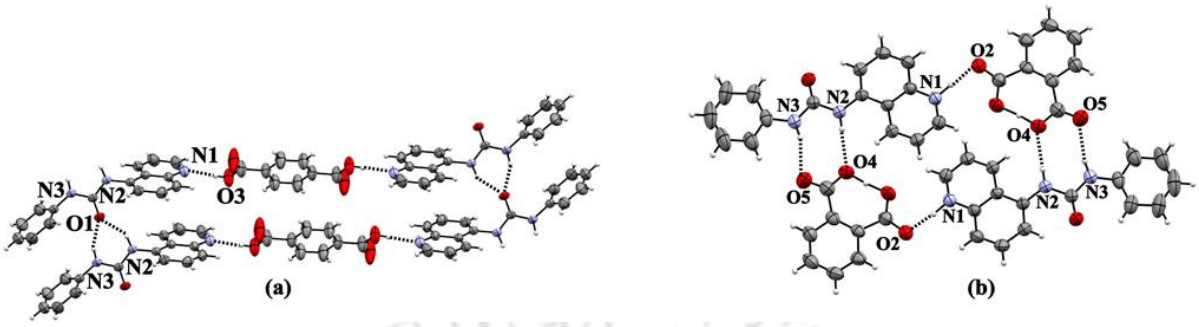

Figure 1.18. Hydrogen bonded network in (a) **1.88**, and (b) **1.89** (ellipsoids are drawn at 50% probability)

The urea moieties linked to macrocycles and podands are widely studied.[162,163] The compound **1.90** is a C_2-symmetrical cavitand; it has two urea moieties and two pyridyl ethynyl groups. It formed a supramolecular hybrid capsule **1.91** with a *cis*-coordinated Pt(II) complex (Scheme 1.8). In this capsule, the guest, such as 4,4′-diiodobiphenyl could be encapsulated.[164,165]

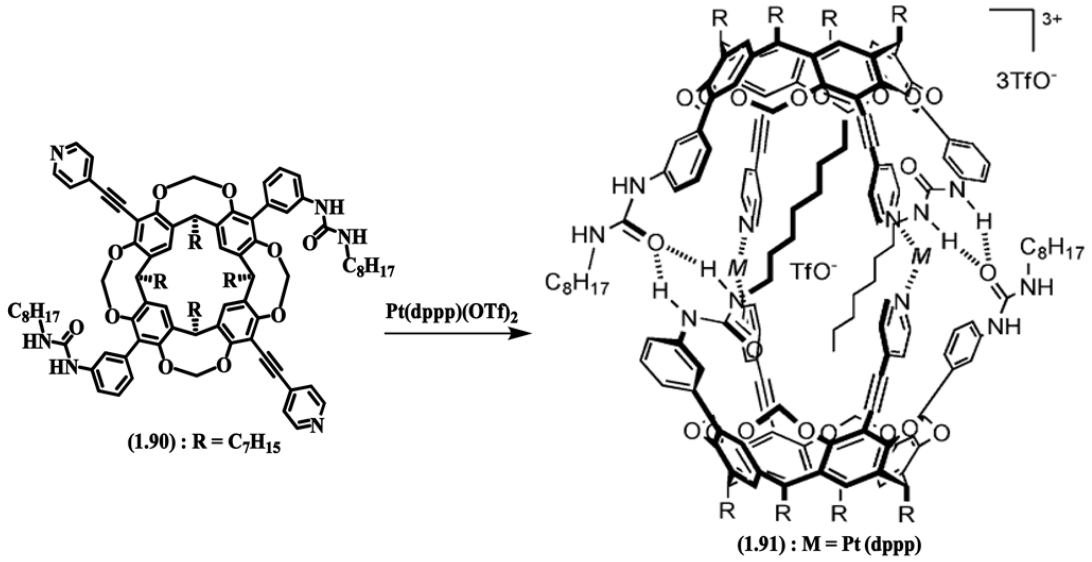

Scheme 1.8. Formation of a hybrid supramolecular capsule **1.91** by C_2-symmetrical pyridyl urea-based cavitand **1.90** {"Reprinted (adapted) with permission from Y. Nito, H. Adachi, N. Toyoda, H. Takaya, K. Kobayashi and M. Yamanaka, *Chem. – An Asian J.*, 2014, **9**, 1076–1082. Copyright {2014} John Wiley and Sons."}

In the above examples, the construction of coordination complexes, as well as the host system of urea derivative, have been discussed. These examples showed the role of the self-assembling ability and participation of hydrogen bonding of urea derivative in stabilizing the host-guest complexes.

1.2. Second coordination sphere from pyridyl amide and pyridyl urea derivatives

In a metal complex, the primary coordination sphere consists of a metal center to which ligands are covalently bonded. In 1912, Alfred Werner advanced the idea that the ligands of the primary coordination sphere can provide non-covalent interactions with the neutral molecules or charged species to create a second coordination sphere.[166] Hydrogen bonds are the most stabilizing interactions in the secondary coordination sphere, but there are many examples of charge transfer interactions, coulombic interactions, polar and dipolar attractions, and dispersion forces.[167,168] Metalloproteins perform a wide range of chemical transformations; they provide ligands to connect the metal ion cofactors to proteins and utilize the secondary coordination sphere for selective binding, transformations, and release. For example, hydrogen bonds in heme proteins, such as hemoglobin and cytochrome P-450, have important biological roles.[169,170] The second coordination sphere of synthetic metal complexes is useful for sensing[171], catalysis,[172,173] and anion binding[174]. Ligands having appended functional groups have contributed to the creation of a secondary coordination sphere adjacent to the metal center.[175] Pyridyl amide[176–178] and pyridyl urea[179] based ligands in their deprotonated form create a pincer cavity via two (in pyridyl amide) or four (in pyridyl urea) -NH groups, and the $N_{pyridyl}$-atom strongly coordinates to the metal center. The appended functional groups generate a secondary coordination sphere.

1.2.1. Pyridyl amides in building secondary coordination sphere

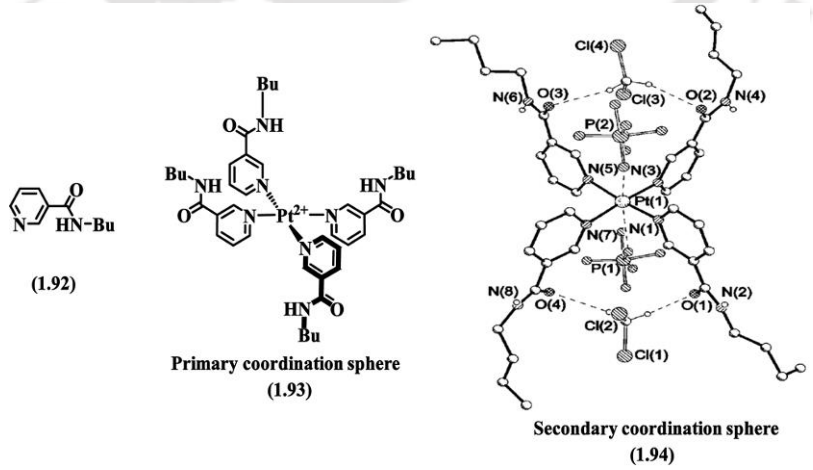

Figure 1.19. Binding of **[Pt(1.92)]**$^{2+}$ complex (**1.93**) with hexafluorophosphate anions (PF_6^-) to form **1.94** {Reproduced from C. R. Bondy, P. A. Gale and S. J. Loeb, *Chem. Commun.*, 2001, 729–730., with permission from the Royal Society of Chemistry}

Pyridyl amide ligands are interesting frameworks for incorporating secondary sphere hydrogen bond interactions in transition metal complexes. For example, **1.92**, n-butyl nicotinamide ligand, its four molecules were coordinated to Pt(II) metal ion to form $[Pt(1.92)]^{2+}$ complex, i.e., **1.93**. In **1.93**, the free amide groups of the ligand **1.92** acted as hydrogen bond donors by binding with PF_6^- anion (Fig. 1.19).[180]

Mononuclear complexes **1.98-1.101** were formed by pyridine 2,6-dicarboxamide ligands (**1.95-1.97**) consisting of an appended heterocyclic ring, thiazole (**1.95**), thiazoline (**1.96**), benzothiazole (**1.97**). In all the cases, a meridional N_3 coordination environment for the metal ion was created by two anionic N_{amide} and one neutral $N_{pyridine}$ atom. Anions or solvent molecules occupied the rest of the sites (Fig. 1.20). These complexes showed the migration of amidic N-H protons to the appended heterocyclic rings. These protonated heterocyclic rings created a hydrogen bonding cavity adjacent to the metal center, assisting the hydrogen bonding of oxygen-based substrates within this cavity. The presence of intramolecular hydrogen bonds between the ligand and the coordinated anions or solvent molecules helped in an enhanced activity as a heterogeneous catalyst for ring-opening reactions of assorted epoxides, cyanation reaction of aldehydes, and epoxidation reaction of olefins.[172]

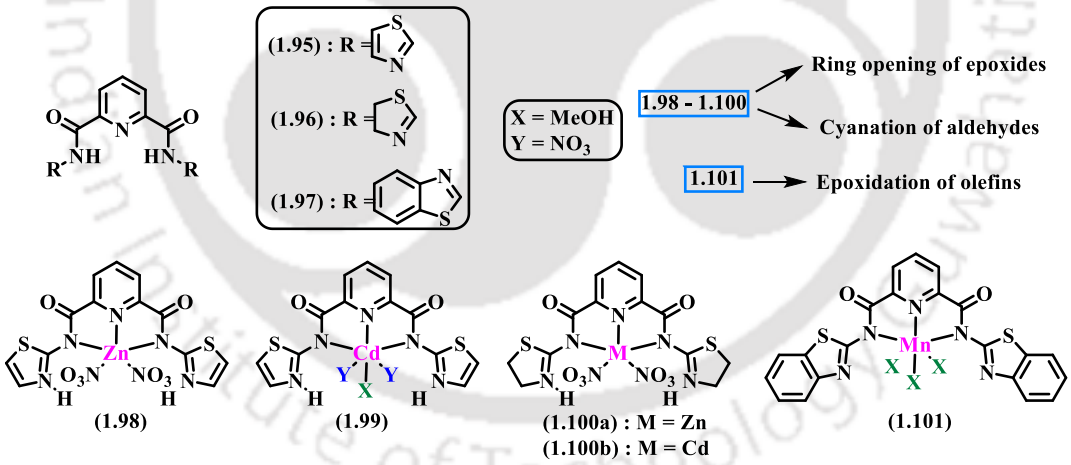

Figure 1.20. Mononuclear complexes with pincer amides

1.102 is also a pyridine 2,6-dicarboxamide ligand with a 2,6-pyridine dicarboxamide appended scaffold. It formed Cu(II) complexes (**1.103a-1.103d**) with CuX_2 salt (where, X = OH^-, Cl^-, OAc^-, CO_3^{2-}) in the presence of a base, tetramethylammonium hydroxide (Scheme 1.9). Cu (II) ion was coordinated to the two N-atoms of the amidate group and an $N_{pyridine}$ atom. An X anion occupied the fourth coordination site of Cu(II). The free -NH groups formed intramolecular hydrogen bonding with the axial ligand X. This scope of hydrogen

bonding resulted in a notable shift in Cu(III) / Cu(II) redox potential.[181] This type of interaction replicates secondary sphere hydrogen bonding in metalloenzyme active sites.[182] The hydrogen bond donating and accepting groups in the secondary coordination sphere of active enzyme sites affect the redox potential of the metal center. There are examples of second-sphere residues which can both raise and lower the redox potential.[182,183]

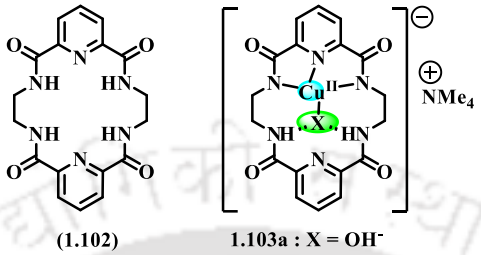

Scheme 1.9. A macrocyclic pyridine 2,6-dicarboxamide **1.102** and its copper(II) complexes

1.2.2. Pyridyl urea derivatives in building secondary coordination sphere

Pyridyl urea compounds widely contribute towards the building of a secondary coordination sphere due to the presence of an additional -NH group compared to the amide-based compounds. Pyridyl urea-based metal complexes are incredibly used as highly tunable components for the design of anion receptors. For example, **1.104** is a pyridyl urea ligand, possessing a pyridyl group and a urea-derived anion binding group. It formed a cationic complex $[Ag(\mathbf{1.104})_2]^+$ (i.e., **1.105**) with $AgNO_3$. The **1.105** cations participated in intermolecular hydrogen bonding via urea -NH groups with the oxo anion nitrate via $R^2_2(8)$ synthon (Scheme 1.10). The nitrate ion was present within the cavity of the cationic host complex **1.105**. However, in other Ag(I) salts, such as silver acetate, the acetate anion is directly coordinated to the metal center.[149]

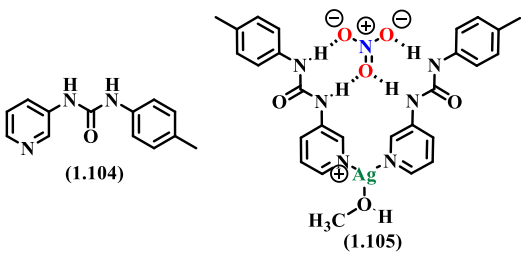

Scheme 1.10. Structure of **1.104** and nitrate ion recognition by its cationic silver (I) complex **1.105**

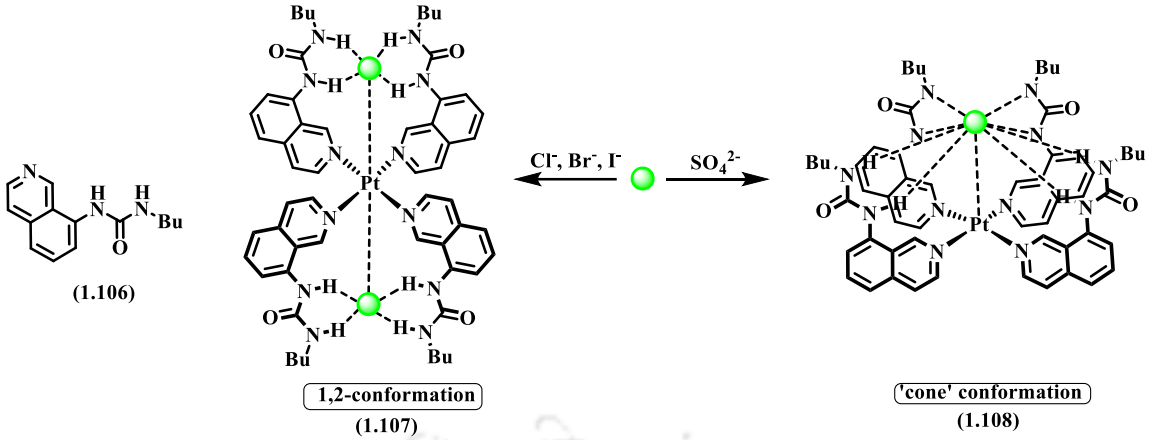

Scheme 1.11. Anion binding by a quinoline urea-based cationic receptor **[Pt(1.50)$_4$]$^{2+}$**

A quinoline urea derivative (**1.106)** based cationic complex [Pt(**1.106**)$_4$]$^{2+}$ (i.e., **1.108**) adopted a cone-shaped conformation while binding to a tetrahedral oxyanion SO_4^{2-}. However, in the case of halide anionic guests, namely, Cl^-, Br^-, and I^-, ^{1}H-NMR studies showed a 1:2 receptor-anion interaction. Despite the fact that when the halide anion is a limiting reagent, all the four urea moieties can surround the halide ion in a cone conformation, a 1,2- or 1,3-conformation was adopted to give a neutral (1.67)[X]$_2$ complex (i.e., **1.107**) (where X = Cl^-, Br^-, and I^-) at high anion concentration. The single crystal structure of **1.107** (for X = Cl^-) confirmed 1,2-alternate conformation, in which two pairs of adjacent -NH groups of urea moieties formed hydrogen bonds with two independent chloride ions. These Cl^- ions were located at the axial positions above and below the Pt(II) center (Scheme 1.11).[155]

2,2´-Bipyridyl-based bis(urea) **1.109** formed a tetrahedral Fe(II) mononuclear complex **1.110**. The Fe(II) metal center was coordinated with the two $N_{bipyridyl}$ atoms, and chloride ligands occupied the rest of the two coordination sites. This complex provided a secondary coordination sphere by the formation of intramolecular hydrogen bonding between one of the -NH of the urea part and chloride ligands (Scheme 1.12).[174]

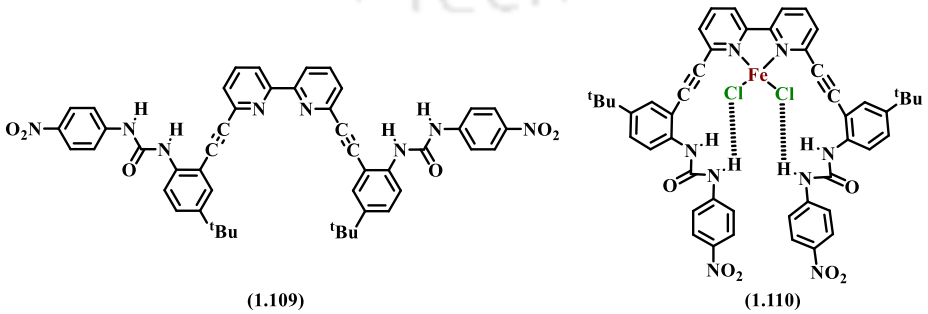

Scheme 1.12. Role of a 2,2'-bipyridyl based bis(urea) (**1.109**) in intramolecular hydrogen-bonded secondary coordination sphere

The secondary coordination effect generated for anion binding has shown that a careful selection of receptors can provide a high level of selectivity that may have applications in anion separations.

1.3. Pyridyl amide and pyridyl urea as anion sensors

Many neutral receptors of urea, thiourea, amide, squaramide, and sulfonamide have been studied for anion binding.[184] The hydrogen bonding ability and polarization of -NH groups of these receptors by an anion depend on the electron-withdrawing group, i.e., the C=O group in urea,[185] amides, squaramide,[186,187] C=S and O=S=O groups in thiourea and sulphonamides contribute.[188] The electron-withdrawing groups increase the acidity of the hydrogen donor groups, such as the -NH group, thereby accelerating the proton transfer process in the presence of basic anions such as fluoride, chloride, acetate, etc.[189] Urea groups attached to electron-poor aromatic rings show a stronger affinity towards anionic species compared to that of aliphatic ureas. Pyridine-based amide and urea receptors provide anion complexation through both amide and pyridinium NH donors.[185] Pyridyl amide and pyridyl urea derivatives are used for designing biomimetic and bioinspired artificial systems such as ion channels.[190,191]

1.3.1. Pyridyl amide in anion sensing

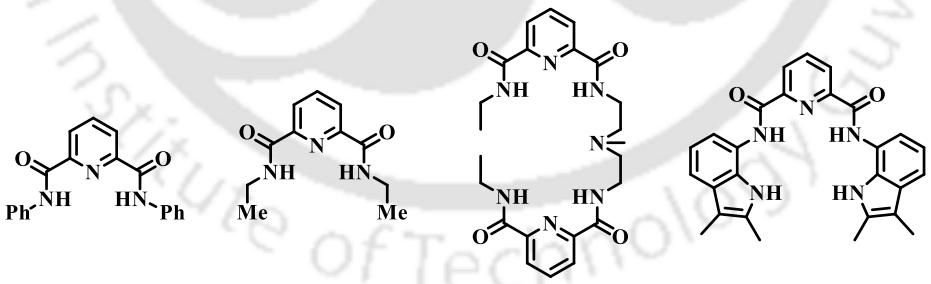

Chart 1.3. Structures of pyridine-based amide clefts

Pyridyl amides are well known to recognize anions and show selectivity towards anions of different geometries.[41] The receptor **1.111** (Chart 1.3) is a pyridine-based diamide derivative, strongly binding to halides and acetates in organic solvents. Due to the presence of a pyridine nitrogen lone pair close to the anion binding site, **1.111** showed a higher selectivity for small anions.[192] In this case, the lone pair was sterically more bulky than an aromatic C-H bond.[193]

The electrostatic repulsion between negatively charged anions and the lone pair decreased the binding ability with anions. Due to this effect, larger anions, such as bromide and iodide, were more weakly bound than smaller anions, such as fluoride or chloride. The anion binding was studied through NMR spectroscopy, which provided valuable suggestions on the hydrogen bonding or deprotonation states of an anion binding to a receptor.

Anion binding of **1.112** and **1.113** (Chart 1.3) was studied by ^{1}H-NMR titrations in water-mixed DMSO-d_6, using the tetra (n-butyl) ammonium (TBA^+) salts of anions (Cl^-, SO_4^{2-}, $H_2PO_4^-$, AcO^-, NO_3^-, ClO_4^-, N_3^-). It was found that both **1.112** and **1.113** showed an affinity for SO_4^{2-} over other anions, and the Job's plot showed that the SO_4^{2-} ion was held in a 1:1 mode by **1.112** and **1.113**. In DMSO-d_6 / 0.5% water, the binding constant (K) of SO_4^{2-} complexes of **1.112** was 7.44 x 10^2 M^{-1}, much less than that of **1.113** (K = 51.49 x 10^2 M^{-1}). Thus, due to an increase in the number of complementing binding sites from two in **1.112** to four in **1.113**, there was a seven-fold affinity enhancement for the hosts.[147]

The compound **1.114** is a pyridine-based symmetric dipodal anion receptor. It has both amine (-NH) and amide (-CONH) as hydrogen bond donors. It showed a high selectivity for fluoride ions compared to other anions. The structure of the chloride complex of receptor **1.114** had less space to encapsulate a chloride ion. The anion was perched over the planar scaffold of the receptor, and it was held by four hydrogen bond donating N-H groups (Fig. 1.21a). On the other hand, fluoride bound to **1.114** had a twisted geometry, in which one indole ring was located above the central aromatic ring of the receptor. The coordinating fluoride anion was held by four hydrogen bonds with -NH groups (Fig. 1.21b). The ^{1}H-NMR titration of **1.114** with chloride or fluoride anions in DMSO-d_6 / 0.5% water showed that the binding of fluoride was 10^4 times higher than chloride.[194]

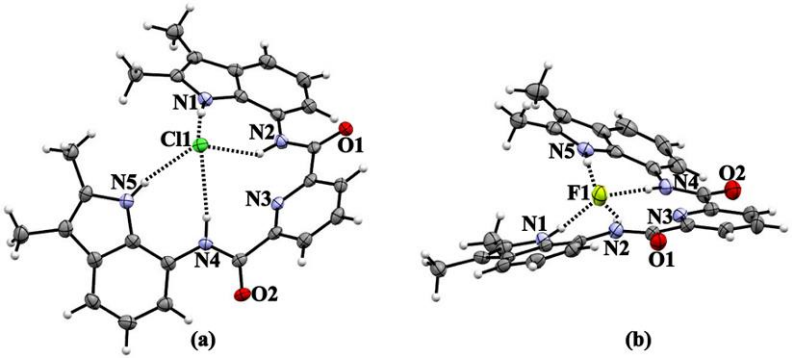

Figure 1.21. Binding of (a) chloride and (b) fluoride ion by **1.114** (cation are omitted for clarity; ellipsoids are drawn at 50% probability)

Pyridyl amide-based macrocycles and cryptands offer more advantages than the acylic, bicyclic, and monocyclic receptors because macrocycles and cryptands possess cage-like structures which capture the anions. The **1.115** and **1.116** are pyridine-based amidocryptands with capsule-like geometries (Scheme 1.13). The cryptand **1.115** formed both chloride and sulphate complexes. In complexes **1.115@chloride** and **1.115@sulphate**, **1.115** was folded with two amide loops directed towards one direction and the third amido loop pointed towards the opposite direction, thus making an inverted Y-shape. This face-to-face orientation of the bridges was due to π-π stacking interactions. In the **1.115@chloride** complex, two chloride ions were bridged by a water molecule, and the chloride ion had a pseudo-tetrahedral coordination geometry (Fig. 1.22a). In the **1.115@sulphate** complex, two

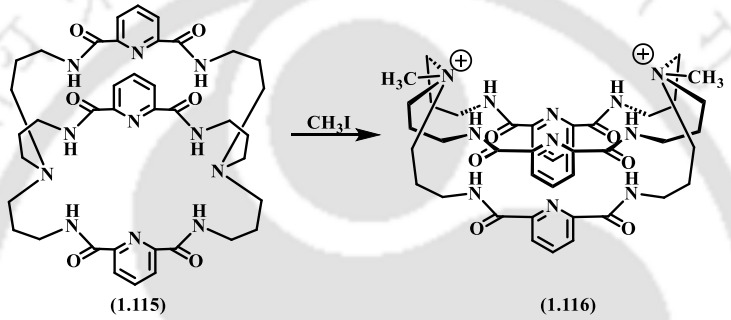

Scheme 1.13. Schematic design of methylation of a pyridylamidocryptand **1.115** to give **1.116**

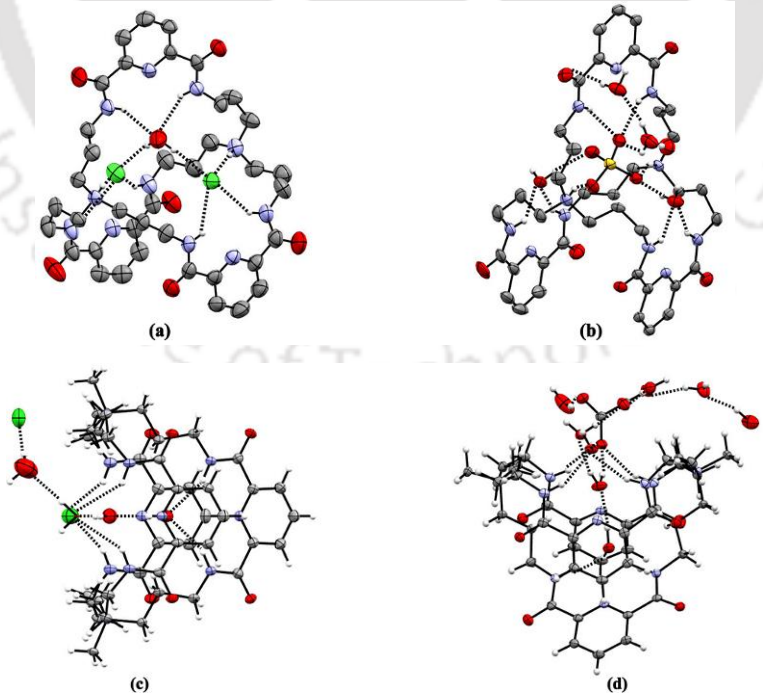

Figure 1.22. Anion encapsulations: (a) **1.115@chloride**, (b) **1.115@sulphate**, (c) **1.116@chloride**, and (d) **1.116@oxalate** (ellipsoids are drawn at 50% probability)

water molecules were bridged by a sulphate ion inside the cavity of **1.115** (Fig. 1.22b). Due to a large cavity in **1.115**, it was quaternized to give **1.116**. In **1.116**, all three amide loops were pointed in the same direction, making it bowl-shaped. It formed complexes with chloride and oxalate ions, respectively. In both these complexes, the water molecules were held within the bowl; and the anions were present at the top of the bowl, held by hydrogen bonding with water molecules and amidic hydrogen atoms. Both chloride and oxalate ions were centered between the two quaternized amines at the top of the bowl-shaped **1.116** in the respective complexes (Figs. 1.22c and 1.22d). Thus, these anions provided a symmetrical balance of negative charge between the two positively charged amines, which resulted in a bowl-shaped geometry.[195]

The pyridine-2,6-dicarboxamide **1.117-1.119** (Chart 1.4) are dicationic receptors consisting of dicationic N-methylated quinolyl moieties. Fluorescent anion sensing of these receptors in water showed their significant affinity towards small anions such as halides, acetate, and neutral guest molecules such as urea and amide. These receptors also showed fluorescence quenching after the addition of nucleoside triphosphates (such as ATP), which was more effective than inorganic anions. The high affinity of these receptors for ATP was due to the π–π interaction of an adenine nucleobase with quinolinium moieties of the receptors. The interaction between the receptor and anion was not electrostatic; instead, it was due to the presence of an electron-withdrawing C=O group, which resulted in a strong acidification of hydrogen donor N_{amide}-H and C-H groups. Thus, these receptors (**1.117-1.119**) showed affinity for halides and acetate. Because the electron-withdrawing C=O group increased the acidity of the hydrogen donating -NH group, thereby accelerating the proton transfer process in the presence of halides and acetate.[196]

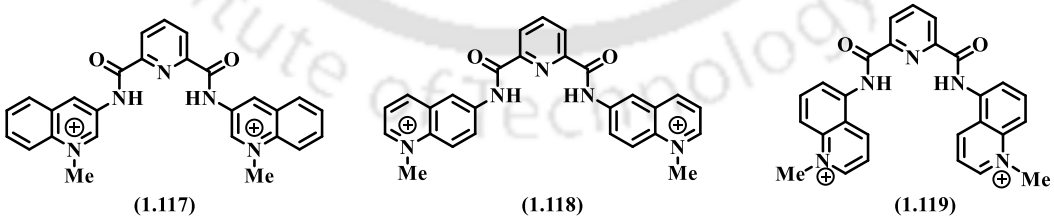

Chart 1.4. Examples of pyridyl amide-based cationic receptor molecules

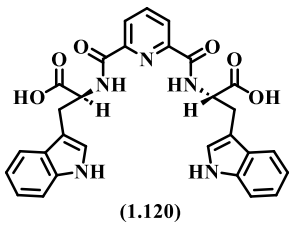

Chart 1.5. Pyridine-2,6-dicarboxamide compound

Another pyridine-2,6-dicarboxamide-based compound, **1.120** (Chart 1.5), has carboxylic acid groups adjacent to the amide -NH groups. Deprotonation of these -COOH functional groups reduced the acidity of the -NH groups, thereby making the receptor **1.120** highly selective towards fluoride ions. When **1.120** was titrated with TBAF salt, ^{1}H-NMR studies showed a downfield shift of one of the -NH protons, which confirmed the formation of **(1.120)**$^{2-}$ adduct and a triplet signal at 16ppm (corresponding to the shift of second -NH proton) appeared due to the presence of HF_2^- ions in the solution. So, it was observed that there was a shift of both the -NH protons, which confirmed that after the initial deprotonation of **1.120** by a strong base TBAF, **(1.120)**$^{2-}$ adduct interacted with F^- ions through hydrogen bonding with -NH groups of amide and indole moieties.[197]

1.3.2. Pyridyl urea in anion sensing

The pyridyl urea derivatives can be used as anion receptors because urea and pyridyl fragments can form hydrogen bonds. Recognition of anions by neutral receptors is due to the hydrogen bond interactions involving polarized -NH fragments of urea, thiourea, amides, sulfonamide, and pyrroles binding groups.[198] Increasing the number of urea groups in a receptor molecule facilitates anion coordination. Depending on the linkages between the urea moieties, the effective binding ability of a receptor toward anion gets modulated due to steric strains.[199] A urea receptor with the same number of -NH groups as that in an amide receptor showed a stronger affinity for anions.[147] On the other hand, metal complexes of pyridyl urea-based ligands show anion-binding abilities by utilizing hydrogen bonding with the -NH groups of the urea part.[150,200,201]

Protonated species of pyridyl urea are more flexible than respective complexes with a transition metal ion, so such flexible geometries are useful in a specific binding with anion by forming reorganized structures. The protonated forms of the two pyridyl urea-based receptors **1.121** and **1.122** (Chart 1.6) with inorganic oxo acids such as perchloric acid, nitric acid, and sulphuric acid were utilized to study their anion coordination chemistry. The acidity of urea -NH groups increases due to the presence of positively charged pyridinium cation, thereby favouring proton transfer process in the presence of anions. The solid-state structures of these anion-bound species revealed that C=O, -NH groups of urea unit, pyridinium cation, and water of crystallization molecules collectively participated in hydrogen bonding with the oxo anions.[129]

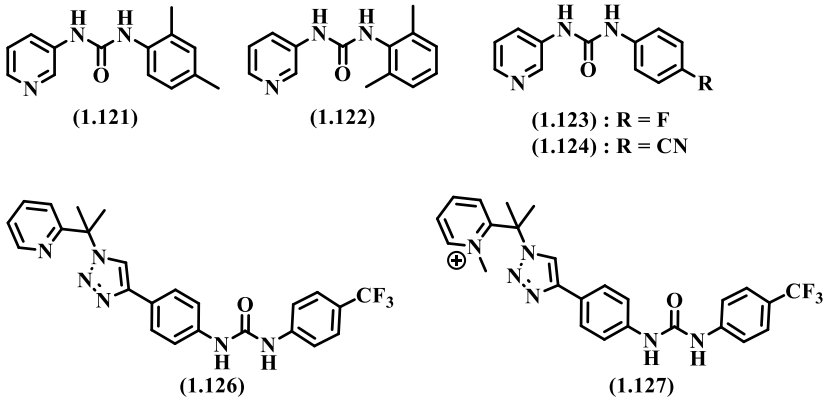

Chart 1.6. Pyridine-derived urea

The metal-based assemblies as hosts for selective recognition and separation of anions by utilizing the secondary coordination sphere are important due to their biological and environmental significance.[202,203] Pyridyl urea-based ligands have been used extensively as metal-based anion hosts. These ligands provide -NH groups to bind with the anions or anionic guests.[204] The effect of the fluoride or cyanide substituents at the 4-position of 3-pyridyl urea derivatives, i.e., **1.123** and **1.124,** respectively, showed that the receptor **1.123** had higher affinity for sulphate ion over other anions (such as NO_3^-, Cl^-, ClO_4^-). The receptor could distinguish Cu^{2+} ion over other transition metal ions such as Co^{2+}/ Ni^{2+}/ Zn^{2+}. It formed a stable coordination complex **1.125**, i.e., **[Cu(1.83)$_4$(H$_2$O)$_2$]SO$_4$**. The receptor **1.123,** together with Cu^{2+}, had higher selectivity for SO_4^{2-} recognition compared to that of the receptor **1.124**.[205]

1.126 and **1.127** are pyridyl urea receptors. The methylation of the pyridyl group of **1.126** yielded **1.127**. Thus, pyridine and pyridinium fragments of **1.126** and **1.127** (Chart 1.6) can participate in hydrogen bonding in an opposite manner: pyridine as H-acceptor (in **1.126**) and pyridinium moiety as H-donor (in **1.127**). UV-visible and ^{1}H-NMR titration studies showed that both receptors formed stable adducts with various anions such as F^-, Cl^-, Br^-, I^-, NO_3^-, and HSO_4^-, CH_3COO^-, $H_2PO_4^-$. Methylation increased the anion affinity of the receptor **1.127**. The electron-withdrawing effect of the positively charged pyridinium cation intensified the acidity of urea -NH groups, thereby favouring the proton transfer process in the presence of anions, as confirmed by the binding constants. The 1:1 adduct formation by **1.127** with anions such as F^- and CH_3COO^- was accompanied by a proton transfer process at the methylene group of the pyridinium moiety. ^{1}H-NMR studies confirmed the formation of a stable neutral methine species, specified by the loss of aromaticity by the pyridyl ring.[206]

1.128 is a tris(3-pyridylurea) tri(aminoethyl)amine compound. Crystallization of **1.128** with various MSO_4 salts (M = Zn, Cd, Co, Mg) yielded $\mathbf{MSO_4(1.128)_2(H_2O)_6}$ (i.e., **1.129**). In the metal complex $\mathbf{MgSO_4(1.128)_2(H_2O)_6}$, the sulphate ion was encapsulated by 12 -NH groups via hydrogen bonding interactions (Fig. 1.23a). This sulphate ion was also held by 12 additional hydrogen bonds from six water molecules, each bridging through its two protons, pyridine N-atom and C=O group of urea part resulting in the formation of hydrogen-bonded capsule framework (Fig. 1.23b).[207]

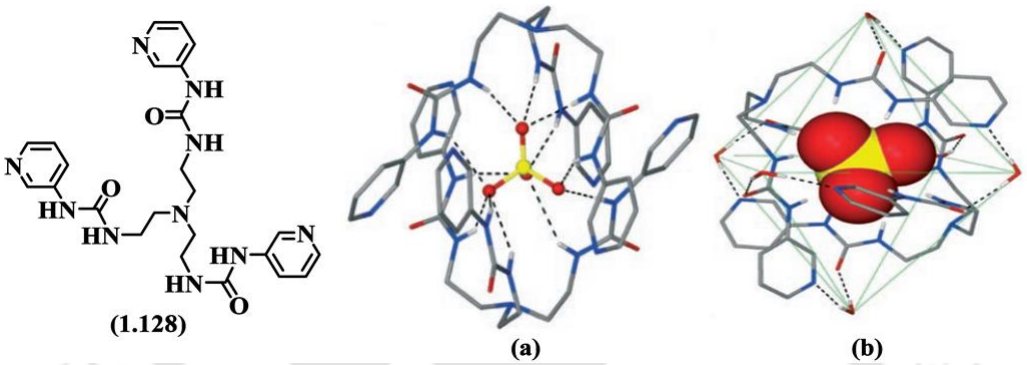

Figure 1.23. The structure of tripodal receptor **1.128** and crystal structure of $\mathbf{MSO_4(1.128)_2(H_2O)_6}$ (i.e., **1.129**) showing (a) SO_4^- encapsulation by hydrogen bonds (dashed lines) with -NH groups, and (b) Hydrogen-bonded capsule formed by six bridging water molecules {"Reprinted (adapted) with permission from R. Custelcean, P. Remy, P. V. Bonnesen, D. Jiang and B. A. Moyer, *Angew. Chemie Int. Ed.*, 2008, **47**, 1866–1870. Copyright {2008} John Wiley and Sons."}

The N, N´-bis (m-pyridyl urea)**1.130** got monoprotonated upon reaction with one equivalent of HX acids (where X = Cl^-, Br^-, I^-, NO_3^-, and ClO_4^-) and formed corresponding salt. These salts have structures of hydrogen-bonded helices held together by pyridinium···pyridine hydrogen bonds as illustrated in Scheme 1.14. The anions were bound to the urea -NH groups through bifurcated hydrogen bonds. The helices were further connected by C-H···X^-, pyridinium···X^- interactions, and π- π stacking interactions.[208]

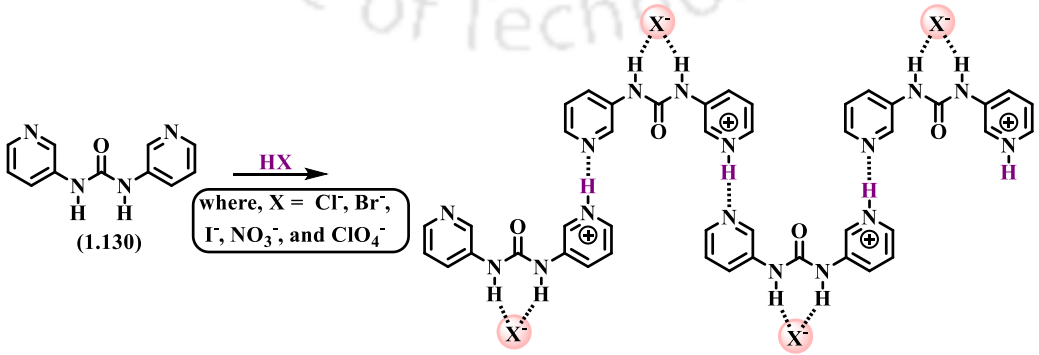

Scheme 1.14. Hydrogen bonds in the anion complexes of the receptor **1.130**

The clusters or chains of hydrated anions are useful in anion transport.[209] The compound **1.131** is a pyridine-based molecule. Depending on the anion, it has the ability to stabilize hydrogen-bonded anion water clusters in specific form. For example, the protonated compound stabilized sulphate-water hexamer $[(SO_4)_2\text{-}(H_2O)_4]_n^{4-}$ (Figs. 1.24a and 1.24b) whereas with dihydrogen phosphate-water, it formed a trimer, $[(H_2PO_4)_2\text{-}H_2O]_n^{2-}$ (Fig. 1.24c). These anion-water clusters were stabilized by hydrogen bonds of urea, water, and pyridinium moieties.[156]

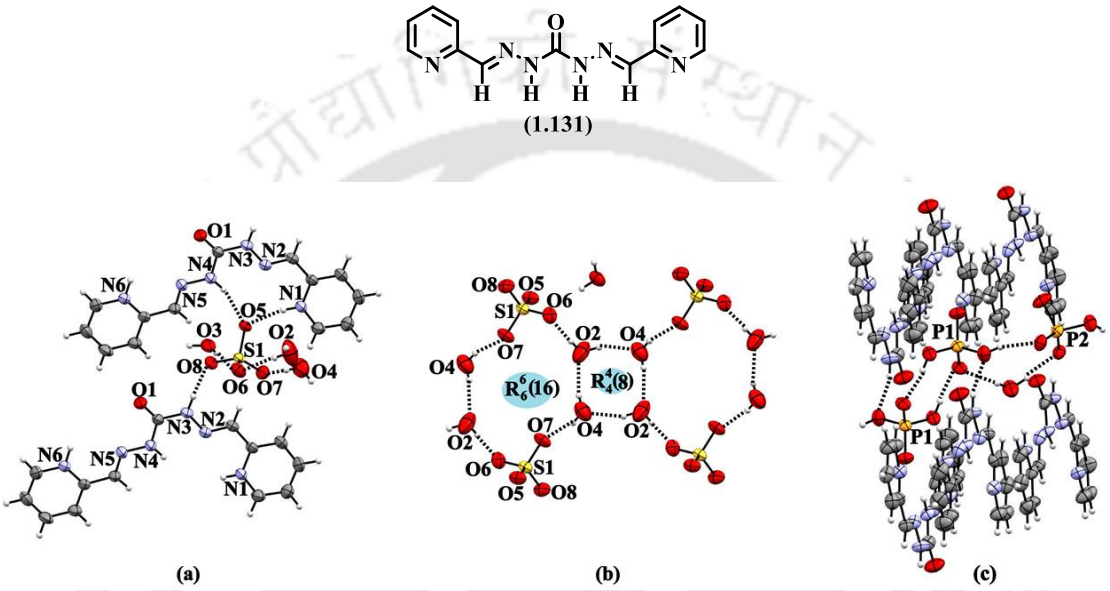

Figure 1.24. The anion receptor **1.131**; and (a) Hydrogen bonds of sulphate ion with cationic receptor **1.131** (b) Fused sulphate-water hexamer $[(SO_4)_2\text{-}(H_2O)_4]_n^{4-}$ (c) hydrogen bonds of phosphate ion with cationic receptor **1.131** (ellipsoid are drawn at 50% probability)

These examples have suggested the versatility of urea and amide moiety with pyridine-appended amides and urea derivatives. These have utilities to understand, and special attention is required to predesign hosts and self-assemblies.

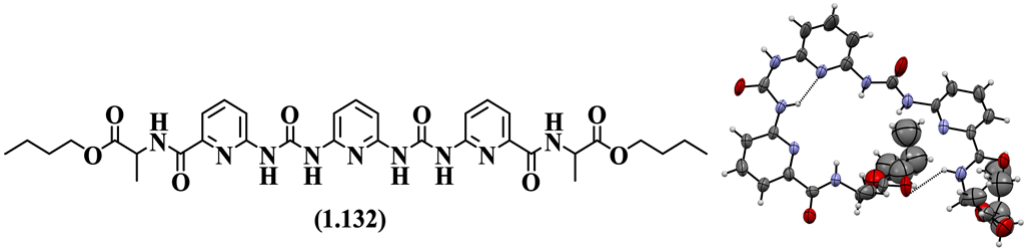

Figure 1.25. Hydrogen bonds between -NH group and pyridyl N-atom in **1.132** (ellipsoids are drawn at 50% probability)

The pyridine urea oligomer **1.132** (Fig. 1.25) is an example that provides a channel-like structure for the transport of chloride ions. **1.132** has an electron-withdrawing property; thus, it interacted with the -NH of adjacent urea to form hydrogen bonds with the chloride ions. The oligomer transported chloride ions by forming a channel. The aggregation of **1.132** oligomer is affected by the chirality of the terminal side chain and solvents, which provides large avenues to study such systems in various applications.[191]

1.4. Pyridyl amide and pyridyl urea as cation sensors

Metal ions, particularly transition metal ions, play an important role in biology, environment, industry, and medical fields.[210–213] They are important for human life and the environment, but some metal ions are hazardous to health and the ecosystem. Thus, the design of a particular coordination pattern from suitable ligands for the selective binding of harmful metal ions is required for detection and separation.

1.4.1. Pyridyl amide in cation sensing

The compound **1.133** was used to recognize both Al^{3+} and Zn^{2+} in living cells successfully, and hence it can be used in biological imaging. **1.133** is a pyridine amide-based non-fluorescent compound, which showed a fluorescent enhancement with Al^{3+} and Zn^{2+} ions respectively [λ_{em} (after binding with Al^{3+}) = 504 nm, and λ_{em} (after binding with Zn^{2+}) = 575 nm] (Scheme 1.15). In this sensing, the O-atom of the phenolic -OH group, N-atoms of imine and pyridine unit coordinated with the metal ion, which resulted in an enhancement of the fluorescence emission spectra. Job's plot and ESI mass data confirmed the 1:1 complex formation of **1.133** with Al^{3+} (**1.134**) or Zn^{2+} (**1.135**), respectively.[214]

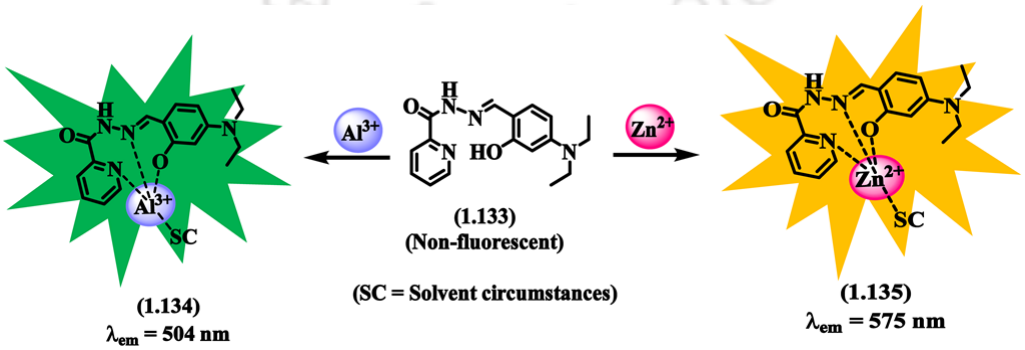

Scheme 1.15. Binding modes of **1.133** with metal cations Al^{3+} and Zn^{2+}

There are certain compounds that, upon substrate binding, stabilize one of the tautomeric forms, showing distinct chromogenic or emission properties. The benzothiazole pyridine amide-based azomethine compound **1.136** emitted at λ_{em} = 560 nm. It showed fluorescent enhancement upon the addition of Al^{3+} along with a significant blue shift (λ_{em} = 473 nm) ($\Delta\lambda$ = ~157 nm). This change was due to the formation of **Al^{3+}-1.136** complex (i.e., **1.137**). The emission at 473 nm was the emission of the enol form of **1.136** complexed with Al^{3+}. The formation of this complex led to an excited state intramolecular proton transfer (ESIPT) and C=N bond reorganization to show chelation-enhanced fluorescence emission. The proton of the phenolic -OH group underwent an exchange between the phenolic and N-atom of the thiazole moieties by forming a six-membered ring intermediate. This intermediate underwent ESIPT in the excited state. Based on Job's plot and electrospray ionization (ESI) mass spectral data, a 1:1 complex between Al^{3+} and **1.136** was involved in the emission mechanism (Scheme 1.16). It was used for the visual detection of Al^{3+} in living cells.[215]

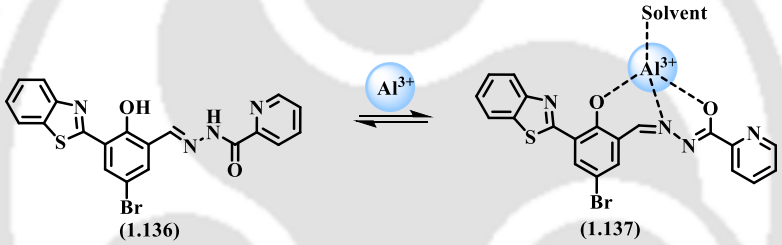

Scheme 1.16. A plausible binding mode of **1.136** with Al^{3+}

Several pyridine 2,6-dicarboxamide-based receptors having pendant phenyl (**1.138**), naphthyl (**1.139**), methylene naphthyl (**1.140**), anthracenyl (**1.141**), fluorene (**1.142**) groups, and 4-hydroxy pyridine based 2,6-dicarboxamide receptors containing naphthyl groups (**1.143** and **1.144**) (Chart 1.7), are useful in detection of cations by emission spectroscopy. These receptors were highly selective towards certain metal cations. **1.139** and **1.141** showed selectivity for Fe^{2+} and Fe^{3+} ions.[216] **1.140** and **1.144** showed selectivity for Pd^{2+} ions, each showing selective fluorescence quenching. The **1.140** formed a 1:1 Pd^{2+} complex. The compounds **1.140** and **1.144** were used in fluorescence-based cell imaging and cell viability studies. These probes were also used as paper-strip or polystyrene film-based sensors.[217] The fluorene-based pyridine 2,6-dicarboxamide receptor **1.142** showed selectivity towards Cu^{2+} and Pb^{2+} metal ions over other metal ions (such as K^+, Na^+, Li^+, Ag^+, Ba^{2+}, Mn^{2+}, Cu^{2+}, Zn^{2+}, Hg^{2+}, Pb^{2+}, Fe^{2+}, Co^{2+}, Mg^{2+}, Al^{3+}, Cr^{3+}). The **1.142** showed fluorescence quenching with Cu^{2+} and Pb^{2+}.[211]

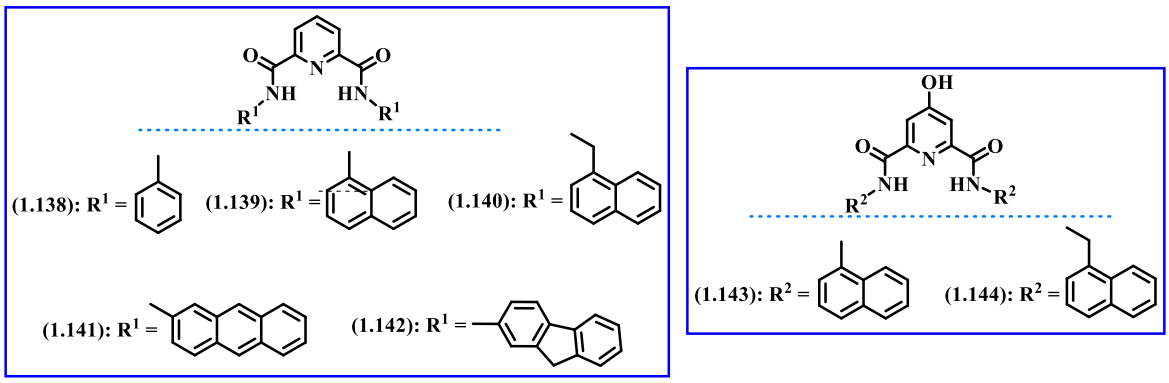

Chart 1.7. Fluorophore-linked pyridyl amide derivatives

The compound **1.145** (Chart 1.8) is an isoniazid functionalized pyridine amide-based sensor of Hg^{2+} and CN^-. The sensing was due to the presence of two binding sites involving two non-identical sensing pathways, which allowed **1.145** to sense two different ions simultaneously. The ^{1}H-NMR spectroscopy revealed the interactions of the **1.145** with Hg^{2+} and CN^- in solution. A progressive addition of Hg^{2+} into **1.145** resulted in a downfield shift of the H_a, H_b, and H_c protons of the pyridine ring, as these protons are located next to the Hg^{2+} ion. The CN^- ion caused deprotonation of its isonicotinyl hydrazone moieties of the **1.145**, causing an upfield shift of the N-H protons. The receptor also showed the ability to remove these two toxic ions from industrial waste.[218]

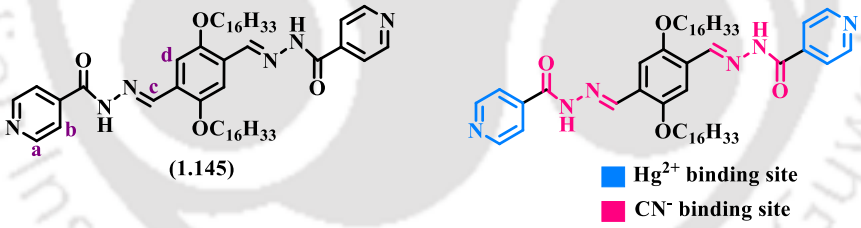

Chart 1.8. A receptor for sensing mercury(II) and cyanide ions

These examples showed that having a fluorophore attached to an amide moiety can help in designing anion receptors to operate with different paths for selective ion recognition, and certain receptors can be useful in selective detection of anion as well as cation in a solution.

1.4.2. Pyridyl urea in cation sensing

The ferrocene-based pyridyl urea **1.146** (Chart 1.9) in DMSO solvent showed a reversible one-electron redox couple of ferrocene/ferrocenium redox process at a relatively low potential of $E_{1/2}$ = -0.310 V versus Fc^+/Fc. The addition of metal cations (Li^+, Na^+, K^+, Ca^{2+},

Mg^{2+}, Ni^{2+}, Zn^{2+}, and Cd^{2+}) to the solution of **1.146** showed no change in its cyclic voltammogram. However, the addition of Cu^{2+} ions increased the current of the reversible redox couple. Also, a quasi-reversible oxidation wave at a positive potential of E_p = +0.007 V versus Fc^+/Fc appeared due to the Cu^{2+}/Cu^+ redox couple enabling a distinction of copper from other ions in solution.[219]

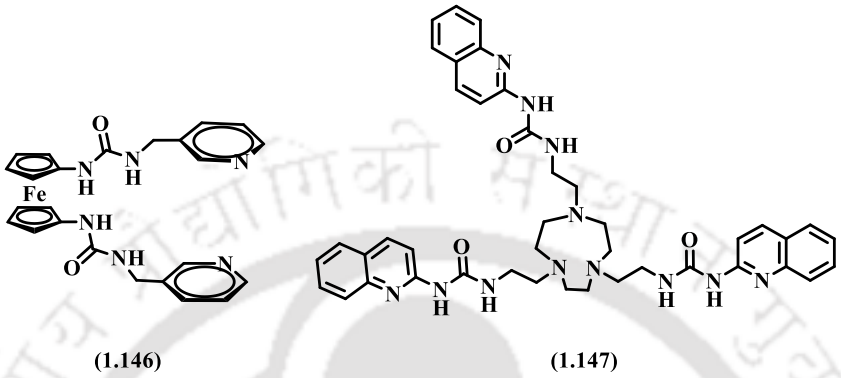

Chart 1.9. Electroactive and fluorogenic urea receptors

The compound **1.147** is an [9]aneN$_3$-based receptor with a quinoline fluorogenic unit and urea functional groups. The absorption and emission spectra of the receptor were studied in solutions in acetonitrile/water (4:1 v/v) solvent mixture in the presence of different metal cations such as Cd^{2+}, Co^{2+}, Cu^{2+}, Fe^{3+}, Hg^{2+}, K^+, Mg^{2+}, Mn^{2+}, Ni^{2+}, Zn^{2+}, and Pb^{2+}. Both the absorbance and fluorescence emission spectra of **1.147** were changed upon the addition of Cd^{2+}, Zn^{2+}, Pb^{2+}, and Cu^{2+}.[220]

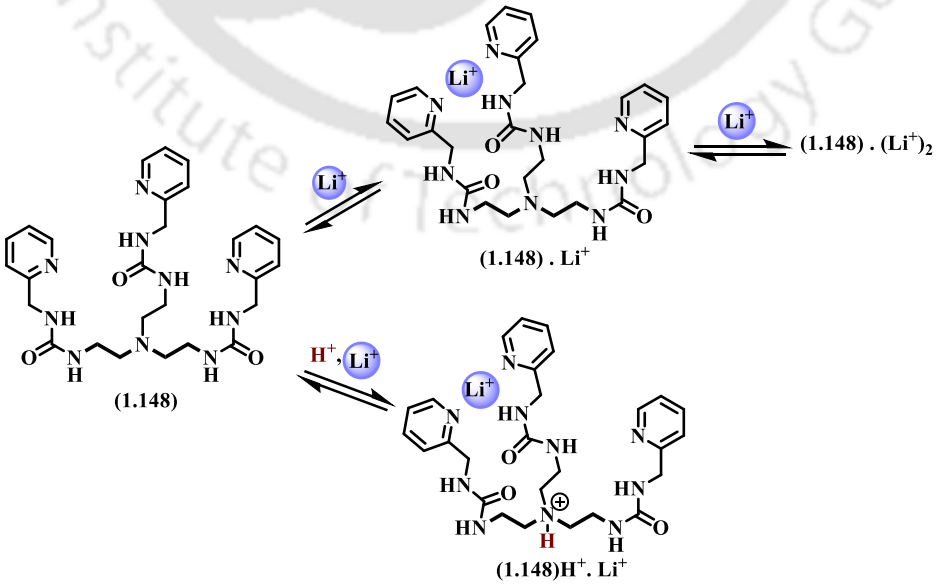

Scheme 1.17. Li^+ ion complexation with **1.148** and **1.148·HClO$_4$**

Pyridyl urea derivatives are efficient ligands of Li^+ by coordinating through the C=O group and pyridyl N-atom. For example, the tripodal ligand **1.148**, tris(2-((pyrid-2-ylmethyl)uredio)ethyl)amine, and its perchlorate salt (**1.148· $HClO_4$**) selectively bind to Li^+ ion to form a 1:1 complex (Scheme 1.17). The pyridyl N-atoms acted as the side arms to encapsulate the Li^+ ion into their cavity. In the complex, the columbic repulsion between the H^+ and Li^+ ions was adjusted by ion-dipole interactions.[221] Lithium ion (Li^+) has various applications in medicines, science, and technology, and the design of artificial lithium ionophores is of particular interest.[222,223]

The macrocyclic host **1.149**, having two 2,2′-bipyridine units and two urea moieties, selectively formed a 1:1 host-guest complex with cadmium ion, **1.150**, i.e., **Cd(1.149)(H_2O)(NO_3)$_2$**. The peculiarity of this ligand is that in the complex, *trans* orientations of the bipyridyl N-atoms of **1.149** were not retained; these were rotated to have both exo (1.150a) and endo (1.150b) conformations the complexation in solution occurred at the exterior or in the interior of the ligand adopting the reorganized structure (Scheme 1.18).[224]

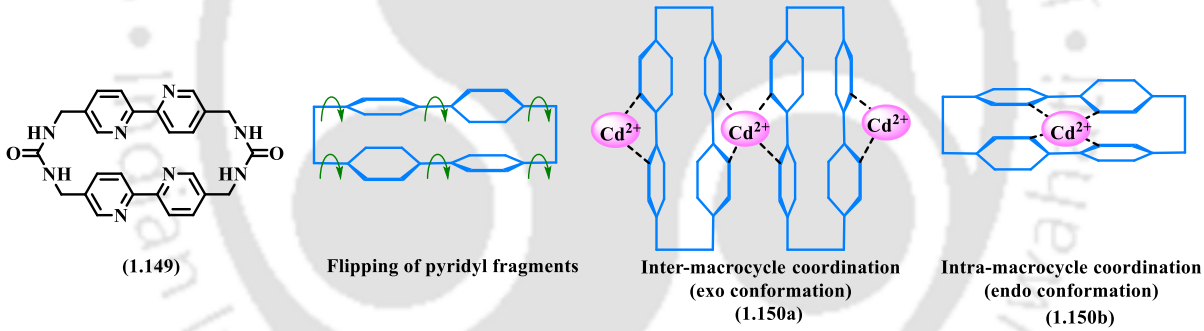

Scheme 1.18. A 2,2′-bipyridine-based bis (urea) macrocyclic host **1.149** and its two different ways of coordination with Cd(II) ion

These have shown the utility of various amide and urea-appended pyridine probes for various metal ion detections and biological imaging. The bio-friendly compounds for such detections with improvement in detection are vital aspects and provide information about the compatibility of these classes of compounds in the supramolecular assembling motifs.

1.5. Coordination chemistry of pyridyl amide and pyridyl urea derivatives

Highly organized structures, both with or without metal ions, can be built with the aid of supramolecular interactions. A variety of supramolecular architectures have been synthesized with a large range of bonding forces; depending on the systems, the interactions can range

from classic M-donor atom bonds to strong halogen or hydrogen bonds to much weaker forces such as weak hydrogen bonds and π···π stacking of small aromatics. Both pyridyl amides and pyridyl urea form a range of coordination complexes with different coordination geometry and nuclearity. In recent years, designing a class of ligands and studying their structural properties and coordination chemistry has been widely studied. These classes of compounds have drawn extensive interest due to their applications in fields such as coordination polymers, materials, and catalysis. The properties of these coordination complexes depend on the nature of the ligands bound to the metal ion. In addition to the metal coordination, the self-assembling features and supramolecular structures originate due to non-covalent interactions such as strong hydrogen bonds, M-donor atom bonds, halogen bonds, ionic interaction with counter ion, weak C-H···O, van der Waals interactions, and π-π stacking interactions between two aromatic rings. Pyridyl amide and pyridyl urea derivatives are of great interest for studying the coordination chemistry due to the presence of pyridyl N-atom as a metal coordination site, and the carboxamide and urea groups can participate in strong hydrogen bonds with counter ions or anionic guest molecules. These interactions are important for the formation of metal-organic frameworks and supramolecular self-assembling systems. Since the last few decades, several metal complexes and coordination polymers involving pyridyl amide and pyridyl urea derivatives as ancillary ligands or linkers have been synthesized, respectively.[103,140,155,225–227]

1.5.1. Coordination chemistry of pyridyl amide derivatives

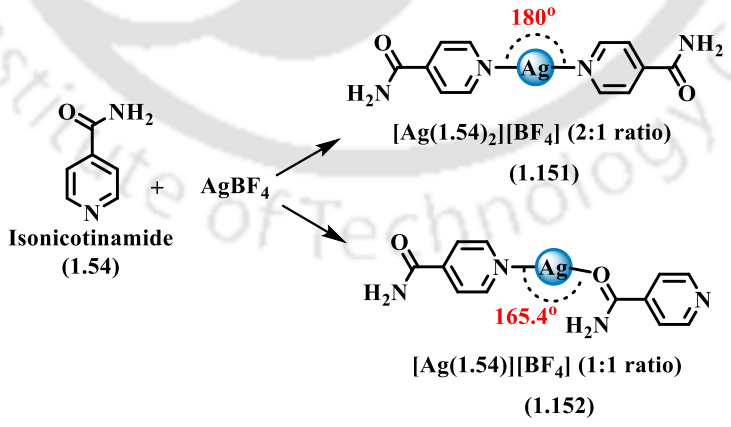

Scheme 1.19. Schematic representation of the formation of coordination metal complexes **1.151** and **1.152** possessing isonicotinamide (**1.54**) as an ancillary ligand

In the reaction of isonicotinamide (**1.54**) with $AgBF_4$, two coordination complexes were formed, both 2:1 complex (**1.151**) and 1:1 complex (**1.152**). In 2:1 complex **1.151**, a linear

tape (180º) of $N_{pyridyl}$-Ag-$N_{pyridyl}$ bond was formed. This linear tape was connected through N-H···O and N-H···F hydrogen bond interactions. However, the 1:1 complex **1.152** comprised of an unusual $N_{pyridyl}$-Ag-O_{amide} bond instead of the regularly formed $N_{pyridyl}$-Ag-$N_{pyridyl}$ bond. The bond angle $N_{pyridyl}$-Ag-O_{amide} was 165.4º (Scheme 1.19).[228] However, an Ag(I)-pyridyl urea compound consisted of an $N_{pyridyl}$-Ag-$N_{pyridyl}$ bond although the carbonyl O-atom of the pyridyl urea has stronger Lewis basicity compared to that of amidic O-atom.[229]

Amide-based metal-organic frameworks are well known for carbon dioxide adsorption through NC=O···CO_2 and NH···O=C=O interactions with the CO_2 molecules.[230] For example, the Zn(II)-based metal-organic framework (**1.154**) of bis(pyridyl) bis(amide) ligand **1.153** (Scheme 1.20) had open-ended channels in which the amide groups of **1.153** formed N-H···O hydrogen bonds with the carboxylate O-atom of terephthalic acid (**1.85**). It showed CO_2 adsorption due to intermolecular hydrogen bonds between the amide groups and CO_2 molecules guiding the adsorption mechanism.[231]

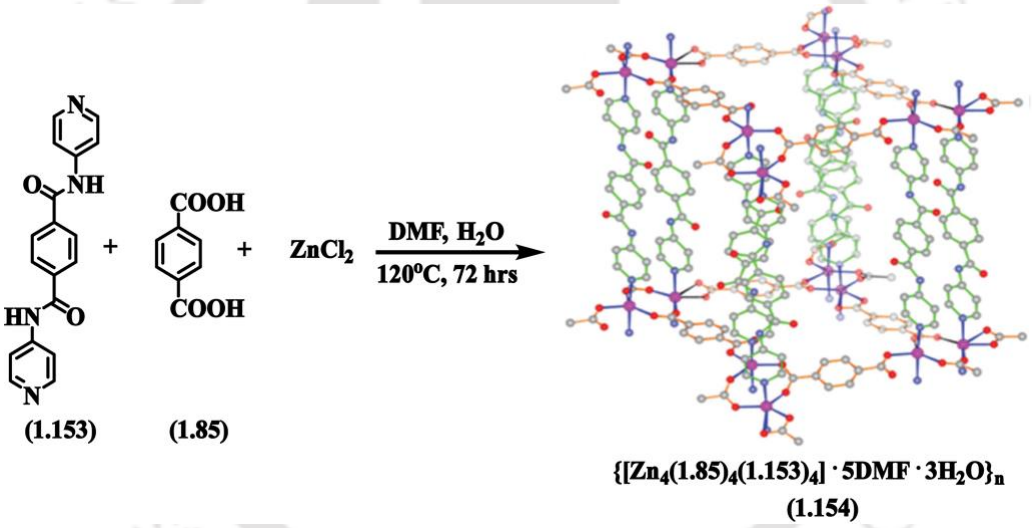

Scheme 1.20. A bis(pyridyl) amide-based Zn (II) MOF **1.154** {"Reprinted (adapted) with permission from C.-H. Lee, H.-Y. Huang, Y.-H. Liu, T.-T. Luo, G.-H. Lee, S.-M. Peng, J.-C. Jiang, I. Chao and K.-L. Lu, *Inorg. Chem.*, 2013, **52**, 3962–3968. Copyright {2013} American Chemical Society."}

The one or two-dimensional nicotinamide **1.53** (or isonicotinamide **1.54**)-based Co(II) mixed ligand coordination polymers **1.157**-**1.159**, trapped solvent molecules such as DMF. Various carboxylates used as one of the linkers are listed in Fig. 1.26. The one-dimensional chain-like structure formed in the coordination polymer **1.157** had the solvent molecules positioned between the chains. Networks with grid-like structures were formed in the **1.158**, where the solvent molecules found a place to occupy. The encapsulation of solvent molecules occurred via NH···O hydrogen bonds of the coordination networks. In the coordination polymer

1.159, the DMF molecules interacted with the aromatic ring of terephthalic acid (**1.85**) through CH···π interactions (Fig. 1.26).[232]

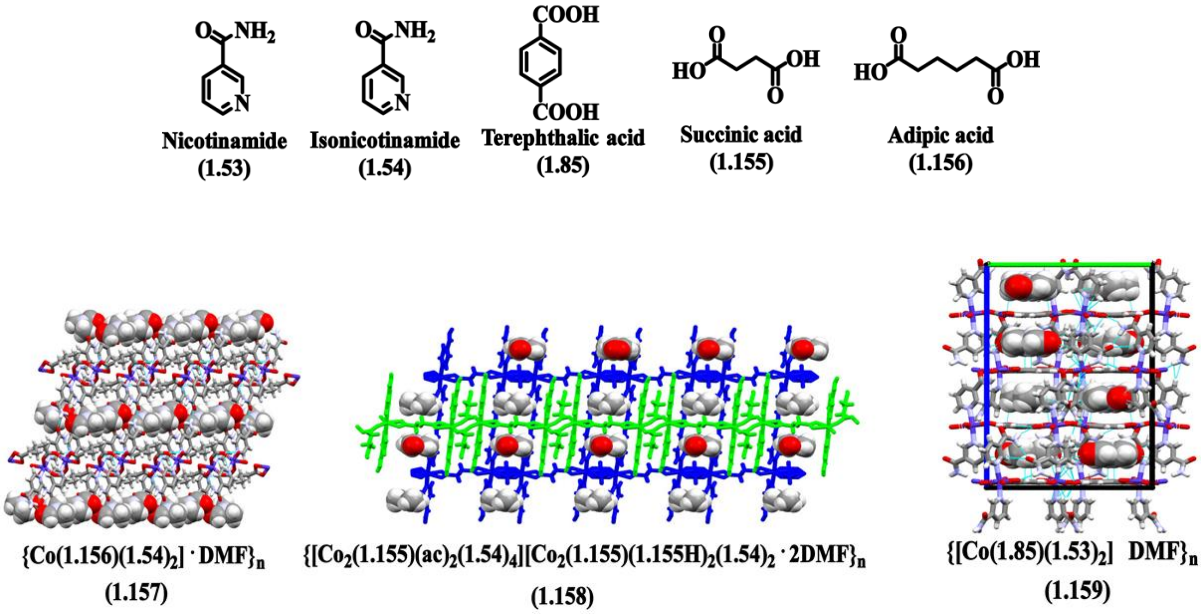

Figure 1.26. Encapsulation of DMF molecules by nicotinamide (**1.53**) and isonicotinamide (**1.54**) based linkers in cobalt(II) coordination polymers **1.157-1.159** (DMF molecules are represented in space fill mode)

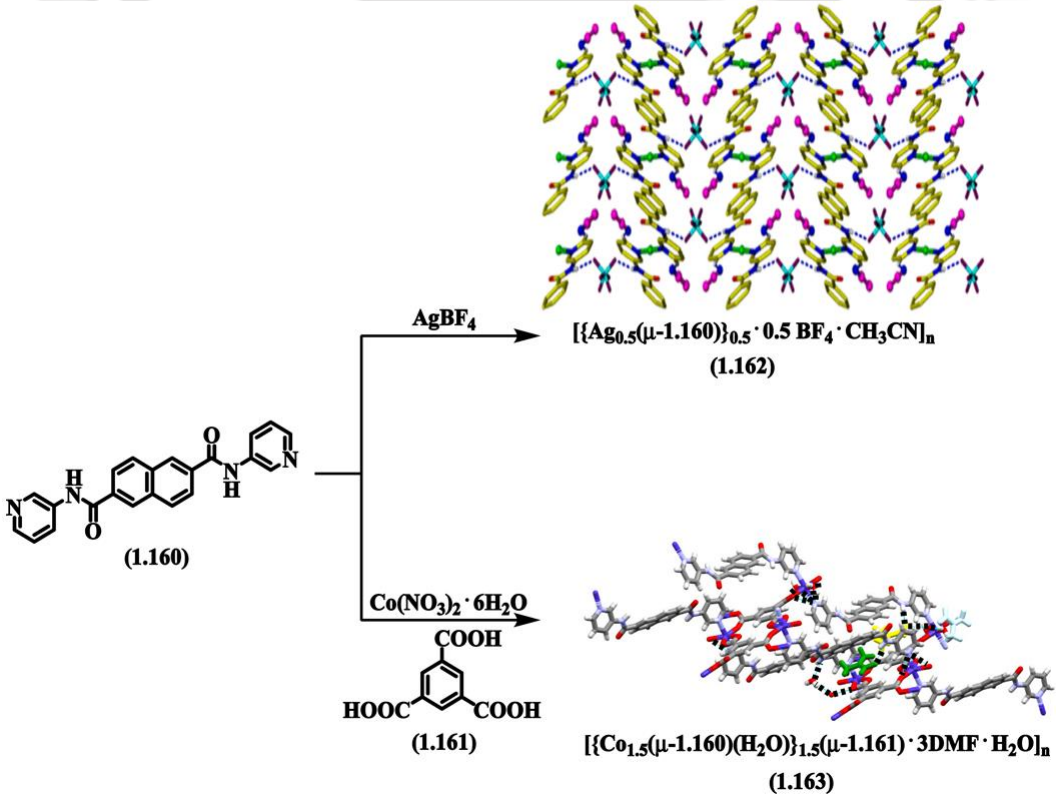

Scheme 1.21. Synthesis of coordination polymers **1.162** and **1.163** ("Reprinted (adapted) with permission from K. Nath, A. Husain and P. Dastidar, *Cryst. Growth Des.*, 2015, **15**, 4635–4645. Copyright {2015} American Chemical Society.")

Pyridyl amide-based coordination polymers can form metallogels. When exposed to light, these metallogels generate nanoparticles. **1.160** is a bis (pyridyl) bis (amide) ligand, which formed coordination polymers **1.162** and **1.163** with $AgBF_4$ and $Co(NO_3)_2.6H_2O$ (in the presence of benzene tricarboxylic acid, respectively (Scheme 1.21). These coordination polymers **1.162** and **1.163** formed metallogels because the presence of amide groups and π-cloud of the naphthyl ring in ligand **1.160** facilitated the gelation assembly through hydrogen bond and π···π stacking interactions.[233]

1.5.2. Flexibility and weak interactions of pyridyl urea ligands in coordination complexes

Pyridyl urea derivatives provide flexibility due to the conformation to have varieties of structures in coordination complexes. The presence of free NH-groups in pyridyl urea-based metal complexes enables them to recognize anions via non-covalent interactions.

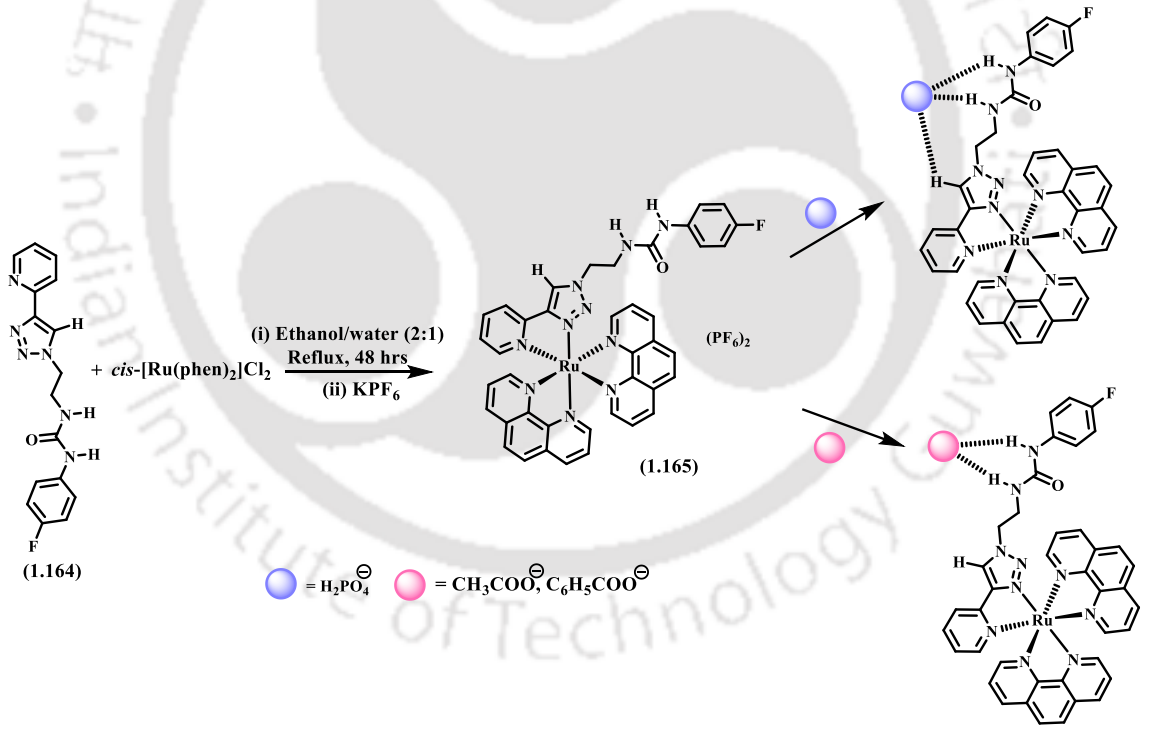

Scheme 1.22. Schematic representation of the binding of $H_2PO_4^-$, CH_3COO^-, $C_6H_5COO^-$ anions to a Ru (II) complex **1.165** consisting of a pyridyl triazole-based urea ligand (**1.164**)

A Ru(II) complex **1.165** having a geometry of the pyridyl triazole-based urea-derived ligand **1.164** such that triazole -CH unit and urea -NH groups act as anion binding sites (Scheme 1.22). ^{1}H-NMR titration studies showed that $H_2PO_4^-$ ion was bound to triazole -CH unit and urea -NH groups. Due to such a reason, the receptor had a weaker affinity for $HP_2O_7^{3-}$ ion.

On the other hand, the CH_3COO^- and $C_6H_5COO^-$ anions were bound to the -NH groups of the urea part, and hence, the recognition of acetate and dihydrogen phosphate had clear distinctions.[234]

The Zn(II) coordination polymers **1.167**-**1.169** and Zn(II) coordination complexes **1.170**-**1.171** consisted of a bis(pyridyl) urea ligand **1.166** (Scheme 1.23) adopted different structural patterns under different conditions. The different forms had different conformation due to the flexible part of the ligand. **1.167**-**1.169** were one-dimensional coordination polymers due to the extended coordination of the ligand **1.166** with the Zn(II) metal center. A two-dimensional network was formed in **1.167** due to the presence of urea tape synthons. In **1.168** and **1.169**, benzene and p-xylene solvent molecules were encapsulated within the cavities of **1.168** and **1.169**, respectively, through CH···π interactions between the CH unit of the benzene solvent (in the case of **1.168**) (or p-xylene solvent in **1.169**) and π-electron cloud of pyridyl ring of the ligand. The presence of aromatic solvents benzene and p-xylene solvent resulted in the formation of macrocycles **1.170** and **1.171**.[235]

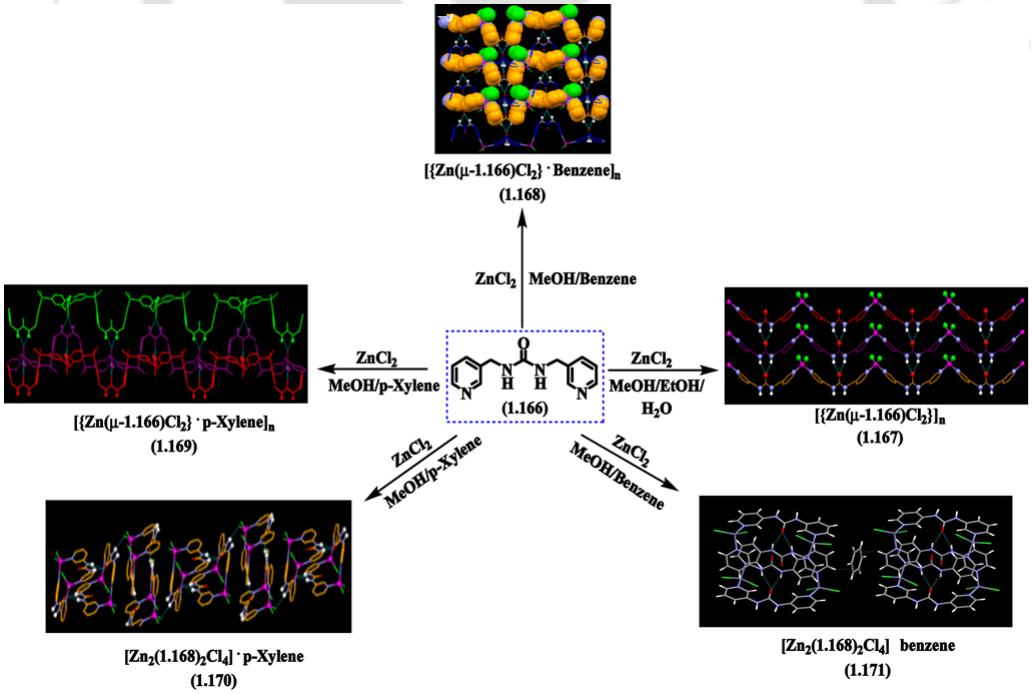

Scheme 1.23. Synthesis of solvent-driven bis(pyridyl) urea-slight variations on the geometrical based Zn(II) coordination polymers **1.167**-**1.169** and coordination complexes **1.170**-**1.171** ("Reprinted (adapted) with permission from S. Banerjee, N. N. Adarsh and P. Dastidar, *Cryst. Growth Des.*, 2012, **12**, 6061–6067. Copyright {2012} American Chemical Society.")

Two Ag(I) coordination complexes, **1.174** and **1.175**, consisted of pyridyl urea ligands **1.172** and **1.173**, respectively (Scheme 1.24). In these two complexes, the $N_{pyridyl}$-atom was involved in complexation with the Ag(I) metal center, and the urea -NH groups formed N-

H···F hydrogen bonds with PF_6 counter anions which were aided by the π···π stacking interactions between the phenyl and pyridyl rings of the respective ligand.[236]

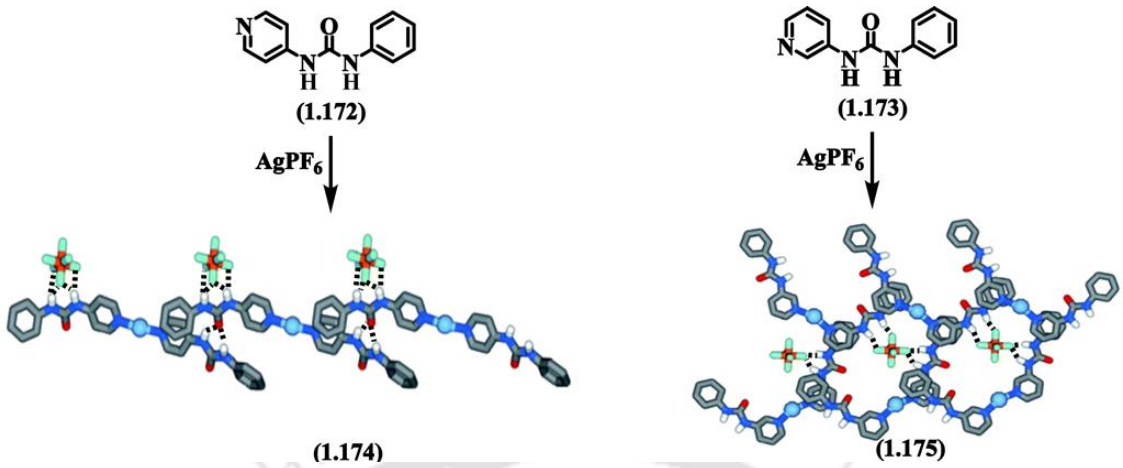

Scheme 1.24. π···π stacking interactions were observed in Ag(I) coordination complexes **1.174** and **1.175** possessing pyridyl urea ligand **1.172** and **1.173**, respectively ("Reprinted (adapted) with permission from P. Blondeau, A. van der Lee and M. Barboiu, *Inorg. Chem.*, 2005, **44**, 5649–5653. Copyright {2005} American Chemical Society.")

These examples have shown that the flexible urea enables adsorption properties, and the slight variation in the position of ligating sites causes a change in the dimensionality of self-assemblies.

1.6. Pharmaceutical applications of pyridyl amide and pyridyl urea derivatives

Amide and urea functionalities are essential in drug development and medicinal chemistry due to their ability to form stable hydrogen bonds with protein and receptor targets. Recently, two excellent reviews have described the role of amide and urea functionalities in biological activities and drug development.[1,237] Carboxamide and urea moieties are introduced in the drug molecules to improve the selectivity and potentiality of the drug molecules and hence contribute to the development of anticancer, antidiabetic, antibacterial, anti-HIV, anticonvulsive agents, and other medicinal compounds. Among those, pyridyl amide and pyridyl urea derivatives have a wide range of biological activities, such as acting as antituberculosis agents,[27,238] enzyme inhibitors,[239,240] anti-trypanosomal agents,[241,242] anticancer activity.[243,244] The highly useful pyridyl amide-based drugs are isoniazid (tuberculosis drug) (**1.176**), niacin (vitamin B3 supplement) (**1.177**), imatinib mesylate (used for leukemia treatment) (**1.178**), netupitant (antiemetic drug) (**1.179**) (Chart 1.10). Many other pyridine amide-based derivatives show antibacterial, anticancer, gastric, and pain-relieving activities; some examples are listed in Chart 1.10. Out of many bioactive

compounds and various clinically approved therapies of pyridyl urea, some examples are listed in Chart 1.10.

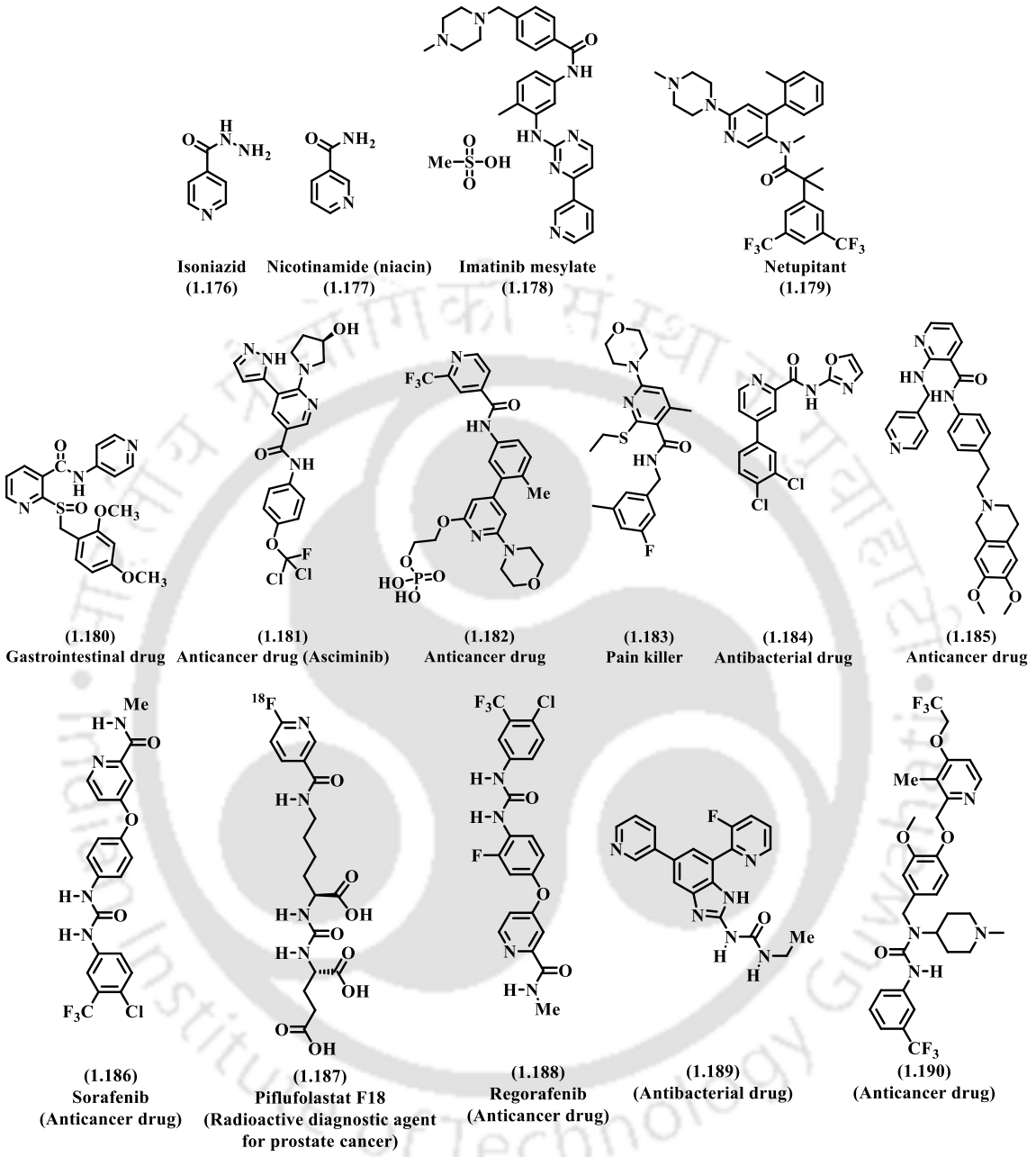

Chart 1.10. Some biologically active pyridyl amide and urea derivatives

The urea portion of the pyridyl urea-based drug sorafenib (**1.186**) plays an important role in molecular recognition by protein kinase active site. The X-ray crystal structure of vascular endothelial growth factor receptor 2 (VEGFR2) in complex with **1.186** proved that the urea part was involved in intermolecular hydrogen bonds with the main chain atoms of Asp1046 and the side chains of Glu885. The N-atom of the pyridyl moiety formed a hydrogen bond with Cys919 (Fig. 1.27).[245] Such studies also provide ideas for screening drug molecules.

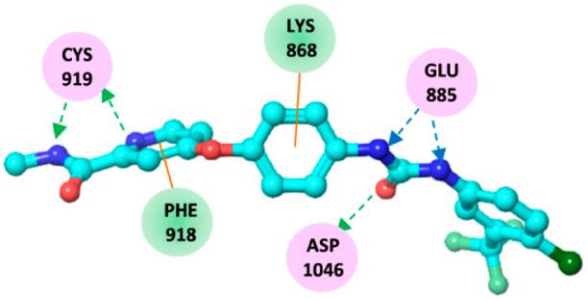

Figure 1.27. Intermolecular hydrogen bonds of **1.186** with Cys919, Asp1046, and Glu885 (blue dashed arrows directed toward the electron donor: hydrogen bonding with amino acid side chains, green dashed arrows directed toward the electron donor: hydrogen bonding with amino acid main chains, and orange lines: π-π interactions) ("Reprinted (adapted) with permission from K. Okamoto, M. Ikemori-Kawada, A. Jestel, K. Von König, Y. Funahashi, T. Matsushima, A. Tsuruoka, A. Inoue and J. Matsui, *ACS Med. Chem. Lett.*, 2015, **6**, 89–94. Copyright {2015} American Chemical Society.")

1.7. Scope of the present work

The forgoing discussions of this chapter have shown that large numbers of composites and sensing nanodevices have emerged based on the compounds having amide bonds. It has also revealed that the pyridyl amide and pyridyl urea-based derivatives have been extensively studied for various applications. Furthermore, pyridyl amide and pyridyl urea derivatives are employed in a range of biomimetic and bioinspired artificial systems such as ion channels.[190,191] The bis(pyridyl) urea **1.191** provided locked conformation sensitive to pH, and the self-assemblies of hydrogen-bonded dimers (Scheme 1.25) had similarity to the intermittent stage of helix-to-sheet transition of peptides.[246]

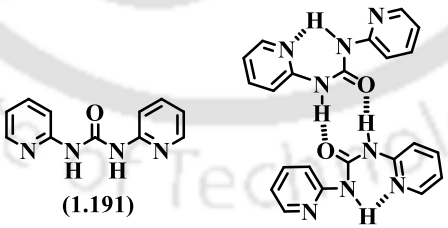

(1.191)

Scheme 1.25. The bis (pyridyl) urea compound **1.191** and an intermolecular hydrogen-bonded unit

Pyrene-based mono-boric acid derivative of cationic pyridinium amide **1.192** (Fig. 1.28) finds utility as a glucose sensor. The sensing of glucose occurred through the aggregation of the receptor due to the pyridinium cation-π interactions in an aqueous solution in the presence of glucose, resulting in a strong excimer emission at 510 nm, which was not observed in the

presence of fructose. The excimer emission in the receptor occurred due to the stacking among pyrene fragments in the complex with glucose, whereas fructose disrupted such stackings.[247]

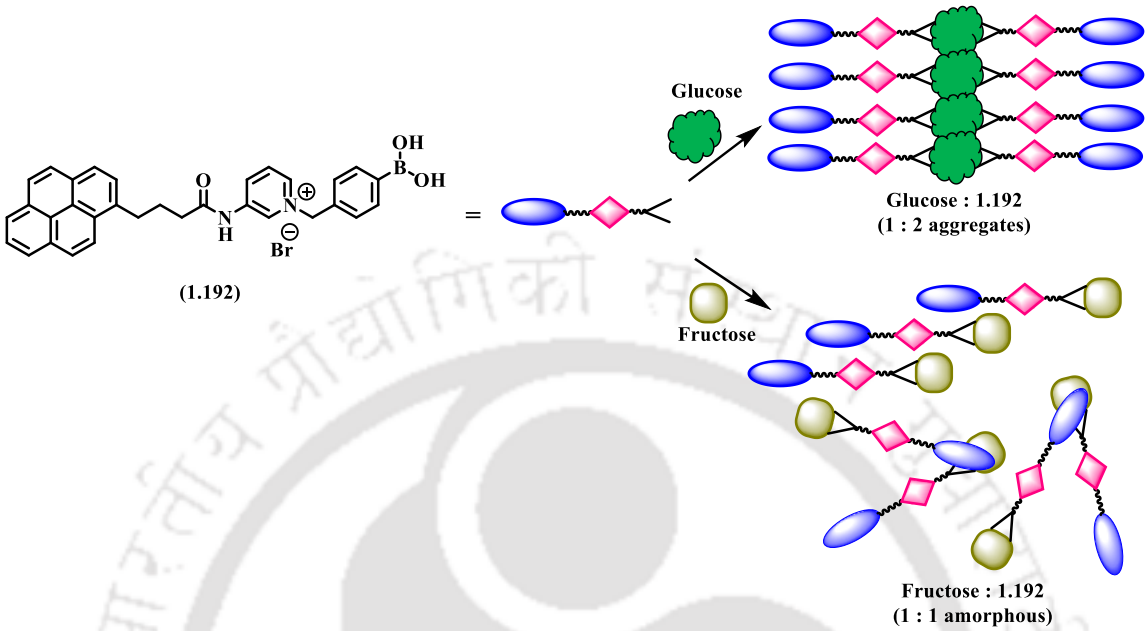

Figure 1.28. Representation of 1:2 glucose and 1:1 fructose complex of **1.192**

The bis-pyridyl amide ligands provide clusters such as cationic complex **[Pt$_3$(bu$_2$bipy)$_3$(1.193)$_3$]$^{6+}$** (i.e., **1.194**) which had a triflate anion inside the cavity (Fig. 1.29).[248] Such clusters have recognition, catalysis, magnetic electrical, and encapsulation properties, but their immobilization and use in different spheres of life have a wider dimension to explore.

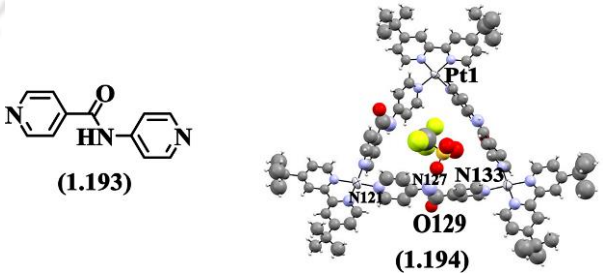

Figure 1.29. A bis(pyridyl) amide-based triangular cationic complex [Pt$_3$(bu$_2$bipy)$_3$(**1.193**)$_3$]$^{6+}$ (i.e., **1.194**) with a triflate anion included in the cavity (ellipsoids are drawn at 50% probablity)

Both pyridyl amide and pyridyl urea derivatives possessing flexible donor properties can coordinate with the metal center and have various catalytic applications.[249,250] These derivatives also form metal-organic frameworks and find applications in detections,[251–256] gas

storage,[257,258] and toxic ion separation[259]. The amide-based polymers provide biodegradable materials with huge prospects as environmentally benign ones. Their utility as biological probes for in vivo and in-vitro study, as a source of medicinally active compounds, optically active compounds, and NLO materials, and their utility as present and forthcoming scopes are undisputable. Their role in adopting various geometries that are tuned by stimuli and properties like dual emissions has great potential.

Based on these, there is a definite scope to study the supramolecular features of pyridyl amide and pyridyl urea compounds. Looking at the future potentials of pyridyl amides and pyridyl urea derivatives in terms of their photophysical properties, host-guest binding and composites for environmental remediation, a study is carried out on the supramolecular assemblies of different pyridyl amide and pyridyl urea-based salts, metal complexes, coordination polymers, and composites to characterize and find out newer aspects from their properties, which are presented in the preceding chapters.

1.8. References

1 S. Kumari, A. V Carmona, A. K. Tiwari and P. C. Trippier, *J. Med. Chem.*, 2020, **63**, 12290–12358.

2 V. R. Pattabiraman and J. W. Bode, *Nature*, 2011, **480**, 471–479.

3 T. Wieland and M. Bodanszky, *The world of peptides: a brief history of peptide chemistry*, Springer Science & Business Media, 2012.

4 A. Choudhary, D. Gandla, G. R. Krow and R. T. Raines, *J. Am. Chem. Soc.*, 2009, **131**, 7244–7246.

5 N. Cheng, Q. Yan, S. Liu and D. Zhao, *CrystEngComm*, 2014, **16**, 4265–4273.

6 R. Adhikary, J. Zimmermann, J. Liu, R. P. Forrest, T. D. Janicki, P. E. Dawson, S. A. Corcelli and F. E. Romesberg, *J. Am. Chem. Soc.*, 2014, **136**, 13474–13477.

7 Y. Takezawa, S. Sakakibara and M. Shionoya, *Chem. – A Eur. J.*, 2021, **27**, 16626–16633.

8 Y. Li, X.-N. Jiang and C.-S. Wang, *J. Comput. Chem.*, 2011, **32**, 953–966.

9 C. B. Aaker and A. M. Beatty, *Chem. Commun.*, 1998, **082**, 1067.

10 W. E. Stewart and T. H. Siddall, *Chem. Rev.*, 1970, **70**, 517–551.

11 G. N. Ramachandran, C. Ramakrishnan and V. Sasisekharan, *J. Mol. Biol.*, 1963, **7**, 95–99.

12 X. Chen, J. Wang, A. P. Boughton, C. B. Kristalyn and Z. Chen, *J. Am. Chem. Soc.*, 2007, **129**, 1420–1427.

13 S. Ye, H. Li, W. Yang and Y. Luo, *J. Am. Chem. Soc.*, 2014, **136**, 1206–1209.

14 A. K. Ghose, V. N. Viswanadhan and J. J. Wendoloski, *J. Comb. Chem.*, 1999, **1**, 55–68.

15 J. M. Humphrey and A. R. Chamberlin, *Chem. Rev.*, 1997, **97**, 2243–2266.

16 A. Greenberg, C. M. Breneman and J. F. Liebman, *The amide linkage: Structural significance in chemistry, biochemistry, and materials science*, John Wiley & Sons, 2000.

17 E. Meaurio, L. Cesteros, L. G. Parada and I. Katime, *Polym. J.*, 2004, **36**, 84–90.

18 J. Z. Yi and S. H. Goh, *Polymer (Guildf).*, 2002, **43**, 4515–4522.

19 M. Nina, R. Fonné-Pfister, R. Beaudegnies, H. Chekatt, P. M. J. Jung, F. Murphy-Kessabi, A. De Mesmaeker and S. Wendeborn, *J. Am. Chem. Soc.*, 2005, **127**, 6027–6038.

20 K. J. Oh, K. J. Cash and K. W. Plaxco, *J. Am. Chem. Soc.*, 2006, **128**, 14018–14019.

21 E. Pazos, O. Vázquez, J. L. Mascareñas and M. Eugenio Vázquez, *Chem. Soc. Rev.*, 2009, **38**, 3348–3359.

22 M. E. Vázquez, M. Nitz, J. Stehn, M. B. Yaffe and B. Imperiali, *J. Am. Chem. Soc.*, 2003, **125**, 10150–10151.

23 C. Panda, M. Ghosh, T. Panda, R. Banerjee and S. Sen Gupta, *Chem. Commun.*, 2011, **47**, 8016–8018.

24 C. P. Decicco, J. L. Seng, K. E. Kennedy, M. B. Covington, P. K. Welch, E. C. Arner, R. L. Magolda and D. J. Nelson, *Bioorg. Med. Chem. Lett.*, 1997, **7**, 2331–2336.

25 C. Chen, M. Zhang, W. Zhang and J. Bai, *Inorg. Chem.*, 2019, **58**, 2729–2735.

26 L.-N. Ma, L. Zhang, W.-F. Zhang, Z.-H. Wang, L. Hou and Y.-Y. Wang, *Inorg. Chem.*, 2022, **61**, 2679–2685.

27 S. Konduri, D. Bhargavi, J. Prashanth, V. S. Krishna, D. Sriram and K. P. Rao, *ACS Omega*, 2021, **6**, 1657–1667.

28 L. Zhang, D. Lin, Y. Kusov, Y. Nian, Q. Ma, J. Wang, A. von Brunn, P. Leyssen, K. Lanko, J. Neyts, A. de Wilde, E. J. Snijder, H. Liu and R. Hilgenfeld, *J. Med. Chem.*, 2020, **63**, 4562–4578.

29 J. H. Yang and S. K. Kim, *Chem. Commun.*, 2023, **59**, 9988–9991.

30 S. N. Timasheff, M. J. Ettinger and M. G. D. Strycharz, *Biochemistry*, 1971, **10**, 824–831.

31 J. Dong, Y. Liu and Y. Cui, *J. Am. Chem. Soc.*, 2021, **143**, 17316–17336.

32 D. A. Barrera, E. Zylstra, P. T. J. Lansbury and R. Langer, *J. Am. Chem. Soc.*, 1993, **115**, 11010–11011.

33 M. Deng, J. Wu, C. A. Reinhart-King and C.-C. Chu, *Biomacromolecules*, 2009, **10**, 3037–3047.

34 Q. Liu, J. Wang and B. J. Boyd, *Talanta*, 2015, **136**, 114–127.

35 A. Lakshmanan, S. Zhang and C. A. E. Hauser, *Trends Biotechnol.*, 2012, **30**, 155–165.

36 S. Yoshida, S. Uehara, N. Kondo, Y. Takahashi, S. Yamamoto, A. Kameda, S. Kawagoe, N. Inoue, M. Yamada, N. Yoshimura and Y. Tachibana, *J. Med. Chem.*, 2022, **65**, 10655–10673.

37 H. Sigel and R. B. Martin, *Chem. Rev.*, 1982, **82**, 385–426.

38 O. Reynes, T. Gulon, J. C. Moutet, G. Royal and E. Saint-Aman, *J. Organomet. Chem.*, 2002, **656**, 116–119.

39 L.-J. Kuo, J.-H. Liao, C.-T. Chen, Huang, C.-S. Chen and J.-M. Fang, *Org. Lett.*, 2003, **5**, 1821–1824.

40 P. Wang, S. M. Batt, B. Wang, L. Fu, R. Qin, Y. Lu, G. Li, G. S. Besra and H. Huang, *J. Med. Chem.*, 2021, **64**, 6241–6261.

41 J. L. Sessler, E. Katayev, G. D. Pantos, P. Scherbakov, M. D. Reshetova, V. N. Khrustalev, V. M. Lynch and Y. A. Ustynyuk, *J. Am. Chem. Soc.*, 2005, **127**, 11442–11446.

42 L. J. Kuo, J. H. Liao, C. T. Chen, C. H. Huang, C. S. Chen and J. M. Fang, *Org. Lett.*, 2003, **5**, 1821–1824.

43 S. Luo, M. A. Siegler and E. Bouwman, *Eur. J. Inorg. Chem.*, 2019, **2019**, 617–627.

44 H. V. Huynh and J. T. Vossen, *Inorg. Chem.*, 2020, **59**, 12486–12493.

45 W. E. Bull, S. K. Madan and J. E. Willis, *Inorg. Chem.*, 1963, **2**, 303–306.

46 H. Sigel and R. B. Martin, *Chem. Rev.*, 1982, **82**, 385–426.

47 S. G. Churusova, D. V Aleksanyan, E. Y. Rybalkina, O. Y. Susova, A. S. Peregudov, V. V Brunova, E. I. Gutsul, Z. S. Klemenkova, Y. V Nelyubina, V. N. Glushko and V. A. Kozlov, *Inorg. Chem.*, 2021, **60**, 9880–9898.

48 B. R. James and G. Rosenberg, *Coord. Chem. Rev.*, 1975, **16**, 153–159.

49 L. Rajput and K. Biradha, *Cryst. Growth Des.*, 2007, **7**, 2376–2379.

50 A. Ingham, T. I. Kostelnik, B. L. McNeil, B. O. Patrick, N. Choudhary, M. de G. Jaraquemada-Peláez and C. Orvig, *Dalt. Trans.*, 2021, **50**, 11579–11595.

51 N. Smrečki, O. Jović, B.-M. Kukovec, E. Šimunić, S. Vuk, A. Skuhala, M. Babić, T. Rončević, N. Ilić, I. Kekez, D. Matković-Čalogović and Z. Popović, *Inorganica Chim. Acta*, 2018, **471**, 521–529.

52 R. S. Mulla, J. Pitarch-Jarque, E. García-España, T. Desa, E. Lurie-Luke and J. A. G. Williams, *ChemistrySelect*, 2017, **2**, 5045–5050.

53 N. Smrečki, V. Stilinović, O. Jović, B.-M. Kukovec and Z. Popović, *Inorganica Chim. Acta*, 2017, **462**, 57–63.

54 D. Das, M. Joshi, S. Kannan, M. Kumar, T. K. Ghanty, A. S. Pente, A. Sengupta and C. P. Kaushik,

Polyhedron, 2021, **201**, 115166.

55 S. Wang, X. Yang, L. Xu, Y. Miao, X. Yang and C. Xiao, *Ind. Eng. Chem. Res.*, 2023, **62**, 15613–15624.

56 E. Makombe, D. Bourgeois, L. Berthon and D. Meyer, *J. Mol. Liq.*, 2022, **368**, 120701.

57 S. Pachisia and R. Gupta, *Dalt. Trans.*, 2020, **49**, 14731–14748.

58 G. K. Ingle, R. W. Watkins, A. M. Arif and L. M. Berreau, *J. Coord. Chem.*, 2008, **61**, 61–77.

59 H. Liu, Y. Tan, Q. Dai, H. Liang, J. Song, J. Qu and W.-Y. Wong, *Dye. Pigment.*, 2018, **158**, 312–318.

60 S.-S. Sun, A. J. Lees and P. Y. Zavalij, *Inorg. Chem.*, 2003, **42**, 3445–3453.

61 U. Manna, R. Chutia and G. Das, *Cryst. Growth Des.*, 2016, **16**, 2893–2903.

62 C. Ghiron, S. N. Haydar, S. Aschmies, H. Bothmann, C. Castaldo, G. Cocconcelli, T. A. Comery, L. Di, J. Dunlop, T. Lock, A. Kramer, D. Kowal, F. Jow, S. Grauer, B. Harrison, S. La Rosa, L. Maccari, K. L. Marquis, I. Micco, A. Nencini, J. Quinn, A. J. Robichaud, R. Roncarati, C. Scali, G. C. Terstappen, E. Turlizzi, M. Valacchi, M. Varrone, R. Zanaletti and U. Zanelli, *J. Med. Chem.*, 2010, **53**, 4379–4389.

63 N. Barooah, R. J. Sarma and J. B. Baruah, *Eur. J. Inorg. Chem.*, 2006, **2006**, 2942–2946.

64 J. K. Nath and J. B. Baruah, *New J. Chem.*, 2013, **37**, 1509–1519.

65 I. Carreira-Barral, T. Rodríguez-Blas, C. Platas-Iglesias, A. de Blas and D. Esteban-Gómez, *Inorg. Chem.*, 2014, **53**, 2554–2568.

66 S. O. Kang, R. A. Begum and K. Bowman-James, *Angew. Chemie Int. Ed.*, 2006, **45**, 7882–7894.

67 E. A. Younes, N. Hussein, M. Shtaiwi, F. Shahrokhi, K. A. Abu Safieh and Y. Zhao, *New J. Chem.*, 2020, **44**, 16546–16556.

68 P. Niedbała, M. Ceborska, M. Mehmet, W. Ignacak, J. Jurczak and K. Dąbrowa, *Materials (Basel).*, 2022, **15**, 692.

69 P. Bhandari and P. S. Mukherjee, *Chem. – A Eur. J.*, 2022, **28**, e202201901.

70 I. Yahaya, E. Keleş, A. U. Putra, M. Yahya, N. Seferoğlu and Z. Seferoğlu, *J. Mol. Struct.*, 2020, **1204**, 127465.

71 B. Deka and R. J. Sarma, *ChemistrySelect*, 2018, **3**, 5786–5791.

72 L. Gao, Y. Zhou, Z. Li, J. He, Y. Qu, X. Zou, B. Liu, C. Ma, J. Sun and K. Guo, *J. CO_2 Util.*, 2022, **65**, 102196.

73 M. A. Martínez-Aguirre, D. M. Otero, M. L. Álvarez-Hernández, T. Torres-Blancas, A. Dorazco-González and A. K. Yatsimirsky, *Heterocycl. Commun.*, 2017, **23**, 171–180.

74 J.-Z. Liao, H. Ke, J.-J. Liu, Z.-Y. Li, M.-J. Lin, J.-D. Wang and C.-C. Huang, *CrystEngComm*, 2013, **15**,

4830–4837.

75 Y.-B. Wang, D.-S. Liu, T.-H. Pan, Q. Liang, X.-H. Huang, S.-T. Wu and C.-C. Huang, *CrystEngComm*, 2010, **12**, 3886–3893.

76 L. A. Clapp, C. J. Siddons, J. R. Whitehead, D. G. VanDerveer, R. D. Rogers, S. T. Griffin, S. B. Jones and R. D. Hancock, *Inorg. Chem.*, 2005, **44**, 8495–8502.

77 R. R. Biekofsky, S. R. Martin, J. P. Browne, P. M. Bayley and J. Feeney, *Biochemistry*, 1998, **37**, 7617–7629.

78 D. Burdinski, J. Lub, J. A. Pikkemaat, D. Moreno Jalón, S. Martial and C. Del Pozo Ochoa, *Dalt. Trans.*, 2008, 4138–4151.

79 K. Lee, V. Dzubeck, L. Latshaw and J. P. Schneider, *J. Am. Chem. Soc.*, 2004, **126**, 13616–13617.

80 C. C. Costain and J. M. Dowling, *J. Chem. Phys.*, 2004, **32**, 158–165.

81 T. J. Collins, R. J. Coots, T. T. Furutani, J. T. Keech, G. T. Peake and B. D. Santarsiero, *J. Am. Chem. Soc.*, 1986, **108**, 5333–5339.

82 J. Wang, R. Huang, W. Qi, R. Su, B. P. Binks and Z. He, *Appl. Catal. B Environ.*, 2019, **254**, 452–462.

83 C. A. Schalley, R. K. Castellano, M. S. Brody, D. M. Rudkevich, G. Siuzdak and J. Rebek, *J. Am. Chem. Soc.*, 1999, **121**, 4568–4579.

84 A. Mishra and R. Gupta, *Dalt. Trans.*, 2014, **43**, 7668–7682.

85 B. Dojer, A. Pevec, F. Belaj, Z. Jagličić, M. Kristl and M. Drofenik, *J. Mol. Struct.*, 2014, **1076**, 713–718.

86 N. Hearne, M. M. Turnbull, C. P. Landee, E. M. Van der Merwe and M. Rademeyer, *CrystEngComm*, 2019, **21**, 1910–1927.

87 G. Yang, H. G. Zhu, B. H. Liang and X. M. Chen, *J. Chem. Soc. Dalt. Trans.*, 2001, 684–689.

88 C. B. Aakeröy, A. M. Beatty, J. Desper, M. O'Shea and J. Valdés-Martínez, *J. Chem. Soc. Dalt. Trans.*, 2003, 3956–3962.

89 C. B. Aakeröy, A. M. Beatty, D. S. Leinen and K. R. Lorimer, *Chem. Commun.*, 2000, 935–936.

90 G. R. Desiraju, *Angew. Chemie Int. Ed. English*, 1995, **34**, 2311–2327.

91 M. C. Etter, *Acc. Chem. Res.*, 1990, **23**, 120–126.

92 S. Saha and G. R. Desiraju, *J. Am. Chem. Soc.*, 2018, **140**, 6361–6373.

93 B. Das and J. B. Baruah, *Cryst. Growth Des.*, 2011, **11**, 5522–5532.

94 A. Bacchi, G. Cantoni, D. Crocco, M. Granelli, P. Pagano and P. Pelagatti, *CrystEngComm*, 2014, **16**, 1001–1009.

95 D. R. Turner, S. N. Pek and S. R. Batten, *CrystEngComm*, 2009, **11**, 87–93.

96 P. Vishweshwar, A. Nangia and V. M. Lynch, *Cryst. Growth Des.*, 2003, **3**, 783–790.

97 L. S. Reddy, A. Nangia and V. M. Lynch, *Cryst. Growth Des.*, 2004, **4**, 89–94.

98 C. B. Aakeröy, J. Desper and B. M. T. Scott, *Chem. Commun.*, 2006, 1445–1447.

99 C. B. Aakeröy, A. M. Beatty and B. A. Helfrich, *J. Am. Chem. Soc.*, 2002, **124**, 14425–14432.

100 L. Rajput and K. Biradha, *Cryst. Growth Des.*, 2009, **9**, 40–42.

101 S. Saha and G. R. Desiraju, *J. Am. Chem. Soc.*, 2018, **140**, 6361–6373.

102 P. Vishweshwar, A. Nangia and V. M. Lynch, *CrystEngComm*, 2003, **5**, 164–168.

103 M. Aković, D. Vila-Viosa, M. J. Calhorda and Z. Popović, *CrystEngComm*, 2011, **13**, 5863–5871.

104 S. M. Fellows and T. J. Prior, *Cryst. Growth Des.*, 2017, **17**, 106–116.

105 T. Dorn, K. M. Fromm and C. Janiak, *Aust. J. Chem.*, 2006, **59**, 22–25.

106 C. B. Aakeröy, A. M. Beatty and B. A. Helfrich, *J. Chem. Soc. Dalt. Trans.*, 1998, 1943–1946.

107 Ž. Soldin, B. M. Kukovec, T. Debač, M. Đaković and Z. Popović, *Heliyon*, 2022, **8**, e09943.

108 V. Leigh, D. J. Carleton, J. Olguin, H. Mueller-Bunz, L. J. Wright and M. Albrecht, *Inorg. Chem.*, 2014, **53**, 8054–8060.

109 M. Navarro, M. Li, H. Müller-Bunz, S. Bernhard and M. Albrecht, *Chem. - A Eur. J.*, 2016, **22**, 6740–6745.

110 K. Salzmann, C. Segarra and M. Albrecht, *Angew. Chemie - Int. Ed.*, 2020, **59**, 8932–8936.

111 A. J. Bukvic and M. Albrecht, *Inorg. Chem.*, 2022, **61**, 14038–14045.

112 P. D. W. Boyd, L. J. Wright and M. N. Zafar, *Inorg. Chem.*, 2011, **50**, 10522–10524.

113 P. Melle, Y. Manoharan and M. Albrecht, *Inorg. Chem.*, 2018, **57**, 11761–11774.

114 T. Haino, T. Fujii and Y. Fukazawa, *J. Org. Chem.*, 2006, **71**, 2572–2580.

115 N. Hisano and T. Haino, *J. Org. Chem.*, 2022, **87**, 4001–4009.

116 S. K. Kim, J. M. Lim, T. Pradhan, H. S. Jung, V. M. Lynch, J. S. Kim, D. Kim and J. L. Sessler, *J. Am. Chem. Soc.*, 2014, **136**, 495–505.

117 I. Okamoto, M. Nabeta, M. Yamamoto, M. Mikami, T. Takeya and O. Tamura, *Tetrahedron Lett.*, 2006, **47**, 7143–7146.

118 I. Okamoto, M. Nabeta, Y. Hayakawa, N. Morita, T. Takeya, H. Masu, I. Azumaya and O. Tamura, *J. Am. Chem. Soc.*, 2007, **129**, 1892–1893.

119 L. Casali, L. Mazzei, O. Shemchuk, L. Sharma, K. Honer, F. Grepioni, S. Ciurli, D. Braga and J. Baltrusaitis, *ACS Sustain. Chem. Eng.*, 2019, **7**, 2852–2859.

120 L. Casali, L. Mazzei, O. Shemchuk, K. Honer, F. Grepioni, S. Ciurli, D. Braga and J. Baltrusaitis, *Chem. Commun.*, 2018, **54**, 7637–7640.

121 I. Gallou, *Org. Prep. Proced. Int.*, 2007, **39**, 355–383.

122 J. Regan, N. Moss, C. Pargellis, S. Pav, A. Proto, A. Swinamer, L. Tong, C. Torcellini, S. Breitfelder, P. Cirillo, T. Gilmore, A. G. Graham, E. Hickey, B. Klaus, J. Madwed and M. Moriak, *J. Med. Chem.*, 2002, **45**, 2994–3008.

123 Y. L. Cho, D. M. Rudkevich and J. Rebek, *J. Am. Chem. Soc.*, 2000, **122**, 9868–9869.

124 R. K. Castellano and J. Rebek, *J. Am. Chem. Soc.*, 1998, **120**, 3657–3663.

125 M. Alajarín, A. Pastor, R.-Á. Orenes, J. W. Steed and R. Arakawa, *Chem. – A Eur. J.*, 2004, **10**, 1383–1397.

126 C. E. Stanley, N. Clarke, K. M. Anderson, J. A. Elder, J. T. Lenthall and J. W. Steed, *Chem. Commun.*, 2006, 3199–3201.

127 Y. Jeong, K. Hanabusa, H. Masunaga, I. Akiba, K. Miyoshi, S. Sakurai and K. Sakurai, *Langmuir*, 2005, **21**, 586–594.

128 M. O. M. Piepenbrock, N. Clarke and J. W. Steed, *Soft Matter*, 2011, **7**, 2412–2418.

129 B. Wu, X. Huang, Y. Xia, X. J. Yang and C. Janiak, *CrystEngComm*, 2007, **9**, 676–685.

130 R. Custelcean and B. A. Moyer, *Eur. J. Inorg. Chem.*, 2007, **2007**, 1321–1340.

131 P. Howlader, P. Das, E. Zangrando and P. S. Mukherjee, *J. Am. Chem. Soc.*, 2016, **138**, 1668–1676.

132 J. M. Roberts, B. M. Fini, A. A. Sarjeant, O. K. Farha, J. T. Hupp and K. A. Scheidt, *J. Am. Chem. Soc.*, 2012, **134**, 3334–3337.

133 D. Esteban-Gómez, L. Fabbrizzi and M. Licchelli, *J. Org. Chem.*, 2005, **70**, 5717–5720.

134 A. Tarai and J. B. Baruah, *ACS Omega*, 2017, **2**, 6991–7001.

135 M. Cametti and K. Rissanen, *Chem. Commun.*, 2009, 2809–2829.

136 A. Alhalaweh, S. George, D. Boström and S. P. Velaga, *Cryst. Growth Des.*, 2010, **10**, 4847–4855.

137 I. Brekalo, V. Martinez, B. Karadeniz, P. Orešković, D. Drapanauskaite, H. Vriesema, R. Stenekes, M. Etter, I. Dejanović, J. Baltrusaitis and K. Užarević, *ACS Sustain. Chem. Eng.*, 2022, **10**, 6743-6754.

138 C. Lee, A. Y. Cho, W. Yoon, H. Yun, J. W. Kang and J. Lee, *Cryst. Growth Des.*, 2019, **19**, 3807–3814.

139 R. Brahma and J. B. Baruah, *CrystEngComm*, 2021, **23**, 3812–3827.

140 S. K. Chandran, R. Thakuria and A. Nangia, *CrystEngComm*, 2008, **10**, 1891–1898.

141 V. Amendola, M. Boiocchi, B. Colasson and L. Fabbrizzi, *Inorg. Chem.*, 2006, **45**, 6138–6147.

142 J. Nath and J. B. Baruah, *Cryst. Growth Des.*, 2021, **21**, 5325–5341.

143 B. P. Hay, T. K. Firman and B. A. Moyer, *J. Am. Chem. Soc.*, 2005, **127**, 1810–1819.

144 R. Custelcean, P. V. Bonnesen, N. C. Duncan, X. Zhang, L. A. Watson, G. Van Berkel, W. B. Parson and B. P. Hay, *J. Am. Chem. Soc.*, 2012, **134**, 8525–8534.

145 R. Chutia, S. K. Dey and G. Das, *Cryst. Growth Des.*, 2015, **15**, 4993–5001.

146 L. S. Reddy, S. Basavoju, V. R. Vangala and A. Nangia, *Cryst. Growth Des.*, 2006, **6**, 161–173.

147 C. Jia, Q. Q. Wang, R. A. Begum, V. W. Day and K. Bowman-James, *Org. Biomol. Chem.*, 2015, **13**, 6953–6957.

148 C. Laurence and M. Berthelot, *Perspect. Drug Discov. Des.*, 2000, **18**, 39–60.

149 D. R. Turner, B. Smith, E. C. Spencer, A. E. Goeta, I. Radosavljevic Evans, D. A. Tocher, J. A. K. Howard and J. W. Steed, *New J. Chem.*, 2005, **29**, 90–98.

150 D. R. Turner, E. C. Spencer, J. A. K. Howard, D. A. Tocher and J. W. Steed, *Chem. Commun.*, 2004, 1352–1353.

151 G. O. Lloyd, M. O. M. Piepenbrock, J. A. Foster, N. Clarke and J. W. Steed, *Soft Matter*, 2012, **8**, 204–216.

152 J. W. Steed, *Chem. Soc. Rev.*, 2010, **39**, 3686–3699.

153 C. Baddeley, Z. Yan, G. King, P. M. Woodward and J. D. Badjić, *J. Org. Chem.*, 2007, **72**, 7270–7278.

154 D. K. Kumar, D. A. Jose, A. Das and P. Dastidar, *Chem. Commun.*, 2005, 4059–4061.

155 C. R. Bondy, P. A. Gale and S. J. Loeb, *J. Am. Chem. Soc.*, 2004, **126**, 5030–5031.

156 M. N. Hoque, A. Basu and G. Das, *Cryst. Growth Des.*, 2014, **14**, 6–10.

157 D. R. Turner, M. J. Paterson and J. W. Steed, *J. Org. Chem.*, 2006, **71**, 1598–1608.

158 P. Byrne, D. R. Turner, G. O. Lloyd, N. Clarke and J. W. Steed, *Cryst. Growth Des.*, 2008, **8**, 3335–3344.

159 P. Byrne, D. R. Turner, G. O. Lloyd, N. Clarke and J. W. Steed, *Cryst. Growth Des.*, 2008, **8**, 3335–3344.

160 A. M. Todd, K. M. Anderson, P. Byrne, A. E. Goeta and J. W. Steed, *Cryst. Growth Des.*, 2006, **6**, 1750–1752.

161 D. Kalita and J. B. Baruah, *J. Chem. Sci.*, 2013, **125**, 267–273.

162 S. Kaur, V. W. Day and K. Bowman-James, *Cryst. Growth Des.*, 2020, **20**, 4212–4216.

163 S. Dawn, M. B. Dewal, D. Sobransingh, M. C. Paderes, A. C. Wibowo, M. D. Smith, J. A. Krause, P. J. Pellechia and L. S. Shimizu, *J. Am. Chem. Soc.*, 2011, **133**, 7025–7032.

164 Y. Nito, H. Adachi, N. Toyoda, H. Takaya, K. Kobayashi and M. Yamanaka, *Chem. – An Asian J.*, 2014, **9**, 1076–1082.

165 M. Yokoya, S. Kimura and M. Yamanaka, *Chem. – A Eur. J.*, 2021, **27**, 5601–5614.

166 A. Werner, *Justus Liebigs Ann. Chem.*, 1912, **386**, 1–272.

167 H. M. Colquhoun, J. F. Stoddart and D. J. Williams, *Angew. Chemie Int. Ed. English*, 1986, **25**, 487–507.

168 M. W. Drover, *Chem. Soc. Rev.*, 2022, **51**, 1861–1880.

169 M. F. Perutz, G. Fermi, B. Luisi, B. Shaanan and R. C. Liddington, *Acc. Chem. Res.*, 1987, **20**, 309–321.

170 N. C. Gerber and S. G. Sligar, *J. Am. Chem. Soc.*, 1992, **114**, 8742–8743.

171 D. Prabha, D. Singh, P. Kumar and R. Gupta, *Inorg. Chem.*, 2021, **60**, 17889–17899.

172 D. Bansal, G. Kumar, G. Hundal and R. Gupta, *Dalt. Trans.*, 2014, **43**, 14865–14875.

173 S. Kim, H. Y. Jeong, S. Kim, H. Kim, S. Lee, J. Cho, C. Kim and D. Lee, *Chem. - A Eur. J.*, 2021, **27**, 4700–4708.

174 J. V. Gavette, C. M. Klug, L. N. Zakharov, M. P. Shores, M. M. Haley and D. W. Johnson, *Chem. Commun.*, 2014, **50**, 7173–7175.

175 A. S. Borovik, *Acc. Chem. Res.*, 2005, **38**, 54–61.

176 D. Wang, S. V Lindeman and A. T. Fiedler, *Eur. J. Inorg. Chem.*, 2013, **2013**, 4473–4484.

177 S. M. Redmore, C. E. F. Rickard, S. J. Webb and L. J. Wright, *Inorg. Chem.*, 1997, **36**, 4743–4748.

178 D. Prabha, D. Singh, P. Kumar and R. Gupta, *Inorg. Chem.*, 2021, **60**, 17889–17899.

179 N. N. Adarsh and P. Dastidar, *Cryst. Growth Des.*, 2010, **10**, 483–487.

180 C. R. Bondy, P. A. Gale and S. J. Loeb, *Chem. Commun.*, 2001, 729–730.

181 B. D. Neisen, P. V Solntsev, M. R. Halvagar and W. B. Tolman, *Eur. J. Inorg. Chem.*, 2015, **2015**, 5856–5863.

182 E. Yikilmaz, J. Porta, L. E. Grove, A. Vahedi-Faridi, Y. Bronshteyn, T. C. Brunold, G. E. O. Borgstahl and A.-F. Miller, *J. Am. Chem. Soc.*, 2007, **129**, 9927–9940.

183 I. J. Lin, E. B. Gebel, T. E. Machonkin, W. M. Westler and J. L. Markley, *Proc. Natl. Acad. Sci. U. S. A.*, 2005, **102**, 14581–14586.

184 P. A. Gale, J. L. Atwood and J. W. Steed, *New York Marcel Dekker*.

185 A. Dorazco-González, H. Höpfl, F. Medrano and A. K. Yatsimirsky, *J. Org. Chem.*, 2010, **75**, 2259–2273.

186 S. Tomàs, R. Prohens, M. Vega, M. C. Rotger, P. M. Deyà, P. Ballester and A. Costa, *J. Org. Chem.*, 1996, **61**, 9394–9401.

187 D. Jagleniec, S. Siennicka, Ł. Dobrzycki, M. Karbarz and J. Romański, *Inorg. Chem.*, 2018, **57**, 12941–12952.

188 T. Gunnlaugsson, A. P. Davis, J. E. O'Brien and M. Glynn, *Org. Lett.*, 2002, **4**, 2449–2452.

189 C. Pérez-Casas and A. K. Yatsimirsky, *J. Org. Chem.*, 2008, **73**, 2275–2284.

190 Y. Huo and H. Zeng, *Acc. Chem. Res.*, 2016, **49**, 922–930.

191 H. Chen, Y. Liu, X. Cheng, S. Fang, Y. Sun, Z. Yang, W. Zheng, X. Ji and Z. Wu, *Angew. Chemie - Int. Ed.*, 2021, **60**, 10833–10841.

192 K. Kavallieratos, C. M. Bertao and R. H. Crabtree, *J. Org. Chem.*, 1999, **64**, 1675–1683.

193 J. E. Huheey, E. A. Keiter, R. L. Keiter and O. K. Medhi, *Inorganic chemistry: principles of structure and reactivity*, Pearson Education India, 2006.

194 G. W. Bates, P. A. Gale and M. E. Light, *Chem. Commun.*, 2007, 2121–2123.

195 S. O. Kang, D. Powell and K. Bowman-James, *J. Am. Chem. Soc.*, 2005, **127**, 13478–13479.

196 A. Dorazco-González, M. F. Alamo, C. Godoy-Alcántar, H. Höpfl and A. K. Yatsimirsky, *RSC Adv.*, 2014, **4**, 455–466.

197 R. Montis, A. Bencini, S. J. Coles, L. Conti, L. Fusaro, P. A. Gale, C. Giorgi, P. N. Horton, V. Lippolis, L. K. Mapp and C. Caltagirone, *Chem. Commun.*, 2019, **55**, 2745–2748.

198 G. W. Bates and P. A. Gale, *Recognit. Anions*, 2008, 1–44.

199 C. Jia, B. Wu, S. Li, X. Huang and X.-J. Yang, *Org. Lett.*, 2010, **12**, 5612–5615.

200 J. M. Russell, A. D. M. Parker, I. Radosavljevic-Evans, J. A. K. Howard and J. W. Steed, *Chem. Commun.*, 2006, **4**, 269–271.

201 B. Akhuli and P. Ghosh, *Dalt. Trans.*, 2013, **42**, 5818–5825.

202 D. J. Mercer and S. J. Loeb, *Chem. Soc. Rev.*, 2010, **39**, 3612–3620.

203 L. Li, J. Tong, F. Guo and J. Martí-Rujas, *CrystEngComm*, 2016, **18**, 2284–2288.

204 Z. Yang, B. Wu, X. Huang, Y. Liu, S. Li, Y. Xia, C. Jia and X. J. Yang, *Chem. Commun.*, 2011, **47**, 2880–2882.

205 B. Akhuli, T. K. Ghosh and P. Ghosh, *CrystEngComm*, 2013, **15**, 9472–9482.

206 G. Bergamaschi, M. Boiocchi, E. Monzani and V. Amendola, *Org. Biomol. Chem.*, 2011, **9**, 8276–8283.

207 R. Custelcean, P. Remy, P. V. Bonnesen, D. Jiang and B. A. Moyer, *Angew. Chemie Int. Ed.*, 2008, **47**, 1866–1870.

208 R. Custelcean, D. Jiang, B. P. Hay, W. Luo and B. Gu, *Cryst. Growth Des.*, 2008, **8**, 1909–1915.

209 Y. Marcus, *Ion solvation*, Wiley, 1985.

210 R. J. P. Williams, *R. Inst. Chem. Rev.*, 1968, **1**, 13–38.

211 H. Rahimi, R. Hosseinzadeh and M. Tajbakhsh, *J. Photochem. Photobiol. A Chem.*, 2021, **407**, 113049.

212 A. K. Mishra, *Transition Metals: Characteristics, Properties and Uses*, Nova Science Publishers, Incorporated, 2012.

213 E. P. Beaumier, A. J. Pearce, X. Y. See and I. A. Tonks, *Nat. Rev. Chem.*, 2019, **3**, 15–34.

214 H. Liu, T. Liu, J. Li, Y. Zhang, J. Li, J. Song, J. Qu and W. Y. Wong, *J. Mater. Chem. B*, 2018, **6**, 5435–5442.

215 J. H. Wang, L. H. Feng, J. Bin Chao, Y. Wang and S. M. Shuang, *Anal. Methods*, 2019, **11**, 5598–5606.

216 P. Kumar, V. Kumar and R. Gupta, *RSC Adv.*, 2015, **5**, 97874–97882.

217 P. Kumar, V. Kumar and R. Gupta, *RSC Adv.*, 2017, **7**, 7734–7741.

218 S. K. Samanta, N. Dey, N. Kumari, D. Biswakarma and S. Bhattacharya, *ACS Sustain. Chem. Eng.*, 2019, **7**, 12304–12314.

219 F. Otón, A. Tárraga, A. Espinosa, M. D. Velasco and P. Molina, *Dalt. Trans.*, 2006, 3685–3692.

220 A. Garau, A. Bencini, A. J. Blake, C. Caltagirone, L. Conti, F. Isaia, V. Lippolis, R. Montis, P. Mariani and M. A. Scorciapino, *Dalt. Trans.*, 2019, **48**, 4949–4960.

221 C.-F. Liao, J.-L. Lai, J.-A. Chen, H.-T. Chen, H.-L. Cheng, G.-R. Her, J. K. Su, Y. Wang, G. H. Lee, M. Leung and C.-C. Wang, *J. Org. Chem.*, 2001, **66**, 2566–2571.

222 U. Olsher, R. M. Izatt, J. S. Bradshaw and N. K. Dalley, *Chem. Rev.*, 1991, **91**, 137–164.

223 A. F. D. de Namor, M. A. L. Tanco, J. C. Y. Ng and M. Salomon, 1995, **67**, 1095–1102.

224 L. Tian, C. Wang, S. Dawn, M. D. Smith, J. A. Krause and L. S. Shimizu, *J. Am. Chem. Soc.*, 2009, **131**, 17620–17629.

225 Ž. Soldin, B.-M. Kukovec, T. Debač, M. Đaković and Z. Popović, *Heliyon*, 2022, **8**, e09943.

226 C. R. Bondy, P. A. Gale and S. J. Loeb, *J. Am. Chem. Soc.*, 2004, **126**, 5030–5031.

227 P. Byrne, G. O. Lloyd, L. Applegarth, K. M. Anderson, N. Clarke and J. W. Steed, *New J. Chem.*, 2010, **34**, 2261–2274.

228 B. R. Bhogala, P. K. Thallapally and A. Nangia, *Cryst. Growth Des.*, 2004, **4**, 215–218.

229 C. L. Schauer, E. Matwey, F. W. Fowler and J. W. Lauher, *J. Am. Chem. Soc.*, 1997, **119**, 10245–10246.

230 B. Zheng, J. Bai, J. Duan, L. Wojtas and M. J. Zaworotko, *J. Am. Chem. Soc.*, 2011, **133**, 748–751.

231 C.-H. Lee, H.-Y. Huang, Y.-H. Liu, T.-T. Luo, G.-H. Lee, S.-M. Peng, J.-C. Jiang, I. Chao and K.-L. Lu, *Inorg. Chem.*, 2013, **52**, 3962–3968.

232 D. Chisca, L. Croitor, E. B. Coropceanu, O. Petuhov, G. F. Volodina, S. G. Baca, K. Krämer, J. Hauser, S. Decurtins, S.-X. Liu and M. S. Fonari, *Cryst. Growth Des.*, 2016, **16**, 7011–7024.

233 K. Nath, A. Husain and P. Dastidar, *Cryst. Growth Des.*, 2015, **15**, 4635–4645.

234 T. K. Ghosh, S. Chakraborty, B. Chowdhury and P. Ghosh, *Inorg. Chem.*, 2017, **56**, 5371–5382.

235 S. Banerjee, N. N. Adarsh and P. Dastidar, *Cryst. Growth Des.*, 2012, **12**, 6061–6067.

236 P. Blondeau, A. van der Lee and M. Barboiu, *Inorg. Chem.*, 2005, **44**, 5649–5653.

237 A. K. Ghosh and M. Brindisi, *J. Med. Chem.*, 2020, **63**, 2751–2788.

238 G. C. Moraski, L. D. Markley, P. A. Hipskind, H. Boshoff, S. Cho, S. G. Franzblau and M. J. Miller, *ACS Med. Chem. Lett.*, 2011, **2**, 466–470.

239 R. Goswami, S. Mukherjee, G. Wohlfahrt, C. Ghadiyaram, J. Nagaraj, B. R. Chandra, R. K. Sistla, L. K. Satyam, D. S. Samiulla, A. Moilanen, H. S. Subramanya and M. Ramachandra, *ACS Med. Chem. Lett.*, 2013, **4**, 1152–1157.

240 T. Knoepfel, P. Furet, R. Mah, N. Buschmann, C. Leblanc, S. Ripoche, D. Graus-Porta, M. Wartmann, I. Galuba and R. A. Fairhurst, *ACS Med. Chem. Lett.*, 2018, **9**, 215–220.

241 C. M. Calvet, D. F. Vieira, J. Y. Choi, D. Kellar, M. D. Cameron, J. L. Siqueira-Neto, J. Gut, J. B. Johnston, L. Lin, S. Khan, J. H. McKerrow, W. R. Roush and L. M. Podust, *J. Med. Chem.*, 2014, **57**, 6989–7005.

242 L. Ferrins, M. Gazdik, R. Rahmani, S. Varghese, M. L. Sykes, A. J. Jones, V. M. Avery, K. L. White, E. Ryan, S. A. Charman, M. Kaiser, C. A. S. Bergström and J. B. Baell, *J. Med. Chem.*, 2014, **57**, 6393–6402.

243 J. Schoepfer, W. Jahnke, G. Berellini, S. Buonamici, S. Cotesta, S. W. Cowan-Jacob, S. Dodd, P. Drueckes, D. Fabbro, T. Gabriel, J.-M. Groell, R. M. Grotzfeld, A. Q. Hassan, C. Henry, V. Iyer, D. Jones, F. Lombardo, A. Loo, P. W. Manley, X. Pellé, G. Rummel, B. Salem, M. Warmuth, A. A. Wylie, T. Zoller, A. L. Marzinzik and P. Furet, *J. Med. Chem.*, 2018, **61**, 8120–8135.

244 N. D. Parikh, A. G. Singal and D. W. Hutton, *Cancer*, 2017, **123**, 3725–3731.

245 K. Okamoto, M. Ikemori-Kawada, A. Jestel, K. Von König, Y. Funahashi, T. Matsushima, A. Tsuruoka, A. Inoue and J. Matsui, *ACS Med. Chem. Lett.*, 2015, **6**, 89–94.

246 P. S. Corbin, S. C. Zimmerman, P. A. Thiessen, N. A. Hawryluk and T. J. Murray, *J. Am. Chem. Soc.*,

2001, **123**, 10475–10488.

247 Y.-J. Huang, W.-J. Ouyang, X. Wu, Z. Li, J. S. Fossey, T. D. James and Y.-B. Jiang, *J. Am. Chem. Soc.*, 2013, **135**, 1700–1703.

248 Z. Qin, M. C. Jennings and R. J. Puddephatt, *Inorg. Chem.*, 2003, **42**, 1956–1965.

249 J. J. Race and M. Albrecht, *ACS Catal.*, 2023, **13**, 9891–9904.

250 S. Banerjee, D. P. Kumar, S. Bandyopadhay, N. N. Adarsh and P. Dastidar, *Cryst. Growth Des.*, 2012, **12**, 5546–5554.

251 X.-S. Zhang, Y. Liu, Y. Liu, L.-J. Xiao, J.-L. Cui, H. Xiang, J. Luan and W.-Z. Li, *CrystEngComm*, 2022, **24**, 5767–5782.

252 A. Azhdari Tehrani, L. Esrafili, S. Abedi, A. Morsali, L. Carlucci, D. M. Proserpio, J. Wang, P. C. Junk and T. Liu, *Inorg. Chem.*, 2017, **56**, 1446–1454.

253 S. J. Toal, J. C. Sanchez, R. E. Dugan and W. C. Trogler, *J. Forensic Sci.*, 2007, **52**, 79–83.

254 S. Bevers, S. Schutte and L. W. McLaughlin, *J. Am. Chem. Soc.*, 2000, **122**, 5905–5915.

255 K. Shirai, M. Matsuoka and K. Fukunishi, *Dye. Pigment.*, 1999, **42**, 95–101.

256 A. Azhdari Tehrani, H. Ghasempour, A. Morsali, G. Makhloufi and C. Janiak, *Cryst. Growth Des.*, 2015, **15**, 5543–5547.

257 R. Yun, Z. Lu, Y. Pan, X. You and J. Bai, *Angew. Chemie Int. Ed.*, 2013, **52**, 11282–11285.

258 M. Singh and S. Neogi, *Inorg. Chem.*, 2023, **62**, 871–884.

259 L. Esrafili, M. Gharib and A. Morsali, *Dalt. Trans.*, 2019, **48**, 17831–17839.

Chapter 2

Zinc (II) nitrobenzoate complexes of isonicotinamide and nicotinamide

In general, the structural features of inorganic metal carboxylate complexes are decided by chelating, monodentate, and bridging modes of carboxylate ligands (Fig. 2.1).[1–3] The bridging modes and combinations as chelating modes are responsible for various homoleptic or heteroleptic multinuclear carboxylate complexes, as well as that of metal-organic frameworks.[4–8]

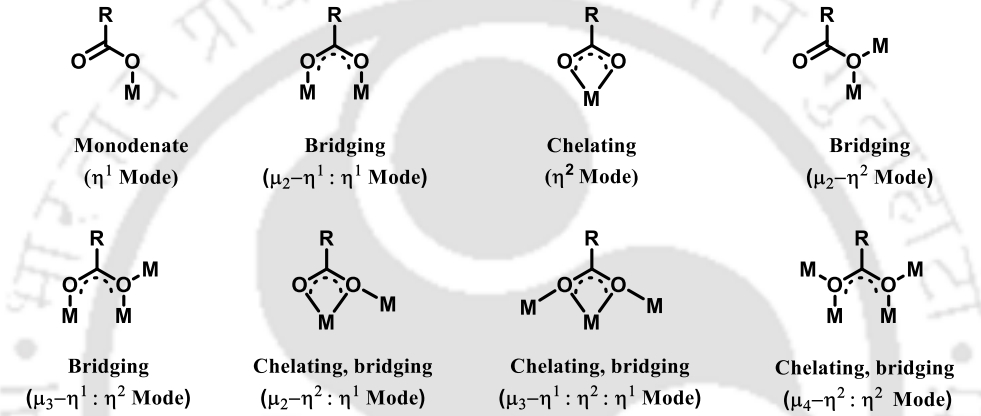

Figure 2.1. Coordination modes of carboxylate ligand

The chemistry of the carboxylate group is important for the construction of inorganic metal complexes having interesting material properties[9] and structural controllability.[10] Depending on the synthetic procedures, solvents, and substituents on carboxylic acid, there is a large complexity in the structures of the complexes derived from simple mono-carboxylate ligands. From our laboratory, we found that the nitro-groups in the carboxylate complex provide wide avenues to synthesize isomeric complexes and different compositions.[11–14] The hydrogen bonding ability and directional effect of the nitro group influence supramolecular features of the nitro benzoate complexes. Depending on the synthetic methods, mononuclear and dinuclear metal carboxylate complexes[11] as well as various pseudo-polymorphs,[14] isomers[12] can be prepared. This is primarily due to the ability of the nitro group to direct electronic, steric, and supramolecular aspects. The Nitro group has a supramolecular analogy to a carboxylate in terms of the ability of its two oxygen atoms to act as hydrogen bond acceptors, which is also possible by a carboxylate. But, from supramolecular consideration, the major differences between the carboxylate and nitro groups are from charge and the latter being an

inferior ligand to the carboxylate ligand. The nitro group of a compound may form intramolecular and intermolecular hydrogen bonds in a solid state[15,16] and in a solution.[17] This chapter is based on the study of a series of zinc nitrobenzoate complexes with pyridine carboxamide of respective positional isomers to understand the non-covalent assemblies through the second coordination sphere. There are examples of nitrobenzoate complexes of cobalt(II), zinc(II), copper(II), and manganese(II) with pyridine carboxamide,[11,18–20] and those studies were from different perspectives; none of them dealt with a systematic structural study of the same metal ion as a series of complexes to provide structural relationships.

The coordination complexes of amide-based ligands are of great interest due to the importance of such metal complexes in biological systems.[21] Besides the biological importance of amide derivatives, they provide various hydrogen bonding motifs to control self-assembly in the supramolecular chemistry of coordination compounds.[22] Pyridine amide-based ligands are vital due to the presence of two functional groups, namely, pyridine and amide, which help in self-assembled structures through coordination bond formation via the pyridine group and hydrogen bonding motifs via amide groups. As discussed in the introduction, these ligands also provide structural flexibility and geometrical requirements to the metal ion and molecular assemblies.[23] This dual ability of self-assembly involving the formation of covalent bonds to a metal center (through pyridyl nitrogen), and supramolecular synthons via hydrogen bonding[24] are used as an important crystal engineering tool.

We have chosen to synthesize 2, 3, and 4-nitrobenzoate zinc(II) complexes with pyridine-3-carboxamide and pyridine-4-carboxamide as ancillary ligands as they would provide amide as a supramolecular site to utilize in the second coordination sphere. Zinc(II) complexes were synthesized from the possible binary combinations of the positional isomers of nitrobenzoic acid and pyridine-3-carboxamide and pyridine-4-carboxamide as listed in Scheme 2.1. A series of reactions were carried out by varying the amounts of the respective nitrobenzoic acid and nicotinamide to obtain suitable crystals for structural study. Out of these six combinations, only from five combinations, we could obtain crystals suitable for diffraction study from complexes. To our surprise, we found in each case, the complexes obtained had different compositions of the ligands listed in Scheme 2.2. Preparation of the crystalline complexes with compositions other than the one depicted in Scheme 2.2 was not successful by changing the stoichiometry of the reactants in the solution. The detailed procedure for the synthesis of zinc(II) complexes **2.1-2.5** is discussed in the experimental section **2.7**. All these

five complexes were characterized by FT-IR, UV-visible, ^{1}H, and ^{13}C-NMR spectroscopy, elemental analysis, thermogravimetry, single crystal X-ray diffraction crystallography, and powder X-ray diffraction.

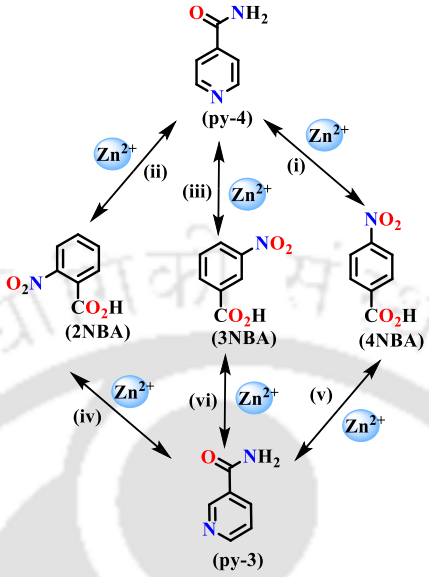

Scheme 2.1. Different combinations of 2, 3, or 4-nitrobenzoate acid and pyridine-3-carboxamide (or pyridine-4-carboxamide) used to prepare the zinc(II) complexes

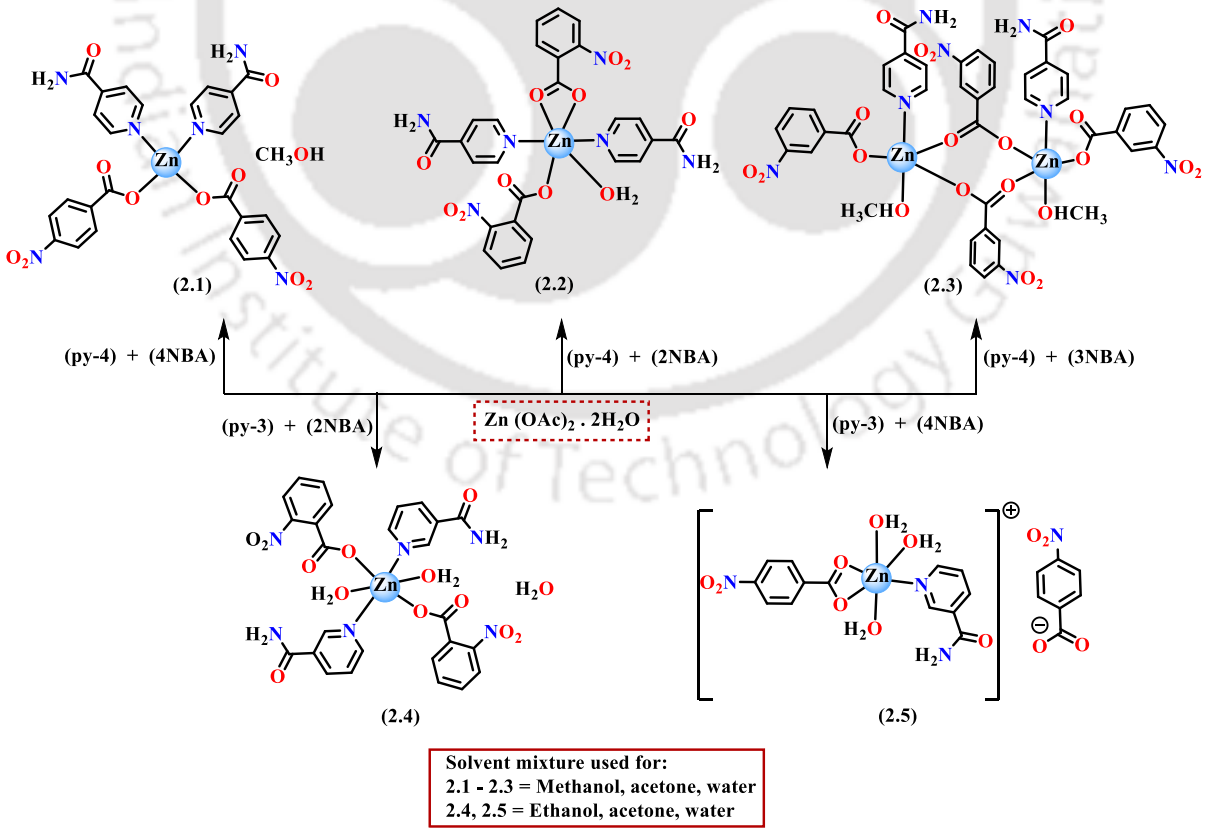

Scheme 2.2. Synthesis of zinc (II) complexes **2.1-2.5**

2.1. Structures and Self-assemblies of complexes 2.1-2.5

The bis(pyridine-4-carboxamide)di(4-nitrobenzoato)zinc(II)·methanol (**2.1**) has a tetracoordinated geometry around the zinc(II) ion (Fig. 2.2a). The complex has two pyridine-4-carboxamide ligands in equatorial positions, and the rest of the sites of the tetrahedron are completed by two monodentate 4-nitrobenzoate. The N1-Zn1-O2 angles are 121.38° and 103.71°. So, the geometry of the complex is determined from the geometry index,[25] calculated by Equation 2.1. For complex **2.1**, τ_4 is 0.83, so it has a pseudo tetrahedral geometry.[26] It has a methanol molecule as a solvent of crystallization. Each ligand, namely, 4-nitrobenzoate or pyridine-4-carboxamide, is related by mirror plane with respect to another ligand of the same origin. The two metal-ligand bond distances (Table 2.1) of Zn-$N_{pyridine}$ bonds are identical (Zn1-N1, 2.033(2) Å), and similarly, the two Zn-$O_{carboxylate}$ bonds have Zn1-O2 distance of 1.951(18) Å. The monodentate nature of the carboxylates is reflected in the Zn1-O2 bond distances as 1.951 Å. In general, the Zn-$O_{carboxylate}$ bond distances found in the literature vary between 1.910-2.136 Å (monodentate), 2.001-2.561 Å (bischelating), 1.982-2.251 Å (bridging).[11,27–29] Hence, the Zn1-O3 distance is large enough to remain uncoordinated with the zinc(II) ion, thereby offering the monodentate carboxylate mode of binding. The complex formed self-assembly through hydrogen bonds. The amide group of the pyridine-4-carboxamide formed intermolecular hydrogen bonding with the carboxylate group of 4-nitrobenzoate and methanol solvate (Fig. 2.2b). A large number of first-row transition metal complexes were reported earlier with a similar combination of the ligands, namely nicotinamide and nitrobenzoate, and suggested that the geometry of the complex changes with the central metal ion. The methanol solvent of crystallization self-assembled through hydrogen bonding with amidic carbonyl and -NH_2 units with bond distances of 2.735 Å and 2.039 Å, respectively (Fig. 2.2b, Table 2.2).

$$\tau_4 = \frac{360^o - (\alpha + \beta)}{141} \quad \text{.....Equation 2.1}$$

Bis(pyridine-4-carboxamide)(aqua)di(2-nitrobenzoato)zinc(II) (**2.2**) is a distorted octahedral complex. It has two pyridine-4-carboxamide ligands at the *trans* position. The other four sites are occupied by a monodentate and a chelating 2-nitrobenzoate ligand, and an aqua ligand. A similar geometry was also observed in the cobalt(II) complex, having a similar combination of ligands. This cobalt(II) complex has a pair of pyridine-4-carboxamide, monodentate 2-

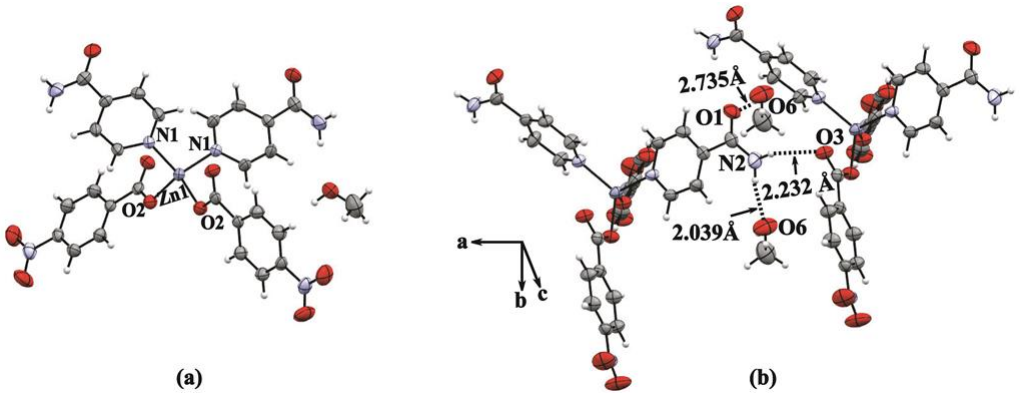

Figure 2.2. (a) Structure, and (b) self-assembly in complex **2.1**

nitrobenzoate, and aqua ligands at *trans* position. It is crystallized in a monoclinic crystal system, having *P*21/*n* space group.[30] On the other hand, our complex **2.2** is crystallized in a triclinic crystal system in the *P*-1 space group. So, complex **2.2** is not isostructural with the reported cobalt(II) complex. In complex **2.2**, the two Zn-N bonds are 2.166(3) and 2.187(3) Å, whereas the four Zn-O bonds are 2.035(3), 2.014 (2), 2.409(3), and 2.152 (3) Å, respectively (Fig. 2.3a, Table 2.1). The Zn-O bonds of the chelating 2-nitrobenzoate ligand are relatively longer, which coordinated to the zinc(II) center in an asymmetric manner, as both Zn-O bonds of the chelating 2-nitrobenzoate are not equal (2.152 (3) and 2.409 (3) Å, respectively) (Table 2.1). The Zn-O_{aqua} bond distance of 2.035(3) Å showed that the aqua ligand is tightly coordinated to the zinc(II) metal center. An amide-amide $R^2_2(8)$ synthon is formed through intermolecular hydrogen bonding between the amide groups of the pyridine-4-carboxamide ligand with longer Zn-$N_{pyridine}$ bond distance {that is 2.187 (3) Å} with a bond distance of 1.953 Å, thereby forming a dimer-like structure (Fig. 2.3b). The amidic -NH_2 group of the second pyridine-4-carboxamide ligand formed an intermolecular hydrogen bond (2.065 Å) with one of the oxygen atoms of the chelating 2-nitrobenzoate. The aqua ligand formed hydrogen bonds with the oxygen atoms of the amidic group (1.906 Å) and monodentate 2-nitrobenzoate (1.977 Å) of two independent molecules (Fig. 2.3c).

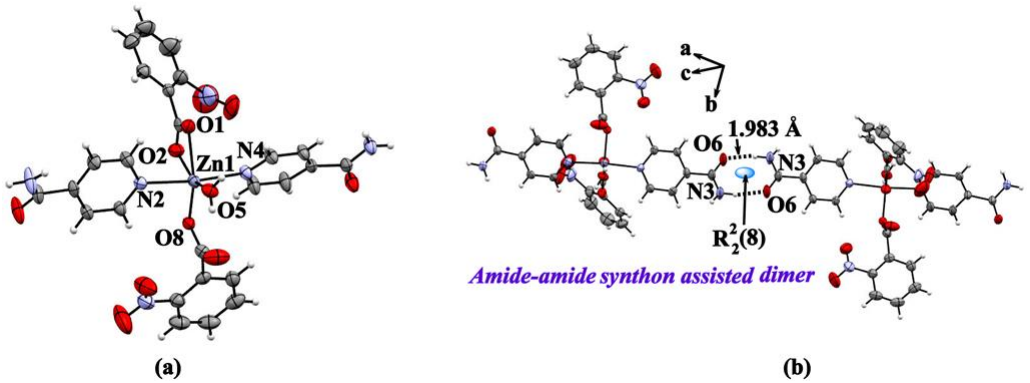

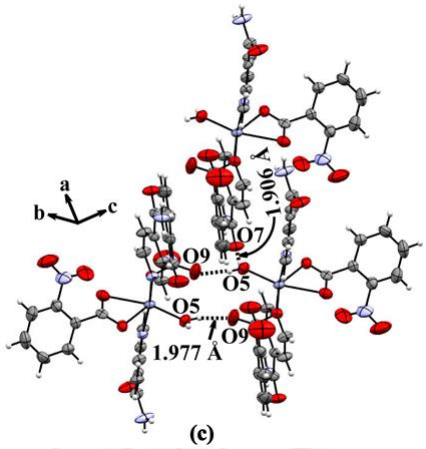

Figure 2.3. (a) Structure, and (b) dimer formed by amide-amide $R^2_2(8)$ synthon, and (c) hydrogen bonds of aqua ligand with oxygen atoms of amide and carboxylate groups in complex **2.2**

The complex **2.3**, di-μ^2-(3-nitrobenzoato)[(methanol)(pyridine-4-carboxamide)(3-nitrobenzoato)zinc(II)] is a pentacoordinated dinuclear complex, having two molecules of 3-nitrobenzoate bridging (*syn-syn* bidentate) and another two monodentate molecules of 3-nitrobenzoate are coordinated to the Zn(II) ion at terminal positions (Fig. 2.4a). The two pyridine-4-carboxamide ligands are independently ligating two zinc(II) ions and are projected on the same side of the complex. Each zinc(II) center has a coordinated methanol molecule. In this complex, each zinc(II) site is pentacoordinated with a slightly distorted trigonal-bipyramidal geometry. The τ_5 values[31] (Equation 2.2) for the two Zn(II) metal centers are

$$\tau_5 = \frac{\beta - \alpha}{60} \quad \text{……Equation 2.2}$$

0.92 and 0.94. Since $\tau_5 < 1$, **2.3** has a distorted trigonal bipyramidal geometry.[32] This geometry is reflected in the bond angles, namely, 124.8(8)° (∠O1-Zn1-O2), 92.9(9)° (∠O1-Zn1-O6), and 141.7(8)° (∠O2-Zn1-O6), whereas the bond angle between the two axial bonds is 177.27(8)° (∠O9-Zn1-N3). The Zn1-O1, Zn1-O2, Zn1-O6, Zn1-O9, and Zn1-N3 bond distances are 2.022(2), 2.024(2), 2.036(2), 2.090(2), and 2.134(2) Å, respectively (Table 2.1). These bond distances are in the range of conventional Zn-O and Zn-N bonds found in zinc(II) carboxylate complexes.[11,27–29] In zinc(II) carboxylate complexes, carboxylate ligand coordinates to the metal ion either in μ^1-bridging[33] or μ^2-bridging[14] modes. In our work, complex **2.3** has two monodentate and two bridging 3-nitrobenzoate ligands (Fig. 2.4a). This bonding scheme provided an uncommon structure and geometry. The amide groups formed intermolecular hydrogen bonds with the oxygen atom of the monodentate 3-nitrobenzoate with a bond distance of 2.173 Å (Fig. 2.4b). The two methanol ligands also contributed to this

self-assembly through intermolecular hydrogen bonding with the oxygen atom of the monodentate 3-nitrobenzoate (1.876 Å) (Fig. 2.4c).

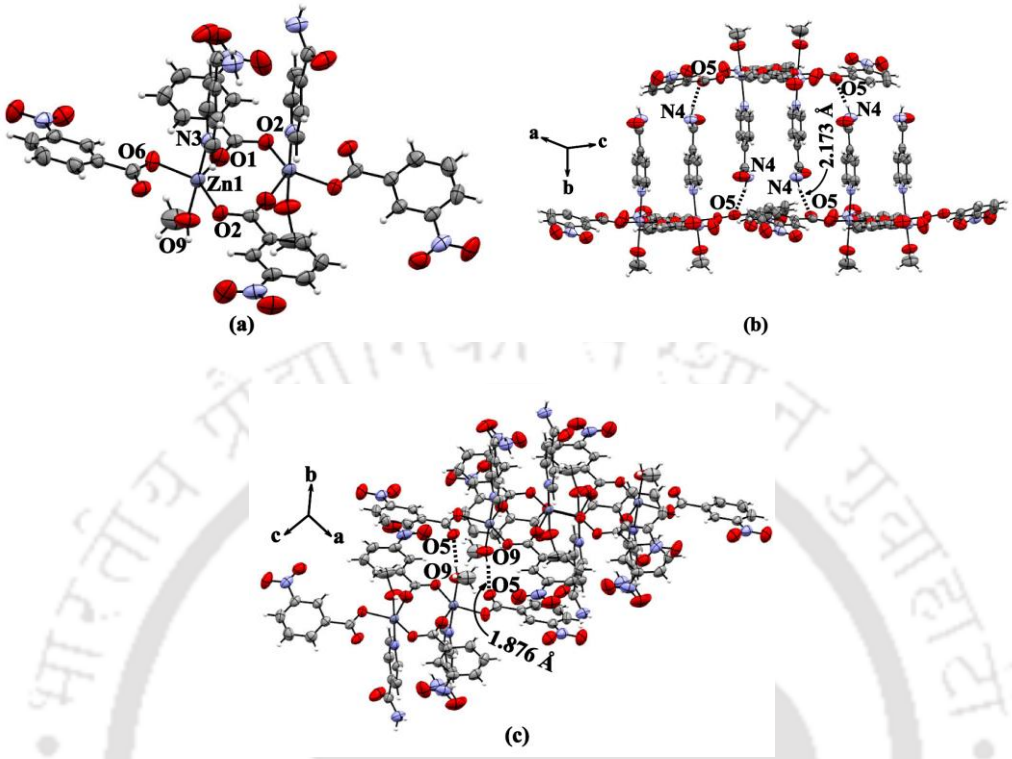

Figure 2.4. (a) Structure, and (b) and (c) are the self-assemblies in complex **2.3**

Complex **2.4**, (di-aqua)bis(pyridine-3-carboxamide)di(2-nitrobenzoato)zinc(II) monohydrate, has a distorted octahedral geometry. The two axial positions are occupied by aqua ligands, *trans* to each other. The remaining four sites are occupied by a pair of the two ligands, 2-nitrobenzoate and pyridine-3-carboxamide. All the similar ligands are at the *trans* position (Fig. 2.5a). In this complex, the metal-ligand bond distances are 2.184(12) Å (Zn-$O_{carboxy}$), 2.120(13) Å (Zn-O_{aqua}), and 2.145(15) Å (Zn-$N_{pyridine}$) (Table 2.1). The secondary coordination sphere formation ability of this complex leads to the formation of an infinite chain through intermolecular hydrogen-bonded amide-amide $R^2_2(8)$ synthon (Fig. 2.5b). This is possible because of the two equivalent Zn-$N_{pyridine}$ bond distances of 2.145(15) Å (Table 2.1). The aqua ligands formed intramolecular hydrogen bonds with the carboxylate group of 2-nitrobenzoate with a bond distance of 1.934 Å (Fig. 2.5c). The water molecules of crystallization contributed to the self-assembly in this complex. They acted as a bridge between the aqua ligand (1.972 Å), amidic oxygen atom (2.068 Å), and the coordinated oxygen atom of the monodentate 2-nitrobenzoate (2.084 Å) through intermolecular hydrogen bond formation (Fig. 2.5c).

Complex **2.5**, [tri-aqua(pyridine-3-carboxamide)(κ-O-κ-O′-4-nitrobenzoato)zinc(II)]4-nitrobenzoate, has a distorted octahedral geometry. Only one molecule of pyridine-3-carboxamide is coordinated to the zinc(II) metal center. The second coordination site is

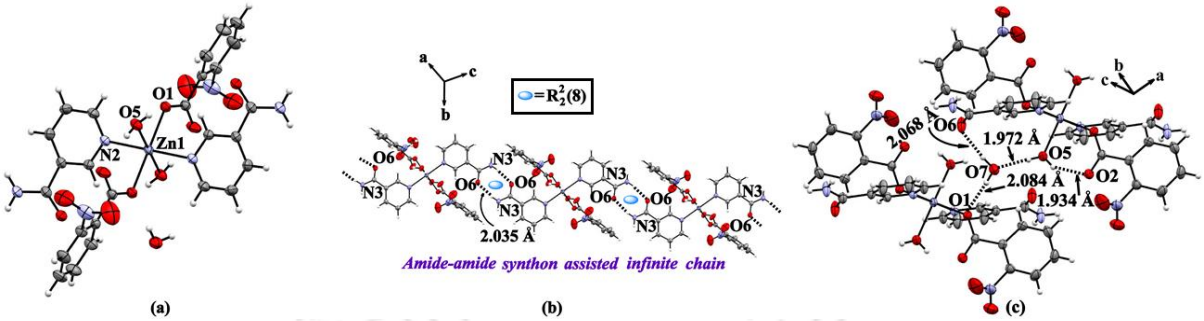

Figure 2.5. (a) Structure; hydrogen-bonded (b) infinite chain, and (c) bridge formed by water molecules of crystallization in complex **2.4**

occupied by a chelating 4-nitrobenzoate ligand, and the rest of the three sites are occupied by three aqua ligands. These three aqua ligands are meridional. Another molecule of 4-nitrobenzoate anion is present outside the coordination sphere (Fig. 2.6a). Thus, complex **2.5** is ionic. The two aqua ligands are tightly bound to the metal center with respective Zn-O_{aqua} bond distances of 2.089(4) and 2.011(3) Å. However, the third aqua ligand is weakly bound, with a Zn-O_{aqua} bond distance of 2.204(3) Å. The Zn-N bond distance is 2.056(4) Å. The chelating 4-nitrobenzoate is almost symmetric, with respective Zn-$O_{carboxy}$ bond distances as 2.167(3) and 2.188(3) Å (Table 2.1). In this complex, the two aqua ligands at *cis* positions formed complementary charge-assisted hydrogen-bonded cyclic synthons with 4-nitrobenzoate anion (Fig. 2.6b). The amidic -NH_2 group and oxygen atom utilized their secondary coordination sphere through intermolecular hydrogen bonding with the oxygen atom of the chelating 4-nitrobenzoate ligand and aqua ligand, respectively (Fig. 2.6b). The

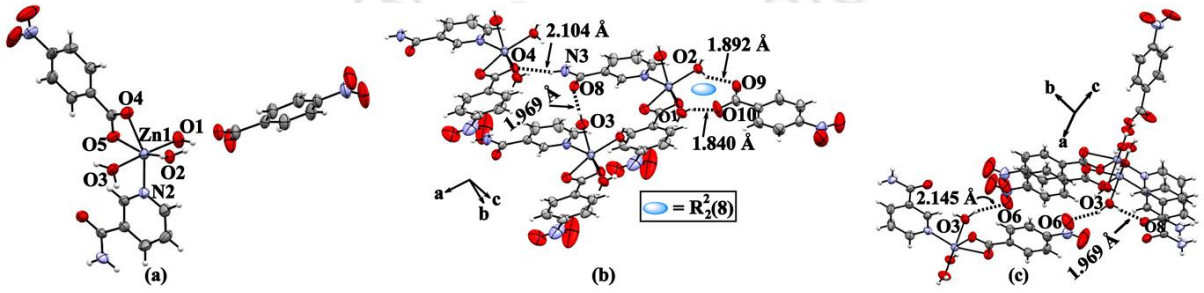

Figure 2.6. (a) Structure, (b) charge-assisted hydrogen-bonded cyclic synthon, and (c) intermolecular hydrogen bonding in complex **2.5**

third aqua ligand formed intermolecular hydrogen bonds with the oxygen atoms of both amide and nitro groups of two independent molecules of the complex (Fig. 2.6c).

Table 2.1. Selected metal-ligand bond distances in complexes 2.1-2.5

Bond	**Bond length (Å) in complexes**				
	2.1	**2.2**	**2.3**	**2.4**	**2.5**
Zn-$N_{pyridine}$	2.033 (2)	2.166 (3)	2.134 (2)	2.145 (15)	2.056 (4)
Zn-$N_{pyridine}$	2.033 (2)	2.187 (3)	-	2.145 (15)	-
Zn-$O_{monodentate\ carboxylate}$	1.951 (18)	2.014 (2)	2.036 (2)	2.184 (12)	-
Zn-$O_{monodentate\ carboxylate}$	1.951 (18)	-	-	2.184 (12)	-
Zn-$O_{bidentate\ carboxylate}$	-	2.152 (3)	-	-	2.167 (4)
Zn-$O_{bidentate\ carboxylate}$	-	2.409 (3)	-	-	2.188 (3)
Zn-$O_{bridging\ carboxylate}$	-	-	2.024 (2)	-	-
Zn-$O_{bridging\ carboxylate}$	-	-	2.022 (2)	-	-
Zn-$O_{solvent}$	-	2.035 (3)	2.090 (2)	2.120 (13)	2.089 (4)
Zn-$O_{solvent}$	-	-	-	2.120 (13)	2.011 (3)
Zn-$O_{solvent}$	-	-	-	-	2.204 (3)

Table 2.2. Hydrogen bond parameters of complexes **2.1-2.5**

Complex	D-H···A	d_{D-H} (Å)	$d_{H\cdots A}$ (Å)	$d_{D\cdots A}$ (Å)	∠D-H···A (°)
2.1	N(2) -H(2A) ···O(3) [1/2+x,-1/2+y,z]	0.86	2.23	3.023 (4)	153
	N(2) -H(2B) ···O(6) [x,y,z]	0.86	2.04	2.871 (4)	162
	O(6) -H(6) ···O(1) [x,1+y, z]	0.82	1.93	2.735 (4)	169
	C(4) -H(4) …O(6) [x,y,z]	0.93	2.58	3.377 (4)	144
2.2	N(3)-H(3A) ···O(6) [-1-x, 1-y, -z]	0.89 (5)	1.98(5)	2.855(5)	167(4)
	N(3) -H(3B) …O(8) [-1+x, y, z]	0.83 (5)	2.40(6)	3.104 (5)	144(4)
	N(5) -H(5A) …O(3) [1-x,2-y,1-z]	0.86	2.28	3.116 (6)	164
	N(5) -H(5B) …O(1) [-x,2-y,1-z]	0.86	2.06	2.864 (4)	154
	O(5)-H(5C)…O(9) [x,y,z]	0.82	1.98	2.708(5)	148
	O(5)-H(5D)…O(7) [-1+x,y,z]	0.80 (5)	1.91 (5)	2.707 (5)	174 (6)
	C(12)-H(12)…O(10) [x,y,z]	0.93	2.49	3.256 (5)	140
	C(17)-H(17)…O(5) [1+x,y,z]	0.93	2.43	3.279 (5)	152
2.3	N(4) -H(4A) ···O(5) [1-x,1-y,1-z]	0.86 (3)	2.17 (3)	3.001 (3)	162 (3)
	N(4) -H(4B) ···O(8) [1/2+x,1/2+y,z]	0.85 (3)	2.42 (4)	3.131 (4)	142 (3)
	O(9) -H(9R) ···O(5) [1-x, -y, 1-z]	0.83 (3)	1.88 (4)	2.678 (3)	161 (4)
	C(15) -H(15) …O(2) [1-x, y,1/2-z]	0.93	2.59	3.126 (3)	117
2.4	N(3)-H(3A) ···O(6) [-1-x,-y,-z]	0.86	2.03	2.863(2)	162
	N(3) -H(3B)…O(2) [x,y,1+z]	0.86	2.18	2.989 (2)	156
	O(5)-H(5R) …O(7) [-1+x,y,z]	0.83 (2)	1.97 (2)	2.804 (2)	177.1(19)
	O(5)-H(5S)…O(2) [x,y,z]	0.82	1.93	2.651(2)	145
	O(7)-H(7R)…O(6) [1+x,y,z]	0.84 (2)	2.07 (2)	2.887 (2)	163 (2)
	O(7)-H(7S)…O(1) [x,y,z]	0.84 (2)	2.09 (2)	2.927 (2)	178 (3)
	C(4)-H(4)…O(7)[-1/2+x,1/2-y,-1/2+z]	0.93	2.54	3.380 (3)	151
	C(9)-H(9)…O(3) [1/2+x,1/2-y,1/2+z]	0.93	2.55	3.226 (3)	130
	C(12)-H(12)…O(6) [x,y,z]	0.93	2.39	2.735 (2)	102
	C(12)-H(12)…O(1) [-x,-y,-z]	0.93	2.46	3.040 (2)	121

2.5	O(1)-H(1R)…O(10) [x,y,z]	0.82	1.84	2.618 (5)	158
	O(1)-H(1S)…O(9) [1+x,y,z]	0.73 (7)	2.07 (7)	2.780 (5)	166 (6)
	O(2)-H(2R) ···O(1) [x,y,z]	0.82	2.58	2.853(5)	101
	O(2) -H(2R)…O(9) [x,y,z]	0.82	1.89	2.643 (4)	152
	O(2)-H(2S)…O(5) [-1+x,y,z]	0.85 (4)	1.98 (4)	2.789 (4)	160 (4)
	N(3)-H(3F)…O(4) [1+x,-1+y,z]	0.84 (6)	2.10 (6)	2.925(6)	167 (6)
	N(3)-H(3G)…O(9) [1+x,y,z]	0.89 (5)	2.29 (5)	3.165 (5)	168 (5)
	O(3)-H(3R)…O(8) [-1+x,y,z]	0.82	1.97	2.789 (5)	178
	O(3)-H(3S)…O(6) [2-x,1-y,-z]	0.85 (3)	2.15 (4)	2.949 (6)	158 (5)
	C(4)-H(4)…O(7) [2-x,2-y,-z]	0.93	2.48	3.319 (10)	151
	C(8)-H(8)…O(12) [-x,1-y,1-z]	0.93	2.59	3.473 (7)	158
	C(10)-H(10)…O(9) [1+x, -1+y,z]	0.93	2.53	3.426 (6)	163
	C(12)-H(12)…O(5) [x,y,z]	0.93	2.55	3.139 (6)	122
	C(12)-H(12)…O(8) [x,y,z]	0.93	2.47	2.799 (6)	101
	C(16)-H(16)…O(9) [x,y,z]]	0.93	2.50	2.814 (6)	100

All complexes **2.1-2.5** have independent compositions; however, in each case, the amide groups in the complexes were free; hence, they participated in the formation of self-assemblies. Monodentate carboxylates require an activation energy of about 6 kJ/mole to form a chelate.[34] Hence, metal-carboxylate complexes with different geometries are possible.

2.2. Characterization of complexes 2.1-2.5

2.2.1. FTIR spectra

The IR spectrum of complex **2.1** showed a broad peak at 3443 cm^{-1} due to the O-H stretching of the methanol solvate. The broad peaks due to N-H stretching of the hydrogen-bonded pyridine-4-carboxamide were observed at 3156 cm^{-1} and 3370 cm^{-1}. It showed a sharp peak at 1408 cm^{-1} due to the N-O stretching of the nitro group in 4-nitrobenzoate (Fig. 2.7a).

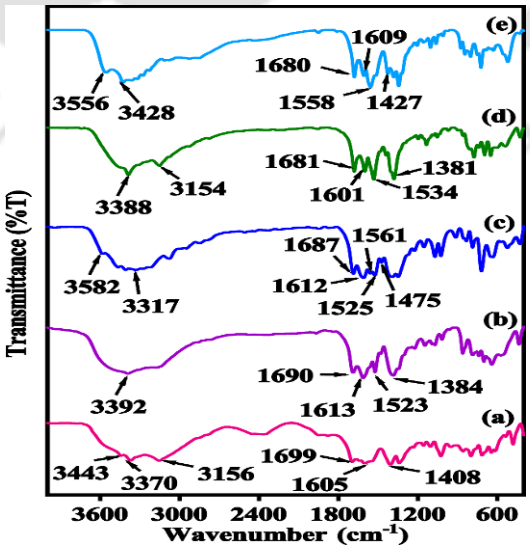

Figure 2.7. FT-IR (KBr pellet) spectra overlay of complexes (a) **2.1**, (b) **2.2**, (c) **2.3**, (d) **2.4**, and (e) **2.5**

Complex **2.2** showed a characteristic N-O stretching peak at 1384 cm^{-1}. It showed a broad peak at 3392 cm^{-1} corresponding to the O-H stretching of the aqua ligand and the N-H stretching of the amide group (Fig. 2.7b). Complex **2.3** showed a broad peak due to O-H stretching of the methanol ligand at 3582 cm^{-1}. The N-H stretching and bending peaks of the amide group appeared at 3317 cm^{-1} and 1561 cm^{-1}, respectively. The N-O stretching of the two nitro groups (one from monodentate and the other from bis-chelating 3-nitrobenzoate) were observed as weak peaks at 1525 cm^{-1} and 1475 cm^{-1} (Fig. 2.7c). In the case of complex **2.4**, a broad peak at 3388 cm^{-1} appeared due to the O-H stretching of the aqua ligand and water solvate. N-H stretching of the amide group was observed as a broad peak at 3154 cm^{-1}. The sharp peaks due to N-O stretching of the nitro group appeared at 1534 cm^{-1} and 1381 cm^{-1} (Fig. 2.7d). Complex **2.5** showed a broad peak at 3556 cm^{-1} due to O-H stretching of the aqua ligand. A broad N-H stretching peak of the amide group appeared at 3428 cm^{-1}. Both strong and weak peaks corresponding to the N-O stretching of the nitro group appeared at 1558 and 1427 cm^{-1}, respectively (Fig. 2.7e).

2.2.2. NMR studies

The complexes **2.1-2.5** were soluble in dimethyl sulphoxide (DMSO), which provided us the scope to study them in the solution phase. The ^{1}H-NMR spectra of the complexes were recorded and compared with the spectra of the parent compounds; the integration of different sets of protons was used to confirm the compositions of the complexes. In the ^{1}H-NMR spectroscopy, complex **2.1** (Fig. 2.8a) showed a multiplet at 7.77 ppm corresponding to the protons of 4-nitrobenzoate. An AA′BB′ pattern at 8.27 ppm and 8.16 ppm was observed due to the protons on pyridine-4-carboxamide. The amidic protons appeared as a broad peak at 8.74 ppm. The integrations of the signals of protons from each ligand in the ^{1}HNMR have shown that the two ligands were in equal proportion. For the complex **2.2** (Fig. 2.8b), the proton NMR spectra had the signals on the pyridine-4-carboxamide ring appearing at 7.76 ppm and 8.70 ppm, whereas the NH_2 protons appeared at 8.31 ppm. The peaks for the protons on the 2-nitrobenzoate ring were found at 7.57, 7.65, and 7.77 ppm. In the case of complex **2.3** (Fig. 2.8c), the proton signals for the pyridine-4-carboxamide ring appeared at 7.78 and 8.73 ppm and amidic protons at 8.66 ppm. Two sharp peaks appeared at 3.26 and 4.21 ppm, corresponding to the protons of the coordinated methanol molecule. The protons on the 3-nitrobenzoate ring appeared at 7.74, 8.29, and 8.35 ppm. The protons on the pyridine-3-

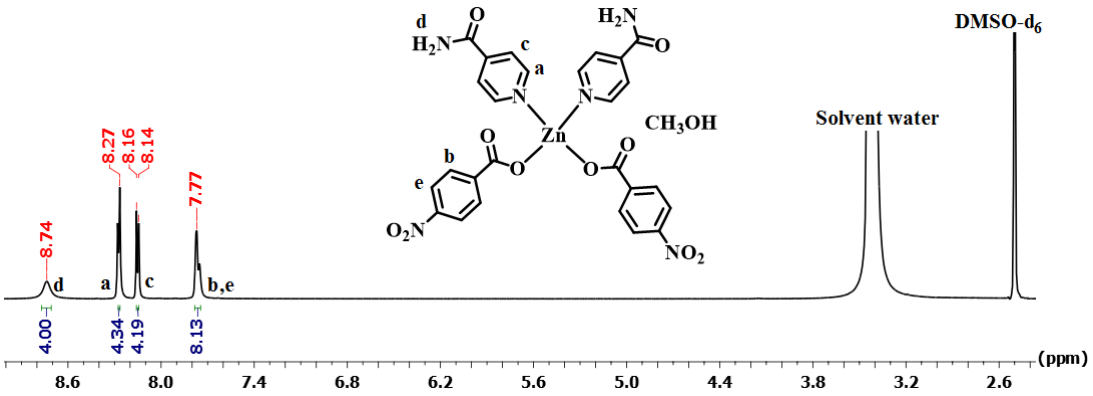

(a)

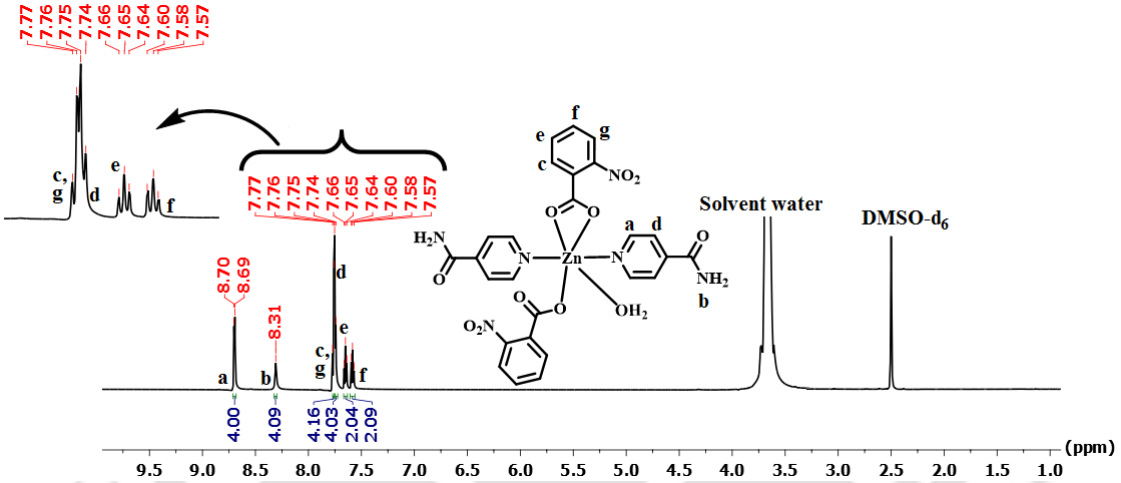

(b)

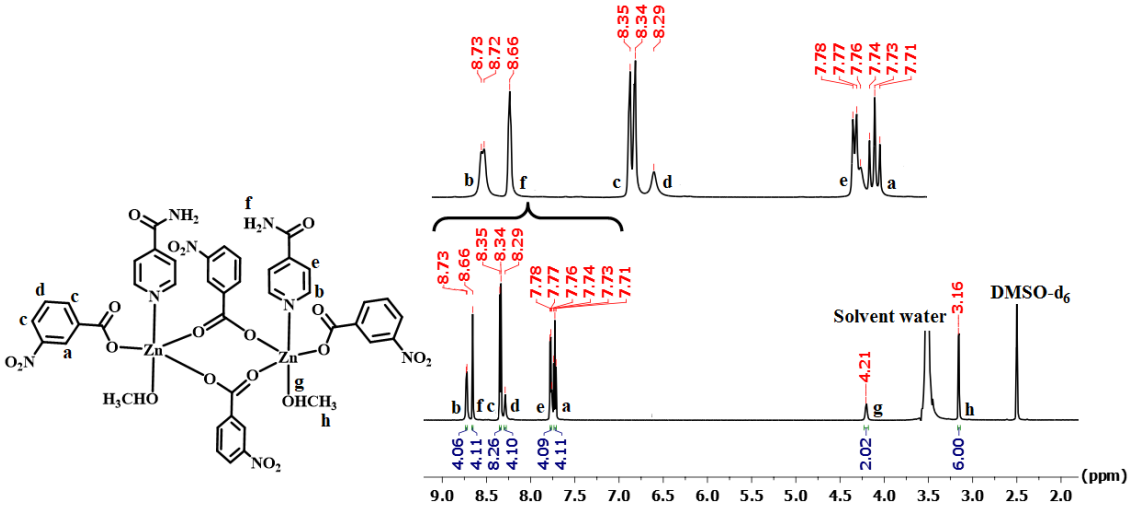

(c)

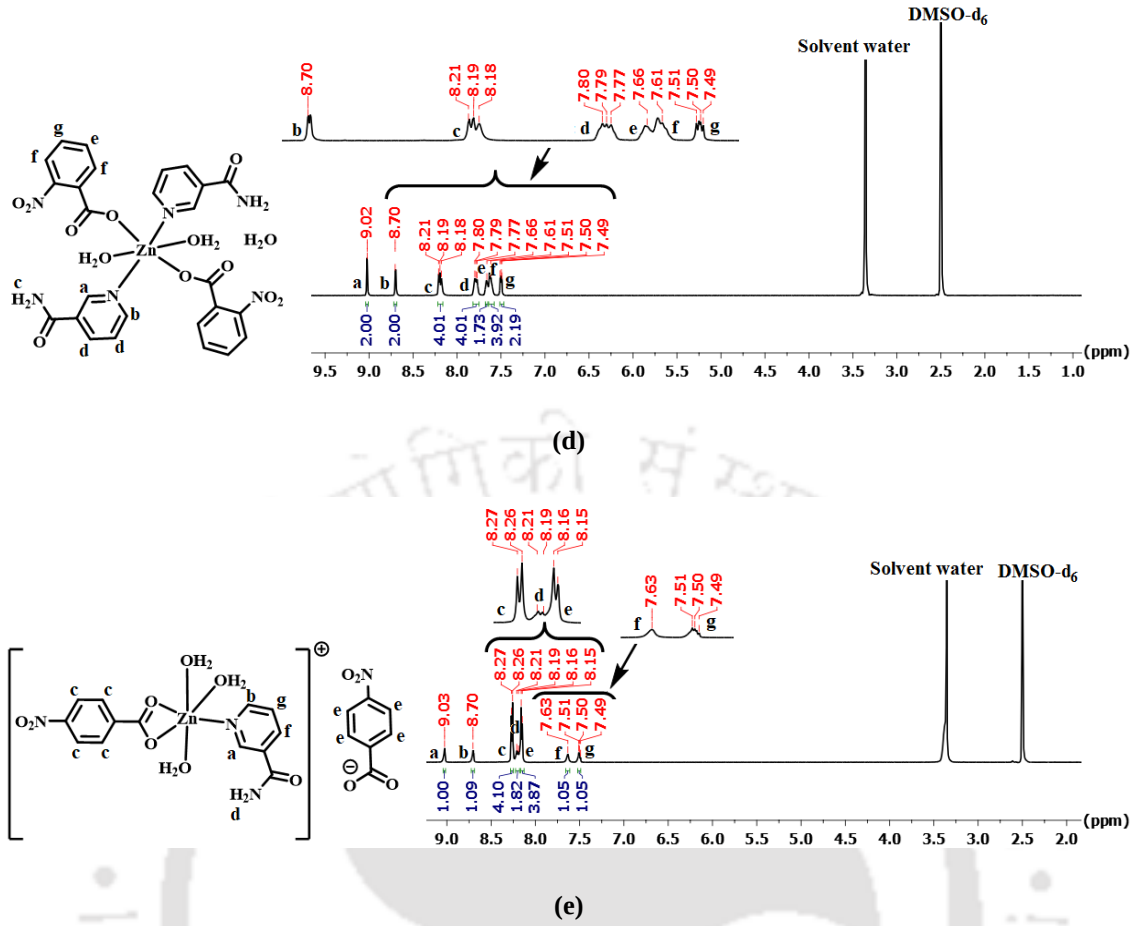

Figure 2.8. ^{1}H-NMR (DMSO-d_6, 600 MHz) of complexes (a) **2.1**, (b) **2.2**, (c) **2.3**, (d) **2.4**, and (e) **2.5**

carboxamide ring of complex **2.4** (Fig. 2.8d) appeared at 7.80, 8.70, and 9.02 ppm, whereas the NH_2 protons appeared at 8.21 ppm. The signals at 7.51, 7.61, and 7.66 ppm corresponded to the protons on the 2-nitrobenzoate ring. For complex **2.5**, amidic protons appeared at 8.21 ppm, and the peaks for the protons on the pyridine-3-carboxamide ring appeared at 7.51, 7.63, 8.70, and 9.03 ppm. The peak at 8.27 ppm corresponded to the protons of the coordinated 4-nitrobenzoate ring; on the other hand, the protons of the anionic 4-nitrobenzoate ring appeared at 8.16 ppm (Fig. 2.8e).

2.2.3. Thermogravimetry study

The thermogravimetry study was carried out to ascertain the amount of solvent loss and the ease of their loss from the respective complexes. The thermograms were also used to compare the thermal stability of the complexes. Complex **2.1** consisted of a methanol molecule of crystallization, which was confirmed by the thermogravimetric analysis. A weight loss of 4.7% was observed, which corresponded to the loss of a methanol molecule (calculated 4.5%) in the temperature range of 69ºC to 150ºC (Fig. 2.9a). It was lost at a

temperature closer to the boiling point of methanol, that is, 64.7°C. A complete weight loss was observed at 345 ºC with the formation of zinc oxide (experimental 11.5%, calculated 11.5%). Complex **2.2** showed a weight loss of 2.6% in the temperature range of 167ºC to 182ºC (Fig. 2.9b). This weight loss corresponded to the loss of an aqua ligand (calculated 2.7%). The weight loss of this ligand occurred at such a higher temperature because it was tightly coordinated to the zinc(II) center with a bond distance of 2.032(3) Å. It is obvious that coordinated water molecules are lost at higher temperatures, whereas the water molecules of crystallization are lost at lower temperatures.[35] Further weight loss was completed at 331ºC, yielding zinc oxide (experimental 12.6%, calculated 12.3%). In **2.3**, a weight loss of 6% was observed between 71ºC to 148ºC temperature range. This weight loss was equivalent to the loss of two coordinated methanol molecules (calculated 5.8%). Weight loss was completed at 353°C, yielding zinc oxide (experimental 7.5%, calculated 7.4%) (Fig. 2.9c). For **2.4**, the two coordinated aqua ligands and a water molecule of crystallization were lost in the temperature range of 73ºC to 127ºC with a weight loss of 7.4% (calculated 7.6%). Further weight loss was completed at 365 ºC, giving zinc oxide (experimental 11.2%, calculated 11.4%) (Fig. 2.9d). In the case of **2.5**, a weight loss of 9.8% was observed from 60ºC to 119ºC, which corresponded to the loss of three coordinated aqua ligands (calculated 10.1%). A complete weight loss was attained at 355 ºC, yielding zinc oxide (experimental 15.5%, calculated 15.1%) (Fig. 2.9e).

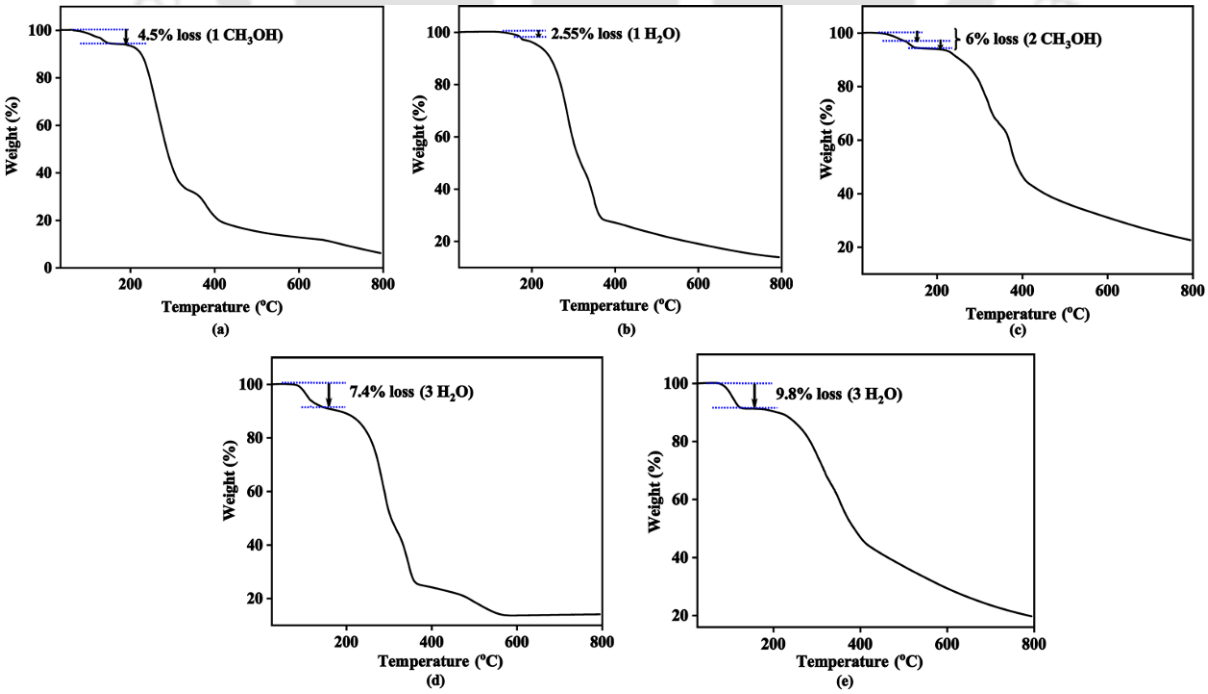

Figure 2.9. Thermogram of complexes (a) **2.1**, (b) **2.2**, (c) **2.3**, (d) **2.4**, and (e) **2.5**

2.2.4. Powder X-ray diffraction study

In the present examples, there was the formation of only crystalline compounds, and thus, it was necessary to find out the bulk purity of the samples after crystallization, as the crystals observed are shown as the yield of the individual complex. The phase of the crystalline compound matched the structure obtained from the single-crystal study. This suggested single phases of the recrystallized products.

The powder X-ray diffraction of these complexes **2.1**-**2.5** was recorded (Fig. 2.10). Indexing of miller indices of powder X-ray diffraction patterns was done based on the crystallographic information files of respective crystal structures determined by single crystal X-ray diffraction. When we compared the simulated powder patterns of these complexes with the experimental data, it was confirmed that the experimental diffraction patterns matched the simulated diffraction pattern obtained from single crystal diffraction data, indicating a high purity of the bulk materials.

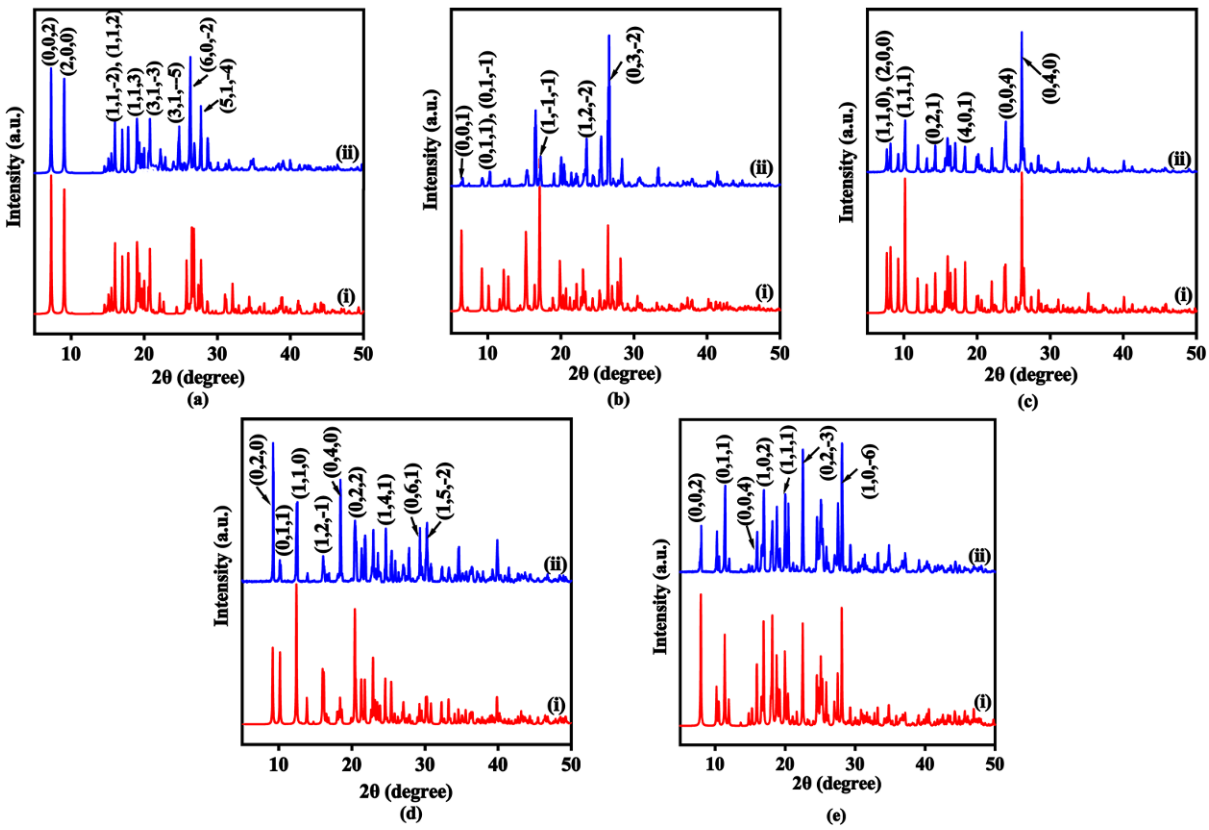

Figure 2.10. Powder X-ray patterns of complex (a) **2.1**, (b) **2.2**, (c) **2.3**, (d) **2.4**, and (e) **2.5** (where, in each case, (i) and (ii) are simulated and experimental powder X-ray patterns respectively)

2.3. Comparison of optimized energy of zinc(II) complexes of the four neutral combinations

From the above discussions, it is clear that only five types of complexes were obtained in crystalline form, and those were specific to a particular combination of ligands. Thus, there was a scope to find out the theoretical energy of the modeled complexes in five forms from each combination. As the structures of the complexes were ligand-dependent and not uniform for a predesigned synthesis, the energy of all the four neutral structures of the two components, namely, 2- (or, 3-, 4-) nitrobenzoate and pyridine -3-(or 4-) carboxamide were optimized by using the B3LYP functional with LANL2DZ as a basis set. Each synthesized complex was taken as a reference to form different combinations. The energies of all the possible forms of the neutral complexes **2.1-2.4** were optimized and compared (Fig. 2.11).

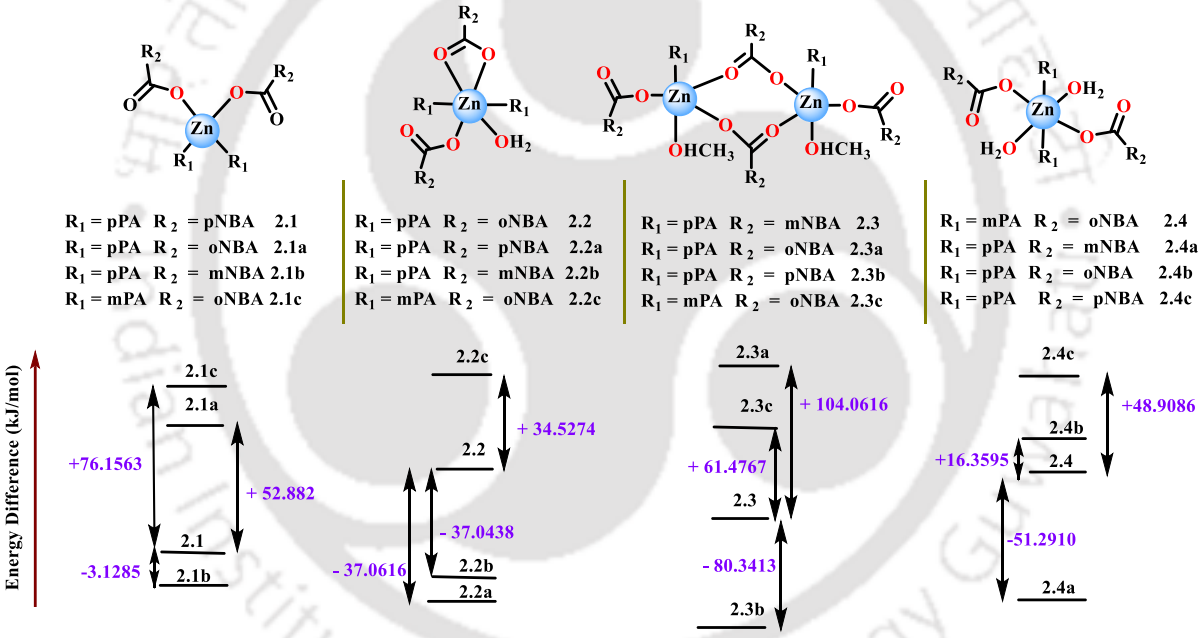

Figure 2.11. Comparative energy of different non-ionic complexes **2.1-2.4** with respect to an experimentally observed structure calculated by DFT using the B3LYP functional with LANL2DZ as a basis set

Complexes **2.1a**, **2.1b,** and **2.1c** had energy differences from the energy of complex **2.1** as +52.8820, −3.1285, and +76.1563 kJ/mol, respectively. Similarly, energy differences of complexes **2.2a**, **2.2b**, and **2.2c** from complex **2.2** were -37.0616, -37.0438, and +34.5274 kJ/mol, respectively. The energy differences of complexes **2.3a**, **2.3b**, and **2.3c** were +104.0616, -80.3413, and +61.4767 kJ/mol, respectively, from the energy of complex **2.3**, whereas complexes **2.4a**, **2.4b**, and **2.4c** had energy differences of -51.2910, +16.3595, and

+48.9086 kJ/mol, respectively, from complex **2.4**. So, the as-synthesized neutral complexes **2.1-2.4** did not have the lowest energy compared to other combinations. This suggested that the lowest energy form was not the one that selectively crystallized out. This indicated that the supramolecular assembling properties had a role in deciding the nuclearity and composition and were not due to steric and electronic effects. The crystallographic data of the five complexes **2.1-2.5** revealed that in complex **2.1**, the amide group of the pyridine-4-carboxamide formed intermolecular hydrogen bonding with the carboxylate group of 4-nitrobenzoate and methanol solvate. An amide-amide $R^2_2(8)$ synthon is formed in complex **2.2** through intermolecular hydrogen bonding between the amide groups of the pyridine-4-

Table 2.3. Optimized structures of the most stable forms obtained from experiments and theoretical calculations

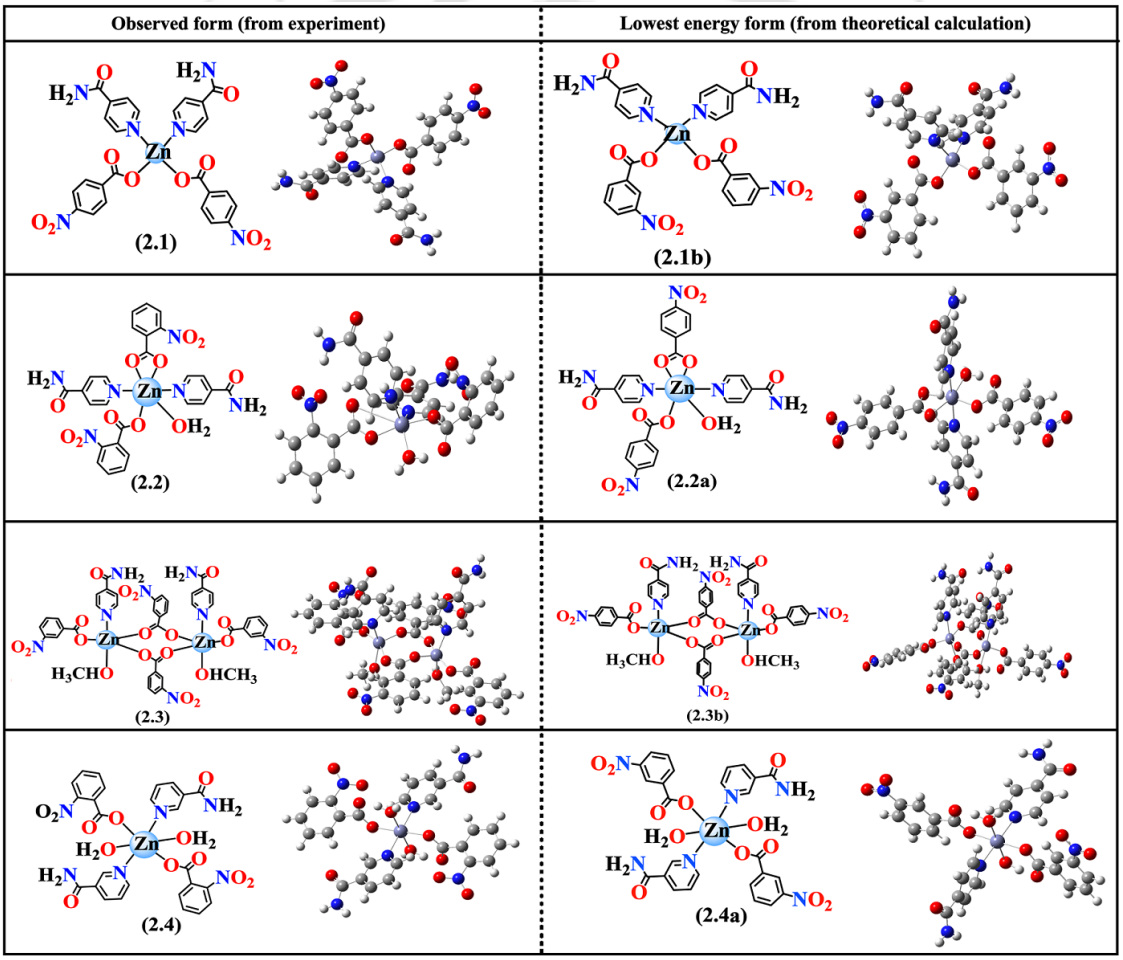

carboxamide ligand, which resulted in a dimer-like structure. Further, the amidic -NH_2 group of the second pyridine-4-carboxamide ligand formed an intermolecular hydrogen bond with one of the oxygen atoms of the chelating 2-nitrobenzoate in complex **2.2**. In complex **2.3**, the amide groups formed intermolecular hydrogen bonds with the oxygen atom of the monodentate 3-nitrobenzoate. The two methanol ligands also contributed to the self-assembly

of this complex through intermolecular hydrogen bonding with the oxygen atom of the monodentate 3-nitrobenzoate. In complex **2.4**, an infinite chain through intermolecular hydrogen-bonded amide-amide $R^2_2(8)$ synthon is formed. The carboxylate group of 2-nitrobenzoate ligands contributed to the building of a secondary coordination sphere through intermolecular hydrogen bonding with aqua ligands and water molecules of crystallization. In complex **2.5**, the two aqua ligands at *cis* positions formed complementary charge-assisted hydrogen-bonded cyclic synthons with 4-nitrobenzoate anion. The amidic -NH_2 group and oxygen atom utilized their secondary coordination sphere through intermolecular hydrogen bonding with the oxygen atom of the chelating 4-nitrobenzoate ligand and aqua ligand. Thus, the secondary coordination sphere of these as-synthesized complexes via ligands guided their geometry and compositions. From the above calculation, the structure of the most stable form in each combination obtained from theory and experiments is shown in Table 2.3.

2.4. UV-Visible, Photoluminescence and Dynamic Light Scattering study

The UV-visible spectra of the solid samples of complexes **2.1-2.5** were recorded, and they showed absorbance ranging from 328 to 379 nm (Fig. 2.12a). In the present case, the absorption bands are attributed to π–π* intraligand charge transfer (ILCT) transition.[36]

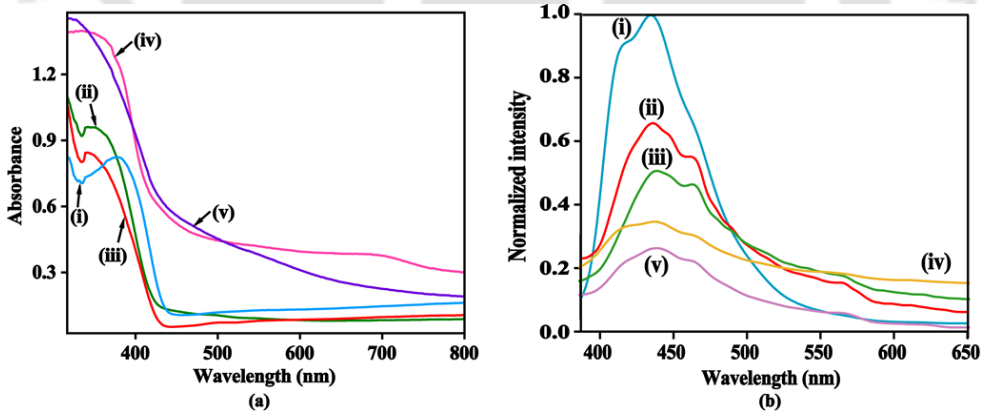

Figure 2.12. (a) UV/visible, and (b) photoluminescence spectra of the solid samples of complexes (i) **2.1**, (ii) **2.2**, (iii) **2.3**, (iv) **2.4**, (v) **2.5**

Zinc(II) complexes, in general, show photoluminescence behaviour.[37–40] In our study, the ligands were independently non-fluorescent, but the complexes were weakly fluorescent. When the solid samples of these five complexes were excited at 350 nm, they showed emissions in the region of 434-463 nm (Fig. 2.12b). Irrespective of the ligands, many zinc(II)

complexes show emission properties near 400-430 nm due to the metal-to-ligand charge transfer transition.[41–47] Various d^{10} zinc (II) complexes are well known to show sample size-dependent emissions[48] and aggregation-induced emission (AIE).[49–52] The broad peaks were observed, the shape of the emissions was different, and vibrational features could also be seen. Such emissions are commonly observed in various zinc complexes; on the other hand, despite the non-emissive nature of the ligand in each complex, the emission occurring in the same region but with a difference in shape and intensity suggested it has a contribution from aggregation-induced emission enhancement. Since our complexes were observed as hydrogen-bonded self-assemblies, these complexes were in an aggregated state.

The lifetime decay of the five complexes showed a biexponential decay. In each case, among the two observed lifetimes, a higher fraction of molecules (approximately 60% in each case) followed a relatively shorter decay path with a lifetime in the range of 0.558-0.727 ns. The rest of the excited molecules followed another path, having a lifetime between 3.025-4.553 ns (Table 2.4). The lifetime studies on the solid samples of zinc(II)-salen complexes showed biexponential lifetimes due to different orientations of the self-assembled molecules in the unit cell.[39] In all five complexes, the relative intensities of the shoulder on the principal emission peak were different from each other. These shoulders on the principal emission peak were due to the fast-exchanging assemblies. Therefore, the overall change in the emission intensity of each of the five complexes was due to the change in the coordination environment contributing to the self-assembly, which provided transition probabilities and emission wavelength.

Table 2.4. Quantum Yield, Lifetime of the Excited State, Rate Constant of Non-radiative and Radiative Decay of Solid Samples of Complexes, and TD-DFT Calculated S_1-S_0 Transition and Oscillator Strengths

Complex	**Observed absorbance wavelength (nm)**	**Observed emission wavelength (nm)**	**Quantum Yield (Φ_F)[a] (%)**	**Lifetime for excited state, τ (ns)**	**k_{nr} (10^7 s^{-1})**	**k_r (10^7 s^{-1})**	**TD-DFT calculated**	
							Wavelength (nm)	**Oscillator Strength (f)**
2.1	379	437	1.48	3.025	25.30	1.093	340	0.0003
2.2	347	438	4.14	3.788	27.40	0.734	383	0.0095
2.3	340	434	2.61	3.554	32.57	0.489	332	0.0002
2.4	350	439	13.56	3.506	24.65	3.867	392	0.0350
2.5	328	448	0.56	3.780	26.30	0.148	326	0.0149

[a] In each case, bi-exponential decay is observed; only the higher lifetime relating to AIE is shown here.

The quantum yield values of complexes **2.1-2.5** varied from 0.56-13.56%. The relative magnitude of quantum yield was in the order **2.4** > **2.2** > **2.3** > **2.1** > **2.5**. Complex **2.5** was

weakly fluorescent with a quantum yield of 0.56%. Complex **2.4** had a 24.2 times higher quantum yield than complex **2.5**. The rates of radiative and non-radiative emission paths were calculated (Table 2.4). The radiative transitions indicated that closely associated multiple energy levels have decayed through energy dissipation, implying an aggregation-induced emission.

The photoluminescence decay profile of complexes **2.1**-**2.4** was recorded in two different solvents, one in DMSO and the other in DMSO containing 50% water. In each case, bi-exponential decay was observed (Table 2.5). In DMSO, each complex showed that a major fraction followed a short emission decay path with a lifetime of less than 1 ns, and a minor portion of the complexes passed through a longer decay path having a lifetime ranging from 4.903 to 11.685 ns. Thus, water-assisted aggregates caused an enhancement and followed a higher lifetime emission path.

Generally, aggregation-induced emission is studied by preparing solutions in different amounts of water fractions in solution. In some of those cases, an initial increase in emission intensity followed by quenching was observed.[39,40,53] In our study, the complexes **2.1**-**2.5** showed emission in the range of 396 to 441 nm in dimethyl sulfoxide (DMSO) solvent. Upon addition of different amounts of water, complexes **2.1**-**2.5** showed aggregation-induced emission and different incremental fractions of water caused enhancement followed by quenching (Fig. 2.13). In complex **2.1**, at 413 nm, enhancement in emission peak was observed till 10% water addition. Then, a significant quenching occurred with increasing water concentration, followed by an emission at 397 nm. A shift in emission peak from 413 nm to 397 nm was observed for **2.1**. At higher concentrations of water, the dominance of one vibrational level was observed at 397 nm due to v_0-to-v_0 transition. Similarly, in the case of complexes **2.2**-**2.5**, enhancement was observed till 20, 10, 10, and 30%, respectively, at respective emission wavelengths. With increasing water concentration in the respective complexes, quenching was observed, followed by a blue shift to 397 nm (complexes **2.2** and **2.4**), 380, 397 nm (complex **2.3**), and 396, 415, 441 nm (complex **2.5**). Such a blue shift in emission peaks was observed because of the changes in vibrational levels due to the symmetry change of the complex. Thus, aggregation caused a change in the symmetry of the complexes. Aggregation-induced emissions in zinc(II) complexes with fluorescent ligands are well known.[49–52] But in our present case, the ligands were non-fluorescent. In dimethyl sulfoxide, the quantum yields of **2.1**-**2.5** were very low, in the range of 0.0052 to 0.0113

(Table 2.5), but they provided enough emission to study both enhancement and quenching due to aggregation.

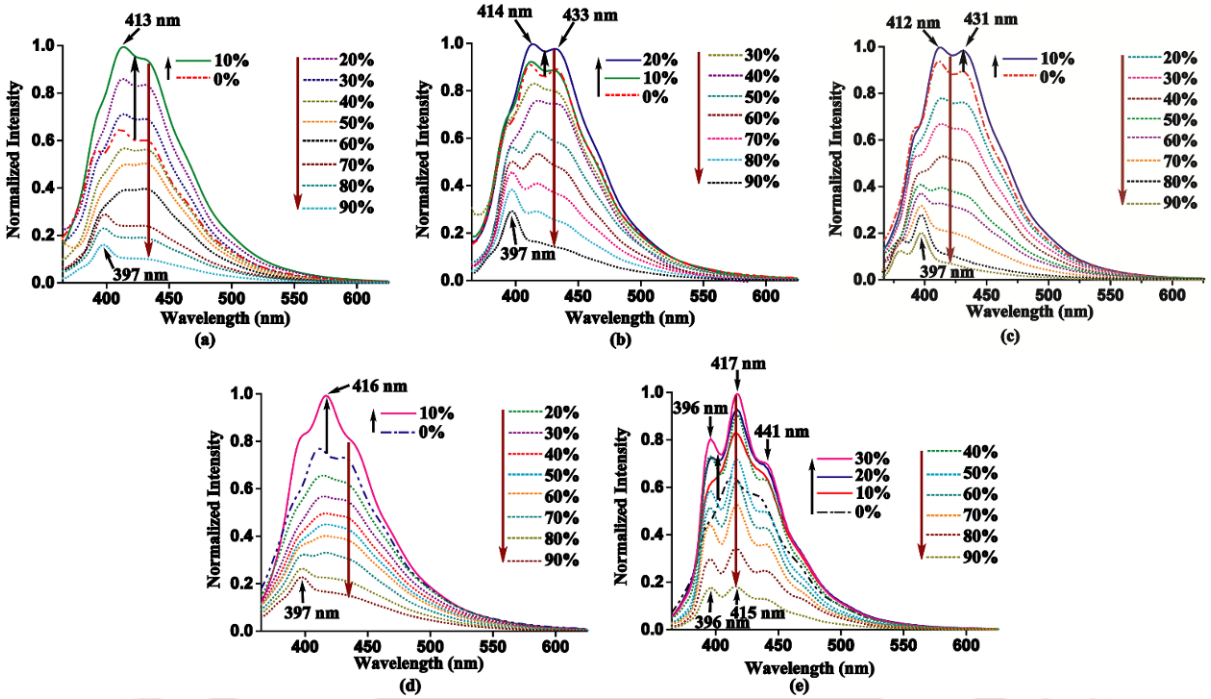

Figure 2.13. Photoluminescence spectra (λ_{ex} = 350 nm) of complexes (a) **2.1**, (b) **2.2**, (c) **2.3**, (d) **2.4**, and (e) **2.5** (each complex is 10^{-4} M in dimethyl sulfoxide) upon addition of different amounts of water (thick lines and dotted lines represented an initial increase and a decrease in emission, respectively)

Table 2.5. Average particle size determined by dynamic light scattering, quantum yields, and emission lifetime of complexes **2.1-2.4** in DMSO and DMSO containing 50% water

Complex	**Average particle size (nm)**	**Poly-dispersity**	**Quantum yield in DMSO (in DMSO + 10 % H_2O)[a]**	**Average particle size (nm)**	**Poly-dispersity**	**Emission lifetime in ns (fraction %)**	
	In DMSO			**In DMSO with 50% water**		**In DMSO**	**In DMSO with 50 % water**
2.1	577.7	0.284	0.0052 (0.108)	765.3	0.239	0.96 (88.80); 4.90 (12.20)	0.96 (64.77); 6.23 (35.23)
2.2	296.3	0.441	0.0160 (0.0188)	570.0	0.240	0.98 (86.87); 6.87 (13.25)	0.93 (76.10); 5.95 (23.90)
2.3	240.9	0.724	0.0136 (0.0189)	701.79	0.266	0.98 (87.78); 6.04 (12.22)	0.99 (55.64); 5.53 (44.36)
2.4	125.0	0.441	0.0113 (0.1089)	409.7	0.793	0.94 (87.85); 5.29 (12.15)	0.90 (82.05); 6.15 (17.95)
a = with respect to quinine sulphate							

An initial addition of water resulted in the competition of water with DMSO solvent to attain an organized structure, making it suitable for aggregation-induced emission. With increasing

water concentration, water molecules reorganized the assembly to segregate the self-assembled zinc(II) complexes, which provided a scope for the formation of new assemblies through fast exchange, undetectable in NMR titration studies.[54] With the change of solvents, such equilibriums were possible in zinc(II) complexes.[55] The dimensionality of zinc(II) carboxylate coordination polymers was also changed due to solvent coordination,[56] and such solvent-dependent change in dimensionality affects the photoluminescence properties.[57] In our study, water-assisted self-assembly of metal complexes at a low concentration initially caused fluorescence enhancement, followed by fluorescence quenching with a blue shift of emission wavelength. This was due to the equilibrium between self-assemblies and low nuclearity hydrated species (Scheme 2.3).

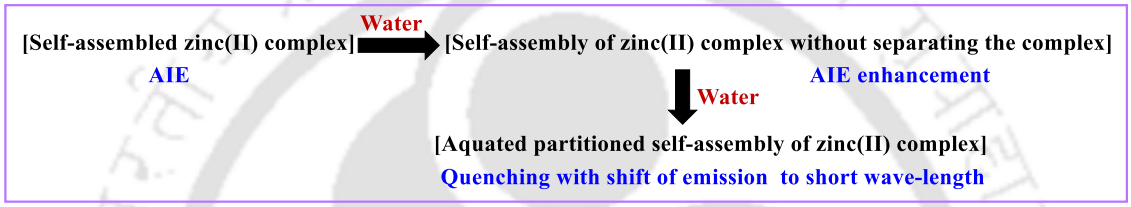

Scheme 2.3. Water-assisted reorganized self-assemblies

The dynamic light scattering studies of complexes **2.1-2.4** in DMSO at different concentrations of water showed that all the complexes remained aggregated in solution (Table 2.5). In DMSO, complex **2.1** showed an average particle size of 577.7 nm, and the same complex solution, upon 50% water addition, had an average particle size of 765.3 nm. For complex **2.2**, the average particle size was 296.3 nm in DMSO solvent, which, in the presence of 50% water, showed a value of 570.1 nm. Thus, an increase in the size of the aggregates was observed upon water addition. Complex **2.3** had three different sets of aggregates, which converted to one set with 50% water dilution, having an average particle size of 701.7 nm. For complex **2.4**, the average particle size was 125 nm in DMSO. However, upon dilution, it showed two different sets of aggregates due to the segregation of particles in the presence of water.

2.5. HOMO-LUMO of the complexes 2.1-2.5

For further understanding, theoretical calculations for these complexes based on density functional theory (DFT) by using B3LYP functional with LANL2DZ as a basis set were performed. These calculations showed that the HOMO-LUMO gaps for complexes **2.1-2.4** were 299.72, 334.22, 328.01, and 317.13 nm, respectively. For complex **2.5**, the cationic part

was optimized. Moreover, the TD-DFT calculations suggested the S_1-S_0 transition for complexes **2.1-2.5** as 340, 383, 332, 392, and 326 nm, respectively (Fig. 2.14, Table 2.4). The experimentally observed emission wavelength is much higher than the theoretically calculated emission wavelength (S_1-S_0) (TD-DFT value).

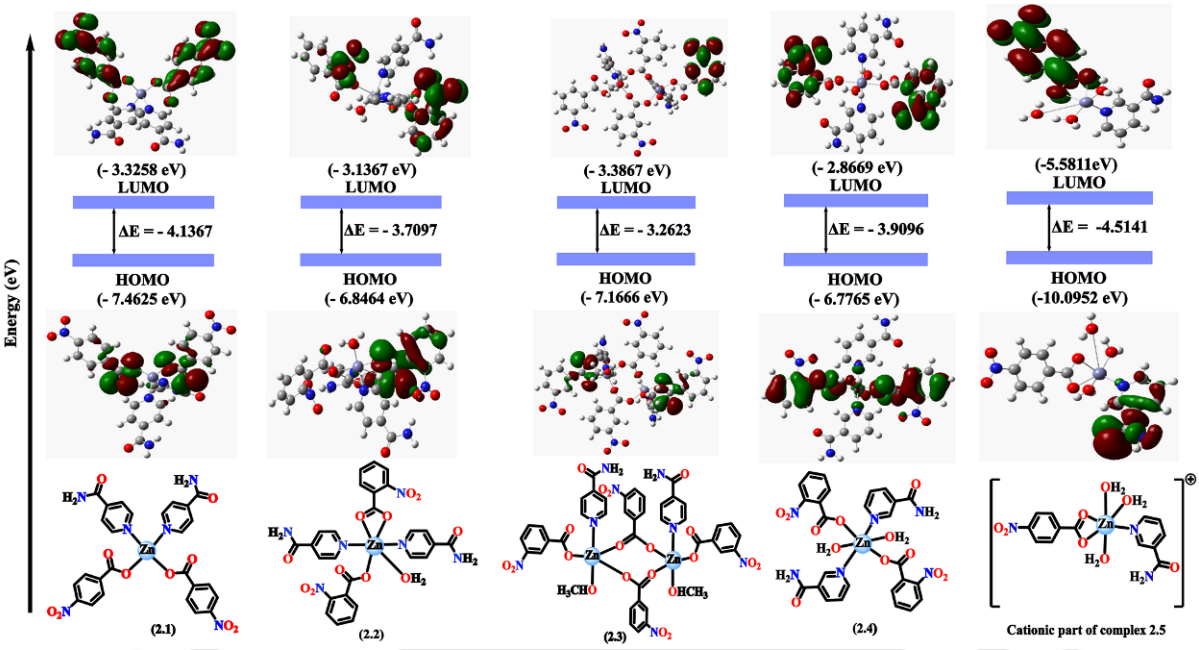

Figure 2.14. HOMO-LUMO gaps of complexes **2.1-2.5** (for complex **2.5**, cationic part was considered) from DFT calculation using B3LYP functional using LANL2DZ as a basis set

This study provided us with the information that zinc(II) complexes composed of non-fluorescent positional isomers of nitrobenzoic acid and pyridine -3-(or 4-) carboxamide have different coordination environments. These complexes acted as aggregation-induced emission luminogens (AIEgens) in both solid and solution states. In solution, after the initial addition of water, these complexes initially showed aggregation-induced emission, followed by quenching and a blue shift of the emission wavelength upon increasing the concentration of water in the solution. This blue shift suggested the formation of water-assisted assemblies. The presence of low water content suggested intermolecular self-assembly in the complexes. As the water concentration was increased, the water molecules participated in the hydrogen bond formation by reorganizing the self-assemblies of the complexes, resulting in quenching and blue shift of the emission peak. The theoretical study suggested that the experimental emission wavelengths of these complexes with or without water addition were higher than the theoretically calculated HOMO-LUMO energy gaps for S_1-S_0 transition. In the presence of excess water, the emission wavelengths were closer to the one calculated for dimeric structure, indicating the disintegration of self-assemblies in the complexes due to excess

water. The comparative HOMO-LUMO energy gap calculation of the possible combinations of ligands with a skeleton of as-synthesized non-ionic complexes suggested that the one with the skeleton of complex **2.3** had the least energies relative to the one with a mononuclear skeleton of complexes **2.1** and **2.2**.

2.6. Conclusion

This study provided us with five zinc(II) complexes with different geometry and compositions. Each of the five complexes utilized the free amide groups for secondary coordination in a different manner. For example, in complex **2.2** (consisting of pyridine-4-carboxamide), the amide-amide $R^2_2(8)$ synthon, through intermolecular hydrogen bonding between the amide groups of pyridine-4-carboxamide ligand, contributed to the dimer-like structure of the complex. On the other hand, an infinite chain through intermolecular hydrogen-bonded amide-amide $R^2_2(8)$ synthon in complex **2.4** with the change of ligand to pyridine-3-carboxamide. This study provided us with the information that zinc(II) complexes composed of non-fluorescent positional isomers of nitrobenzoic acid and pyridine -3-(or 4-) carboxamide have different coordination environments. These complexes acted as AIEgens in both solid and solution states. In solution, after the initial addition of water, these complexes initially showed aggregation-induced emission, followed by quenching and blue shift of the emission wavelength upon increasing the concentration of water in the solution. This blue shift suggested the formation of water-assisted assemblies. The presence of low water content suggested intermolecular self-assembly in the complexes. As the water concentration was increased, the water molecules participated in the hydrogen bond formation by reorganizing the self-assemblies of the complexes, resulting in quenching and blue shift of the emission peak. The theoretical study suggested that the experimental emission wavelengths of these complexes with or without water addition were higher than the theoretically calculated HOMO-LUMO energy gaps for S_1-S_0 transition. In the presence of excess water, the emission wavelengths were closer to the one calculated for dimeric structure, indicating the disintegration of self-assemblies in the complexes due to excess water.

2.7. Experimental section

The detailed synthetic methodologies for the synthesis of the metal complexes are described. Analytical data are provided with each compound. The instrumental details and crystallographic parameters are provided in Appendix section at the end of this chapter. The following abbreviations are used for identification of spin multiplicities in ^{1}H-NMR spectra: s = singlet, d = doublet, t = triplet, q = quartet, m = multiplet; and for FTIR spectra, following abbreviations were used to identify the absorption bands: s = strong, w = weak, br = broad, m = medium.

Synthesis of bis(pyridine-4-carboxamide)di(4-nitrobenzoato)zinc(II)·methanol (2.1): To a well-stirred solution of pyridine-4-carboxamide (161.2 mg, 1.32 mmol) and 4-nitrobenzoic acid (334.2 mg, 2.0 mmol) in methanol, zinc(II) acetate dihydrate (219.5 mg, 1 mmol) was added. The resulting reaction mixture was stirred for three hours at room temperature. A dirty white precipitate was formed, which was dissolved in 5mL water, giving a clear transparent solution. The solution was filtered and kept undisturbed for evaporation. Yield: 61%. Elemental analysis calculated for $C_{28}H_{28}N_6O_{12}Zn$: C, 47.59; H, 3.96; N, 11.89; found C, 47.20; H, 4.11; N, 11.81. ^{1}H NMR (DMSO-d_6, 600 MHz): 8.74 (s, 4H), 8.27 (m, 4H), 8.16 (d, J = 12 Hz, 4H), 7.77 (m, 8H). ^{13}C NMR (DMSO-d_6, 151 MHz): 166.44, 150.36, 149.67, 141.49, 130.88, 123.67, 121.66 ppm. IR (KBr, cm^{-1}): 3443 (w), 3370 (m), 3156 (m), 1695 (m), 1602 (m), 1408 (s), 1341 (s), 1157 (m), 1106 (m), 1027 (s), 951 (m), 858 (m), 799 (s), 716 (s), 644 (m), 616 (w), 536 (w), 481 (s).

Synthesis of bis(pyridine-4-carboxamide)(aqua)di(2-nitrobenzoato)zinc(II) (2.2): Complex **2.2** was prepared by following the procedure similar to the synthesis of **2.1**, but 2-nitrobenzoic acid (334.2 mg, 2 mmol) was used in place of 4-nitrobenzoic acid. Yield: 62%. Elemental analysis calculated for $C_{26}H_{22}N_6O_{11}Zn$: C, 47.28; H, 3.33; N, 12.73; found C, 46.42; H, 3.36; N, 12.89. ^{1}H NMR (DMSO-d_6, 600 MHz): 8.70 (d, J = 6 Hz, 4H), 8.31 (s, 4H), 7.77 (m, J = 6 Hz, 4H), 7.75 (m, J = 6 Hz, 4H), 7.66 (t, J = 6 Hz, 2H), 7.60 (t, J = 6 Hz, 2H). ^{13}C NMR (DMSO-d_6, 151 MHz): 168.94, 166.79, 150.36, 149.24, 141.61, 132.30, 131.72, 130.68, 130.28, 123.00, 121.74 ppm. IR (KBr, cm^{-1}): 3392 (br, w), 1690 (m), 1613 (s), 1523 (s), 1481 (w), 1384 (s), 1224 (w), 1147 (m), 1072 (w), 1018 (m), 860 (s), 786 (m), 740 (m), 701 (m), 641 (s), 573 (w), 436 (s).

Synthesis of di-μ^2-(3-nitrobenzoato)[(methanol)(pyridine-4-carboxamide)(3-nitrobenzoato)zinc(II)] (2.3): Complex **2.3** was prepared by following the procedure similar to the synthesis of **2.1**, but 3-nitrobenzoic acid (334.2 mg, 2 mmol) was used in place of 4-

nitrobenzoic acid. Yield: 60%. Elemental analysis calculated for $C_{42}H_{36}N_8O_{20}Zn_2$: C, 45.67; H, 3.26; N, 10.15; found C, 45.88; H, 3.31; N, 10.76. ^{1}H NMR (DMSO-d_6, 600 MHz): 8.73 (s, 4H), 8.66 (s, 4H), 8.35 (d, J = 6 Hz, 8H), 8.29 (s, 4H), 7.78 (d, J = 6 Hz, 4H), 7.74 (s, 4H), 4.21 (s, 2H), 3.16 (s, 6H). ^{13}C NMR (DMSO-d_6, 151 MHz): 169.34, 166.67, 150.49, 147.93, 141.80, 137.03, 136.00, 130.18, 125.91, 124.11, 121.87, 48.92 ppm. IR (KBr, cm^{-1}): 3582 (w), 3465 (w), 3409 (w), 3317 (w), 3078 (m), 2856 (w), 1953 (w), 1687 (s), 1612 (s), 1561 (w), 1525 (w), 1475 (w), 1393 (m), 1349 (m), 1225 (w), 1154 (m), 1071 (s), 1026 (s), 913 (s), 833 (s), 787 (s), 720 (s), 633 (s), 525 (m), 430 (m).

Synthesis of (di-aqua)bis(pyridine-3-carboxamide)di(2-nitrobenzoato)zinc(II) monohydrate (2.4): 2-nitrobenzoic acid (334.2 mg, 2 mmol), pyridine-3-carboxamide (161.2 mg, 1.32 mmol), and zinc(II) acetate dihydrate (219.5 mg, 1 mmol) were dissolved in ethanol. The resulting solution was stirred at room temperature for three hours. A white precipitate was formed, which was dissolved in 5 mL water to get clear transparent solution. The solution was filtered and kept for evaporation. Yield: 60%. Elemental anal. calcd for $C_{26}H_{28}N_6O_{14}Zn$: C, 43.70; H, 3.92; N, 11.76; found C, 43.28; H, 3.97; N, 11.21. ^{1}H NMR (600 MHz, DMSO-d_6): 9.02 (s, 2H), 8.70 (m, 2H), 8.21 (m, 4H), 7.80 (m, J = 6 Hz, 4H), 7.66 (s, 2H), 7.61 (m, 4H), 7.51 (m, J = 6 Hz, 2H). ^{13}C NMR (151 MHz, DMSO-d_6) 166.75, 152.21, 150.10, 149.57, 148.97, 135.50, 135.36, 132.29, 130.52, 129.98, 123.76, 123.11 ppm. IR (KBr, cm^{-1}): 3388 (m), 3154 (m), 1681 (s), 1601 (s), 1534 (s), 1440 (w), 1381 (s), 1197 (w), 1136 (s), 1054 (w), 970 (w), 859 (w), 776 (s), 739 (m), 695 (s), 650 (s), 538 (w), 426 (s).

Synthesis of [tri-aqua(pyridine-3-carboxamide)(κ-O-κ-O′-4-nitrobenzoato)zinc(II)]4-nitrobenzoate (2.5): Complex **2.5** was prepared by following the procedure similar to the synthesis of **2.4**, but 4-nitrobenzoic acid (334.2 mg, 2 mmol) was used in place of 2-nitrobenzoic acid. Yield: 62%. Elemental analysis calculated for $C_{20}H_{20}N_4O_{12}Zn$: calculated C, 41.82; H, 3.49; N, 9.76; found C, 41.96; H, 3.58; N, 9.51. ^{1}H NMR (600 MHz, DMSO-d_6): 9.03 (s, 1H), 8.70 (m, 1H), 8.27 (m, J = 6 Hz, 4H), 8.21 (m, J = 12 Hz, 2H), 8.16 (m, J = 6 Hz, 4H), 7.63 (s, 1H), 7.51 (m, J = 6 Hz, 1H). ^{13}C NMR (151 MHz, DMSO-d_6) 169.60, 166.76, 152.21, 149.33, 148.98, 141.15, 135.57, 131.04, 130.03, 123.81, 123.59 ppm. IR (KBr, cm–1): 3556 (m), 3428 (w), 3364 (w), 3319 (w), 3277 (w), 3230 (w), 3115 (w), 2926 (w), 1952 (m), 1680 (s), 1609 (m), 1558 (s), 1427 (m), 1382 (m), 1345 (s), 1206 (w), 1158 (m), 1105 (s), 1062 (s), 1011 (m), 875 (s), 845 (m), 802 (s), 751 (w), 724 (s), 685 (w), 630 (m), 520 (s).

2.8. References

1 Y. A. Kondratenko, D. A. Zavyalova, M. Y. Arsentev, A. A. Zolotarev, E. I. Sysoev, V. L. Ugolkov and T. A. Kochina, *Cryst. Growth Des.*, 2022, **22**, 6886–6902.

2 B. Lee, I. H. Park and J. Park, *ACS Mater. Lett.*, 2022, **4**, 2388–2393.

3 P. Tshuma, B. C. E. Makhubela, C. A. Ndamyabera, S. A. Bourne and G. Mehlana, *Front. Chem.*, 2020, **8**, 1–11.

4 M. Lackinger and W. M. Heckl, *Langmuir*, 2009, **25**, 11307–11321.

5 T. Bala, B. L. V Prasad, M. Sastry, M. U. Kahaly and U. V Waghmare, *J. Phys. Chem. A*, 2007, **111**, 6183–6190.

6 F. A. Cotton, C. Lin and C. A. Murillo, *Acc. Chem. Res.*, 2001, **34**, 759–771.

7 F. S. Delgado, M. Hernández-Molina, J. Sanchiz, C. Ruiz-Pérez, Y. Rodríguez-Martín, T. López, F. Lloret and M. Julve, *CrystEngComm*, 2004, **6**, 106–111.

8 H. Kumagai, C. J. Kepert and M. Kurmoo, *Inorg. Chem.*, 2002, **41**, 3410–3422.

9 C. Mellot-Draznieks and G. Férey, *Prog. Solid State Chem.*, 2005, **33**, 187–197.

10 H. H. Wang, L. N. Jia, L. Hou, W. J. Shi, Z. Zhu and Y. Y. Wang, *Inorg. Chem.*, 2015, **54**, 1841–1846.

11 A. M. Baruah, A. Karmakar and J. B. Baruah, *Inorganica Chim. Acta*, 2008, **361**, 2777–2784.

12 A. Karmakar, R. J. Sarma and J. B. Baruah, *Eur. J. Inorg. Chem.*, 2007, **2007**, 643–647.

13 A. Karmakar, K. Deka, R. J. Sarma and J. B. Baruah, *Inorg. Chem. Commun.*, 2006, **9**, 836–838.

14 A. Karmakar, K. Bania, A. M. Baruah and J. B. Baruah, *Inorg. Chem. Commun.*, 2007, **10**, 959–964.

15 T. W. Panunto, Z. Urbanczyk-Lipkowska, R. Johnson and M. C. Etter, *J. Am. Chem. Soc.*, 1987, **109**, 7786–7797.

16 J. M. A. Robinson, D. Philp, K. D. M. Harris and B. M. Kariuki, *New J. Chem.*, 2000, **24**, 799–806.

17 W. F. Baitinger, P. vo. R. Schleyer, T. S. S. R. Murty and L. Robinson, *Tetrahedron*, 1964, **20**, 1635–1647.

18 G. Ş. Aşkin, H. Necefoğlu, A. M. Tonbul, N. Dilek and T. Hökelek, *Acta Crystallogr. Sect. E Crystallogr. Commun.*, 2016, **72**, 656–658.

19 Z. Vasková, N. Kitanovski, Z. Jagličić, P. Strauch, Z. Růžičková, D. Valigura, M. Koman, B. Kozlevčar and J. Moncol, *Polyhedron*, 2014, **81**, 555–563.

20 E. Bozkurt, Y. Çelik, F. Çöpür, N. Dege, Y. Topcu and B. Karabulut, *Chem. Phys. Lett.*, 2016, **659**, 186–191.

21 H. Sigel and R. B. Martin, *Chem. Rev.*, 1982, **82**, 385–426.

22 C. B. Aaker and A. M. Beatty, *Chem. Commun.*, 1998, **082**, 1067.

23 A. Mishra and R. Gupta, *Dalt. Trans.*, 2014, **43**, 7668–7682.

24 B. Das and J. B. Baruah, *Cryst. Growth Des.*, 2011, **11**, 5522–5532.

25 L. Yang, D. R. Powell and R. P. Houser, *Dalt. Trans.*, 2007, 955–964.

26 K. D. Karlin, R. W. Cruse, Y. Gultneh, A. Farooq, J. C. Hayes and J. Zubieta, *J. Am. Chem. Soc.*, 1987, **109**, 2668–2679.

27 R. Sarma, D. Kalita and J. B. Baruah, *Dalt. Trans.*, 2009, 7428–7436.

28 N. Phukan and J. B. Baruah, *A supramolecular assembly and complexes of zinc 2-hydoxy-3-naphthoate*, The Royal Society of Chemistry, 2013, vol. 3.

29 S. Hazra, B. Sarkar, S. Naiya, M. G. B. Drew and A. Ghosh, *Polyhedron*, 2012, **46**, 8–15.

30 J. G. Lin, L. Qiu, W. Cheng, S. N. Luo, K. Wang and Q. J. Meng, *Inorg. Chem. Commun.*, 2010, **13**, 855–858.

31 A. Tarai and J. B. Baruah, *Dalt. Trans.*, 2018, **47**, 4921–4930.

32 A. G. Blackman, E. B. Schenk, R. E. Jelley, E. H. Krenske and L. R. Gahan, *Dalt. Trans.*, 2020, **49**, 14798–14806.

33 A. Karmakar, R. J. Sarma and J. B. Baruah, *Inorg. Chem. Commun.*, 2006, **9**, 1169–1172.

34 W. M. Singh and J. B. Baruah, *Dalt. Trans.*, 2009, 2352–2358.

35 N. Barooah, R. J. Sarma, A. S. Batsanov and J. B. Baruah, *Polyhedron*, 2006, **25**, 17–24.

36 A. Vogler and H. Kunkely, *Coord. Chem. Rev.*, 2007, **251**, 577–583.

37 C. A. Barboza, J. C. Germino, A. M. Santana, F. J. Quites, P. A. M. Vazquez and T. D. Z. Atvars, *J. Phys. Chem. C*, 2015, **119**, 6152–6163.

38 A. Terenzi, A. Lauria, A. M. Almerico and G. Barone, *Dalt. Trans.*, 2015, **44**, 3527–3535.

39 G. Salassa, M. J. J. Coenen, S. J. Wezenberg, B. L. M. Hendriksen, S. Speller, J. A. A. W. Elemans and A. W. Kleij, *J. Am. Chem. Soc.*, 2012, **134**, 7186–7192.

40 L. Le Bras, K. Chaitou, S. Aloïse, C. Adamo and A. Perrier, *Phys. Chem. Chem. Phys.*, 2019, **21**, 46–56.

41 J. Holub, A. Santoro and J.-M. Lehn, *Inorganica Chim. Acta*, 2019, **494**, 223–231.

42 S. Dey, A. Efimov, C. Giri, K. Rissanen and H. Lemmetyinen, *European J. Org. Chem.*, 2011, **2011**, 6226–6232.

43 R. Diana, B. Panunzi, A. Tuzi and U. Caruso, *J. Mol. Struct.*, 2019, **1197**, 672–680.

44 Y. Chen, Y. Bai, Z. Han, W. He and Z. Guo, *Chem. Soc. Rev.*, 2015, **44**, 4517–4546.

45 Z. Xu, K.-H. Baek, H. N. Kim, J. Cui, X. Qian, D. R. Spring, I. Shin and J. Yoon, *J. Am. Chem. Soc.*, 2010, **132**, 601–610.

46 S.-L. Zheng, J.-H. Yang, X.-L. Yu, X.-M. Chen and W.-T. Wong, *Inorg. Chem.*, 2004, **43**, 830–838.

47 F. Borbone, U. Caruso, S. Concilio, S. Nabha, B. Panunzi, S. Piotto, R. Shikler and A. Tuzi, *Eur. J. Inorg. Chem.*, 2016, **2016**, 818–825.

48 A. S. Berezin, O. V Antonova, E. V Lider, A. I. Smolentsev, V. A. Nadolinny and M. S. Mel'gunov, *J. Lumin.*, 2017, **190**, 261–266.

49 D. A. Evans, L. M. Lee, I. Vargas-Baca and A. H. Cowley, *Organometallics*, 2015, **34**, 2422–2428.

50 D. A. Evans, L. M. Lee, I. Vargas-Baca and A. H. Cowley, *Dalt. Trans.*, 2015, **44**, 11984–11996.

51 Y.-Z. Xie, G.-G. Shan, P. Li, Z.-Y. Zhou and Z.-M. Su, *Dye. Pigment.*, 2013, **96**, 467–474.

52 D. Qiao, J.-Y. Wang, L.-Y. Zhang, F.-R. Dai and Z.-N. Chen, *Dalt. Trans.*, 2019, **48**, 11045–11051.

53 D. W. Christianson and R. S. Alexander, *J. Am. Chem. Soc.*, 1989, **111**, 6412–6419.

54 J. Nath, A. Tarai and J. B. Baruah, *ACS Omega*, 2019, **4**, 18444–18455.

55 A. Karmakar and J. B. Baruah, *Polyhedron*, 2008, **27**, 3409–3416.

56 W. M. Singh and J. B. Baruah, *Dalt. Trans.*, 2009, 2352–2358.

57 B. Liu, L.-Y. Pang, L. Hou, Y.-Y. Wang, Y. Zhang and Q.-Z. Shi, *CrystEngComm*, 2012, **14**, 6246–6251.

Appendix- Chapter 2

Physical measurements: ^{1}H-NMR and ^{13}C-NMR spectra were recorded on a Bruker Ascend-600 MHz using TMS as an internal standard. Thermogravimetric analyses were performed using a thermal analyzer (SDTQ600) with a simultaneous DTA/TGA system under nitrogen with a heating rate of 10°C min^{-1}. Powder X-ray diffraction patterns were recorded using a Bruker powder X-ray diffractometer D2 phaser with Cu-Kα radiation (l = 1.54056 Å), 40 kV of operating voltage, and 125 mA of operating current (step size = 0.02 (2 θ), time = 5º/min, Quartz plate XRD (0.5 mm depth) sample holder). Infrared spectroscopy of the solid samples was recorded on a Perkin Elmer Spectrum Two FT-IR spectrometer in the region 4000-400 cm^{-1} by using a KBr pellet. Fluorescence spectra in both solid and liquid states were measured in a Horiba Scientific FluoroMax-4 Spectrofluorometer. UV-visible spectroscopy of the solid samples was measured in Perkin Elmer Lambda 750 UV/Vis spectrometer. The dynamic light scattering (DLS) experiment was performed in Malvern Zetasizer Nano ZS90. The quantum yield of the solid samples was measured by taking a definite amount of the solid and exciting at a required wavelength in a Horiba Fluoromax plus spectrofluorometer using the Petite Integrating Sphere method. The fluorescence emission (E_c) and the scatter (L_c) for the sample and blank (L_a and E_a) were recorded. From these spectral measurements (sample and blank), the quantum yields were calculated by using the equation $\phi = [(E_c - E_a)/(L_a - L_c)]$. Lifetime of the complex **2.1-2.5** in solid and solution phases was recorded on a Picosecond Time-resolved and Steady State Luminescence Spectrometer, Make: Edinburg Instruments, Model: Lifespec II & FSP 920.

Determination of quantum yield in solution: In solution, the quantum yield was determined by using quinine sulphate as a reference in DMSO at room temperature.

Quantum yield

$$= \frac{\text{Area of the Complex}}{\text{Area of Quinine Sulphate}} \times \frac{\text{Absorbance at 333 nm (Quinine sulphate)}}{\text{Absorbance at 333 nm (complex)}} \times \frac{\eta^2}{\eta_R^2} \times Q_R$$

……*Equation A2.1*

where, η = Refractive Index of solvent used of sample preparation

η_R = Refractive Index of solvent used of reference preparation

Q_R = Quantum yield of reference

Computational method: All theoretical calculations, including optimization, energy calculation, and HOMO-LUMO energy gaps, were performed by using the B3LYP[A.1,] functional with LANL2DZ[A.2] as a basis set in Gaussian 09W software.[A.3]

Crystallographic data: X-ray single crystal diffraction data of the complexes **2.1** and **2.2** were collected on an Oxford SuperNova diffractometer whereas for the complexes **2.3**, **2.4**, and **2.5** were collected by using a Bruker Nonius SMART APEX CCD diffractometer equipped with a graphite monochromator. The data were collected at 296 K with Mo Kα radiation (λ = 0.71073 A). Data reduction and cell refinement were carried out by CrysAlisPro software. Structures were solved using SHELXS-14 by direct method and refined by full-matrix least-squares on F^2 using SHELXL-14. All non-hydrogen atoms were refined in anisotropic approximation against F^2 of all reflections. The hydrogen atoms were placed in calculated positions and refined isotropically. The crystallographic parameters are listed in Table 1S. (Reference: Sheldrick GM. ActaCrystallogr. C Struct. Chem. 2015, *71*, 3 - 8.)

Table A.1: Crystallographic parameters of the complexes **2.1**-**2.5**

Parameters	Complex **2.1**	Complex **2.2**	Complex **2.3**	Complex **2.4**	Complex **2.5**
Formula	$C_{28}H_{28}N_6O_{12}Zn$	$C_{26}H_{22}N_6O_{11}Zn$	$C_{42}H_{36}N_8O_{20}Zn_2$	$C_{26}H_{28}N_6O_{14}Zn$	$C_{20}H_{20}N_4O_{12}Zn$
CCDC	1964042	1964041	1964043	1964039	1964040
Mol.wt.	705.93	659.86	1103.53	713.91	573.77
Space group	*C* 2/*c*	*P*-1	*C* 2/*c*	*P* $2_1/n$	*P*-1
a(Å)	20.1428(11)	8.0671(6)	22.0343(8)	7.8574(4)	5.9866(7)
b(Å)	6.2816(3)	12.718(2)	13.6328(5)	19.2849(9)	8.7293(10)
c (Å)	25.1031(13)	14.3069(18)	15.1548(6)	9.9755(5)	22.354(3)
α (°)	90	81.172(13)	90	90	96.624(3)
β (°)	104.399(5)	76.060(9)	100.7150(10)	102.3550(10)	90.797(4)
γ (°)	90	74.624(12)	90	90	90.264(3)
V ($Å^3$)	3076.5(3)	1367.3(3)	4473.0(3)	1476.57(13)	1160.2(2)
Density, g cm^{-3}	1.524	1.603	1.639	1.606	1.642
Abs. coeff., mm^{-1}	0.872	0.972	1.165	0.914	1.133
F (000)	1456	676	2256	736	588
Total no. of reflections	2722	4830	3966	2617	4117
Reflections, I > 2σ(I)	2211	3589	3065	2299	3653
Max. θ/°	25.000	25.044	25.044	25.047	25.050
Ranges (h, k, l)	$-23 \le h \le 15$	$-9 \le h \le 9$	$-26 \le h \le 26$	$-9 \le h \le 9$	$-7 \le h \le 7$
	$-6 \le k \le 7$	$-10 \le k \le 15$	$-16 \le k \le 16$	$-22 \le k \le 22$	$-10 \le k \le 10$
	$-23 \le l \le 29$	$-17 \le l \le 15$	$-18 \le l \le 18$	$-11 \le l \le 11$	$-26 \le l \le 26$
Complete to 2θ (%)	99.9	99.9	100	100	100
Data/restraints/parameters	2736/0/223	4830/2/413	3966/2/338	2617/4/227	4117/2/357
GooF (F^2)	1.038	1.007	1.040	1.025	1.012
R indices [I > 2σ(I)]	0.0406	0.0523	0.0318	0.0256	0.0544

wR_2 [I > 2σ(I)]	0.0788	0.0992	0.0877	0.0503	0.1793
R indices (all data)	0.0552	0.0755	0.0469	0.0311	0.0623
wR_2 (all data)	0.0861	0.1178	0.0979	0.0528	0.1902

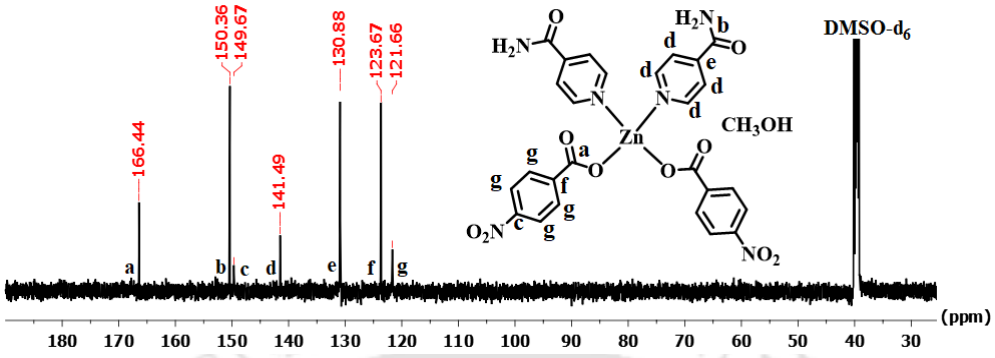

Figure A2.1. ^{13}C NMR (DMSO-d_6, 151 MHz) spectrum of complex **2.1**

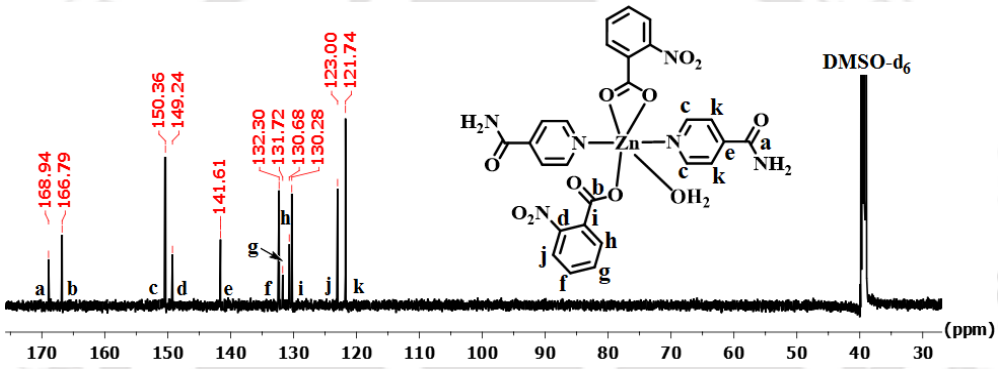

Figure A2.2. ^{13}C NMR (DMSO-d_6, 151 MHz) spectrum of complex **2.2**

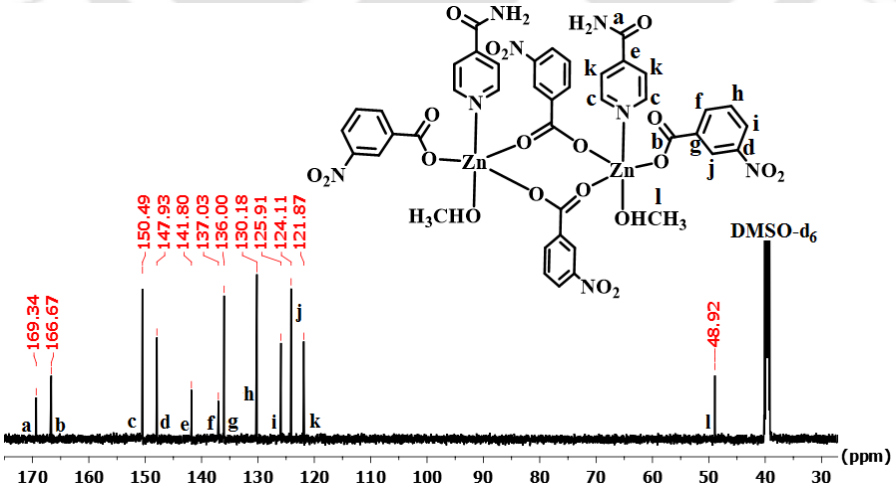

Figure A2.3. ^{13}C NMR (DMSO-d_6, 151 MHz) spectrum of complex **2.3**

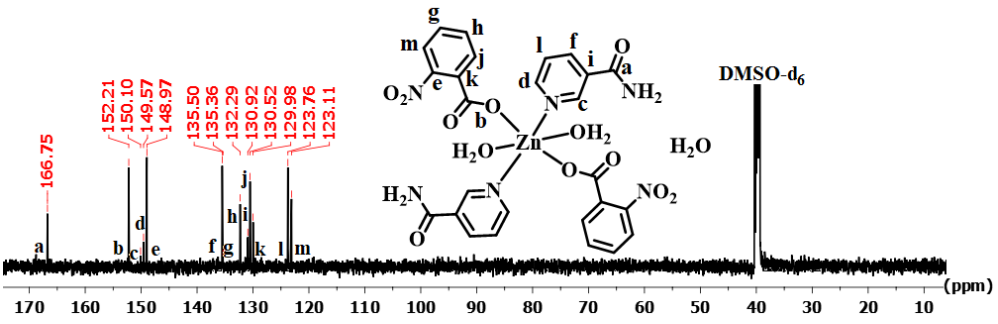

Figure A2.4. ^{13}C NMR (DMSO-d$_6$, 151 MHz) spectrum of complex **2.4**

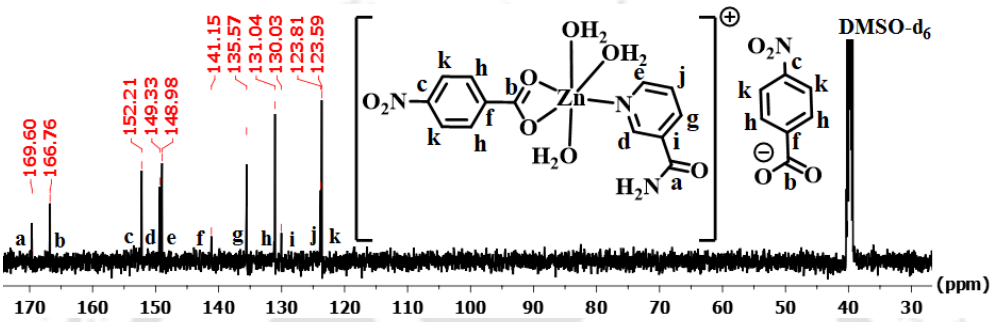

Figure A2.5. ^{13}C NMR (DMSO-d$_6$, 151 MHz) spectrum of complex **2.5**

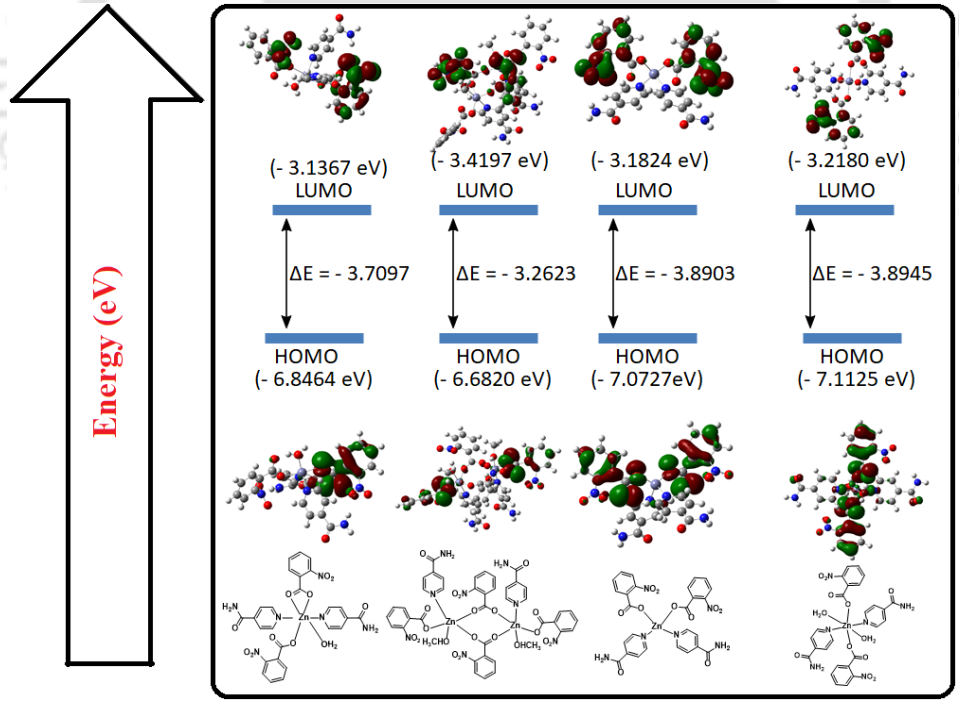

Figure A2.12. The HOMO and LUMO of zinc(II) complexes having pyridine-4-carboxamide and 2-nitrobenzoate having different coordination, calculated by DFT using B3LYP function with LANL2DZ as basis set

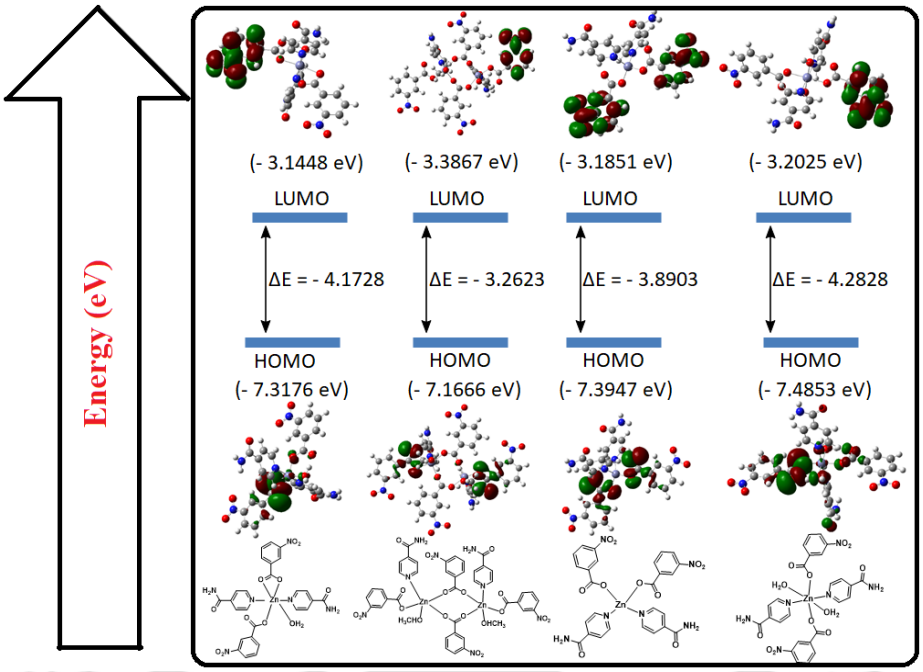

Figure A2.13. The HOMO and LUMO of different non-ionic zinc(II) complexes having pyridine-4-carboxamide and 3-nitrobenzoate, calculated by DFT using B3LYP function with LANL2DZ as basis set

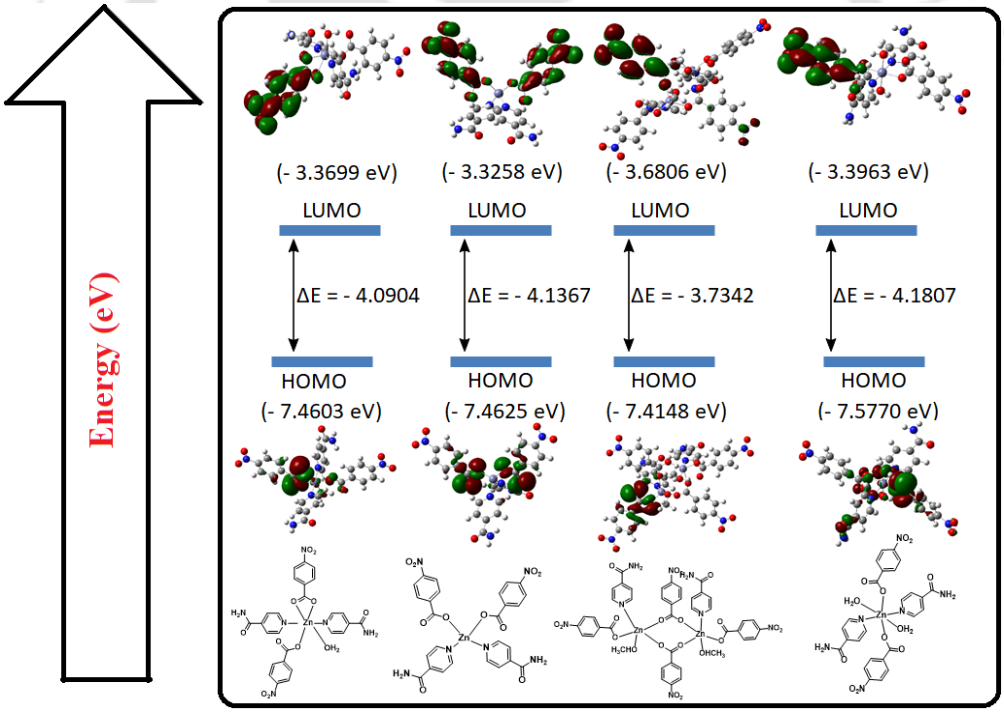

Figure A2.14. The HOMO and LUMO of different non-ionic zinc(II) complexes having pyridine-4-carboxamide and 4-nitrobenzoate complexes, calculated by DFT using B3LYP function with LANL2DZ as basis set

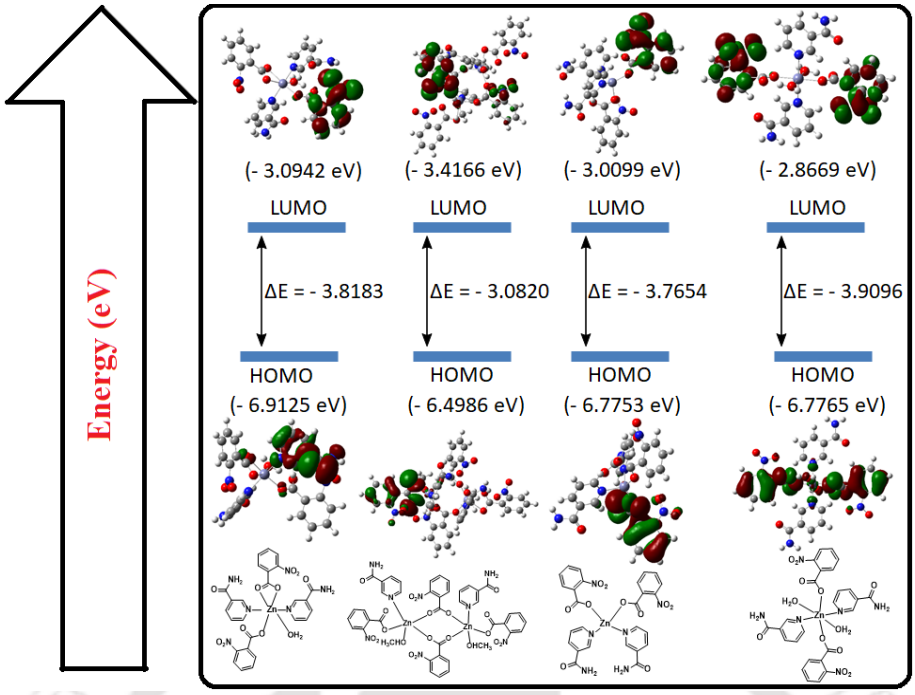

Figure A2.15. The HOMO and LUMO different non-ionic zinc(II) complexes having pyridine-3-carboxamide and 2-nitrobenzoate, calculated by DFT using B3LYP function with LANL2DZ as basis set

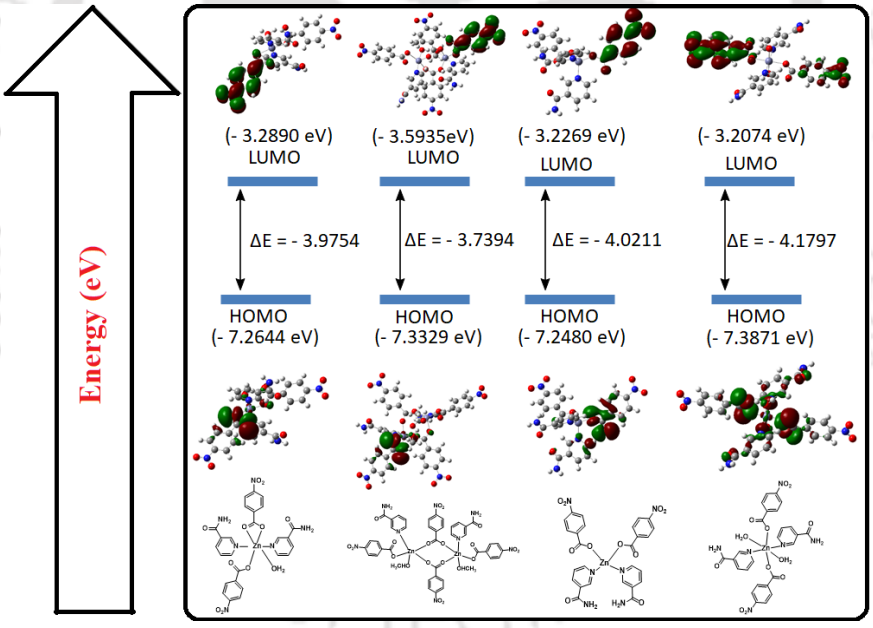

Figure A2.16. The HOMO and LUMO of different non-ionic zinc(II) complexes having pyridine-3-carboxamide 4-nitrobenzoate, calculated by DFT using B3LYP function with LANL2DZ as basis set

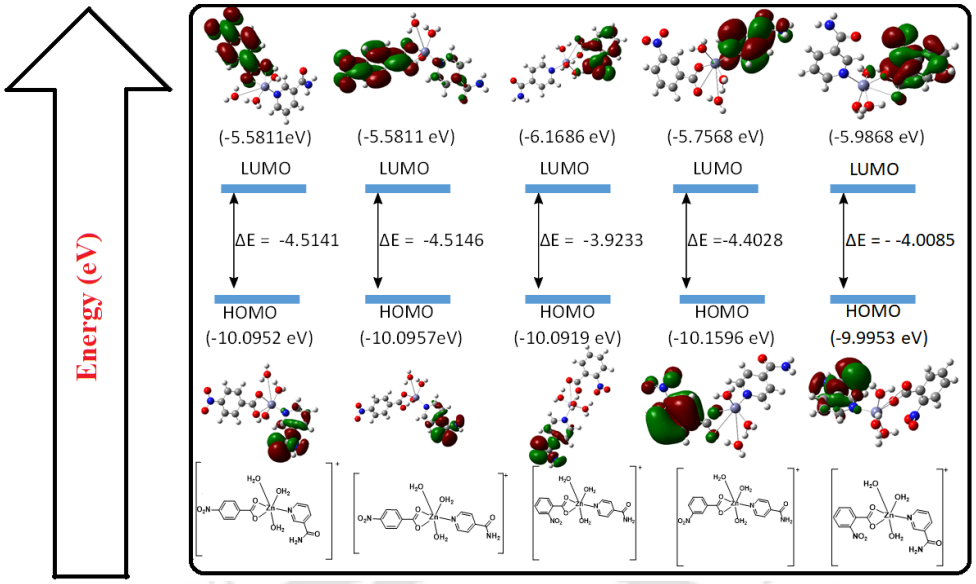

Figure A2.17. The HOMO and LUMO of different zinc(II) complexes having coordination of complex 5 (cationic form) from DFT calculation using B3LYP functional using LANL2DZ as basis set and +1 charge

References:

A.1. E. A. Amin and D. G. Truhlar, *J. Chem. Theory Comput.*, 2008, **4**, 75–85.

A.2. Y. Yang, M. N. Weaver and K. M. J. Merz, *J. Phys. Chem. A*, 2009, **113**, 9843–9851.

A.3. M. Frisch, G. Trucks, H. Schlegel, G. Scuseria, M. Robb, J. Cheeseman, G. Scalmani, V. Barone, G. Petersson, H. Nakatsuji, *Gaussian 09*, *Revision A.02*; Gaussian, Inc.: Wallingford, CT, 2016.

Chapter 3

Characterization of assemblies of semi-flexible urea and thiourea derivatives and their salts with mineral acids

The urea and thiourea derivatives have structural similarities, hence, their supramolecular aspects have close resemblances, but differences arise due to the influence of the oxygen or sulphur atom as well as from the functional units. As mentioned in the introduction, they act as hydrogen bond donor and acceptors. A wide variety of supramolecular homo and hetero synthons are being examined in literature and some common ones are listed in Fig. 3.1.[1] The N,N-disubstituted thiourea derivatives adopt *syn-syn* or *syn-anti* geometries depending on the substituent, supramolecular effects and partner molecules in an assembly (Fig. 3.2).[1,2]

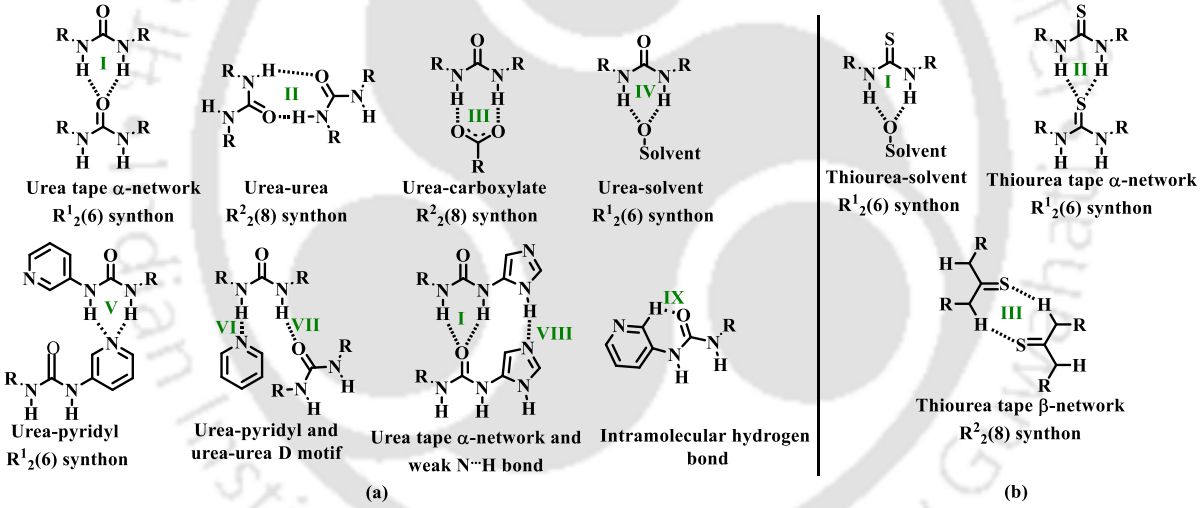

Figure 3.1. Some examples of supramolecular synthons found in non-covalent assemblies of (a) urea and (b) thiourea derivatives

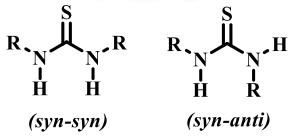

Figure 3.2. (a) *syn-syn* and (b) *syn-anti* forms of a symmetric thiourea

As mentioned in the introduction, the urea and thiourea derivatives have the potential for biological studies in ion transport, medicine, and fertilizer.[3,4] The soluble urea complexes

have advantages and control the delivery of nitrogenous material or degrade urea through hydrolysis. Furthermore, the controlled release of urea from composites helps in the availability of nitrogen in the soil.[5] Calcium oxide-based composites are, in general, biocompatible, easy to prepare pellets and serve as mild base their composites with urea generate interests.[6]

In this study, the self-assembling properties of pyridylurea and pyridylthiourea derivatives and their self-assemblies with two oxy acids, perchloric acid and nitric acid, were studied. The primary objective was to have a comparative structural aspect of the urea and their counterparts and to understand the self-assemblies of salts or ionic cocrystals. A series of composites of the selected derivatives with calcium oxide were studied to understand the release of the urea counterpart.

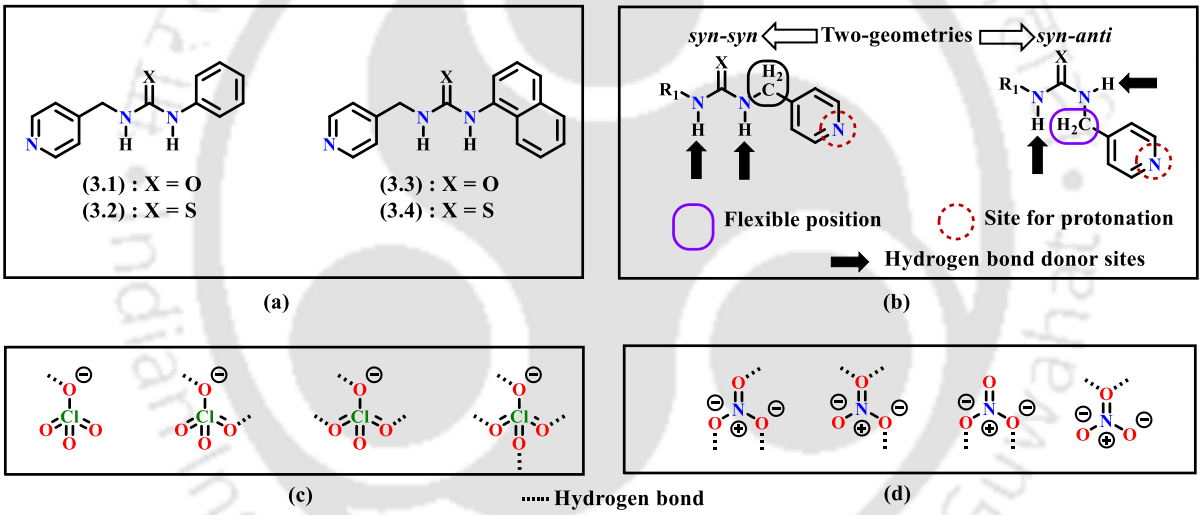

Figure 3.3. Pyridylmethyl functionalized phenyl and naphthylurea (or thiourea) derivatives **3.1**-**3.4**; (b) two orientations; and some of the hydrogen bonding mode of (c) perchlorate anion and (d) nitrate anion (dotted line showing the sites)

3.1. Synthesis and characterization of pyridylmethyl functionalized phenyl (or naphthyl) urea (or thiourea) derivatives 3.1-3.4

The compounds **3.1** and **3.2** were synthesized by the reaction of phenylisocyanate or phenylisothiocyanate with 4-aminomethylpyridine at room temperature. Similarly, compounds **3.3** and **3.4** were synthesized from the respective reactions of naphthylisocyanate or naphthylisothiocyanate with 4-aminomethylpyridine. All the compounds were

characterized by various spectroscopic techniques, such as FTIR spectroscopy, ^{1}H-NMR and High Resolution Mass Spectrometry. The mass spectrum of **3.1** showed a peak at 228.1194 (Calculated 228.1092), corresponding to the [M+1] peak (Fig. A3.1a). Compounds **3.2**, **3.3**, and **3.4** showed peaks at 244.0660 (Calculated 244.0684), 278.0993 (Calculated 278.1249), and 294.0937 (Calculated 294.1020), corresponding to [M+1] peak respectively (Figs. A3.1b, A3.1c, A3.1d). In ^{1}H-NMR, the characteristic proton peaks of the two -NH groups (designated as 'a' and 'g') in **(3.1)·H$_2$O** and **3.2** appeared at 8.69 ppm, 6.73-6.71 ppm (for **3.1**, Fig. A3.2a) and 9.77 ppm, 7.16-7.13 ppm (for **3.2**, Fig. A3.2b) respectively. In the case of compounds **3.3** and **3.4**, the proton peaks of the two -NH groups (designated as 'a' and 'k' for **3.3**; 'a' and 'j' for **3.4**) appeared at 8.72 ppm, 7.14-7.12 ppm (for **3.3**, Fig. A3.2c) and 9.90 ppm, 7.51-7.49 ppm (for **3.4**, Fig. A3.2d), respectively.

Crystallization of compound **3.1** from a methanol-water solvent mixture (1:1 v/v) solution yielded the crystals of the corresponding hydrate, **(3.1)·H$_2$O**. The crystals were of the orthorhombic crystal system of *Pna*2$_1$ space group. The crystal structure of the anhydrous form of **3.1** was reported in the literature.[7] It belonged to a monoclinic crystal system of space group *P*2$_1$/*a*. The compounds **3.2-4.4** were crystallized from different binary mixed solvent systems (1:1 v/v) by slow evaporation of solution at room temperature. Namely, the compound **3.2** was crystallized from the methanol-acetone mixture (1:1 v/v)), **3.3** from methanol-dimethyl formamide, and **3.4** from methanol-dimethyl formamide mixture. Among these, the crystals of compound **3.3** were in the form of monohydrate, **(3.3)·H$_2$O**. The identity of each crystalline form of the compounds as anhydrous or hydrate form, depending on the crystals, was characterized by IR, ^{1}H-NMR, elemental analysis, and thermogravimetry.

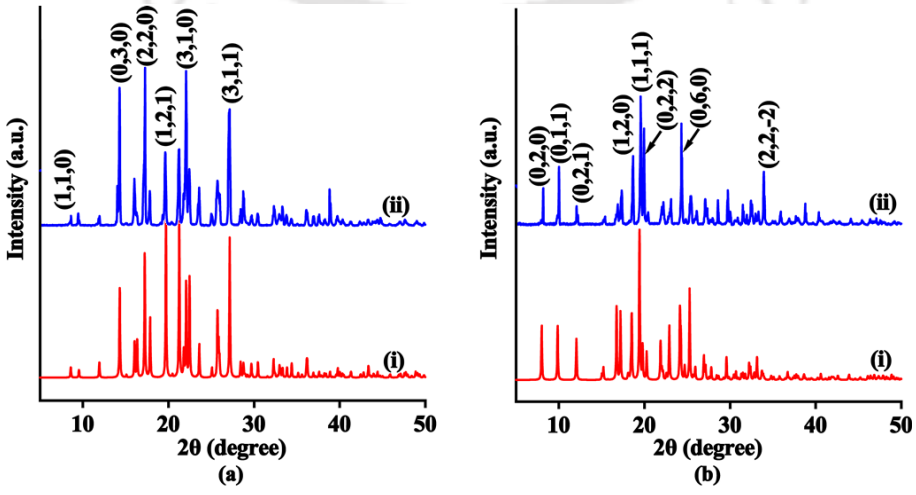

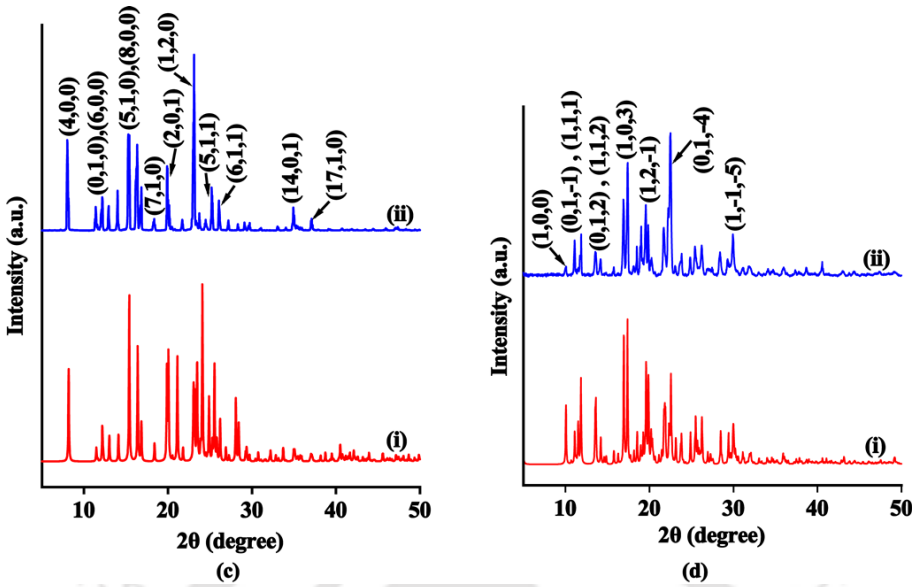

Figure 3.4. Powder X-ray patterns of (a) **(3.1)·H_2O**, (b) **3.2**, (c) **(3.3).H_2O**, and (d) **3.4** (where (i) and (ii) are simulated and experimental powder X-ray patterns respectively)

The structures of each were determined by single crystal X-ray followed by recording the powder X-ray diffraction patterns. The phase purities of each of these compounds were analyzed by recording their powder X-ray patterns and comparing them with the simulated X-ray patterns generated from the CIF files by MERCURY software[8] (Figs. 3.4a-3.4d). The comparisons of the Miller indices have shown that in each case, a single phase was observed.

3.2. Self-assemblies of (3.1)·H_2O, 3.2, (3.3).H_2O, and 3.4

The crystal structure of the compound **(3.1)·H_2O** showed that the two -NH groups were in a *syn-syn* arrangement. The water molecule formed intermolecular hydrogen bonds with the two -NH groups [N1–H···O2, $d_{D\cdots A}$ = 2.924(5) Å and N2–H···O2, $d_{D\cdots A}$ = 2.981(5) Å], carbonyl oxygen atom [$d_{D\cdots A}$ = 2.819(5) Å] and pyridyl nitrogen atom [$d_{D\cdots A}$ = 2.876(5) Å] of **3.1**, to provide a four-coordinated hydrogen-bonded environment to the water molecule (Fig. 3.5a). The water molecule acted as a hydrogen bond donor as well as a hydrogen bond acceptor. Accordingly, the water of crystallization acted as a bridge between two molecules of **3.1**. The intermolecular hydrogen bonding between the two -NH groups and carbonyl oxygen atom are common in urea. But in the hydrate **(3.1)·H_2O**, the water molecules intervened in the formation of α-urea tape synthons by participating in the hydrogen bonds with the urea part of the molecule. The $N_{pyridyl}$ atom, as illustrated in Fig. 3.5a, is involved in a hydrogen bond with the water molecule. The flexible methylene unit of the molecule helped

the molecule to adopt a puckered geometry. This type of N_{urea}-H···O_{water} and $N_{pyridyl}$···H-O_{water} intermolecular hydrogen bonds are commonly observed in the hydrates of pyridylurea derivatives.[9] In the literature reported structure of the anhydrous form of **3.1**, there is an intermolecular hydrogen bonding between the pyridyl nitrogen atom and one of the two -NH groups of **3.1** [$d_{D\cdots A}$ = 2.042 Å].[7] This made a significant difference in the packing of the two forms.

The compound **3.2** has a *syn-anti* arrangement of the urea moiety. It has intermolecular hydrogen bonds between one of the two -NH groups with a pyridyl nitrogen atom [N2–H···N3, $d_{D\cdots A}$ = 3.005 (3) Å] (Fig. 3.5b). In this case, there is a homo-dimeric thioamide-thioamide $R^2_2(8)$ synthon formed due to the $N_{thiourea}$-H···S hydrogen bonds [N1–H···S1, $d_{D\cdots A}$ = 3.340 (2) Å]. These hydrogen-bonded homodimers are self-assembled to form hexamers (Fig. 3.5c). The homomeric synthons of such a kind are also present in many thiourea derivatives.[10–12] In the present case, each homomeric unit is further linked through N-H···S bonds, resulting in a hexameric cyclic assembly, as shown in Fig. 3.5c. Thus, the geometrical features across the urea and thiourea derivatives having identical substituents are different due to synthon variations.

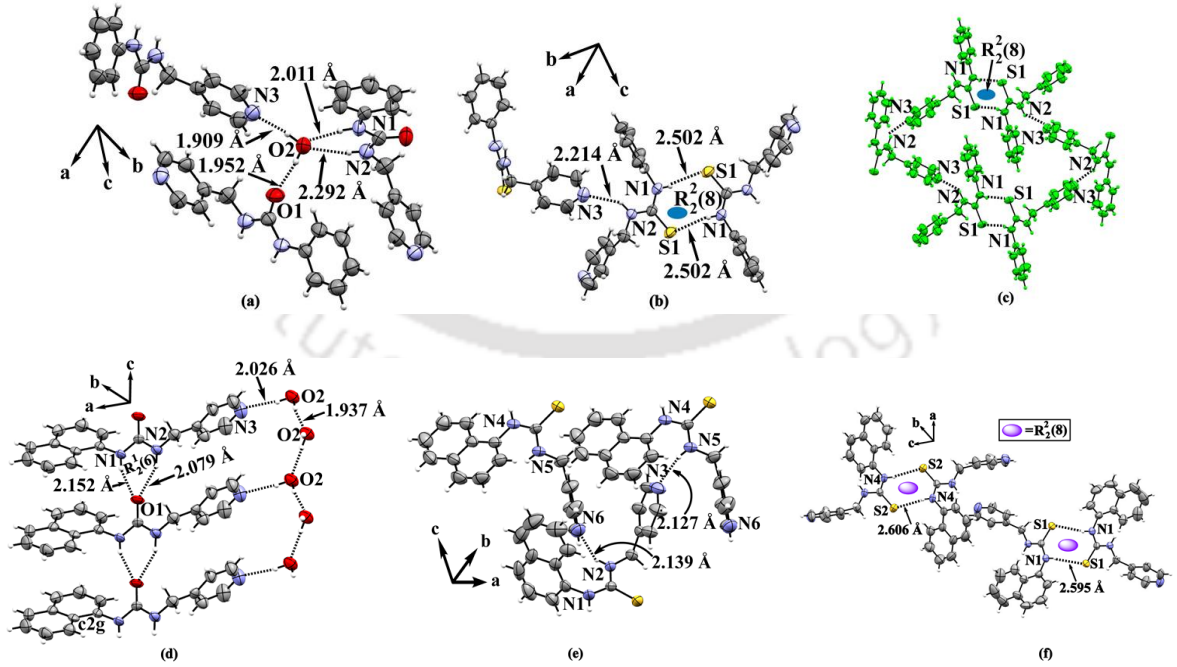

Figure 3.5. Hydrogen-bonded assembly of (a) **(3.1)·H_2O**, (b) **3.2**, (c) assembling of hydrogen-bonded homodimers of the **3.2**; self-assemblies of (d) **(3.3)·H_2O**, and (e) **3.4**, and (f) thioamide-thioamide synthon assisted tetramer

The monohydrate of the urea-derived compound **3.3** has the *syn-syn* orientation of the urea part. The self-assembly of this hydrate is different from the hydrated form of the **3.1**; this compound has an intermolecular hydrogen-bonded urea α-tape $R^1_2(6)$ synthon (Fig. 3.5d). These tapes are formed between the two -NH groups and carbonyl oxygen atoms, which allowed a parallel alignment of the naphthyl units. The parent molecules are held together by solvated water through intermolecular hydrogen bonds formed between the pyridyl nitrogen atom. This kind of hydrogen bond resulted in the formation of a chain-like arrangement (Fig. 3.5d). The water chains are extended in one dimension along the crystallographic *a*-axis. As a consequence of the stacking arrangement among the naphthalene rings, there is a significant difference in the packing patterns of **(3.1)·H$_2$O** and **(3.3)·H$_2$O**. The urea tapes are observed in the latter case but not in the former.

Compound **3.4** has the *syn-anti* orientations of the thiourea moiety. The -NH groups are not in one plane to facilitate the N-H···$N_{pyridyl}$ hydrogen bond with neighbouring molecules. The self-assembly is comprised of chain-like structures with a puckered-like structure of the parent compound (Fig. 3.6e). It is self-assembled to provide a spiral chain-like arrangement due to intermolecular hydrogen bonds. The thiocarbonyl group participated in hydrogen bonds and formed a thioamide-thioamide $R^2_2(8)$ synthon, resulting in a tetramer (Fig. 3.6f).

Table 3.1. Hydrogen bond parameters of **(3.1)·H$_2$O**, **3.2**, **(3.3)·H$_2$O**, and **3.4**

Compound	D-H···A	d_{D-H} (Å)	$d_{H\cdots A}$ (Å)	$d_{D\cdots A}$ (Å)	∠D-H···A (°)
(3.1)·H$_2$O	N(1)-H(1A) ···O(2) [x,y,z]	0.93 (5)	2.01 (5)	2.92 (5)	166 (4)
	N(2) -H(2A) …O(2) [x,y,z]	0.83 (5)	2.29 (5)	2.98 (5)	141 (5)
	O(2) -H(2B) …O(1) [1/2+x,1/2-y,z]	0.87 (5)	1.95 (5)	2.82 (5)	174 (4)
	O(2) -H(2C) …N(3) [1/2-x,1/2+y,-1/2+z]	0.98 (7)	1.91 (7)	2.88 (5)	169 (6)
3.2	N(1) -H(1) ···S(1) [-x, -y, 1-z]	0.85 (2)	2.50 (2)	3.34 (2)	169 (19)
	N(2) -H(2) ···N(3) [x, 1/2-y, -1/2+z]	0.91(2)	2.21 (2)	3.01 (3)	145(18)
(3.3)·H$_2$O	N(1) -H(1A) ··· O(1) [x, y, -1+z]	0.77 (9)	2.15 (9)	2.86 (9)	153 (8)
	N(2) -H(2A) ···O(1) [x, y, -1+z]	0.83 (9)	2.12(9)	2.87 (9)	151 (7)
	O(2) -H(2C) ···O(2) [1/2-x, y, -1/2+z]	0.82 (12)	1.94 (12)	2.75(11)	172 (9)
	O(2) -H(2D) ···N(3) [x, 1+y, -1+z]	0.86 (9)	2.03 (10)	2.87 (11)	170 (8)
3.4	N(1) -H(1) ···S(1) [1-x, -y, 1-z]	0.82 (3)	2.60 (3)	3.39 (2)	164 (3)
	N(2) -H(2) ···N(6) [-x, 1-y, 1-z]	0.84 (2)	2.1 (19)	2.89 (3)	147 (17)
	N(4) -H(4A) ···S(2) [1-x, -y, -z]	0.82 (3)	2.61 (3)	3.42 (2)	169 (2)
	N(5) -H(5) ···N(3) [1-x, 1-y, 1-z]	0.80 (3)	2.13 (3)	2.89 (4)	158 (2)

3.3. Self-assemblies of perchlorate and nitrate salts of 3.1- 3.4

As our objectives have been to search for crystalline salts or ionic cocrystals of the aforesaid pyridine containing urea and thiourea for structural study, we pursued suitable crystals for structure determination from the reaction solution of different acids with compounds **3.1**-**3.4**. Accordingly, these compounds were treated with several inorganic acids such as hydrochloric, hydrobromic, hydrofluoric, nitric, perchloric, and sulphuric acids; from those series of reactions, we could obtain suitable crystals with two oxy-acids, namely nitric acid and perchloric acid. Reactions of **3.1** and **3.4** with perchloric acid provided crystalline salt, whereas compounds **3.2** and **3.3** provided the crystalline forms of the perchlorate and nitrate salts (Scheme 3.1). The perchlorate salt of **3.3** is obtained as a monohydrate. All these salts, namely **3.1a**, **3.2a**, **3.2b**, **3.3a**, **3.3b**, and **3.4a**, were characterized by powder X-ray pattern, single crystal X-ray diffraction analysis, FTIR, ^{1}H-NMR spectroscopy and thermogravimetric methods.

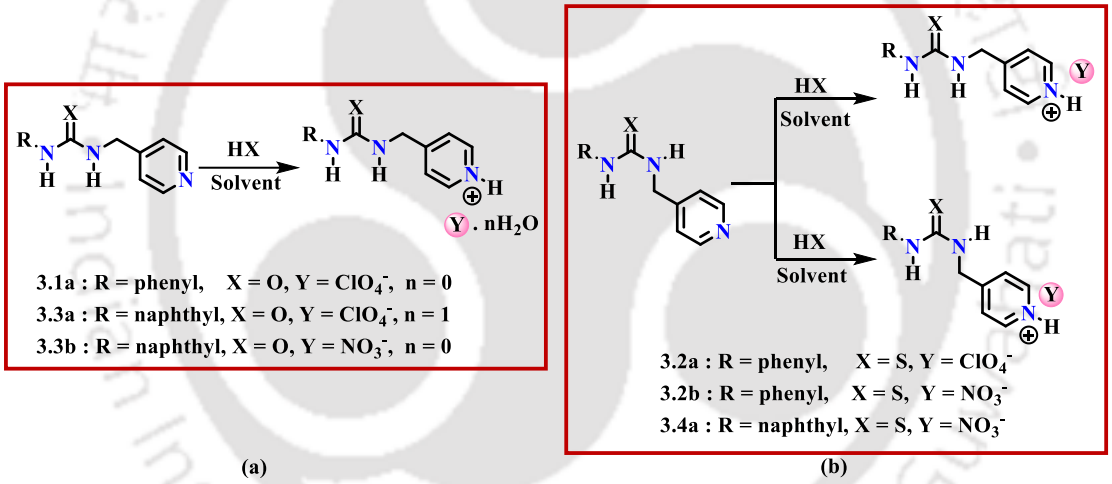

Scheme 3.1. Crystalline salts of **3.1**-**3.4**

3.3.1. Perchlorate salt of compound 3.1

The perchlorate salt **3.1a** crystallized in the orthorhombic *Pbca* space group. It has a protonated parent compound and a disordered perchlorate anion. The urea -NH groups of the salt has a *syn-syn* arrangement. The cations were linked by urea tape network through bifurcated N-H···O hydrogen bonds [N2–H···O1 {$d_{D\cdots A}$ = 3.034(3) Å} and N1–H···O1 {$d_{D\cdots A}$ = 2.833(3) Å}]. The disordered perchlorate anions formed hydrogen bonds with the pyridinium cation [$d_{D\cdots A}$ = 2.750(10) Å] (Fig. 3.6). The perchlorate ions formed anion chain,

whereas the cationic part is organized parallel to each other in another chain next to the anionic chain through urea tape network.

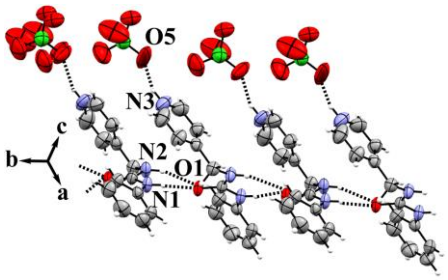

Figure 3.6. Self-assembly of salt **3.1a**

3.3.2. Perchlorate salt of compound 3.2

The asymmetric unit of the perchlorate salt **3.2a** has a protonated host **3.2** and a perchlorate anion. It crystallized in a monoclinic *I*2/*a* space group. The two -NH groups of the thiourea part have *syn-anti* orientation. The obvious differences in the hydrogen bonding pattern in the perchlorate salts **3.1a** and **3.2a** are due to the presence of an oxygen atom (in **3.1a**) instead of sulphur in the latter (**3.2a**) in the host compound. The location of the perchlorate anion with respect to the cation in the crystal lattice was different as a consequence of size effect and packing requirements. In **3.2a**, the perchlorate anion acted as a bridge between two protonated host molecules by forming hydrogen bonds with an H-N^+ unit of pyridinium cation ($d_{D\cdots A}$ = 2.75 (10) Å) and -NH group adjacent to the methylene unit ($d_{D\cdots A}$ = 2.94 (8) Å). This resulted in a one-dimensional hydrogen-bonded chain-like arrangement (Fig. 3.7a).

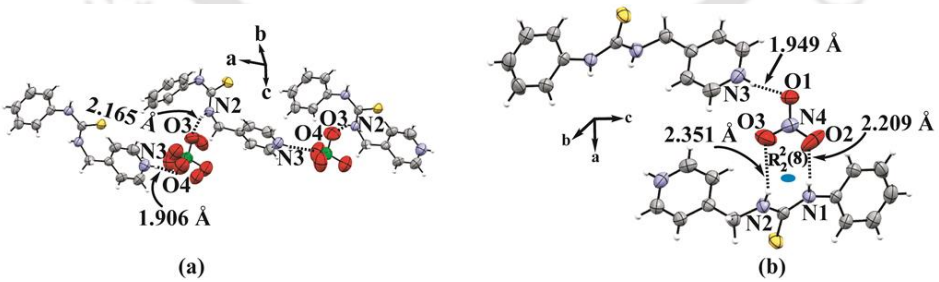

Figure 3.7. Self-assemblies in the salts (a) **3.2a**, (b) **3.2b**

In our present case, the sulphur atoms of each cationic host molecule are projected away from each other, which provided a non-planar geometry to the cations. This non-planar arrangement is possible due to the presence of two -NH groups arranged in an *anti-syn*

manner and a flexible methylene unit in the cationic host. Usually, some of the commonly observed synthons in thiourea derivatives are the *syn-syn* arrangement of -NH groups to form either thiourea α-tape network,[13] or the -NH groups arranged in an *anti-syn* manner form thioamide-thioamide synthon.[14]

It is well known that both urea and thiourea compounds form hydrogen-bonded dimers by providing specific conformation to the receptor or by perpendicular orientations generating a non-planar geometry.[15] The two salts **3.1a** and **3.2a** are derived from a semi-flexible parent compound due to the presence of an intervening methylene group. The torsion angles contributing to the *syn-syn* and *syn-anti* arrangement of the urea and thiourea parts of **3.1a** and **3.2a** are represented in Table 3.2.

Table 3.2. Comparison of torsion angles contributing to the geometries of the parent and protonated form of the urea (**3.1**) and thiourea (**3.2**) derivatives

Torsion	**Torsion angle (°)**			
	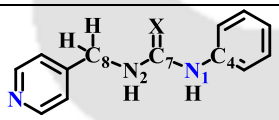		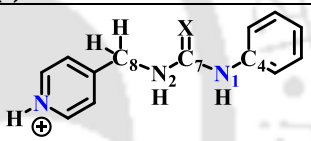	
	(3.1).H$_2$O (X = O1)	**3.2 (X = S1)**	**3.1a (X = O1)**	**3.2a (X = S1)**
C8-N2-C7-S1/O1	5.1(6)	4.5(3)	-13.7(5)	-10.6(6)
C8-N2-C7-N1	-174.0(4)	-177.6(2)	166.8(3)	171.0 (4)
C4-N1-C7-S1/O1	0.5(6)	-176.9(2)	-2.5(5)	175.8 (3)
C4-N1-C7-N2	179.6(4)	5.2(3)	177.0(3)	-5.7 (6)

3.3.3. Nitrate salt of compound 3.2

The nitrate salt **3.2b** crystallized in monoclinic $P2_1/c$ space group. It consisted of a cationic host and a nitrate anion. The thiourea part has a *syn-syn* orientation due to the complementary hydrogen bonding of this part with the nitrate anion [N1–H···O2 {$d_{D\cdots A}$ = 3.052(3) Å}, N2–H···O3 {$d_{D\cdots A}$ = 3.000(3) Å}], forming a hydrogen-bonded $R^2_2(8)$ synthon consisting of two hydrogen bonds, (Fig. 3.7b). The third oxygen atom (O1) is hydrogen bonded to the H-N$^+$ unit ($d_{D\cdots A}$ = 1.949 Å) of the pyridinium fragment of a neighbouring molecule as illustrated in Fig. 3.7b. This provided a planar arrangement to both cation and anion, thereby contributing to the self-assembly of the cationic hosts. Thus, nitrate anion acted as a bridge between two cations. The sulphur atoms of these two bridged cations are projected in an

opposite direction. The salt **3.2a** is arranged as discrete units due to the complementary hydrogen bonds and flexible methylene units.

3.3.4. Perchlorate salt of compound 3.3

The perchlorate salt **3.3a** crystallized in a monoclinic $P2_1/c$ space group, having one cation, a perchlorate anion, and a molecule of water of crystallization. The water molecule acted as a bridge between the two cations through hydrogen bonding with the carbonyl oxygen atom and pyridinium H-N^+ unit of two cations (Fig.3.8a). The alternate cations adopted head-to-tail orientations, forming bifurcated hydrogen bonds projecting in one direction. Due to these bifurcated hydrogen bonds, the parallel alignment of the cationic host molecules led to $\pi\cdots\pi$ stacking interaction between the pyridinium and naphthalene fragments (Fig. 3.8b). The perchlorate ions are not involved in hydrogen bonds and were surrounded by hydrated cations.

3.3.5. Nitrate salt of compound 3.3

The nitrate salt **3.3b** crystallized in the orthorhombic *Pbca* space group, having a host cation and nitrate ion in the asymmetric unit. The urea part has a *syn-syn* orientation. An $R^2_2(8)$ hydrogen-bonded synthon is formed due to the hydrogen bonding of nitrate ion with the urea part of the cation. Each of the two cations assembled through intermolecular hydrogen bonding between the carbonyl oxygen atom and pyridinium cation (Fig. 3.8c).

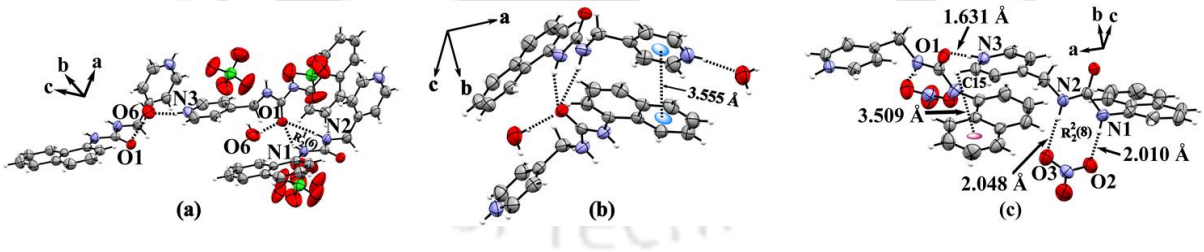

Figure 3.8. Self-assemblies in the salts (a) and (b) **3.3a**, (c) **3.3b**

3.3.6. Perchlorate salt of compound 3.4

The asymmetric unit of the perchlorate salt **3.4a** consisted of a cationic host and a disordered nitrate ion. It crystallized in the orthorhombic Pbca space group, with a *syn-anti* arrangement of the thiourea part. The perchlorate ion formed hydrogen bonds with the pyridinium cation and -NH group adjacent to the methylene unit. The two cationic hosts are held together by the

sulphur atom of the thiourea part through hydrogen bonding with the -NH group next to the naphthyl unit [N(1) -H(1)···S(1), $d_{D\cdots A}$ = 3.264 (3) Å] (Fig. 3.9).

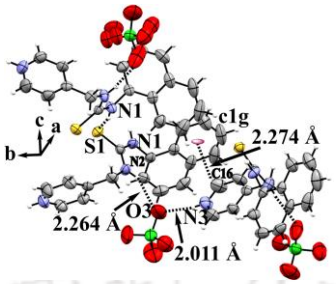

Figure 3.9. Self-assemblies in the salts **3.4a**

The difference in the torsion angles of the salts **3.3a** and **3.3b** is due to the presence of tetrahedral (perchlorate) and planar (nitrate) anions in the salts (Table 3.3). The torsion angles of the perchlorate salts, namely **3.3a** and **3.4a,** were different due to the presence of C=O and C=S bonds, respectively, and the syn-syn and syn-anti orientations of the urea (or thiourea part) also contributed to the difference in their torsion angles (Table 3.3).

Table 3.3. Comparison of torsion angles contributing to the geometries of parent compounds and the salts **3.3a**, **3.3b**, and **3.4a**

Torsion	**Torsion angle (°)**				
	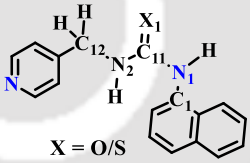 X = O/S		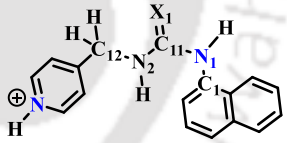 X = O/S		
	(3.3).H₂O (X = O)	**3.4 (X = S)**	**3.3a (X = O)**	**3.4a (X = S)**	**3.3b (X = O)**
C12–N2–C11–S1/O1	11(1)	3.4(3)	1.7(4)	6.9(4)	3.1(5)
C12–N2–C11–N1	-167.4(7)	-176.6(2)	−177.7(3)	−173.7(3)	−177.1(3)
C1–N1–C11–S1/O1	-1(1)	-172.8(2)	−172.1 (2)	1.9(4)	−1.8(5)

3.4. Spectroscopic characterization of the salts of 3.1-3.4

3.4.1. ^{1}H-NMR spectroscopy

To check the shift in the -NH peaks of the urea and thiourea parts due to their self-assembly with the anions in the respective salts, we recorded their ^{1}H-NMR spectra. In all the salts, we observed an upfield shift of the two -NH protons. Initially, in compound **3.1**, the two characteristic -NH peaks, which appeared at 8.69 ppm and 6.73-6.71 ppm, were shifted to

8.92 ppm and 6.93-6.90 ppm, respectively, in its perchlorate salt **3.1a** (Fig. A3.3a). Thus, an upfield chemical shift was observed in this salt due to the presence of an electronegative perchlorate anion. Similarly, the -NH peaks of compound **3.2** (appeared at 9.77 ppm and 7.16-7.13 ppm) showed an upfield shift to 10.02 ppm, 7.20-7.17 ppm in **3.2a**, and 10.02 ppm and 7.19-7.16 ppm in **3.2b** (Figs. A3.3b and A3.3c). For the perchlorate and nitrate salts of compound **3.3**, the -NH peaks appeared at 8.81 ppm, 7.31-7.29 ppm, and 8.91 ppm, 7.43-7.33 ppm, respectively (Figs. A3.3d and A3.3e). In **3.4**, the -NH peaks appeared at 9.90 ppm and 7.51-7.49 ppm respectively. These peaks were shifted towards the upfield region at 10.14 ppm and 8.11 ppm, respectively, in its perchlorate salt **3.4a** (Fig. A3.3f).

3.4.2. Powder X-ray diffraction

The phase purity of the respective salts was analyzed by recording their powder X-ray pattern and comparing it with the simulated X-ray patterns generated from the CIF files by MERCURY software[8] (Fig. A3.4). The comparison of the Miller indices showed the presence of a single phase.

3.4.3. FTIR spectra

The IR spectra of the respective salts were compared with their parent compounds (Table 3.4). In the case of urea compounds **(3.1)·H_2O**, **(3.3)·H_2O** and their salts, the C=O stretch appeared in the range of 1619-1675 cm^{-1}. On the other hand, for their thiourea counterparts, namely, **3.2**, **3.4** and their salts, the C=S stretch was between 1199-1202 cm^{-1}. This is obvious due to the weaker strength of the C=S bond than the C=O bond. Additionally, the absorption bands of the C=S bonds were less intense than that of the C=O bond (Fig. 3.10) because of the lesser polarity of the former compared to the latter. In **(3.1)·H_2O**, the N-H stretching and bending peaks appeared at 3323 cm^{-1} and 1599 cm^{-1}, which were shifted to 3385 cm^{-1} and 1595 cm^{-1}, respectively, in its perchlorate salt **3.1a**. The formation of this salt **3.1a** was also confirmed from the bands at 891 and 1071 due to the Skeletal motion of the cation host and perchlorate ion, respectively (Fig. 3.10a). The N-H stretch and bend peaks at 3154 cm^{-1} and 1595 cm^{-1} in **3.2**, appeared at 3345 cm^{-1}, 1590 cm^{-1}, and 3305 cm^{-1}, 1625 cm^{-1}, in the salts **3.2a** and **3.2b**, respectively. The characteristic bands corresponding to perchlorate and nitrate ions appeared at 1065 cm^{-1} and 1344 cm^{-1} in **3.2a** and **3.2b,** respectively (Fig. 3.10b). In compound **(3.3)·H_2O**, the O-H stretch of the water molecule of crystallization appeared at

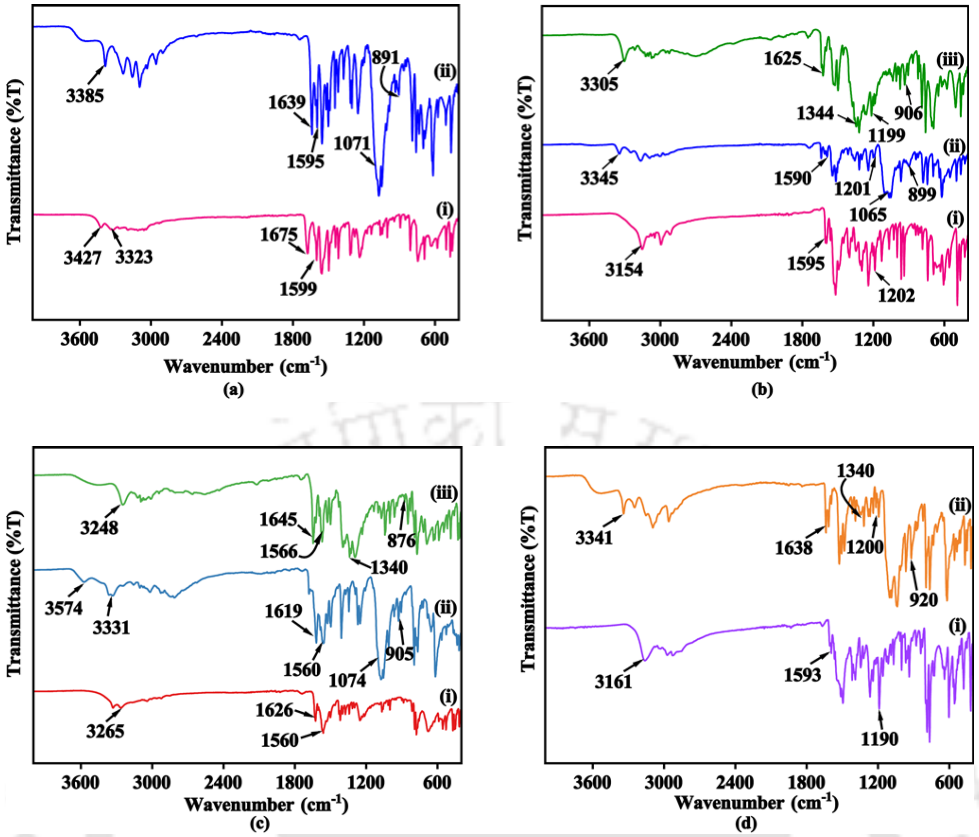

Figure 3.10. FTIR (ATR) spectra of (a) (i) **(3.1)·H₂O** , (ii) **3.1a**, (b) (i) **3.2**, (ii) **3.2a**, (iii) **3.2b**, (c) (i) **(3.3)·H₂O**, (ii) **3.3a**, (iii) **3.3b**, and (c) (i) **3.4**, (ii) **3.4a**

Table 3.4. Stretching frequencies observed in compounds **3.1-3.4** and their salts

Compound	Stretching frequency (cm^{-1}) (appearance)								
	O-H stretch (H_2O)	N-H stretch	C=X stretch (X = O or, S)	N-H bend	C-N stretch (between carbonyl C and N of N-H group)	C-N stretch (between aromatic C and N of N-H group)	C=N stretch (in pyridyl ring)	Skeletal motion of cation	oxidant group ClO_4^- or NO_3^- ion
(3.1)·H₂O	3427(m)	3323(m)	1675(s)	1599(s)	1555(s)	1497(s)	1316(s)	-	-
3.1a	-	3385(m)	1639(s)	1595(s)	1553(s)	1488(s)	1314(s)	891(w)	1071(s)
3.2	-	3154(m)	1202(s)	1595(s)	1563(w)	1493(m)	1297(s)	-	-
3.2a	-	3345(m)	1201(m)	1590(m)	1547(s)	1516(s)	1319(s)	899(m)	1065(s)
3.2b	-	3305(m)	1199(m)	1625(s)	1525(s)	1498(s)	1320(s)	906(m)	1344(s)
(3.3)·H₂O	3331(m)	3265(m)	1626(s)	1560(s)	1501(w)	1418(s)	1316(m)	-	-
3.3a	3574(m)	3331(m)	1619(s)	1560(s)	1497(w)	1409(s)	1345(s)	905(m)	1074(s)
3.3b	-	3248(m)	1645(m)	1566(s)	1526(s)	1500(s)	1396(s)	876(m)	1340(s)
3.4	-	3161(m)	1190(s)	1593(w)	1513(w)	1495(m)	1267(s)	-	-
3.4a	-	3341(m)	1200(s)	1638(s)	1526(s)	1506(s)	1390(s)	920(m)	1340(m)

3331 cm^{-1}, N-H stretch and bend at 3265 cm^{-1} and 1560 cm^{-1} (Fig. 3.10c.i). In its perchlorate salt **3.3a**, the O-H stretch of the water molecule of crystallization appeared at 3574 cm^{-1}. The

N-H stretch and bending, perchlorate ion skeletal motion peaks appeared at 3331 cm^{-1}, 1560 cm^{-1}, and 1074 cm^{-1} respectively (Fig. 3.10c.ii). In its nitrate counterpart, **3.3b**, 3248 cm^{-1} (N-H stretch), 1566 cm^{-1} (N-H bend), and 1340 cm^{-1} (NO_3^- ion skeletal motion) were observed. Similarly, the N-H stretch and bending of **3.4** were shifted from 3161 cm^{-1}, 1593 cm^{-1} to 3341 cm^{-1}, 1638 cm^{-1}, respectively in **3.4a**.

3.5. Thermogravimetric analysis of hydrated compounds and their salts

The thermogravimetry of the hydrated compounds **(3.1)·H_2O**, **(3.3)·H_2O** and the perchlorate salt **3.3a** were studied to determine their dehydration and thermal stability. The water molecule of crystallization is hydrogen-bonded to both carbonyl O1 ($d_{H\cdots A}$ = 1.95 (5) Å) and pyridyl N3 ($d_{H\cdots A}$ = 1.91 (7) Å) atoms of compound **3.1** (Table 3.1). It is obvious that with higher hydrogen bond strength, additional heat energy is required to separate them.[16] Thus, a total weight loss of 7.88% (calculated 7.34%) was observed (Fig. 3.11a) at two different temperature ranges, 61 °C to 90 °C (weight loss of 5%) (corresponding to $d_{H\cdots A}$ = 1.95 (5) Å)

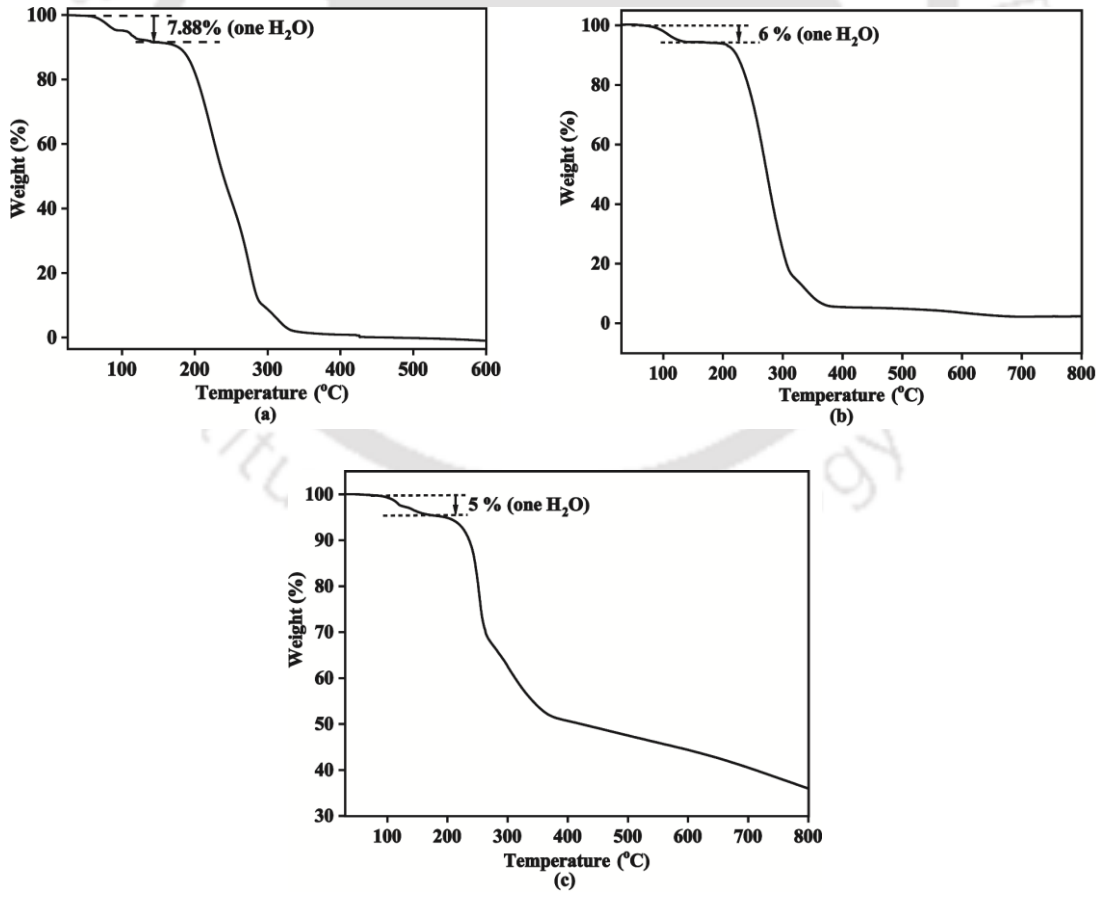

Figure 3.11. Thermogram of (a) **(3.1)·H_2O**, (b) **(3.3)·H_2O**, and (c) **3.3a**

and second from 90 °C to 121 °C (weight loss of 2.88%) (corresponding to $d_{H\cdots A}$ = 1.91 (7) Å). This weight loss was due to the loss of a water molecule of crystallization. In **(3.3)·H_2O**, a weight loss of 6% in the temperature range of 86 °C to 125 °C (Fig. 3.11b) corresponding to dehydration was observed. This weight loss corresponds to the loss of one molecule of water of crystallization (calculated 6.10%). The perchlorate salt **3.3a** was also obtained as a monohydrate. This one water molecule of crystallization was lost at two different temperature ranges, 84 °C to 121 °C (2% weight loss) and 121 °C to 160 °C (3% weight loss). Thus, a two-step weight loss of 5% (calculated 4.55%) was observed (Fig. 3.11c). The two-step weight loss of the water molecule was due to its different hydrogen bond strength with pyridinium N3 ($d_{H\cdots A}$ = 1.89 Å) and carbonyl O1 ($d_{H\cdots A}$ = 2.04 Å) atoms of the cationic part of **3.3a** (Table A3.2). The weaker hydrogen bond O(6) -H(6A) ···O(1) ($d_{H\cdots A}$ = 2.04 Å) was lost first (from 84 °C to 121 °C) followed by the stronger hydrogen bond N(3) -H(3) ···O(6) ($d_{H\cdots A}$ = 1.89 Å) from 121 °C to 160 °C.

3.6. Absorbance and photoluminescence studies of 3.1-3.4 and their salts

Both absorbance and photoluminescence spectra of the solid samples of compounds **3.1-3.4** were studied.

3.6.1. Absorbance spectral study

The solid samples of the compound **(3.1)·H_2O**, **3.2**, **(3.3)·H_2O**, and **3.4** showed absorbance at 291 nm, 295 nm, 306 nm, and 306 nm, respectively, due to n-π^* transition (Figs. A3.5a.i, A3.6a.i, 3.12a.i, A3.7a.i). An absorbance at 309 nm was observed for the solid sample of the perchlorate salt **3.1a**, corresponding to the n-π^* transition (Fig. A3.5a.ii). Stabilization of the non-bonding electrons by hydrogen bond caused a bathochromic shift of 18 nm in **3.1a** compared to the parent compound **3.1**. Both the salts of **3.2**, namely **3.2a** and **3.2b**, showed the same absorbance at 307 nm due to n-π^* transition (Fig. A3.6a.ii). Similarly, the naphthyl urea-based salts **3.3a** and **3.3b** showed absorbance of 385 nm and 335 nm, respectively, due to n-π^* transition (Fig. 3.12a.ii). The perchlorate salt **3.4a** showed two absorptions, one at 312 nm due to n-π^* transition and the second at 353 nm, which corresponded to the vibronic signal (Fig. A3.7a.ii).

3.6.2. Photoluminescence spectral study

Upon excitation at 330 nm, the solid sample of **(3.1)·H_2O** showed a broad emission at 473 nm, and the perchlorate salt **3.1a** showed a broad emission at 440 nm (λ_{ex} = 309 nm) due to aggregation-induced emission (Fig. A3.5b). The HOMO-LUMO gap of the **(3.1)·H_2O** (Fig. A3.8a) was 5.395 eV (229 nm), which was very large for electronic excitation in the UV-visible region. In its perchlorate salt **3.1a**, HOMO was localized on the urea part and phenyl ring of the cationic host, whereas the LUMO was localized from the urea part to the pyridinium unit of the host. The gap was 2.198 eV (564 nm) (Fig. A3.8b). Similarly, upon excitation at 295 nm, **3.2** showed emission at 530 nm due to aggregation-induced emission (Fig. A3.6b.i). Both perchlorate and nitrate salts **3.2a** and **3.2b** showed negligible emissions (Figs. A3.6b.ii and A3.6b.iii). The HOMO-LUMO gap for **3.2** was 4.66 eV (266 nm). Thus, aggregation-induced emission occurred because the S_1-S_0 emission of **3.2** did not match this gap. In the case of the cationic hosts in **3.2a** and **3.2b**, the gaps were 2.781 eV (446 nm) and 2.64 eV (470 nm), respectively (Fig. A3.9). The solid samples of **3.4** and **3.4a** showed emissions at 468 nm and 456 nm, respectively (Fig. A3.7b). The S_1 to S_0 emissions in both these compounds did not match the respective gaps. Based on long wavelength emission with respect to the excitation wavelength, these are attributed to aggregation-induced emissions.

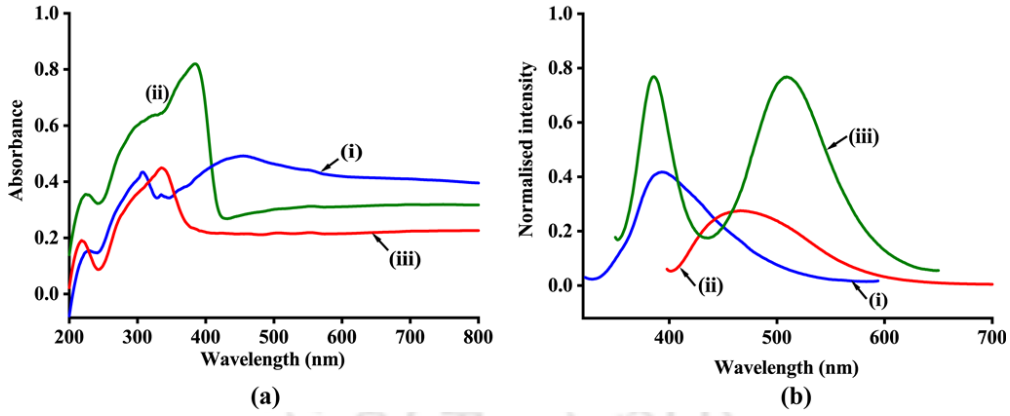

Figure 3.12. (a) absorbance and (b) photoluminescence spectra of the solid samples of (i) **(3.3)·H_2O** (λ_{abs} = 306 nm, λ_{ex} = 307 nm, λ_{em} = 393 nm), (ii) **3.3a** (λ_{abs} = 385 nm, λ_{ex} = 383 nm, λ_{em} = 471 nm), and (iii) **3.3b** (λ_{abs} = 335 nm, λ_{ex} = 335 nm, λ_{em} = 386 nm, 509 nm)

The broad peaks were observed, the shape of the emissions was different, and also vibrational features were observed. Despite the non-emissive nature of compounds **(3.1)·H_2O**, **3.2**, and the salt **3.1a**, the emission occurring in the same region but with a difference in shape and intensity suggested it has a contribution from aggregation-induced emission enhancement.[17]

As hydrogen-bonded self-assemblies were present in both **(3.1)·H_2O**, **3.2**, **3.4** and their respective salts, they were in an aggregated state.

Upon excitation at 307 nm, the solid sample of **(3.3)·H_2O** showed an emission at 393 nm. The perchlorate salt **3.3a** showed emission at 471 nm (λ_{ex} = 383 nm). The nitrate salt **3.3b** showed dual emission at 386 nm, and 509 nm (λ_{ex} = 335 nm) (Fig. 3.12b). The first emission was due to a locally excited (LE) state, and the second emission corresponded to twisted intramolecular charge (TICT) transfer (Fig. 3.13). The dual emission due to locally excited

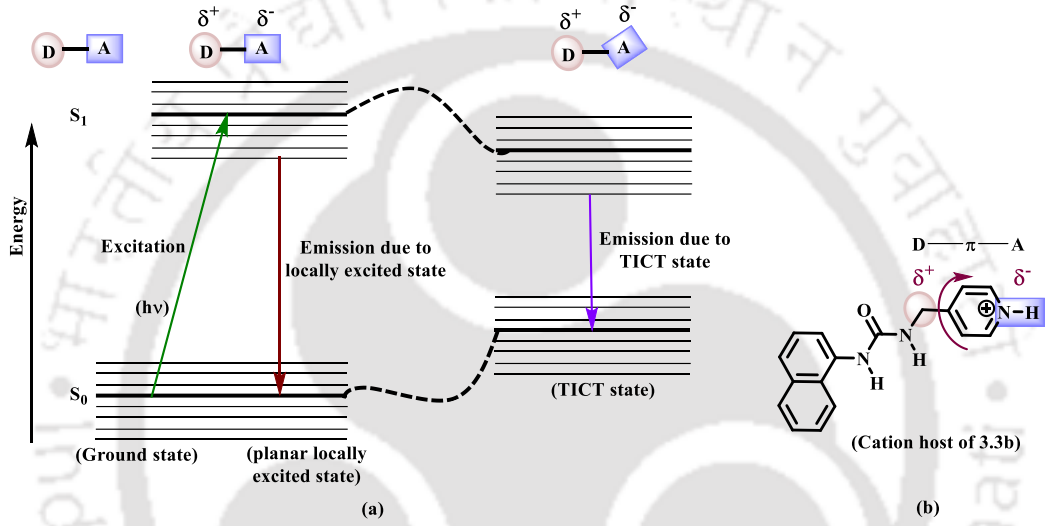

Figure 3.13. (a) Twisted intramolecular charge transfer (TICT) model, (b) plausible twisting in the cationic host of **3.3b**

and TICT states are usually observed in solution. However, such an effect in the solid state is rare and occurs because of concentration quenching and structural restriction.[18] It is reported in the literature that both hydrated and anhydrous forms of amide derivatives showed single or dual emission due to the geometrical changes that influenced the delocalization in the compounds.[19] Naphthyl urea compounds are well known to show dual emission with a significant Stoke's shift, and the emission occurred due to the presence of neutral and hydrogen-bonded species in the solution.[20] So, we compared the hydrogen bonding patterns in the monohydrate of the parent compound **3.3** and its salts **3.3a** and **3.3b** to understand their effect on the photoluminescence behaviour. In **(3.3)·H_2O**, the urea molecules were held together by bifurcated N-H···O hydrogen bonds forming a urea α-tape $R^1_2(6)$ synthon remaining in one plane (Fig. 3.14a). In the perchlorate salt **3.3a**, the perchlorate anions remained in the interstices. The cationic host molecules formed bifurcated hydrogen bonds,

and the molecules were in different planes, causing an oblique orientations among the urea units of the cations (Fig. 3.14b). This packing difference in **3.3a** (compared to the starting compound) caused aggregation-induce emission, resulting in a red shift to 471 nm. In the nitrate salt **3.3b**, bifurcated hydrogen bonds were absent, and the urea part of the cations was hydrogen-bonded with the nitrate ions forming urea-nitrate $R^2_2(8)$ synthon. Thus,

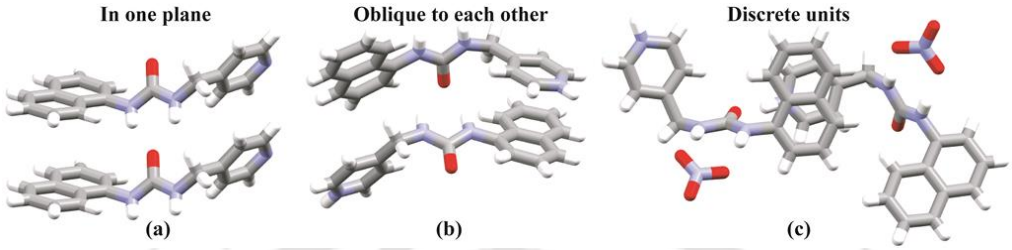

Figure 3.14. Planar arrangements of neighbours of (a) **(3.3)·H$_2$O** (water molecules omitted), (b) oblique orientations of hydrogen-bonded cations of **3.3a** (anions omitted), and (c) two cations of **3.3b** in the closest proximity in the self-assembly of the nitrate salt

the cations were present as discrete units (Fig. 3.14c). The carbonyl oxygen atom of the cation was hydrogen-bonded to the pyridinium N^+-H unit [$d_{D\cdots A}$ = 2.663(4) Å]. Thus, both **(3.3)·H$_2$O** and **3.3a** consisted of urea tapes and showed single emission (Figs. 3.12b.i, 3.12.b.ii). On the other hand, the nitrate salt **3.3b** loosed the weakest N-H bond in the excited state, which caused an accumulation of a higher electron density on the nitrogen atom of the N-H bond adjacent to the naphthyl group. Thus, the breaking of the weakest hydrogen bond of the -NH group created a more negative character on the nitrogen atom next to the naphthalene ring. This caused a delocalization over naphthalene, creating degenerate states leading to a dual emission. It is reported in the literature that the solid compounds show dual emission due to domain change[21] and the presence of symmetry non-equivalent molecules in a unit cell. In our present case, degenerate states formed due to hydrogen bonds that may be mixing in the excited state.

3.7. Stability of the salts of 3.3 in water

In the aqueous solution, compound **3.3** showed an emission at 385 nm (λ_{ex} = 258 nm). As **3.3** was soluble in water, it enabled us to examine the changes in its emission spectrum upon the addition of perchloric acid. Quenching in emission was observed with the subsequent

addition of the perchloric acid due to the protonation of the pyridine, resulting in the reorganization of intermolecular hydrogen bonds (Fig. 3.15a). So, we initially attempted to distinguish arsenite (As^{3+}) and sodium arsenate (As^{5+}) salts by emission spectroscopy through possible interactions with **3.3**. Fluorescence emission titration of an aqueous solution of **3.3** with sodium arsenite (As^{3+}) and sodium arsenate (As^{5+}) salts showed fluorescence enhancement at 385 nm in an identical manner (Fig. 3.15b.i and 3.15c.ii), but relative changes were different. So, another set of experiments was carried out with hydroxide ions, and a similar trend was observed, but the relative increase in intensity was higher. This occurred because of the basic nature of the sodium salts, which was confirmed by comparing this effect with that in the case of arsenite and arsenate salts (Fig. 3.15b.iii). From these results, it was felt that the acid-base properties of **3.3** can be utilized for studying the release of the compound if it is prepared as a composite.

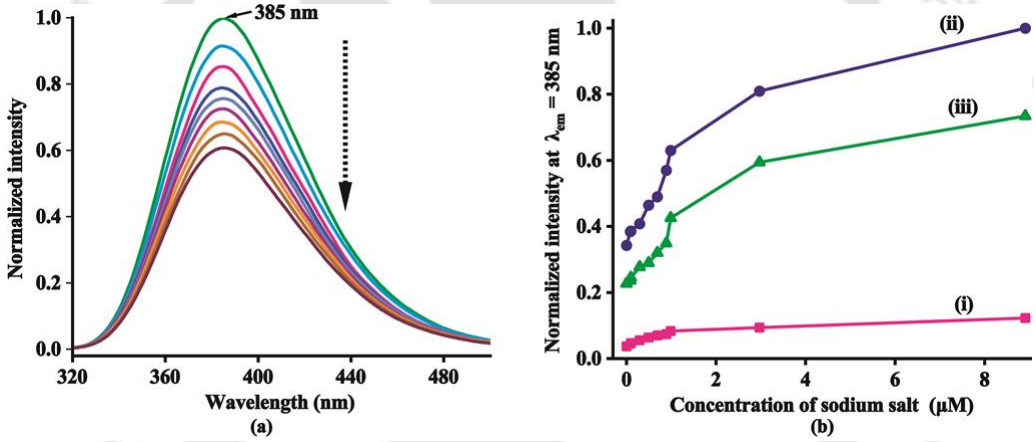

Figure 3.15. (a) Changes in the photoluminescence spectrum of **3.3** (1mM) (λ_{ex} = 258 nm, λ_{em} = 385 nm) by titrating with perchloric acid (15mM, 10 μL per aliquot); (b) intensity versus concentration plot of titration of aqueous solution of **3.3a** (10μM) with 10 μL aliquots of the sodium salts of (i) As^{3+} (10μM), (ii) As^{5+} (10μM), and (iii) NaOH (10μM)

As the basic nature of the sodium salts was able to break the perchlorate salt **3.3a** and released compound **3.3** in the aqueous solution, we prepared composite pellets of **3.3**, **3.3a**, and **3.3b** with calcium oxide in different molar ratios, such as 1:1, 2:1, 3:1, and 4:1, keeping a constant mole of calcium oxide and only varying the moles of **3.3** and its salts respectively. The composites were prepared by blending **3.3** and its salts **3.3a** and **3.3b** with calcium oxide by grinding and pressing under a hydraulic pellet press. The pellets were characterized by powder X-ray diffraction studies and comparing them with the powder X-ray patterns of the

compound, salts, and calcium oxide (Fig. A3.12). Calcium oxide-based compounds are biofriendly, and in water, calcium oxide transforms into calcium hydroxide.[22]

The respective composite pellets were suspended in aqueous solution, and emission spectra were recorded in different time intervals (Figs. 3.16a-3.16c), showing an emission at 385 nm (λ_{ex} = 258 nm). Thus, in the presence of water, calcium oxide was transformed to calcium hydroxide, which helped in the release of substrate in a neutral form **3.3**, as was observed in the emission spectra. A controlled release is supported by pH and chemical reactivity.[23,24] The breaking of the salts **3.3a** and **3.3b** was possible because calcium oxide helped in an easy diffusion of the urea compound **3.3** into the aqueous medium in a controlled manner.

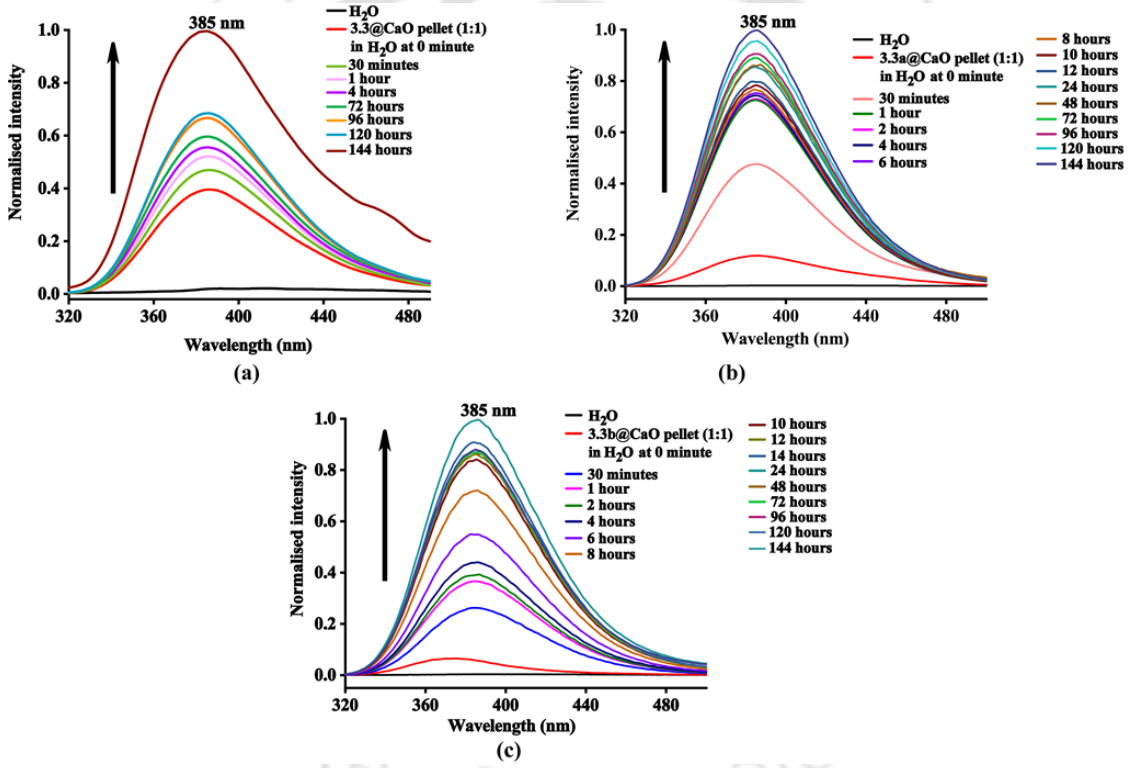

Figure 3.16. Changes in the photoluminescence spectra due to the release of **3.3** from the composites (a) **3.3@CaO** (1:1), (b) **3.3a@CaO** (1:1), and (c) **3.3b@CaO** (1:1)

While performing a comparative study on the release of **3.3** from the composites of different molar ratios, we found that in the case of **3.3a@CaO** composite, the trend for the release was 1:1 < 2:1 ~ 3:1 < 4:1 (Fig. 3.17b). Thus, for this salt, the composite with a 4:1 molar ratio showed the highest release of **3.3**. This implied that a small amount of calcium oxide was sufficient for breaking the perchlorate salt **3.3a** and releasing **3.3**. However, **3.3@CaO** and

3.3b@CaO, the relative release followed the trend 1:1 < 4:1 < 3:1 < 2:1 (Figs. 3.17a, 3.17c). So, a higher amount of calcium oxide was required for the composites having less ionic form **3.3** and tightly intramolecularly hydrogen-bonded nitrate salt **3.3b**. On comparing the release of compound **3.3** from the 1:1 composites of **3.3**, **3.3a**, and **3.3b** with calcium oxide, the perchlorate salt **3.3a** released **3.3** with ease compared to that from the composites of **3.3** and nitrate salt **3.3b** (Fig. 3.17d).

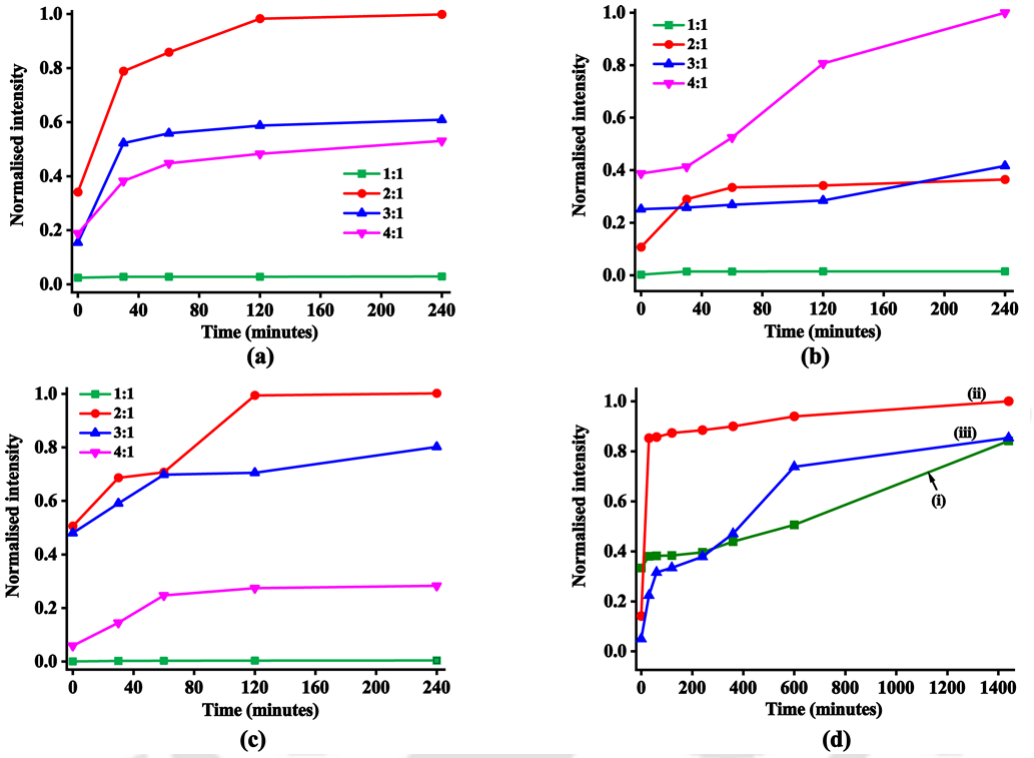

Figure 3.17. Intensity versus time plot of pellets (a) **3.3@CaO**, (b) **3.3a@CaO**, and (c) **3.3b@CaO**, (d) comparison of 1:1 pellets of (i) **3.3@CaO**, (ii) **3.3a@CaO**, and (iii) **3.3b@CaO** in water (λ_{ex} = 258 nm, λ_{em} = 385 nm)

3.8. Conclusions

Analysis of different assemblies revealed different synthons in the compounds **3.1-3.4** and their salts (Fig. 3.18). The geometries of the urea and thiourea parts of the compounds in different assemblies varied. In compound **(3.1)·H$_2$O**, the water of crystallization acted as a bridge between two molecules of **3.1**. and prevented the formation of α-urea tape synthons by participating in the hydrogen bonds with the two -NH groups and $N_{pyridyl}$ atom, adopting a puckered geometry of the hydrated compound. In its perchlorate salt **3.1a**, the perchlorate

ions hydrogen bonded with the protonated pyridinium fragment and the cationic host molecules were connected through an α-urea tape network synthon (Fig. 3.18c). **(3.1)·H₂O**

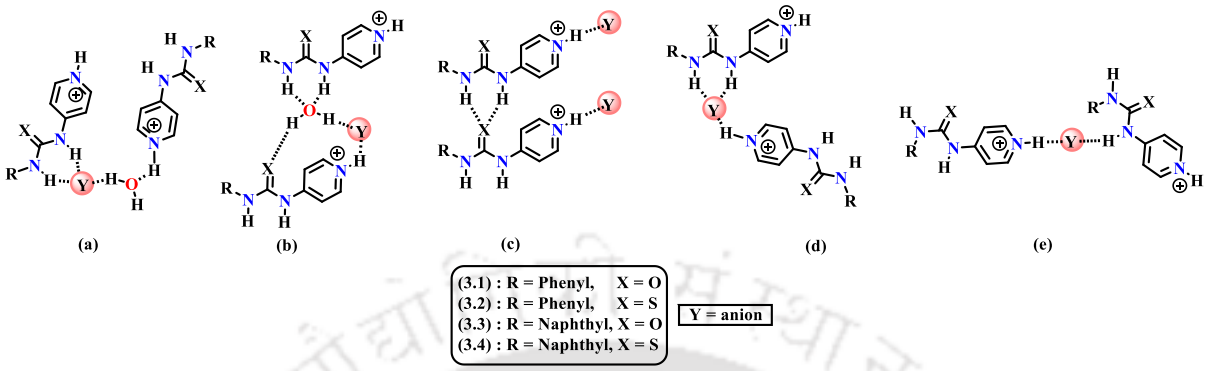

Figure 3.18. Different hydrogen-bonded synthons found in n phenyl (or naphthyl) tethered pyridyl urea (or thiourea) derivatives with oxyanions

and its **3.1a** salt have a *syn-syn* orientation of the urea part. On the other hand, the thiourea counterpart, **3.2**, has a *syn-anti* orientation of the urea part. In the perchlorate and nitrate salts of **3.2**, perchlorate anions provided *syn-anti* orientation (in **3.2a**), whereas nitrate anions provided *syn-syn* orientation (in **3.2b**) to the cations of **3.2**. This proved that recognition of two anions is possible by the cationic host **3.2**. The perchlorate ion in **3.2a** acted as a bridge between two cationic host molecules, resulting in a one-dimensional hydrogen-bonded chain-like arrangement. The non-planar arrangement is possible in **3.2a** because of the presence of two -NH groups arranged in an *anti-syn* manner and a flexible methylene unit in the cationic host. In the case of **(3.3)·H₂O** and its salts **3.3a** and **3.3b**, the urea part has a *syn-syn* orientation. The self-assembly of **(3.3)·H₂O** is much different from the hydrated form of its phenyl counterpart, **(3.1)·H₂O**, such that **(3.3)·H₂O** has an intermolecular hydrogen-bonded urea α-tape $R^1_2(6)$ synthon forming a parallel alignment of the naphthyl units. The parent molecules in **(3.3)·H₂O** are held together by solvated water through intermolecular hydrogen bonds formed between the pyridyl nitrogen atom. This kind of hydrogen bond resulted in the formation of a chain-like arrangement. As a consequence of the stacking arrangement among the naphthalene rings, there is a large difference in the packing patterns of **(3.1)·H₂O** and **(3.3)·H₂O**. The urea tapes are observed in the latter case, whereas not in the former case. Secondly, the ^{1}H-NMR spectroscopic studies of the salts of **3.1**-**3.4** showed a significant downfield shift of the -NH and pyridyl protons compared to the respective parent compounds. Thirdly, upon excitation at 335 nm, the solid sample of the nitrate salt **3.3b** showed dual emission at 386 nm and 509 nm due to a locally excited (LE) state and twisted intramolecular

charge (TICT) transfer. Such an observation in the solid state is rare because of concentration quenching and structural restriction. In in the time-dependent study on the calcium oxide composites of **3.3** and its nitrate salt **3.3b**, the relative rate of release followed the trend 1:1 < 4:1 < 3:1 < 2:1, whereas the perchlorate salt composite **3.3a@CaO** showed relative rates of release as 1:1 < 2:1 ~ 3:1 < 4:1. The relative release of **3.3** from the respective composites with calcium oxide showed that composite of the salts, namely, **3.3a@CaO** and **3.3b@CaO** can release **3.3** easily as compared to **3.3@CaO**. The composite **3.3a@CaO** released **3.3** easily compared to its nitrate salt composite **3.3b@CaO**. The salts of **3.3** released their anions upon treatment with calcium oxide at different proportions, indicating that a small amount of calcium oxide efficiently released the parent compound with high efficiency, but having the salts trapped in a larger amount of calcium oxide provided higher stability to composites.

3.9. Experimental section

The detailed synthetic methodologies for the synthesis of the metal complexes are described. Analytical data are provided with each compound. The instrumental details and crystallographic parameters are provided in the Appendix section at the end of this chapter. The following abbreviations are used for the identification of spin multiplicities in 1H-NMR spectra: s = singlet, d = doublet, t = triplet, q = quartet, m = multiplet; and for FTIR spectra, the following abbreviations were used to identify the absorption bands: s = strong, w = weak, br = broad, m = medium.

Synthesis of 1-phenyl-3-(pyridin-4-ylmethyl) urea (3.1): Phenyl isocyanate (108 µL, 1 mmol) was dissolved in diethyl ether (15 mL). To this solution, 4-aminomethylpyridine (102 µL, 1 mmol) was added dropwise and stirred at room temperature overnight. A white precipitate was formed, which was filtered and dried. Yield: 90%. ESI MS: calculated [M+1] $C_{13}H_{13}N_3O$, 228.1092; found, 228.1194 [M+1]. The white precipitate was dissolved in a methanol-water mixture (10 mL, v/v) and the solution was allowed to evaporate at 25 ºC, yielding colourless crystals of **(3.1)·H$_2$O**. ^{1}H NMR (DMSO-d$_6$, 600 MHz): 8.69 (s, 1H), 8.50 (d, J = 6 Hz, 1H), 7.40 (d, J = 6 Hz, 1H), 7.29 (d, J = 6 Hz, 1H), 7.23 (t, J = 6 Hz, 1H), 6.91 (m, J = 6 Hz, 1H), 6.73 (t, J = 6 Hz, 1H), 4.33 (d, J = 6 Hz, 2H). IR (cm^{-1}): 1675 (s), 1599 (s), 1555 (s), 1497 (s), 1440 (s), 1415 (s), 1316 (s), 1236 (m), 808 (s), 744 (m), 688 (s), 631 (w), 579 (s), 471 (s), 454 (s). UV, solid (λ_{max}): 291 nm.

Synthesis of 1-phenyl-3-(pyridin-4-ylmethyl) thiourea (3.2): Compound **3.2** was prepared by following a procedure similar to the synthesis of **3.1**, but phenyl isothiocyanate (119 μL, 1 mmol) was used in place of phenyl isocyanate. A white precipitate was formed, filtered, and dried. Yield: 98%. ESI MS: calculated [M+1] $C_{13}H_{13}N_3S$, 244.0684; found, 244.0660 [M+1]. The white precipitate was dissolved in methanol–acetone (10 mL, 1:1 v/v) and the solution was allowed to evaporate slowly at room temperature. Off-white block crystals of **3.2** were formed after two days. ^{1}H NMR (DMSO-d_6, 500 MHz): 9.77 (s, 1H), 8.50 (d, J = 5.5 Hz, 2H), 8.23 (s, 1H), 7.42 (d, J = 7.5 Hz, 2H), 7.36 (d, J = 7.5 Hz, 2H), 7.29 (d, J = 5.5 Hz, 2H), 7.16 (t, J = 7.5 Hz, 1H), 4.77 (d, J = 5.5 Hz, 2H). IR (cm^{-1}): 3154 (m), 1595 (s), 1563 (w), 1493 (m), 1297 (s), 1202 (s). UV, solid (λ_{max}): 295 nm.

Synthesis of 1-(naphthalen-1-yl)-3-(pyridin-4-ylmethyl) urea (3.3): 1-naphthyl isocyanate (144 μL, 1 mmol) and 4-aminomethylpyridine (102 μL, 1 mmol) were dissolved in dichloromethane (15 mL), and the solution was stirred for eight hours at room temperature. A white precipitate of **3.3** was formed, which was filtered and dried. Yield: 89%. ESI MS: calculated [M+1] $C_{17}H_{15}N_3O$, 278.1249; found, 278.0993 [M+1]. Dissolution of white precipitate in a methanol-dimethylformamide solvent mixture (10 mL, 1:1 v/v) yielded rod-shaped yellow crystals of **(3.3)·H$_2$O**. ^{1}H NMR (DMSO-d_6, 500 MHz): 8.72 (s, 1H), 8.53 (d, *J* = 6 Hz, 2H), 8.11 (d, *J* = 8.5 Hz, 1H), 7.95 (d, *J* = 7 Hz, 1H), 7.91 (d, *J* = 7.5 Hz, 1H), 7.60 (m, *J* = 8.5Hz, 1H), 7.56 (m, *J* = 7 Hz, 1H), 7.54 (t, *J* = 7 Hz, 1H), 7.44 (t, *J* = 8 Hz, 1H), 7.34 (d, *J* = 5.5 Hz, 2H), 7.14 (t, *J* = 6 Hz, 1H), 4.40 (d, *J* = 6Hz, 2H). IR (cm^{-1}): 3265 (m), 1626 (s), 1560 (s), 1501 (w), 1418 (s), 1316 (m). UV, solid (λ_{max}): 306 nm, 455 nm.

Synthesis of 1-(naphthalen-1-yl)-3-(pyridin-4-ylmethyl) thiourea (3.4): Compound **3.4** was prepared by following a procedure similar to the synthesis of **3.3**, but 1-naphthyl isothiocyanate (185 mg, 1 mmol) was used in place of 1-naphthyl isocyanate. A white precipitate of **3.4** was formed. Yield: 83%. ESI MS: calculated [M+1] $C_{17}H_{15}N_3S$, 294.1020; found, 294.0937 [M+1]. Yellow plate-shaped crystals of **3.4** were formed by dissolving the white precipitate in a methanol-dimethylformamide solution (10 mL, 1:1 v/v). ^{1}H-NMR (DMSO-d_6, 500 MHz): 9.90 (s, 1H), 8.47 (d, *J* = 5 Hz, 2H), 7.99 (d, *J* = 7.5 Hz, 2H), 7.90 (d, *J* = 8.5 Hz, 2H), 7.61-7.57 (m, *J* = 6.5 Hz, 1H), 7.56-7.53 (m, *J* = 7.5 Hz, 2H), 7.51 (d, *J* = 7 Hz, 1H), 7.24 (d, *J* = 3.5 Hz, 2H), 4.72 (d, *J* = 6 Hz, 2H). IR (cm^{-1}): 3161 (m), 1593 (w), 1513 (w), 1495 (m), 1367 (s), 1190 (s). UV, solid (λ_{max}): 306 nm.

Synthesis of salt [(3.1)$H^+ClO_4^-$] (3.1a): Salt **3.3a** was formed by adding a few drops of perchloric acid (60%, 400 µL) to a solution of compound **3.1** (227 mg, 1 mmol) in methanol (10 mL). After the addition of the acid, the solution was stirred for 30 minutes at room temperature and filtered. The filtrate, upon standing under ambient conditions, yielded colourless crystals of **3.1a** after three days. Yield: 97%. ^{1}H NMR (DMSO-d_6, 500 MHz): 8.92 (s, 1H), 8.83 (d, J = 6 Hz, 2H), 7.94 (d, J = 6 Hz, 2H), 7.40 (d, J = 7.5 Hz, 2H), 7.24 (t, J = 7.5 Hz, 2H), 6.93 (m, J = 7.5 Hz, 2H), 4.57 (d, J = 5.5 Hz, 2H). IR (cm^{-1}): 3385 (m), 1639 (s), 1595 (s), 1553 (s), 1488 (s), 1314 (s), 1071 (s), 891 (w). UV, solid (λ_{max}): 309 nm.

Synthesis of salt [(3.2)$H^+ClO_4^-$] (3.2a): Salt **3.2a** was prepared by following a procedure similar to the synthesis of salt **3.1a**. But, compound **3.2** (243 mg, 1 mmol) was used instead of compound **3.1**. After four hours of standing the filtrate at room temperature, colourless rod-shaped crystals of the salt **3.2a** were formed. Yield: 95%. ^{1}H NMR (DMSO-d_6, 500 MHz): 10.00 (s, 1H), 8.80 (s, 2H), 8.33 (s, 1H), 7.89 (d, *J* = 13.5 Hz, 2H), 7.43 (d, *J* = 7.5 Hz, 2H), 7.39 (t, *J* = 7.5 Hz, 2H), 7.20 (t, *J* = 7.5 Hz, 1H), 4.97 (s, 2H). IR (cm^{-1}): 3167 (m), 1590 (s), 1547 (s), 1516 (s), 1319 (s), 1201 (m), 1065 (s), 899 (m). UV, solid (λ_{max}): 307 nm.

Synthesis of salt [(3.2)$H^+NO_3^-$] (3.2b): Salt **3.2b** was prepared by following a procedure similar to the synthesis of salt **3.2a**. But, nitric acid (65%, 400 µL) was used instead of perchloric acid. After 12 hours, needle-shaped yellow crystals of the salt **3.2b** were formed. Yield: 95%. ^{1}H NMR (DMSO-d_6, 500 MHz): 10.02 (s, 1H), 8.83 (d, *J* = 6.5 Hz, 2H), 8.39 (t, *J* = 5 Hz, 1H), 7.91 (d, *J* = 6 Hz, 2H), 7.44 (d, *J* = 7.5 Hz, 2H), 7.39 (t, *J* = 7.5 Hz, 2H), 7.19 (t, *J* = 7.5 Hz, 1H), 4.99 (d, *J* = 5.5 Hz, 2H). IR (cm^{-1}): 3305 (m), 1625 (s), 1525 (s), 1498 (s), 1344 (s),1320 (s),1199 (m), 906 (m). UV, solid (λ_{max}): 307 nm.

Synthesis of salt [(3.3)$H^+ClO_4^-\cdot H_2O$] (3.3a): Compound **3.3** (277 mg, 1 mmol) and perchloric acid (65%, 400 µL) were dissolved in methanol-DMF (10 mL, 1:1 v/v) and stirred for 30 minutes at room temperature. The reaction mixture was filtered and allowed to stand. Block-shaped colourless crystals of **3.3a** were formed after three days. Yield: 91%. ^{1}H NMR (DMSO-d_6, 500 MHz): 8.91 (s, 1H), 8.84 (d, *J* = Hz, 2H), 8.13 (d, *J* = Hz, 1H), 7.96 (d, *J* = Hz, 2H), 7.92-7.88 (m, *J* = Hz, 2H), 7.62-7.53 (m, *J* = Hz, 3H), 7.45 (t, *J* = Hz, 1H), 7.31 (t, *J* = Hz, 1H), 4.64 (d, *J* = Hz, 2H).IR (cm^{-1}): 3331 (m), 1619 (s), 1560 (s), 1497 (w), 1409 (s), 1345 (s), 1074 (s), 905 (m). UV, solid (λ_{max}): 385 nm.

Synthesis of salt [(3.3)$H^+NO_3^-$] (3.3b): Salt **3.3b** was synthesized by following a procedure similar to the synthesis of salt **3.3a**. But nitric acid (65%, 400 μL) was used in place of perchloric acid. The solution was filtered and left undisturbed for crystallization. After five days, colourless plate-shaped crystals of **3.3b** were formed. Yield: 93%.^{1}H NMR (DMSO-d_6, 500 MHz): 8.91 (s, 1H), 8.87 (d, *J* = 5.5 Hz, 2H), 8.14 (d, *J* = 8.5 Hz, 1H), 7.99 (s, 2H), 7.92 (t, *J* = 8.5 Hz, 2H), 7.62-7.52 (m, *J* = 8 Hz, 3H), 7.45 (t, *J* = 8 Hz, 1H), 7.33 (s, 1H), 4.66 (d, *J* = 5.5 Hz, 2H). IR (cm^{-1}): 3248 (m), 1623 (m), 1647 (s), 1526 (s), 1500 (s), 1396 (s), 1340 (s), 876 (m). UV, solid (λ_{max}): 336 nm.

Synthesis of salt [(3.4)$H^+ClO_4^-$] (3.4a): Salt **3.4a** was prepared by dissolving compound **3.4** (293 mg, 1 mmol) and perchloric acid (65%, 400 μL) in methanol-acetone (10 mL, 1 : 1 v/v). The reaction mixture was stirred at room temperature for 30 minutes, resulting in a clear colourless solution. The solution was filtered and allowed to evaporate under ambient conditions. Colourless plate-shaped crystals of **3.4a** were formed after three days. Yield: 85%. ^{1}H NMR (DMSO-d_6, 500 MHz): 10.14 (s, 1H), 8.81 (d, *J* = 6 Hz, 2H), 8.11 (s, 1H), 8.01 (d, *J* = 7.5 Hz, 1H), 7.94 (d, *J* = 7.5 Hz, 2H), 7.85 (d, *J* = 5.5 Hz, 2H), 7.64-7.53 (m, *J* = 7 Hz, 4H), 4.92 (d, *J* = 5.5 Hz, 2H). IR (cm^{-1}): 3341 (m), 1638 (s), 1616 (s), 1526 (s), 1506 (s), 1390 (s), 1340 (m), 920 (m). UV, solid (λ_{max}): 312 nm, 353 nm.

3.10. References

1 N. Phukan and J. B. Baruah, *CrystEngComm*, 2016, **18**, 3877–3890.

2 N. Phukan and J. B. Baruah, *Cryst. Growth Des.*, 2014, **14**, 2640–2653.

3 M. O. M. Piepenbrock, N. Clarke and J. W. Steed, *Soft Matter*, 2011, **7**, 2412–2418.

4 B. Wu, X. Huang, Y. Xia, X. J. Yang and C. Janiak, *CrystEngComm*, 2007, **9**, 676–685.

5 E. I. Pereira, A. R. A. Nogueira, C. C. T. Cruz, G. G. F. Guimarães, M. M. Foschini, A. C. C. Bernardi and C. Ribeiro, *ACS Sustain. Chem. Eng.*, 2017, **5**, 9993–10001.

6 O. Khan, M. Bilal Khan Niazi, G. Abbas Shah, A. Hazafa, Z. Jahan, M. Sadiq and F. Sher, *J. Saudi Soc. Agric. Sci.*, 2021, **20**, 519–529.

7 K. Yamaguchi and K. Shudo, *J. Agric. Food Chem.*, 1991, **39**, 793–796.

8 C. F. Macrae, I. Sovago, S. J. Cottrell, P. T. A. Galek, P. McCabe, E. Pidcock, M. Platings, G. P. Shields, J. S. Stevens and Towler, Matthew, Wood, Peter A, *J. Appl. Crystallogr.*, 2020, **53**, 226–235.

9 L. S. Reddy, S. Basavoju, V. R. Vangala and A. Nangia, *Cryst. Growth Des.*, 2006, **6**, 161–173.

10 W. Kaminsky, D. R. Kelman, J. M. Giesen, K. I. Goldberg, K. A. Claborn, L. F. Szczepura and D. X. West, *J. Mol. Struct.*, 2002, **616**, 79–89.

11 B. Piotrkowska, A. Wasilewska, M. Gdaniec and T. Połoński, *CrystEngComm*, 2008, **10**, 1421–1428.

12 R. Jawaria, M. Hussain, Z. Shafiq, H. B. Ahmad, M. N. Tahir, H. A. Shad and M. M. Naseer, *CrystEngComm*, 2015, **17**, 2553–2561.

13 G. L. Succaw, T. J. R. Weakley, F. Han and K. M. Doxsee, *Cryst. Growth Des.*, 2005, **5**, 2288–2298.

14 R. Benny and S. De, *Dalt. Trans.*, 2023, **52**, 16767–16772.

15 C. D. Jones, S. R. Kennedy, M. Walker, D. S. Yufit and J. W. Steed, *Chem*, 2017, **3**, 603–628.

16 R. Yankova and I. Tankov, *J. Mol. Struct.*, 2021, **1238**, 130416.

17 S. Halder, S. Samanta and G. Das, *Analyst*, 2019, **144**, 2696–2703.

18 H. Naito, K. Nishino, Y. Morisaki, K. Tanaka and Y. Chujo, *Angew. Chemie Int. Ed.*, 2017, **56**, 254–259.

19 A. Tarai and J. B. Baruah, *Cryst. Growth Des.*, 2018, **18**, 456–465.

20 M. Takahashi, Y. Enami, H. Ninagawa and M. Obata, *New J. Chem.*, 2019, **43**, 3265–3268.

21 A. P. Singh and J. B. Baruah, *Mater. Adv.*, 2022, **3**, 3513–3525.

22 M. Williams, *Drug Dev. Res.*, 2013, **74**, 339.

23 S.-Q. Chen, S.-N. Yu, W. Zhao, L. Liang, Y. Gong, L. Yuan, J. Tang, X.-J. Yang and B. Wu, *Inorg. Chem. Front.*, 2022, **9**, 6091–6101.

24 M. Yokoya, S. Kimura and M. Yamanaka, *Chem. – A Eur. J.*, 2021, **27**, 5601–5614.

Appendix- Chapter 3

Materials and physical techniques: All starting materials, including phenyl isothiocyanate, 1-naphthyl isocyanate, 1-naphthylisothiocyanate, 4-(aminomethyl)pyridine, were purchased from Aldrich and Merck and used as received. Phenyl isocyanate was purchased from Spectrochem, and it was used as received. Perchloric acid (60%) and nitric acid (65%) were purchased from Merck. Infrared spectroscopy of the solid samples was performed with a PerkinElmer Spectrum Two FT-IR spectrophotometer in the region 4000–400 cm^{-1} by using the ATR method. Powder X-ray diffraction patterns were recorded using a Bruker powder X-ray diffractometer D2 phaser with Cu-Kα radiation (l = 1.54056 Å), 40 kV of operating voltage, and 125 mA of operating current (step size = 0.02 (2 θ), time = 5º/min, Quartz plate XRD (0.5 mm depth) sample holder). ^{1}H-NMR spectra were recorded in DMSO-d_6 solvent in a Bruker Avance Neo 500 MHz FT NMR and Bruker AVANCE III HD 600 MHz nuclear magnetic resonance spectrometer using TMS as an internal standard. The ESI-mass spectrum of **(3.1)·H_2O** was recorded on an Agilent QTOF 6520 mass spectrometer, and the ESI-mass spectra of **3.2**, **(3.3)·H_2O** and **3.4** were recorded on a Waters Xevo G2 Qtof mass spectrometer. The ESI-mass spectra of all four compounds **3.1**-**3.4** were recorded in an isopropanol solvent. Thermogravimetric analysis was performed on a PerkinElmer thermogravimetric analyzer TGA 4000 under nitrogen with a heating rate of 5°C min^{-1}. Fluorescence emission spectra of both the solid samples and aqueous medium were recorded on a Horiba Scientific Fluoromax-4 spectrofluorometer.

Thermal treatments on perchlorate salts are a potential hazard; hence, small quantities are to be dealt with, or experiments should be performed by taking care of the safety aspects.

Computational methodology: Density Functional Theory (DFT) calculations of all the compounds were performed with the B3LYP[A.1,A.2] functional using 6-31G[A.2] as the basis set. Calculations were performed using the Gaussian 09W package.[A.3] Gauss View (version 5.0.9) software[A.4] was used to visually analyze the calculated data.

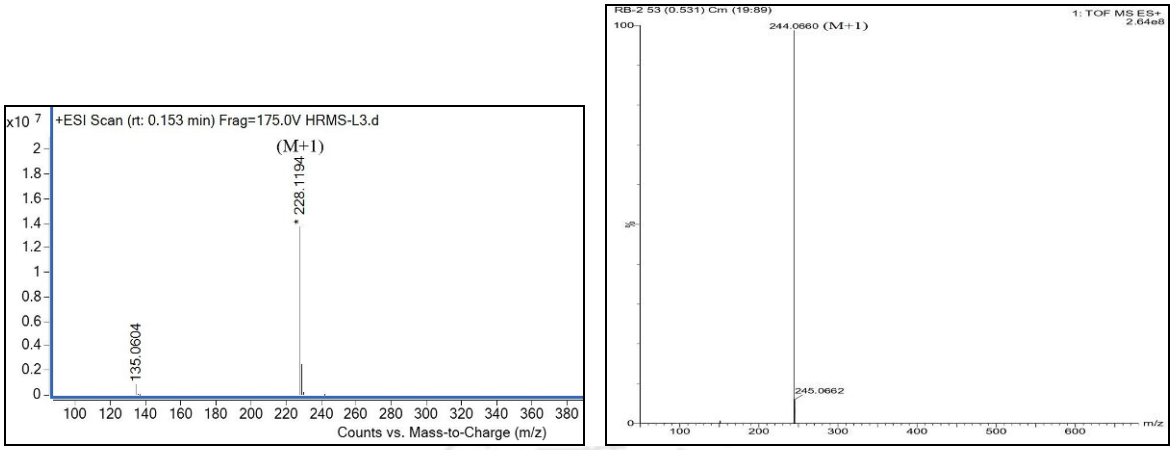

(a) **(b)**

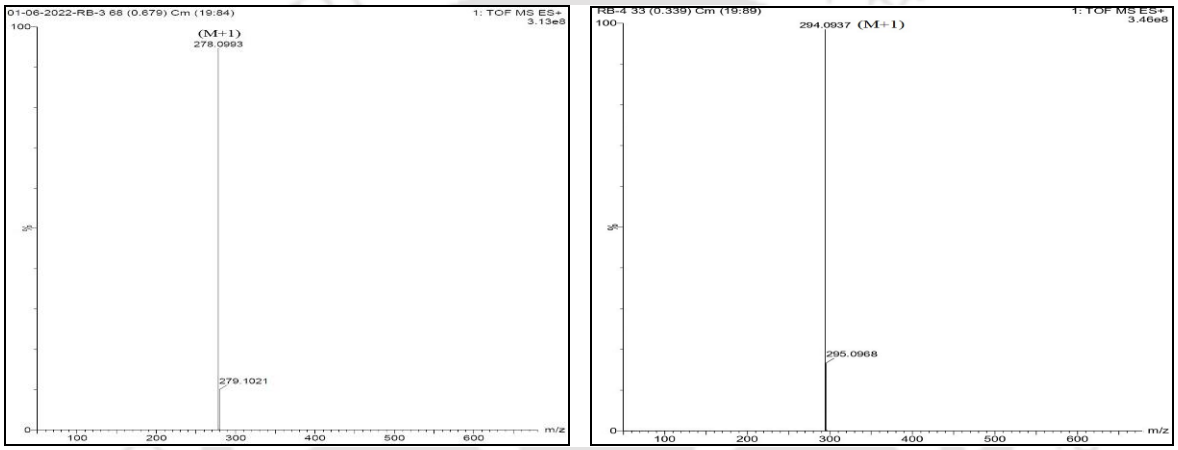

(c) **(d)**

Figure A3.1. ESI-mass spectrum of (a) **3.1**, (b) **3.2**, (c) **3.3**, and (d) **3.4**

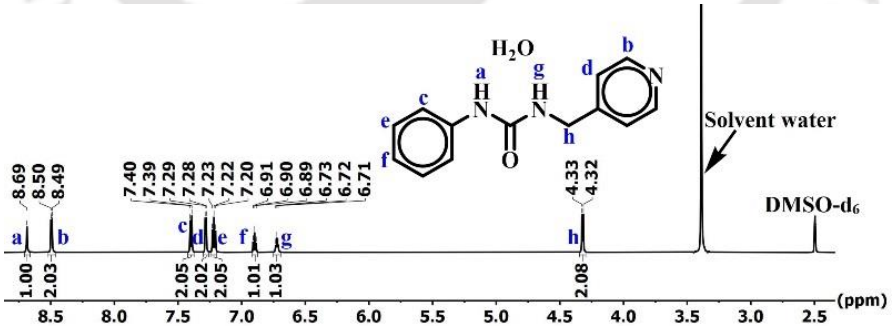

(a)

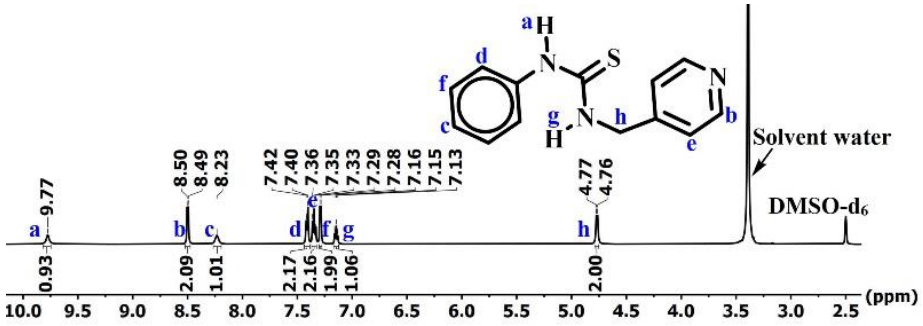

(b)

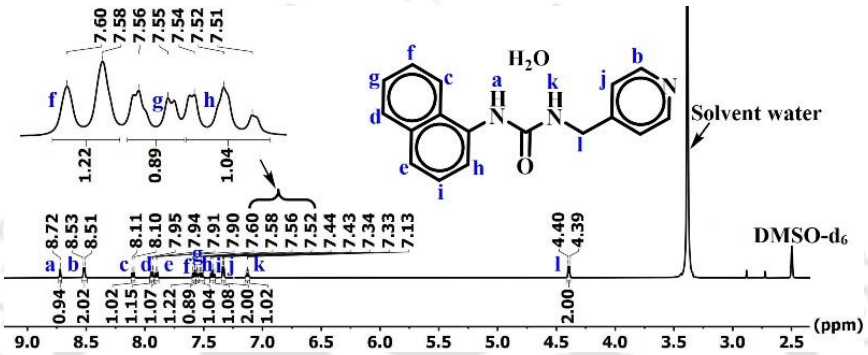

(c)

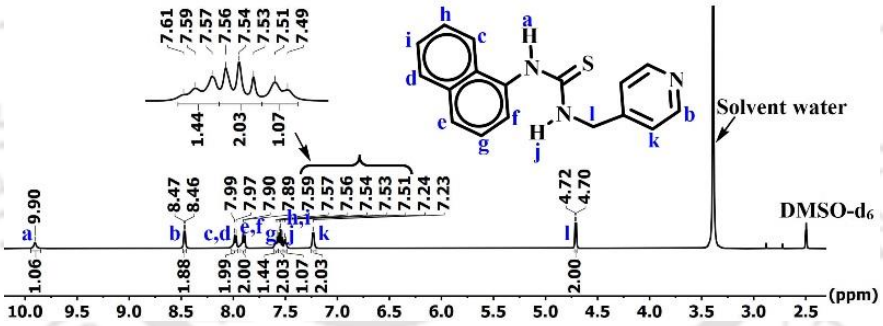

(d)

Figure A3.2. ^{1}H-NMR (DMSO-d$_6$, 600 MHz) of (a) **(3.1)·H$_2$O**; ^{1}H-NMR (DMSO-d$_6$, 500 MHz) of (b) **3.2**, (c) **(3.3)·H$_2$O**, and (d) **3.4**

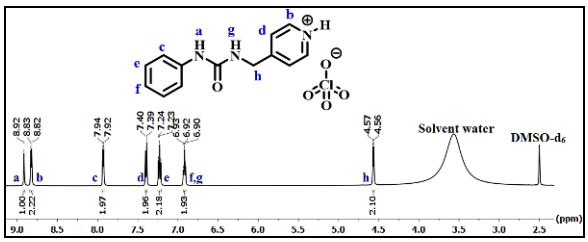

(a)

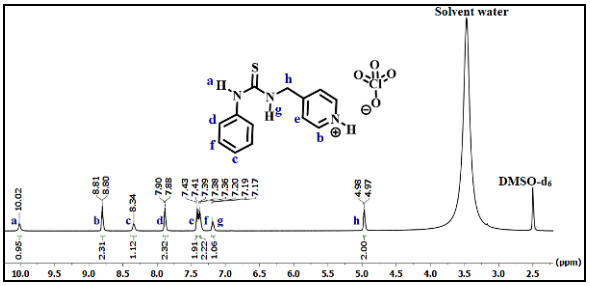

(b)

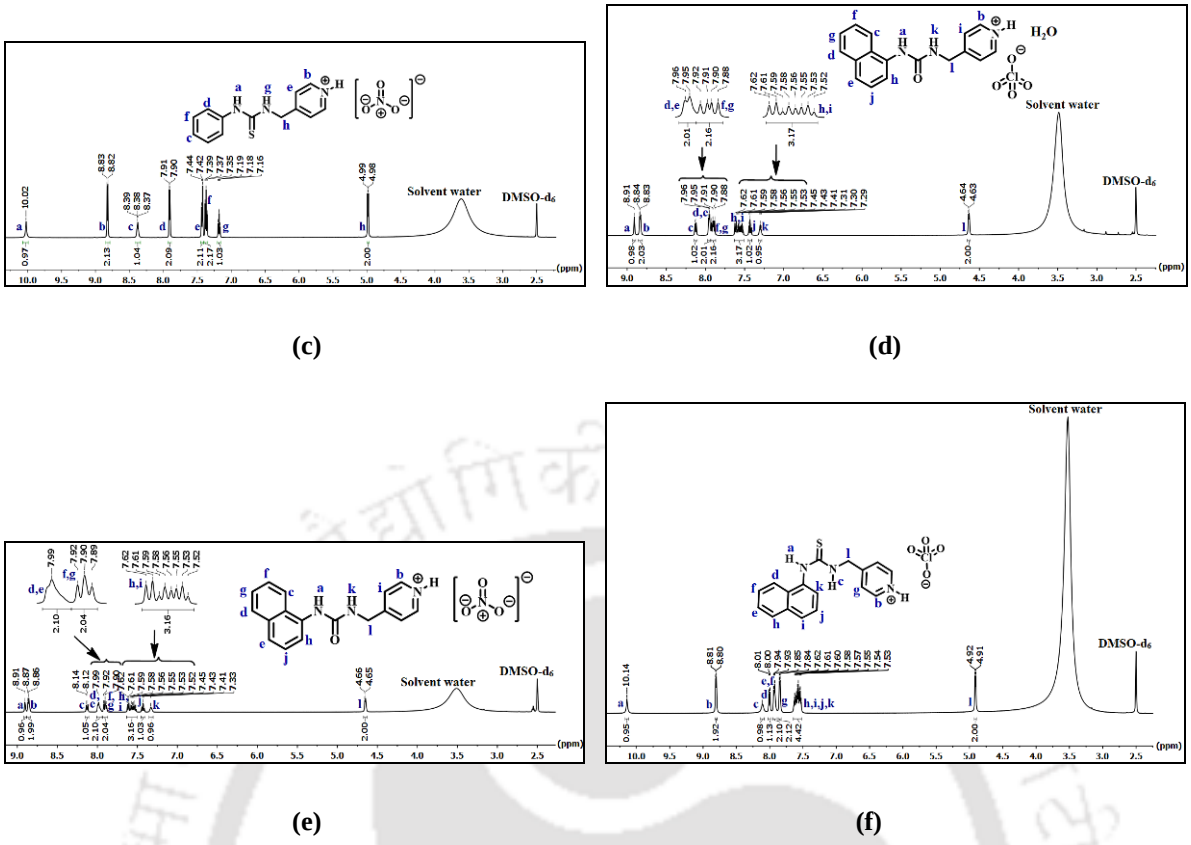

Figure A3.3. ^{1}H-NMR (DMSO-d_6, 500 MHz) of (a) **3.1a**, (b) **3.2a**, (c) **3.2b**, (d) **3.3a**, (e) **3.3b**, and (f) **3.4a**

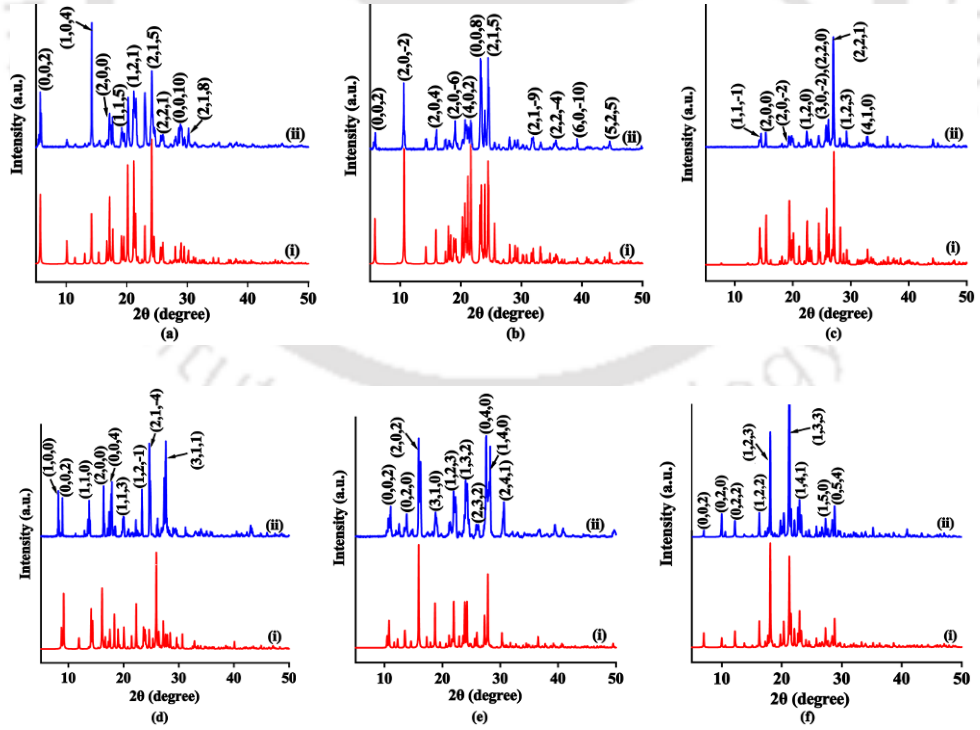

Figure A3.4. Powder X-ray pattern of (a) **3.1a**, (b) **3.2a**, (c) **3.2b**, (d) **3.3a**, (e) **3.3b**, and (f) **3.4a** (where, (i) and (ii) are simulated and experimental powder X-ray patterns respectively)

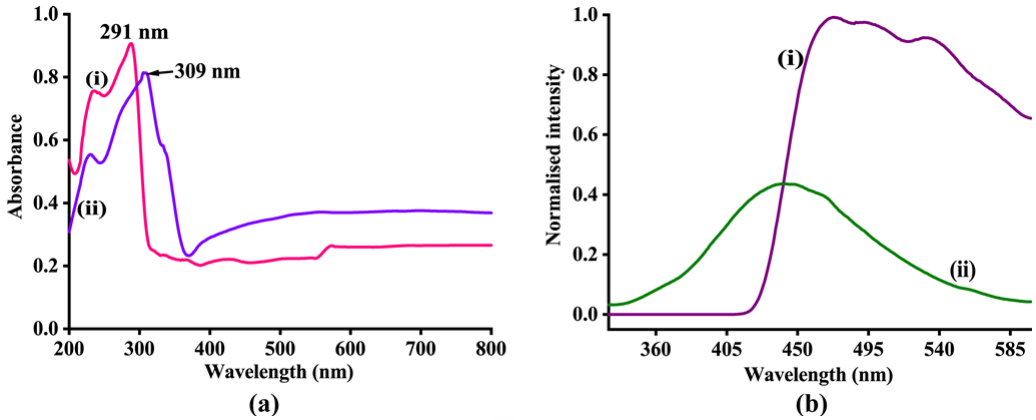

Figure A3.5. (a) absorbance and (b) photoluminescence spectra of the solid samples of (i) **(3.1)·H$_2$O** (λ_{abs} = 291 nm, λ_{ex} = 330 nm, λ_{em} = 473 nm, 492 nm, 530 nm), (ii) **3.1a** (λ_{abs} = 309 nm, λ_{ex} = 309 nm, λ_{em} = 440 nm)

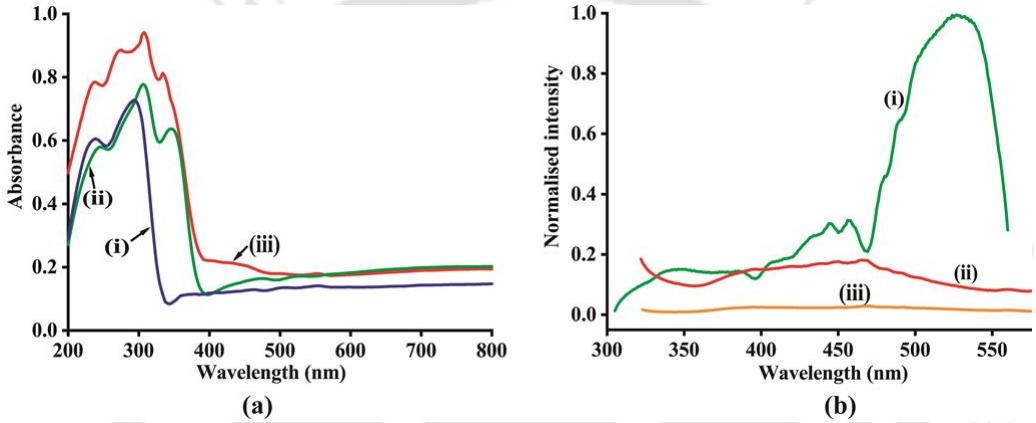

Figure A3.6. (a) absorbance and (b) photoluminescence spectra of the solid samples of (i) **3.2** (λ_{abs} =295 nm, λ_{ex} = 295 nm, λ_{em} = 530 nm), (ii) **3.2a** (λ_{abs} = 307 nm, λ_{ex} = 307 nm, λ_{em} = non-emissive), and (iii) **3.2b** (λ_{abs} = 307 nm, λ_{ex} = 307 nm, λ_{em} = non-emissive)

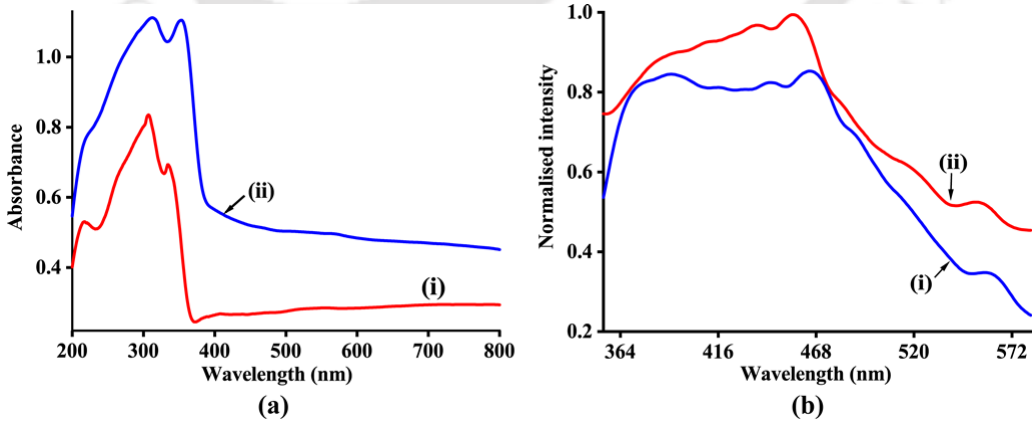

Figure A3.7. (a) absorbance and (b) photoluminescence spectra of the solid samples of (i) **3.4** (λ_{abs} = 306 nm, λ_{ex} = 306 nm, λ_{em} = 468 nm), (ii) **3.4a** (λ_{abs} = 312 nm, 353 nm, λ_{ex} =321 nm, λ_{em} = 468 nm)

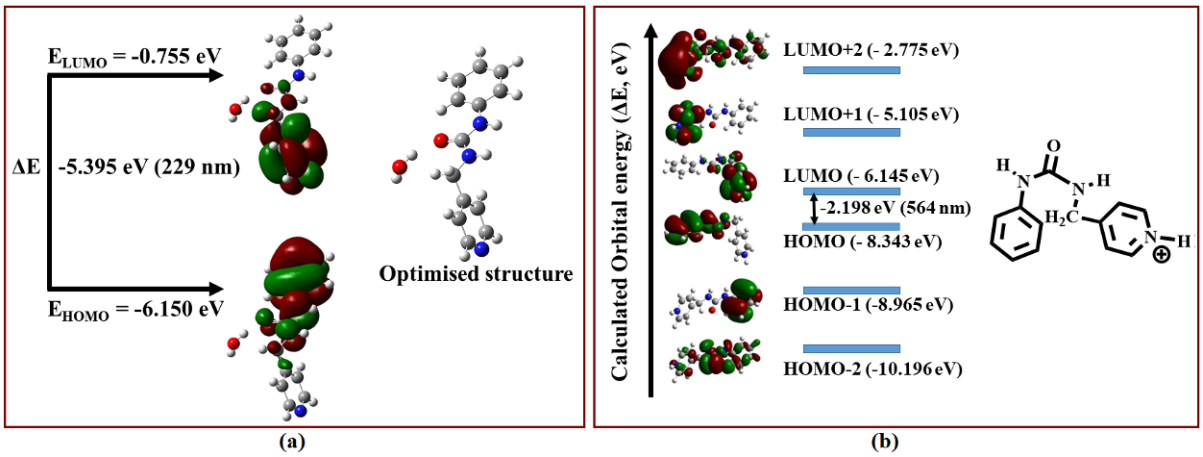

Figure A3.8. Electronic energy levels calculated by DFT showing the HOMO-LUMO gap in (a) **(3.1)·H_2O**, (b) **3.1a**

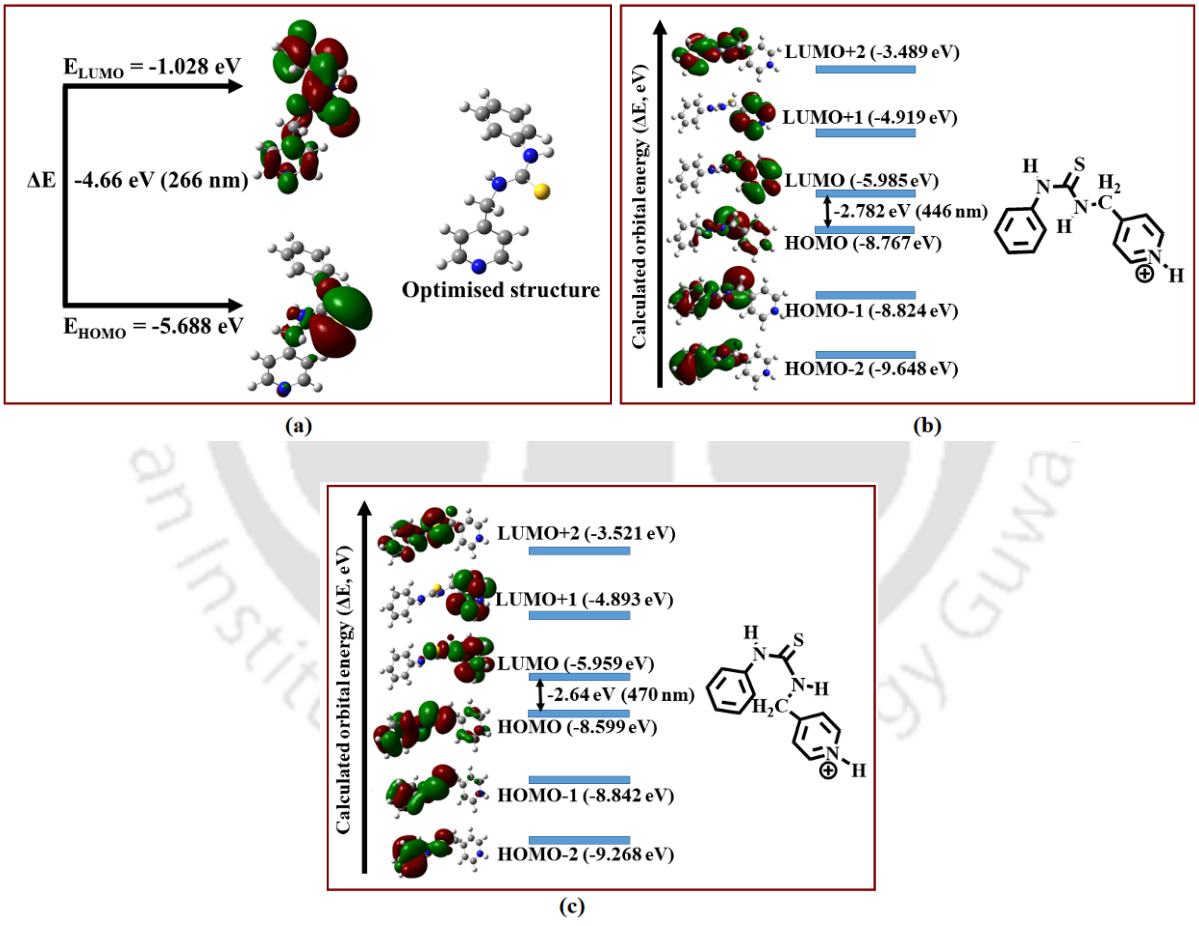

Figure A3.9. Electronic energy levels calculated by DFT showing the HOMO-LUMO gap in (a) **3.2**, (b) **3.2a**, and (b) **3.2b**

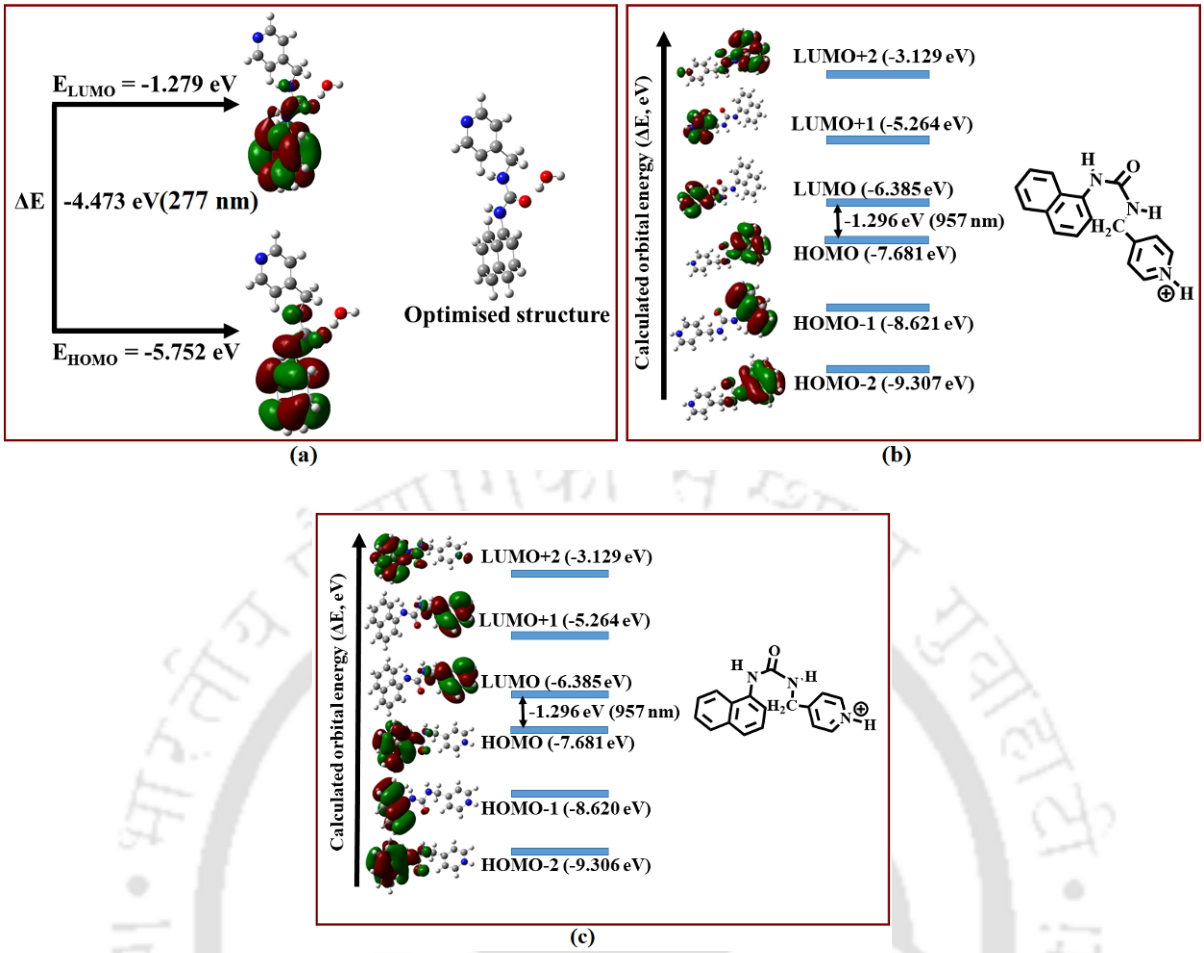

Figure A3.10. Electronic energy levels calculated by DFT showing the HOMO-LUMO gap in (a) **(3.3)·H₂O**, (b) **3.3a**, and (b) **3.3b**

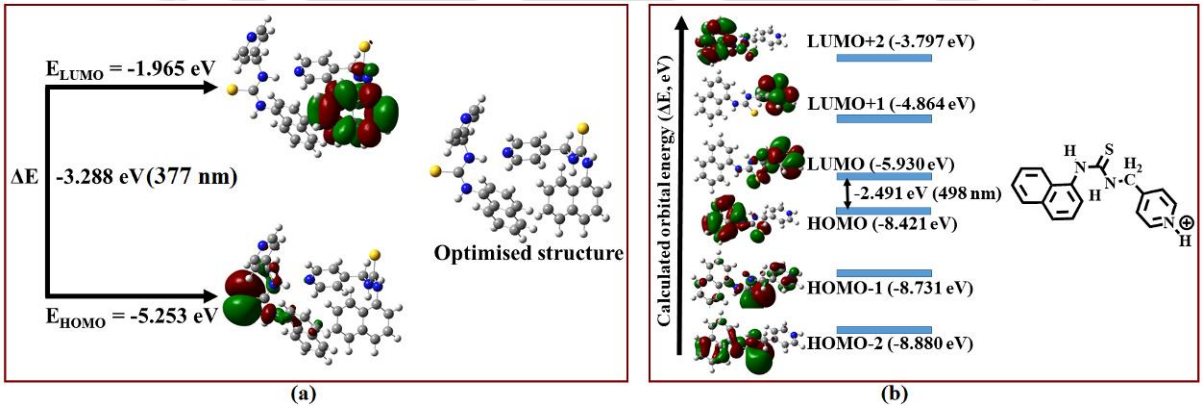

Figure A3.11. Electronic energy levels calculated by DFT showing the HOMO-LUMO gap in (a) **3.4**, and (b) **3.4a**

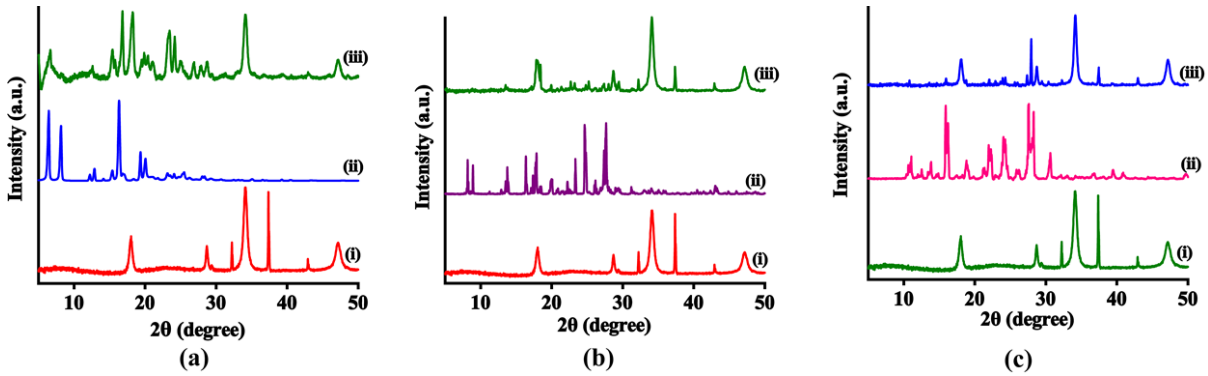

Figure A3.12. Powder X-ray patterns of (a) (i) CaO, (ii) **3.3**, (iii) **3.3@CaO** (1:1) (b) (i) CaO, (ii) **3.3a**, (iii) **3.3a@CaO** (1:1); (c) (i) CaO, (ii) **3.3b**, (iii) **3.3b@CaO** (1:1)

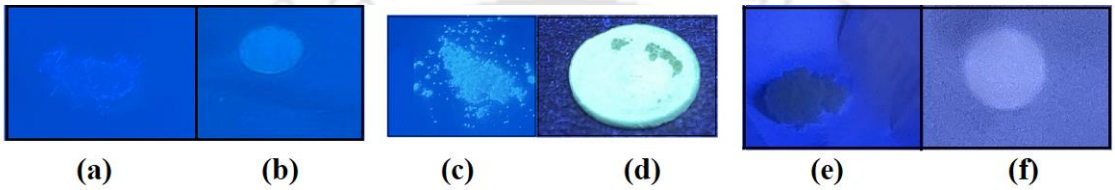

Figure A3.13. Images of the solid samples of (a) **(3.3)·H_2O**, and (b) **(3.3)·H_2O@CaO (1:1)**, (c) **3.3a**, (d) **3.3a@CaO (1:1)**, (e) **3.3b**, and (f) **3.3b@CaO (1:1)** under UV lamp at 365 nm

Table A3.1.(a) Crystallographic parameters of **3.1-3.4** and their respective salts

Parameters	**(3.1)·H_2O**	**3.1a**	**3.2**	**3.2a**	**3.2b**
Formula	$C_{13}H_{15}N_3O_2$	$C_{13}H_{14}ClN_3O_5$	$C_{13}H_{13}N_3S$	$C_{13}H_{14}ClN_3O_4S$	$C_{13}H_{14}N_4O_3S$
CCDC	2063021	2171843	2171848	2172477	2171845
Mol.wt.	245.28	327.72	243.32	343.78	306.34
Space group	*Pna*2_1	*Pbca*	*P*2_1/*c*	*I*2/*a*	*P*2_1/*c*
a(Å)	12.3714(12)	10.6033(11)	5.9160(4)	18.618(3)	11.5055(9)
b(Å)	18.5178(17)	9.1856(9)	22.1005(16)	5.4981(8)	8.4091(7)
c (Å)	5.6651(5)	30.910(3)	9.9693(5)	30.636(4)	14.4045(13)
α (°)	90	90	90	90	90
β (°)	90	90	100.216(6)	96.336(8)	92.059(3)
γ (°)	90	90	90	90	90
V (Å^3)	1297.8(2)	3010.5(5)	1282.79(14)	3116.9(8)	1392.7(2)
Density, g cm^{-3}	1.255	1.446	1.260	1.465	1.461
Abs. coeff., mm^{-1}	0.087	0.281	0.233	0.400	0.249
F (000)	520	1360	512	1424	640
Total no. of reflections	3226	2666	2256	2749	2461
Reflections, I > 2σ(I)	2393	1762	1630	2029	1890
Max. θ/°	28.285	25.047	25.040	24.999	25.046
Ranges (h, k, l)	$-16 \le h \le 16$ $-24 \le k \le 24$ $-7 \le l \le 7$	$-11 \le h \le 12$ $10 \le k \le 10$ $-36 \le l \le 36$	$-7 \le h \le 7$ $-26 \le k \le 24$ $-6 \le l \le 11$	$-22 \le h \le 22$ $-6 \le k \le 6$ $-36 \le l \le 36$	$-13 \le h \le 13$ $-10 \le k \le 10$ $-17 \le l \le 17$
Complete to 2θ (%)	100	99.7	99.9	99.8	99.8
Data/restraints/parameters	3226/1/179	2666/6/ 220	2256/0/162	2749/ 173/ 218	2461/1/190
GooF (F^2)	1.093	1.046	1.060	1.088	0.984
R indices [I > 2σ(I)]	0.0641	0.0650	0.0410	0.0779	0.0446
wR$_2$ [I > 2σ(I)]	0.1804	0.1792	0.0834	0.1771	0.1116
R indices (all data)	0.0928	0.0997	0.0645	0.1089	0.0614
wR$_2$ (all data)	0.2067	0.2044	0.0948	0.1906	0.1264

Table A3.1.(b) Crystallographic parameters of **3.1-3.4** and their respective salts

Parameters	**(3.3)·H$_2$O**	**3.3a**	**3.3b**	**3.4**	**3.4a**
Formula	$C_{17}H_{17}N_3O_2$	$C_{17}H_{18}ClN_3O_6$	$C_{17}H_{16}N_4O_4$	$C_{17}H_{15}N_3S$	$C_{17}H_{16}ClN_3O_4S$
CCDC	2171849	2171846	2171847	2173492	2171850
Mol.wt.	295.33	395.79	340.34	293.38	393.84
Space group	*Pca*2$_1$	*P*2$_1$/*c*	*Pbca*	*P*-1	*Pbca*
a(Å)	43.205(6)	10.886(3)	15.1546(10)	9.4256(6)	8.241(2)
b(Å)	7.7050(11)	8.2613(18)	13.0529(9)	9.744(2)	17.685(5)
c (Å)	4.5617(6)	20.140(5)	16.4184(11)	17.9657(12)	25.201(7)
α (°)	90	90	90	85.658(2)	90
β (°)	90	98.990(6)	90	85.018(2)	90
γ (°)	90	90	90	69.168(2)	90
V (Å^3)	1518.6(4)	1789.0(7)	3247.7(4)	1535.35(17)	3672.9(18)
Density, g cm^{-3}	1.292	1.470	1.392	1.269	1.424
Abs. coeff., mm^{-1}	0.087	0.255	0.102	0.207	0.349
F (000)	624	824	1424	616	1632
Total no. of reflections	2570	3124	2397	5374	3225
Reflections, I > 2σ(I)	1986	2554	1862	4443	2744
Max. θ/°	24.684	25.046	23.490	25.000	24.998
Ranges (h, k, l)	-50≤ h ≤ 50	-12≤ h ≤ 12	-16≤ h ≤ 16	-11≤ h ≤ 11	-9≤ h ≤ 9
	-9≤ k ≤ 9	-9≤ k≤ 9	-14≤ k ≤ 14	-11≤ k ≤ 11	-21≤ k ≤ 21
	-5≤ l ≤ 5	-23≤ l ≤ 23	-18≤ l ≤ 18	-21≤ l ≤ 21	-29≤ l ≤ 29
Complete to 2θ (%)	99.7	99.0	99.8	99.4	99.8
Data/restraints/parameters	2570/1/215	3124/0/260	2397/0/238	5374/1/ 395	3225/0/248
GooF (F^2)	1.133	1.063	1.244	1.091	1.087
R indices [I > 2σ(I)]	0.0890	0.0630	0.0669	0.0485	0.0640
wR$_2$ [I > 2σ(I)]	0.2066	0.1675	0.1172	0.0995	0.1602
R indices (all data)	0.1236	0.0774	0.0895	0.0617	0.0753
wR$_2$ (all data)	0.2288	0.1880	0.1323	0.1089	0.1668

Table A3.2. Hydrogen bond parameters of the salts of compound **3.1-3.4**

Salts	D-H···A	d_{D-H} (Å)	$d_{H\cdots A}$ (Å)	$d_{D\cdots A}$ (Å)	∠D-H···A (º)
3.1a	N(1) -H(1) ···O(1) [3/2-x, -1/2+y, z]	0.85 (2)	2.00 (2)	2.833 (3)	166 (3)
	N(2) -H(2) ···O(1) [3/2-x, -1/2+y, z]	0.849 (19)	2.30 (2)	3.034 (3)	145 (3)
	N(3) -H(3) ···O(5A) [1-x,1-y,-z]	0.86	1.88	2.675 (10)	153
	N(3) -H(3) ···O(3A^B) [1-x,1-y,-z]	0.86	2.31	3.051 (19)	144
	N(3) -H(3) ···O(5A^B) [1-x,1-y,-z]	0.86	2.23	3.05 (3)	160
	C(8) -H(8B) ···O(4A) [x,y,z]	0.97	2.40	3.314 (8)	157
	C(8) -H(8B) ···O(2A^B) [x,y,z]	0.97	2.36	3.24 (3)	151
	C(11) -H(11) ···O(2A) [1/2+x,1/2-y,-z]	0.93	2.49	3.367 (8)	157
3.2a	N(1) –H(1A)···S(1) [1/2-x, 5/2-y, 1/2-z]	0.86	2.53	3.355 (4)	162
	N(2) -H(2A) ···O(3) [x, y, z]	0.86	2.17	2.940 (8)	150
	N(3) -H(3A) ···O(4) [1/2+x, 1-y, z]	0.86	1.91	2.750 (10)	167
3.2b	N(1) -H(1) ···O(2) [1-x, 1/2+y, 1/2-z]	0.86	2.21	3.052 (3)	167
	N(3) -H(3) ···O(1) [x, 1/2-y, 1/2+z]	0.86	1.95	2.803 (3)	173
3.3a	O(6) -H(6A) ···O(1) [x, 1+y, z]	0.85	2.04	2.892 (4)	177
	N(1) -H(1) ···O(1) [1-x, 1/2+y, 1/2-z]	0.86	2.22	3.010 (3)	153
	O(6) -H(6B) ···O(2) [x, 1+y, z]	0.85	2.40	3.183 (7)	154
	N(2) -H(2) ···O(1) [1-x, 1/2+y, 1/2-z]	0.86	2.17	2.975 (3)	156
	N(3) -H(3) ···O(6) [-x, -1/2+y, 1/2-z]	0.86	1.89	2.723 (5)	164
	C(4) -H(4) ···O(2A^B) [1-x, -y, -z]	0.93	2.58	3.50 (4)	169
	C(14) -H(14) ···O(2) [x, y, z]	0.93	2.51	3.377 (7)	156
	C(15) -H(15) ···O(5A^B) [x, y, z]	0.93	2.33	3.10 (2)	141
	C(16) -H(16) ···O(4A^B) [x, 1/2-y, 1/2+z]	0.93	2.56	3.349 (7)	143

3.3b	N(1) -H(1) ···O(2) [x, 1/2-y, -1/2+z]	0.86 (3)	2.01 (3)	2.860 (4)	170 (4)
	N(2) -H(2) ···O(3) [x, 1/2-y, -1/2+z]	0.87 (4)	2.05 (4)	2.903 (4)	169 (3)
	N(3) -H(3) ···O(1) [-1/2+x, y, 1/2-z]	1.04 (5)	1.63 (5)	2.663 (4)	170 (4)
	C(15) -H(15) ···O(4) [-1/2+x, y, 1/2-z]	0.93	2.58	3.506 (4)	171
3.4a	N(1) -H(1) ···S(1) [-1/2+x, y, 1/2-z]	0.86	2.46	3.265 (3)	157
	N(2) -H(2) ···O(3A) [x, y, z]	0.86	2.26	3.055 (10)	152
	N(2) -H(2) ···O(3A^B) [x, y, z]	0.86	2.31	3.02 (4)	140
	N(3) -H(3) ···O(3A) [1/2-x, 1/2+y, z]	0.86	2.01	2.85 (10)	164
	N(3) -H(3) ···O(3A^B) [1/2-x, 1/2+y, z]	0.86	2.06	2.83 (4)	148
	N(3) -H(3) ···O(4A^B) [1/2-x, 1/2+y, z]	0.86	2.40	3.125 (19)	142
	C(15) -H(15) ···O(4A^B) [-x, 1-y, -z]	0.93	2.47	3.28 (18)	145

References:

A.1. J. Tirado-Rives and W. L. Jorgensen, *J. Chem. Theory Comput.*, 2008, **4**, 297–306.

A.2. S. Meng, W. Li, X. Yin and J. Xie, *Comput. Theor. Chem.*, 2013, **1006**, 76–84.

A.3. M. Frisch, G. Trucks, H. Schlegel, G. Scuseria, M. Robb, J. Cheeseman, G. Scalmani, V. Barone, G. Petersson, H. Nakatsuji, *Gaussian 09, Revision A.02*; Gaussian, Inc.: Wallingford, CT, 2016.

A.4. R. D. Dennington II, T. A. Keith, J. Millam, A. B. Nielsen, A. J. Holder, *GaussView, Version 5.0.9*, Gaussian, Inc., Wallingford, CT, 2009.

Chapter 4

Zinc (II) and cobalt (II) dicarboxylate coordination polymers having pyridine urea-based ligand

Urea-based metal complexes have been widely studied for sensing different ions,[1–5] and are well known for interesting conducting properties.[6–8] Different self-assemblies are observed in the self-assemblies of the urea-based metal complexes,[9–16] anion-assisted,[17–21] or guest-assisted assemblies[22–27] of the urea derivatives. Urea-based metal-organic frameworks,[28,29] coordination polymers,[30–32] and inorganic cages[33,34] find applications in ion sensing, catalysis, separation, etc. As stated in the introduction, urea derivatives can self-assemble through hydrogen bonds and urea tape synthon formation due to the presence of two -NH groups.[22–27] In metal complexes, the competition to form complementary hydrogen bonds with the substrates is utilized in building a secondary coordination sphere.[35–37] These properties make them prominent candidates for sensing and detection of contaminants. Furthermore, the adsorption and desorption properties of urea derivatives have great promise due to their ability to serve as a template for ionic as well as neutral substrates. Both symmetrical and non-symmetrical urea-based compounds adopt different conformations, and some of these conformers are stabilized through hydrogen bonds or metal complexation.[9] Accordingly, there is ample scope to understand selectivity in substrate binding in various coordination polymers with diverse architectures or with subtle differences in non-covalently linked structures. In this chapter, we have studied cobalt(II) and zinc(II) dicarboxylate coordination polymers (dicarboxylates chosen were terephthalate, fumarate, and succinate) of a semi-flexible pyridyl urea-based ligand, namely, 1-phenyl-3-(pyridin-4-ylmethyl)urea (**L$_{4.1}$**) (Fig. 4.1) and their binding with selective dyes. The metal dicarboxylates with **L$_{4.1}$** was chosen with anticipation of providing different types of coordination polymers with different nodes. Some of the possible nodes are shown in Fig. 4.1a-c. The formation of these nodes will be highly sensitive to various steric and electronic features associated with each counterpart and will have different ways of having complementary hydrogen bonds with substrates.

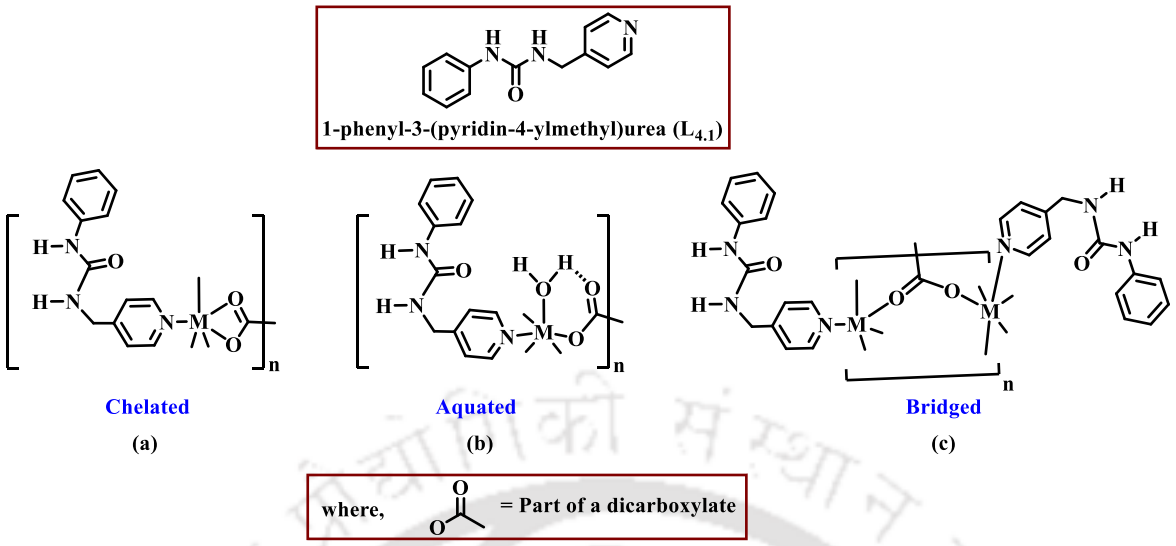

Figure 4.1. Ligand 1-phenyl-3-(pyridin-4-ylmethyl)urea (**L**$_{4.1}$) and (a-c) are some of the possible binding modes of dicarboxylate in the metal dicarboxylate coordination polymers of **L**$_{4.1}$

4.1. Synthesis of coordination polymers (CPs)

A series of coordination polymers enlisted in Scheme 4.1 were synthesized and characterized. When ligand **L**$_{4.1}$ was treated with cobalt(II) acetate tetrahydrate in the presence of maleic acid (*cis*-regiomer), instead of fumaric acid (*trans*-regiomer), it also yielded the coordination polymer **CP-4.2**. By changing the metal salt to zinc(II) acetate dihydrate, the same reaction yielded the **CP-4.5,** as illustrated in Scheme 4.1. During the course of these reactions, the observed dicarboxylates had the *trans* geometry; hence, there was a *cis*-to-*trans* conversion during the reactions. *Cis-to-trans* isomerization of maleate to fumarate was earlier observed in the zinc(II) complexes.[38] When zinc(II) acetate dihydrate was reacted with **L**$_{4.1}$ in the presence of terephthalic acid, the ligand was not coordinated to the metal center; instead, it yielded a two-dimensional zinc(II) terephthalate coordination polymer (**CP-4.6**) (Fig. 4.3e). The unit cell of **CP-4.6** was similar to the CCDC deposit GECXUH02.[39] **L**$_{4.1}$, and all the coordination polymers were characterized by FT-IR, UV-visible spectroscopy, elemental analysis, thermogravimetry, single crystal X-ray diffraction crystallography, powder X-ray diffraction. The diversities in these coordination polymers were observed due to the different coordination modes of the dicarboxylates[40,41] with the central metal ion (Fig. 4.1a-c). The coordinated water molecules or aqua ligands in these coordination polymers (**CPs**) provided new self-assembling scaffolds.

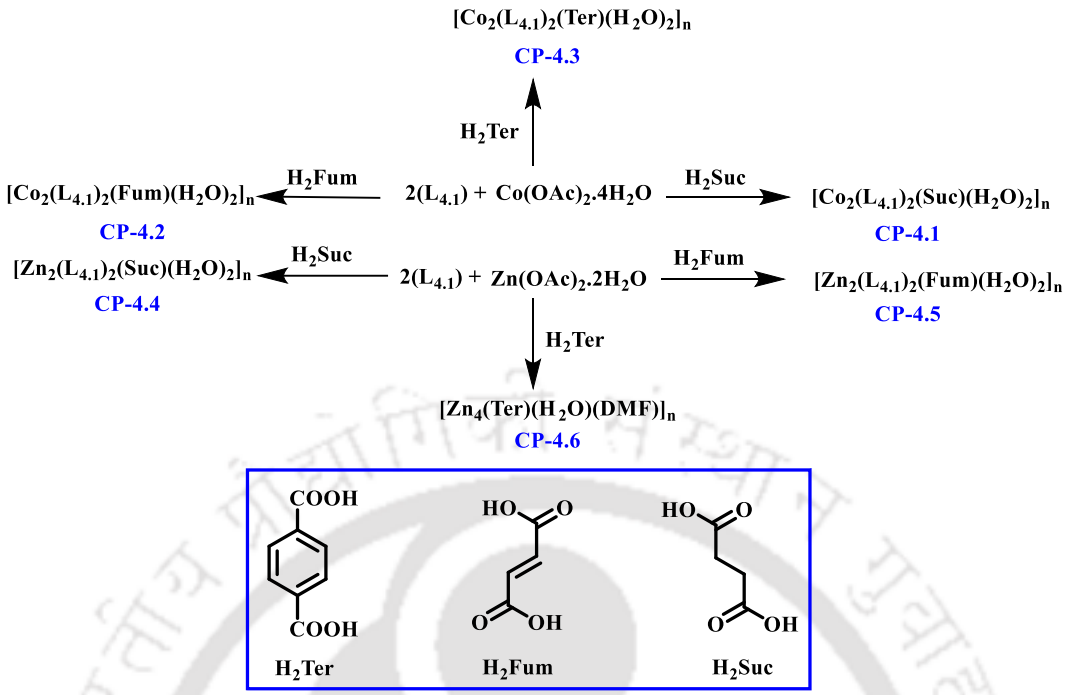

Scheme 4.1. Synthesis of $\mathbf{L_{4.1}}$ and coordination polymers **4.1-4.6**

4.2. Synthesis and characterization of ligand 4.1

$\mathbf{L_{4.1}}$ was synthesized following the procedure used to synthesize compound **3.1,** as mentioned in Chapter 3. The mass spectrum of the $\mathbf{L_{4.1}}$ showed a peak at 228.1194 (Calculated 228.1092), corresponding to the [M+1] peak (Fig. 4.2a). Crystallization of $\mathbf{L_{4.1}}$ from a solution of methanol-water mixture (1:1 v/v) yielded $\mathbf{(L_{4.1})\cdot H_2O}$. In ^{1}H-NMR, the characteristic proton peaks of the two -NH groups (designated as ′a′ and ′g′) in $\mathbf{(L_{4.1})\cdot H_2O}$ appeared at 8.69, 6.73-6.71 (Fig. 4.2b). The FT-IR spectrum of $\mathbf{(L_{4.1})\cdot H_2O}$ (Fig. 4.2c) showed that the O-H stretching of the water molecule of crystallization appeared as a sharp peak at 3427 cm^{-1}. The N-H stretching and bending were observed as medium and sharp bands at 3323 and 1599 cm^{-1}, respectively. The IR bands corresponding to C=O and C-N (pyridyl ring) bonds appeared at 1675 and 1316 cm^{-1}, respectively. Comparison of the powder X-ray pattern of $\mathbf{(L_{4.1})\cdot H_2O}$ (Fig. 4.2d) with its simulated data (generated from a CIF file in MERCURY software) showed the presence of a single phase of the Miller indices.

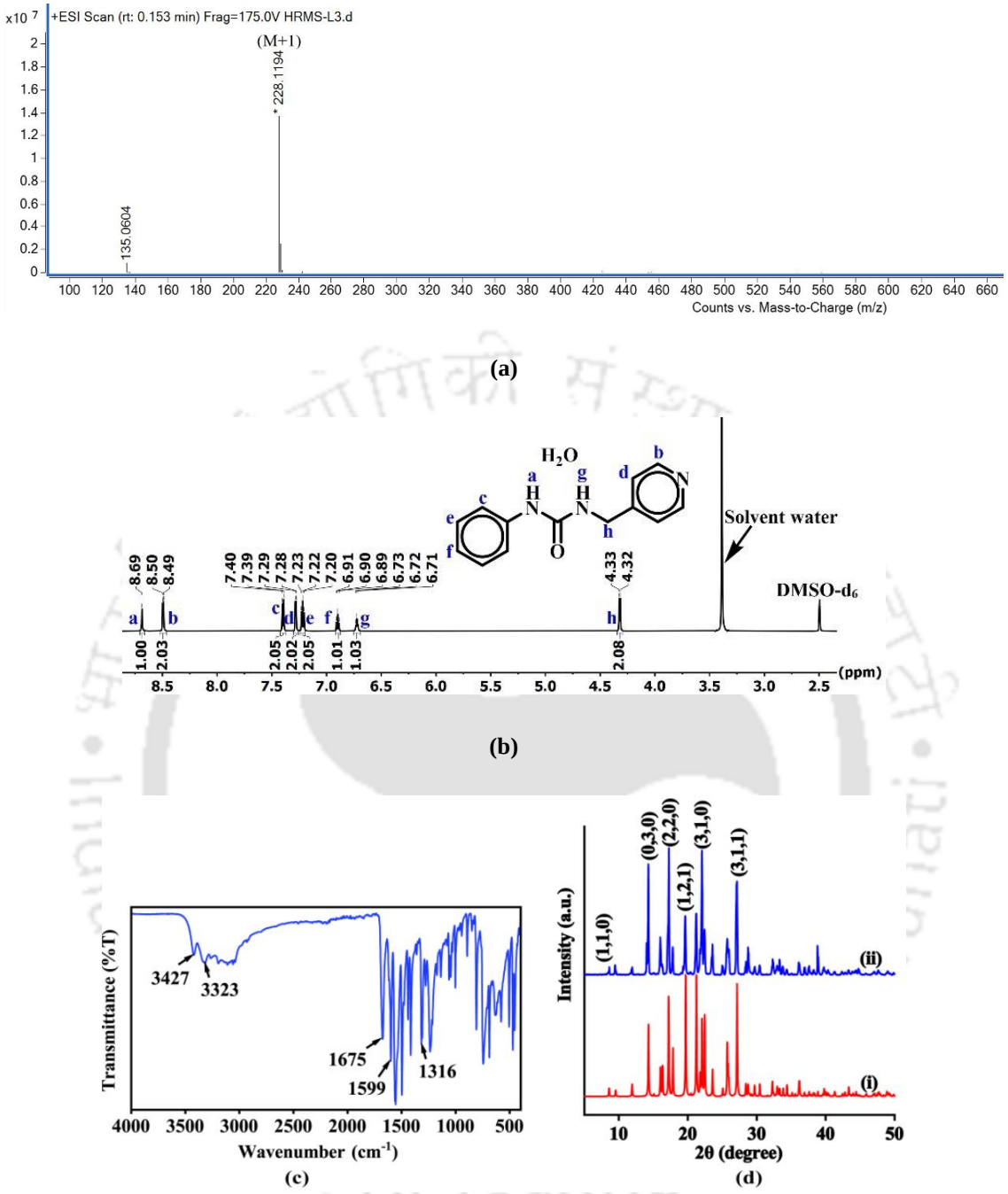

Figure 4.2. (a) ESI-mass spectrum of **L4.1**, (b), (c), and (d) are ^{1}H-NMR (DMSO-d_6, 600 MHz), FT-IR (ATR) spectrum, and powder X-ray pattern {(i) and (ii) are simulated and experimental patterns respectively} of the solid sample of **(L4.1)·H2O**, respectively

4.3. Structure and self-assemblies of coordination polymers (CPs) 4.1-4.5

The crystal structures of five coordination polymers **CP4.1-CP4.5** having analogous compositions, $[M_2(\mathbf{L_{4.1}})_2(dicarb)(H_2O)_2]_n$ {where dicarb = succinate or fumarate for M = Co(II) and Zn(II); and terephthalate for M = Co(II)} were determined. Among these, the four

coordination polymers **CPs 4.1, 4.2, 4.4, and 4.5** were crystallized in an orthorhombic crystal system in the *Pccn* space group (Table 4.1). As these polymers are closely related and belong to the same space group, they may form an isostructural or isomorphous series. In general, isostructural crystals refer to the ones with the same crystal structure (may not have the same cell dimensions or same chemical composition), and isomorphous ones have the same unit cell dimensions and space group. In general, the isostructurality among structures is determined by factors such as cell similarity index.[42] The cell similarity index is calculated by Equation 4.1. If the cell similarity index is close to zero, the two unit cells will be similar and have an isostructural relationship. The unit cell parameters of each of the pair of **CPs 4.1**, **4.2**, **4.4**, and **4.5** were used to calculate the similarity index among them and were compared. The calculated cell similarity parameter indices for each chosen pair were close to zero (Table 4.2). Thus, all the four **CPs** were isostructural.

Table 4.1. Crystallographic parameters of coordination polymers **CPs 4.1**, **4.2**, **4.4**, and **4.5**

Coordination Polymer (CP)	Space group crystal system	Space group	Unit cell parameters (Å)			Volume ($Å^3$)
			a	b	c	
4.1	Orthorhombic	*Pccn*	11.653(7)	30.448(14)	8.960(5)	3179(3)
4.2	Orthorhombic	*Pccn*	30.4091(14)	11.6865(5)	8.9577(3)	3183.4(2)
4.4	Orthorhombic	*Pccn*	11.626(7)	30.46(2)	8.952(4)	3170(3)
4.5	Orthorhombic	*Pccn*	11.700(4)	30.466(10)	8.959(3)	3193.4(19)

$$\textit{Cell similarity index}, \pi = \left| \frac{a+b+c}{a'+b'+c'} - 1 \right| \quad \ldots\ldots\ldots\ldots\ldots \textit{Equation 4.1}$$

where a, b, c, and a′, b′, c′, are the orthogonal lattice parameters of the two related crystals.

Table 4.2. Cell similarity index of the pairs of coordination polymers **CPs 4.1**, **4.2**, **4.4**, and **4.5**

Pair of CPs	π
4.1/4.2	0.000
4.1/4.4	0.000
4.1/4.5	0.001
4.2/4.4	0.000
4.2/4.5	0.001
4.4/4.5	0.002

The asymmetric unit of all the five **CPs 4.1-4.5** are shown in Fig. 4.3. Growing of the asymmetric unit of the individual coordination polymers revealed the skeleton of the

coordination polymers. All these coordination polymers have an octahedral geometry around the metal ions. Each metal ion has two **L4.1**, two dicarboxylates, and two aqua ligands completing the respective coordination sphere. The two ligands of the same kind are located at *trans* positions with respect to each other in the node. As the coordination environment of these **CPs** was similar, these examples provided scope to compare metal-ligand bond parameters in a systematic manner, which are listed in Table 4.3. Due to the size difference of the two metal ions, the zinc-ligand bond distances are slightly longer than the cobalt-ligand bond distances. The M-O bond distances associated with the aqua ligand and dicarboxylate ligands were in the range of 2.06 Å-2.11 Å. The M-N bond distances are in the range of 2.15 Å-2.21 Å, similar to the conventional M-N bond distances observed in pyridine complexes of zinc(II) and cobalt(II).[43–45] The M-O bond distances are also similar to the Co-O or Zn-O bond distances observed in literature in the common metal complexes.[46–50]

Table 4.3. Metal-ligand bond and ligand-metal-ligand bond angle parameters of the coordination polymers **CPs 4.1-4.5**

Bond-distance(Å)/ Angle (˚)	**CP-4.1** (M = Co)	**CP-4.2** (M = Co)	**CP-4.3** (M = Co)	**CP-4.4** (M = Zn)	**CP-4.5** (M = Zn)
M1-O3	2.066(2)	2.061(2)	2.083(1)	2.071(2)	2.068(2)
M1-O2	2.099(1)	2.091(1)	2.105(2)	2.097(1)	2.093(1)
M1-N3	2.197(4)	2.188(3)	2.149(3)	2.214(3)	2.211(3)
O3-M1-O2	91.28(1)	91.22(1)	89.38(1)	88.43(1)	88.34(5)
O3-M1-O2	88.72(8)	88.78(8)	90.62(3)	91.57(8)	91.66(1)
O3-M1- N3	88.28(6)	87.04(6)	88.92(2)	88.21(6)	87.33(6)
O3-M1-N3	91.72(7)	92.96(7)	91.08(4)	91.79(7)	92.67(8)
O2-M1-N3	87.86(2)	87.72(2)	87.98(8)	87.62(3)	87.86(2)
O2-M1-N3	92.14(3)	92.28(3)	92.02(6)	91.38(2)	92.14(4)

In the isostructural **CPs 4.1**, **4.2**, **4.4**, and **4.5**, the central metal ion is present in an inversion center (Figs. 4.3a, 4.3b, 4.3d, 4.3e) relating the dicarboxylate coligand or the pyridine urea coligand (**L4.1**). The four isostructural **CPs** have extensive hydrogen bonds and C-H···π interactions to form non-covalent assemblies. A cyclic motif having $R^1_1(6)$ graph set notation[46–50] is formed in each case due to intramolecular hydrogen bonds between the aqua ligand and the carboxylate group of the monodentate fumarate or succinate {Figs. 4.3 (a)(i)-(d)(i)}. The metal-dicarboxylate bridges of the coordination polymers are arranged such that the pyridyl urea ligand **L4.1** occupied the spaces between metal-dicarboxylate bridging chains {Figs. 4.3(a)(ii)-(d)(ii)}. The intermolecular hydrogen bonds between the adjacent **L4.1** molecules formed urea α-tape $R^1_2(6)$ synthons {Figs. 4.3(a)(i)-(d)(i)}. The distances between

the two metal centers in these isostructural **CPs** are 15.87 Å in **CP-4.1**, 15.85 Å in **CP-4.2**, 18.87 Å in **CP-4.4**, and 15.88 Å in **CP-4.5**. Due to this wide separation between the two chains, there is enough space for the orientation of the phenyl ring with respect to the neighbouring pyridine ring of the two independent chains. The orientations are suitable to have C-H···π interactions between these two rings. The C-H···π interactions contributed to the two-dimensional supramolecular arrangement {Figs. 4.3(a)(ii)-(d)(ii)} of the **CPs**. The C-H···π distances for the interactions between the rings ranged from 3.2 Å - 3.4 Å. This weak interaction contributed to the orientation of the phenyl rings in our coordination polymers (Fig. 4.3). Weak C-H···π interaction generally contributes about 1.5-2.5 kcal mol^{-1}, which is an important factor in providing suitable orientations to aromatic rings of flexible molecules.[51] The four isostructural **CPs** have C=O···H-O hydrogen bonds, forming an $R^2_3(13)$ synthon[52] (Fig. 4.5a). These interactions provided a two-dimensional network to the coordination polymers **CPs 4.1**, **4.2**, **4.4**, and **4.5**.

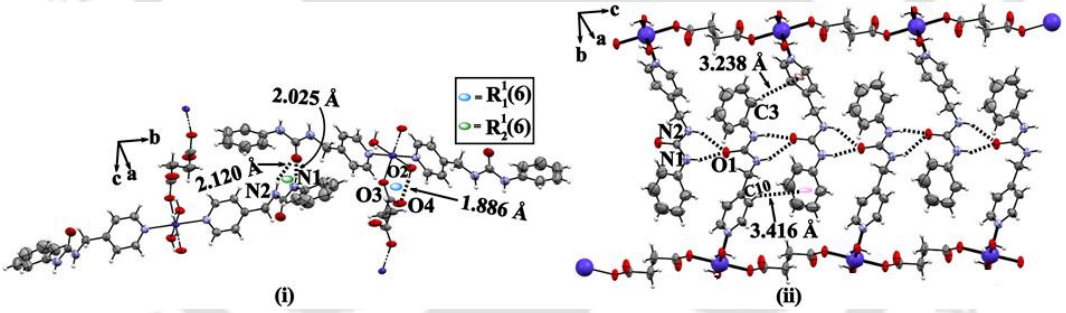

(a)

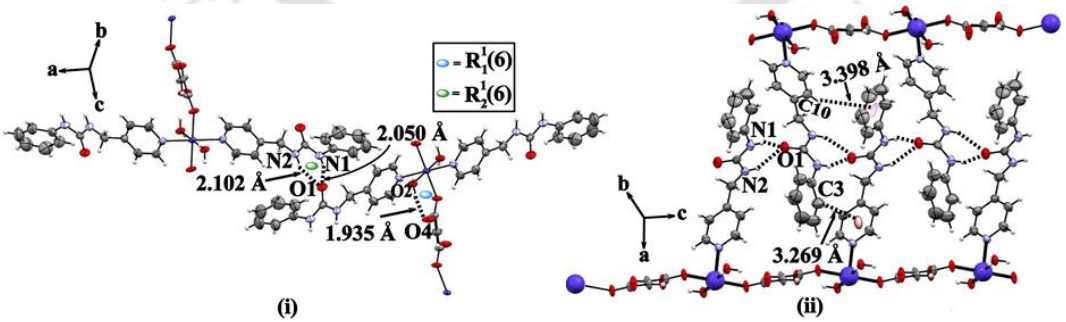

(b)

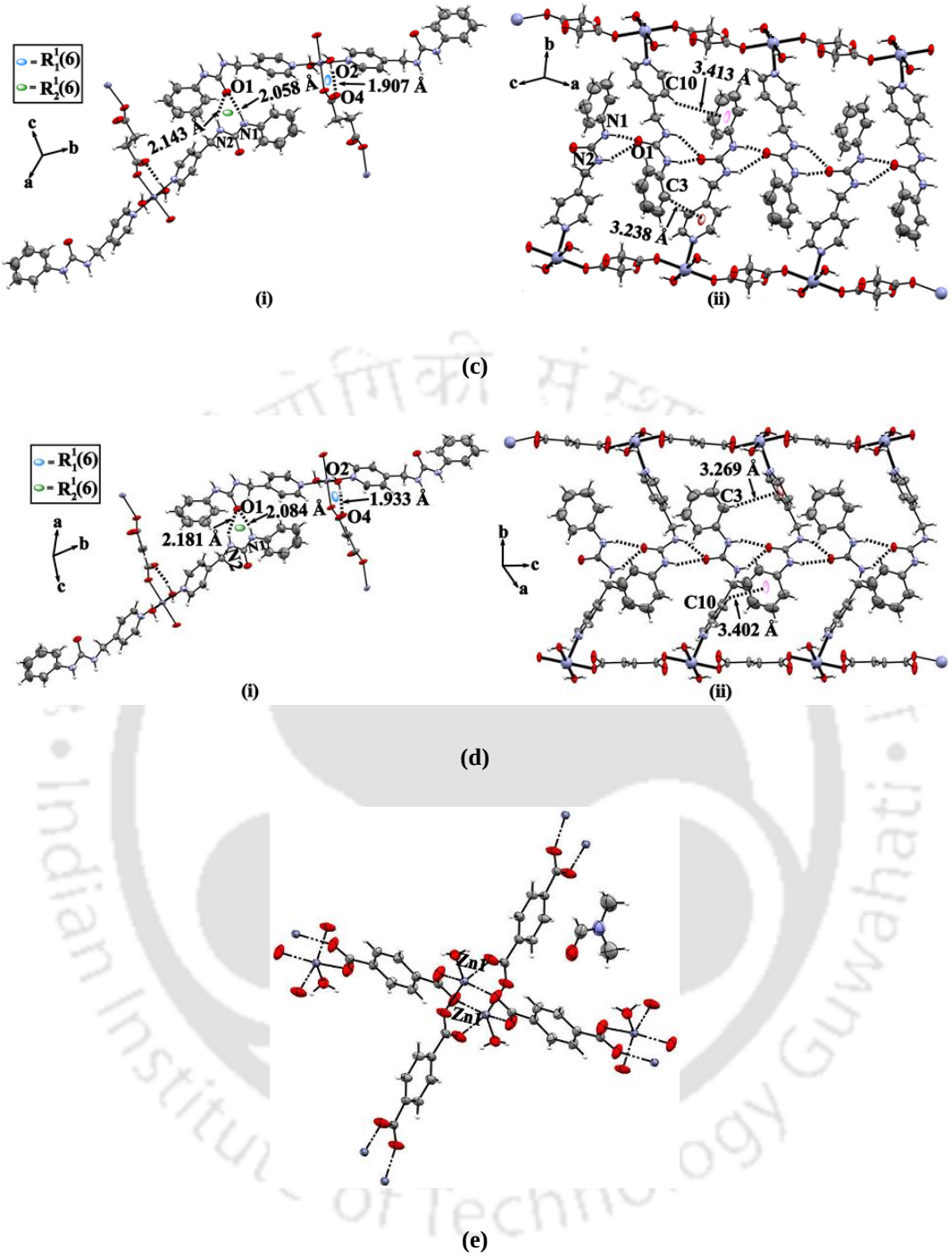

Figure 4.3. (i) urea α-tape network and intramolecular hydrogen-bonded cyclic motif having $R^1_1(6)$ synthon, (ii) C-H···π interactions in isostructural **CPs** (a) **4.1**, (b) **4.2**, (c) **4.4**, and (d) **4.5**; (e) ORTEP structure of **CP-4.6**

In the cobalt(II) terephthalate coordination polymer **CP-4.3**, terephthalate bridges (Fig. 4.4a) are present, and the orientations of the **L4.1** are different from the other coordination polymers. The carboxylate group formed intramolecular hydrogen bonds with the aqua ligand, giving an $R^1_1(6)$ synthon (Figs. 4.4b, 4.5c). No urea tapes are present in this

coordination polymer (Fig. 4.4b). The inter-chain interactions are formed through an intermolecular hydrogen bond between the carbonyl oxygen atom of **L4.1** and the aqua ligand (Fig. 4.4c). CH···π interaction is formed between the phenyl rings of **L4.1** and terephthalate (Fig. 4.4d). A three-dimensional coordination network is formed by intermolecular hydrogen bonding between the carboxylate group of the coordinated terephthalate and the -NH group adjacent to the phenyl ring of the **L4.1** molecules (Fig. 4.4e).

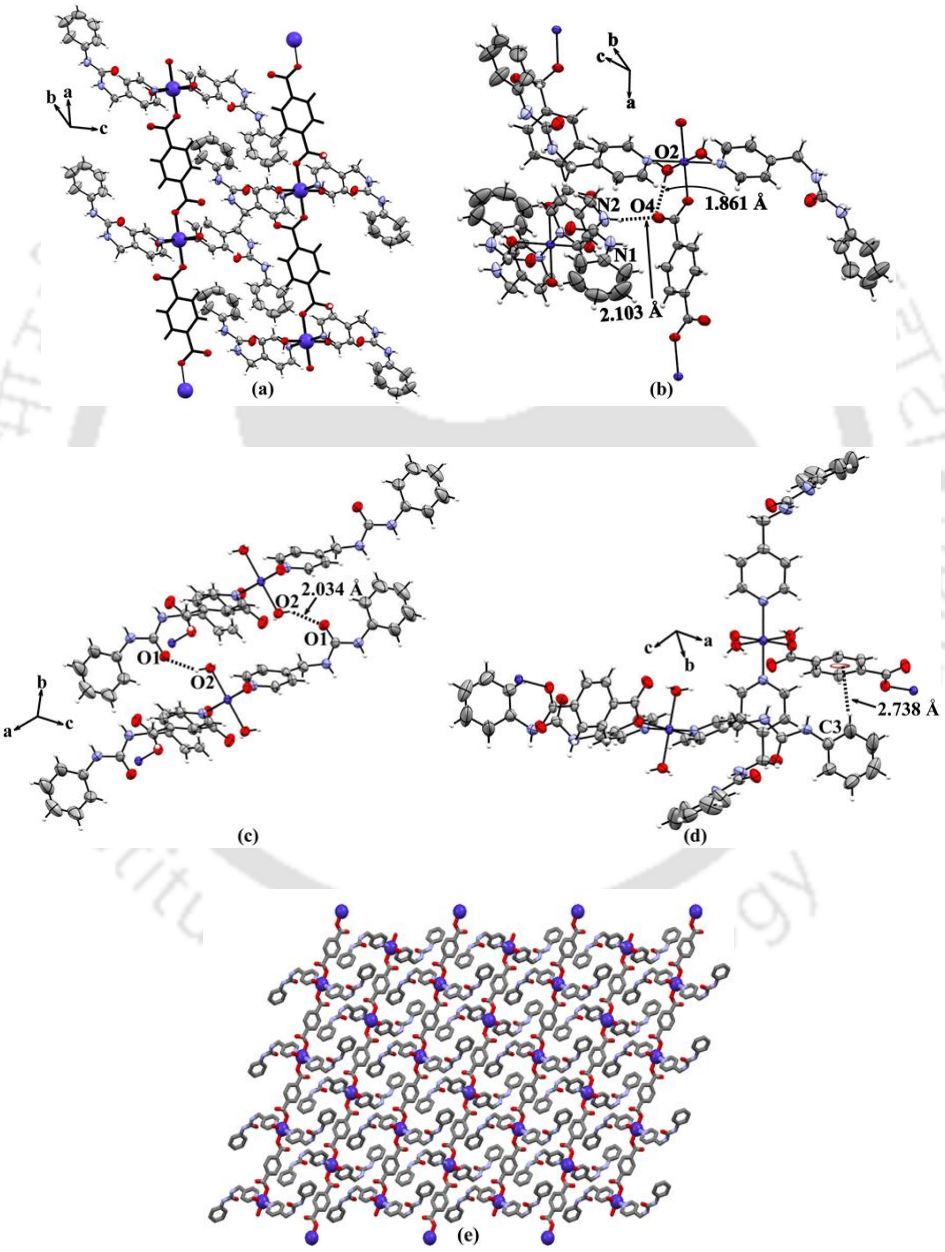

Figure 4.4 (a) Terephthalate bridges (carbon and hydrogen atoms of terephthalate ring were presented as capped sticks for clarity), (b) absence of urea tapes, (c) inter-chain hydrogen bond, (d) CH···π interaction, and (e) three-dimensional network along crystallographic *b*-axis in **CP-4.3**

The supramolecular assemblies and the related properties of the first-row transition metal carboxylate coordination polymers having naphthalimide-based pyridine ancillary ligands were guided by the π-π stacking interactions between the naphthalimide rings.[53] In our study, the supramolecular features of both **$L_{4.1}$** and dicarboxylate coligand contributed to the packing pattern of the coordination polymers.

Table 4.4. Hydrogen bond parameters in coordination polymers **CPs 4.1-4.5**

Distance(Å), angle (°)	**CP-4.1**	**CP-4.2**	**CP-4.3**	**CP-4.4**	**CP-4.5**
N1-H···O1 ($d_{D\cdots A}$)	2.835 (4)	2.829 (3)	No interaction	2.830 (3)	2.834 (3)
N2-H···O1 ($d_{D\cdots A}$)	2.876(3)	2.870 (3)	No interaction	2.874 (3)	2.870 (3)
N2-H···O4 ($d_{D\cdots A}$)	No interaction	No interaction	2.922(2)	No interaction	No interaction
O2-H···O1 ($d_{D\cdots A}$)	No interaction	No interaction	2.753 (2)	No interaction	No interaction
O2-H···O4 ($d_{D\cdots A}$)	2.674 (3)	2.688 (3)	2.669 (16)	2.676 (3)	2.685 (3)
O2-H···O4 ($d_{D\cdots A}$)	2.675 (3)	2.662 (3)	2.669 (2)	2.672 (3)	2.668 (2)
∠N1-H···O1	160 (3)	158(4)	No interaction	149	157 (3)
∠N2 -H···O1	149 (4)	151 (4)	No interaction	143	149 (3)
∠N2 -H···O4	No interaction	No interaction	167 (2)	No interaction	No interaction
∠O2-H···O4	166	152	No interaction	150	152
∠O2-H···O1	No interaction	No interaction	146	No interaction	No interaction
∠O2-H···O4	156 (3)	178 (5)	166 (2)	177	176 (4)
CP-4.3 had no bifurcated hydrogen bonds among urea moieties. Atom labels are as in Figure 4.3					

(a) Robust hydrogen-bonded motif in all CPs other than CP-4.3

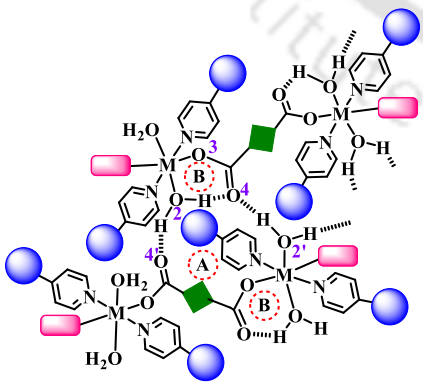

(b) Urea tapes found in CPs other than CP-4.3

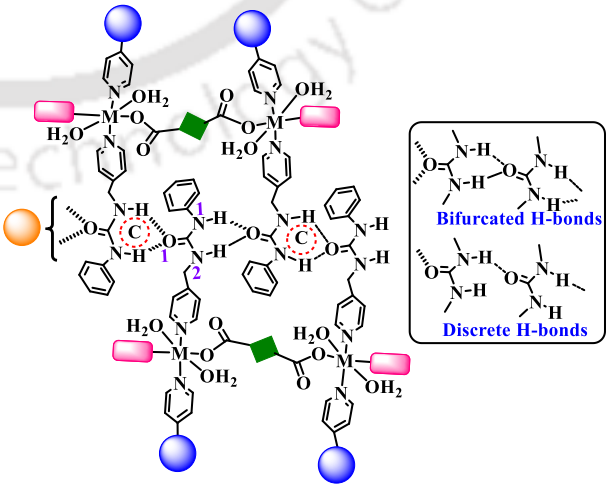

(c) Hydrogen-bonded motif in CP-4.3

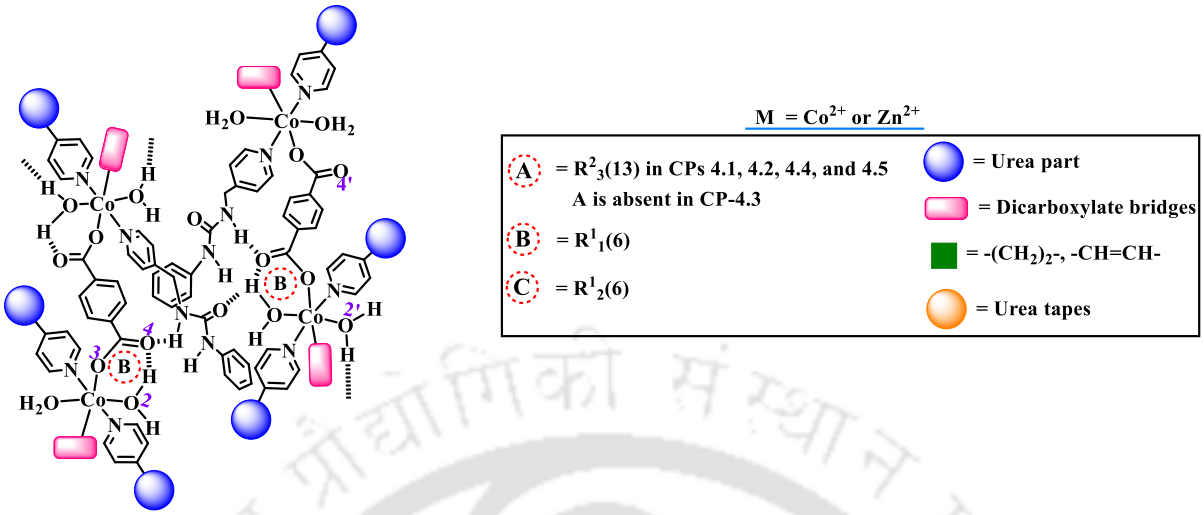

Figure 4.5. Schematic representation of different hydrogen-bonded motifs in the coordination polymers: (a) and (b) in the self-assemblies of **CPs 4.1**, **4.2**, **4.4**, **4.5**; and (c) in **CP-4.3**

4.4. Hirshfeld surface analyses of isostructural CPs

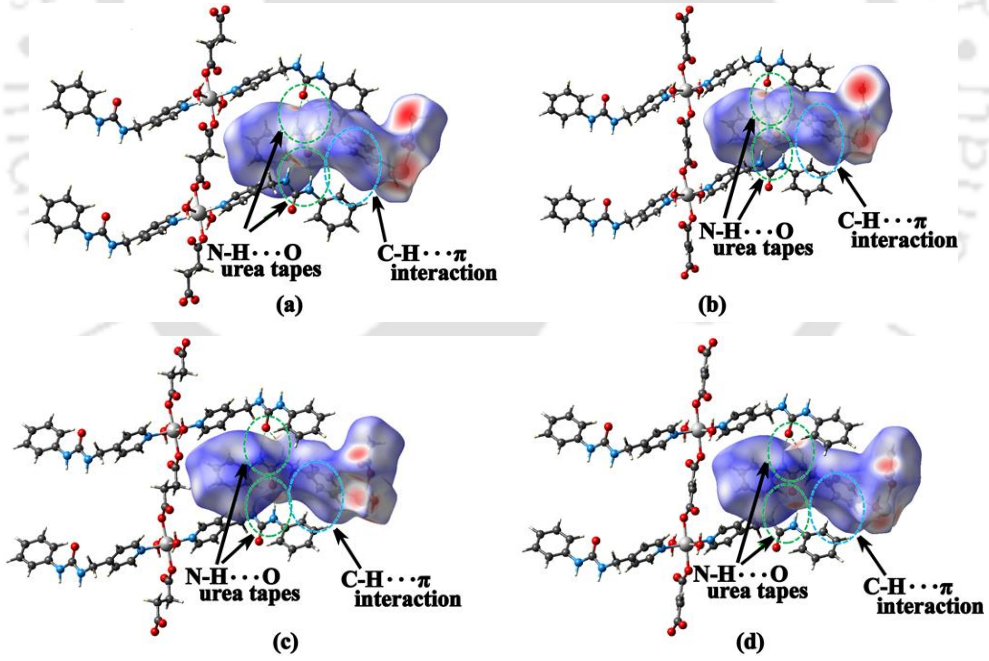

Figure 4.6. (i) Hirshfeld surfaces of isostructural **CPs** (a) **CP-4.1**, (b) **CP-4.2**, (c) **CP-4.4**, and (d) **CP-4.5**

To compare structural similarities among the isostructural coordination polymers, the Hirshfeld surface and 2D-finger print plot analysis of intermolecular hydrogen bond contributions in the isostructural **CPs 4.1**, **4.2**, **4.4**, and **4.5** were analyzed. As shown in Fig. 4.6, the red spots at the contact points represent the strong tendency to form hydrogen bonds.

All these four isostructural **CPs 4.1**, **4.2**, **4.4**, and **4.5** have higher percentage of hydrophobic H···H interactions in the range of 42-46% in comparison to a heteroatom (N or O)···H hydrophilic interactions (Table 4.5).

Table 4.5. Percentages of the H···C, H···H, H···O, H···N, and H···anion interaction (included reciprocal contacts) in 2D fingerprint plots

CPs	Interaction (%)			
	C···H	H···H	N···H	O···H
4.1	22.7	46.3	4.0	20.5
4.2	24.3	42.4	3.9	21.3
4.4	22.1	45.1	3.2	23.0
4.5	24.4	42.5	3.9	21.3

4.5. Spectroscopic characterization of the coordination polymers CPs 4.1-4.5

4.5.1. FTIR (ATR) spectral study

The IR spectra of the coordination polymers were compared together with those of the ligands. As discussed in section 4.2, the ligand showed N-H stretching at 3323 cm^{-1}. The IR bands corresponding to C=O and C-N (pyridyl ring) bonds appeared at 1675 and 1316 cm^{-1}, respectively. As compared to the observed bands in a free form, a significant shift in the IR stretching frequencies of $\mathbf{L_{4.1}}$ and dicarboxylates, namely, succinate, fumarate, and terephthalate, were observed after complexation in all the five **CPs 4.1-4.5** (Fig. 4.7, Table 4.6). The C=O stretching of $\mathbf{L_{4.1}}$ shifted from 1675 cm^{-1} to the region between 1634-1655 cm^{-1} upon complexation in the **CPs 4.1-4.5**. A characteristic shift in the N-H stretching at 3278-3323 cm^{-1} was also observed after complexation. For the coordinated monodentate dicarboxylates, the C=O stretch appeared in the range 1574-1606 cm^{-1}. In general, the C=O stretch appeared at 1720 cm^{-1} (in succinic acid) and 1680 cm^{-1} (in fumaric and terephthalic acids). The C=N stretching bands of the pyridine ring appeared at 1311-1313 cm^{-1} in these **CPs**. Broad peaks of O-H stretching of the aqua ligand appeared in the range of 3029-3112 cm^{-1}. However, in the case of **CP-4.3**, two O-H bands were observed, 3065 (br) and 3278 (br). It was due to the hydrogen bond formation of the aqua ligand of **CP-4.3** with two different atoms, namely, carboxylate O2 of terephthalate (O2-H···O4, $d_{H\cdots A}$ = 1.861 (2) Å) and the carbonyl O1 of $\mathbf{L_{4.1}}$ (O2-H···O1, $d_{H\cdots A}$ = 2.034 Å). It is evident that the formation of the X-H···Y hydrogen bond weakens the X-H bond strength and results in a red shift of the X-H stretching frequency, followed by an increase in intensity and band broadening.[54] Thus,

3065 (br) and 3278 (br) bands in **CP-4.3** corresponded to the O-H stretching due to O2-H···O1 and O2-H···O4 hydrogen bonds, respectively.

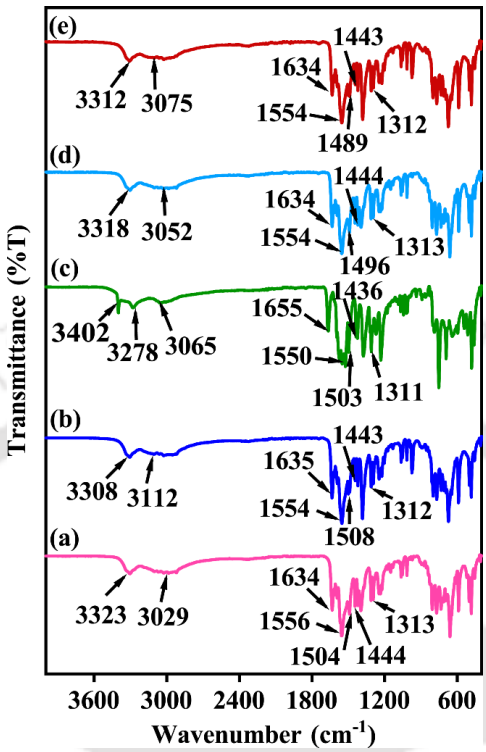

Figure 4.7. FT-IR (ATR) spectra overlay of the solid samples of coordination polymers (a) **CP-4.1**, (b) **CP-4.2**, (c) **CP-4.3**, (d) **CP-4.4**, and (e) **CP-4.5**

Table 4.6. IR stretching frequencies of **$L_{4.1}$** and **CPs 4.1-4.5**

Group	**Stretching frequencies (cm^{-1}), appearance**					
	$L_{4.1}$	**CP-4.1**	**CP-4.2**	**CP-4.3**	**CP-4.4**	**CP-4.5**
O-H (aqua)	3427 (s)	3029 (br)	3112 (br)	3065 (br), 3278 (br)	3052 (br)	3075 (br)
N-H stretch	3323 (m)	3323 (m)	3308 (m)	3402 (m)	3318 (m)	3312 (m)
C=O stretch ($L_{4.1}$)	1675 (s)	1634 (s)	1635 (s)	1655 (s)	1634 (s)	1634 (s)
C=O stretch (dicarb)	-	1600 (m)	1596 (w)	1574 (w)	1604 (w)	1606 (m)
N-H bend	1599 (s)	1556 (s)	1554 (s)	1550 (w)	1554 (s)	1554 (s)
C-N stretch (between carbonyl C and N of N-H group)	1555 (s)	1504 (w)	1508 (w)	1503 (w)	1496 (w)	1489 (w)
C-N stretch (between aromatic C and N of N-H group)	1497 (s)	1444 (s)	1443 (s)	1436 (s)	1444 (s)	1443 (s)
C=N stretch (in pyridyl ring)	1316 (s)	1313 (s)	1312 (s)	1311 (s)	1313 (s)	1312 (s)

4.5.2. Powder X-ray diffraction study

As we obtained **$(L_{4.1})\cdot H_2O$** and **CPs 4.1-4.6** in crystalline form, it was necessary to compare their phase purity with the simulated pattern generated from the CIF files of the respective compounds. MERCURY software[55] was used to determine the Miller indices of the powder X-ray patterns. In all six cases, the experimental patterns matched the simulated ones, indicating the high purity of the bulk materials (Fig. 4.8). The similarity of the experimental powder X-ray pattern of **CP-4.6** with the simulated pattern confirmed that this coordination polymer was the same as GECXUH02.[39]

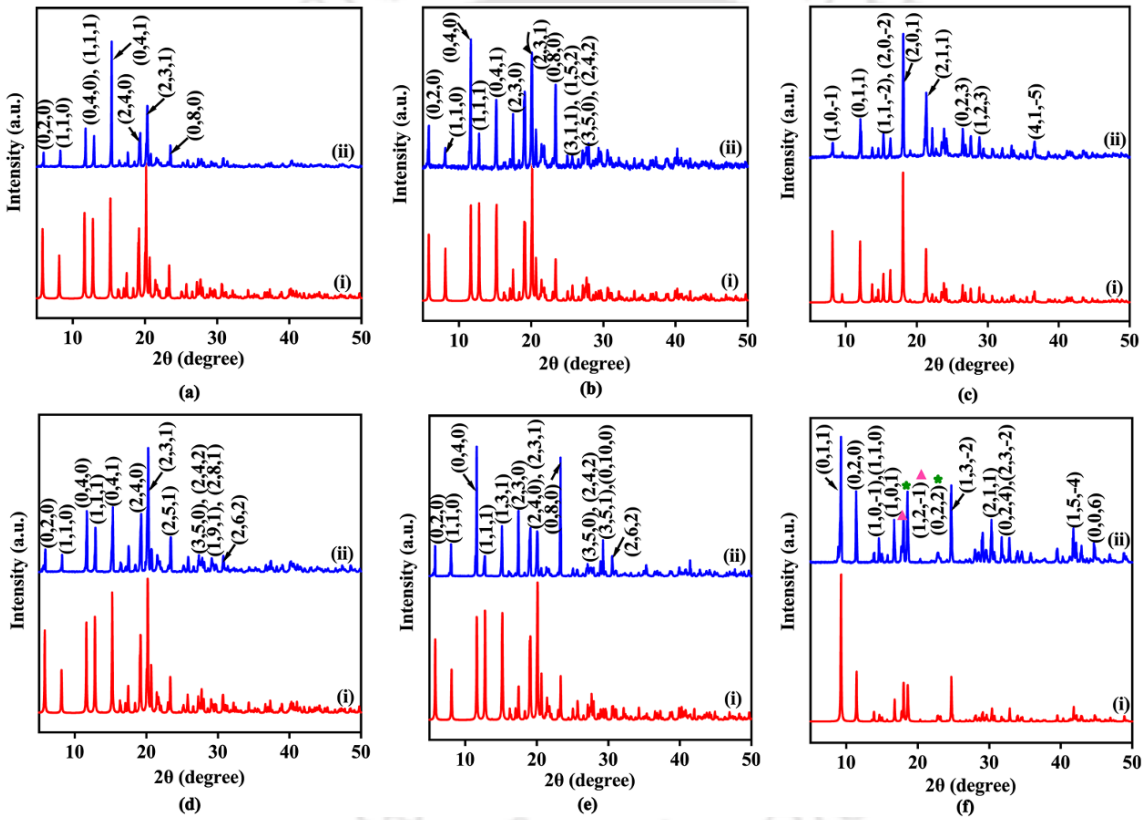

Figure 4.8. Powder X-ray patterns of **CPs** (a) **4.1**, (b) **4.2**, (c) **4.3**, (d) **4.4**, (e) **4.5,** and (f) **4.6** (where, in each case, (i) and (ii) are simulated and experimental powder X-ray patterns respectively)

4.5.3. Thermogravimetric analysis

The thermogravimetry of **$L_{4.1}$** and **CPs 4.1-4.5** were studied to determine their dehydration and thermal stability. The different types of hydrogen bond environments of the coordinated water molecule in the **CPs 4.1-4.5** were reflected in their respective thermograms. The ligand

$L_{4.1}$·H_2O showed a weight loss of 7.88% from 63 °C to 121 °C due to the loss of one water molecule of crystallization (calculated 7.34%) (Fig. 4.9a). In **CP-4.1**, a weight loss of 5.45% in the temperature range 150 °C to 175 °C was observed. This occurred due to the loss of two coordinated aqua ligands (calculated 5.41%). Further weight loss was completed at 342 °C, which yielded cobalt oxide (experimental 11.76%, calculated 11.25%) (Fig. 4.9b). For **CP-4.2**, the loss of 2.7% for one coordinated aqua ligand occurred from 121 to 156 °C. The second aqua ligand was lost at 3.82% from 156 to 184 °C (calculated 2.72%). Weight loss was completed at 385 °C, yielding cobalt oxide (experimental 11.41%, calculated 11.30%) (Fig. 4.9c). In **CP-4.3**, a weight loss of 4.37% was observed from 86 °C to 111 °C due to the

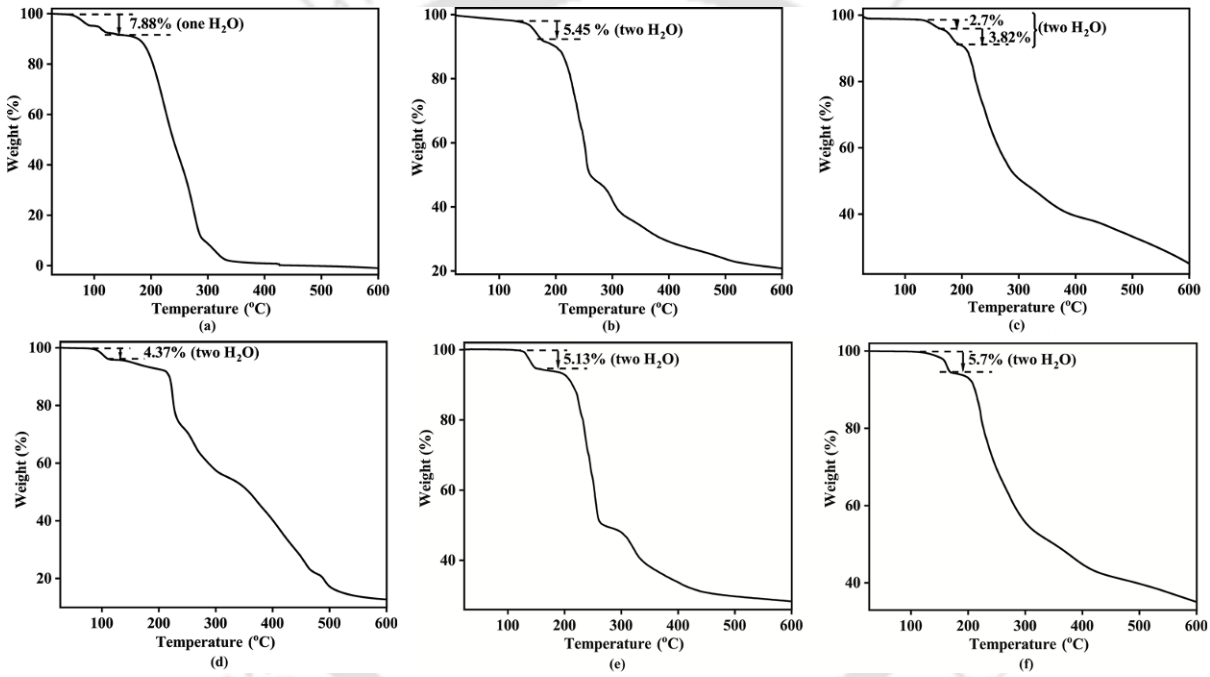

Figure 4.9. Thermogram of (a) **$L_{4.1}$**, and **CPs** (b) **4.1**, (c) **4.2**, (d) **4.3**, (e) **4.4**, and (f) **4.5**

loss of two aqua ligands (calculated 5.05%). Further weight loss was completed at 468 °C, which yielded cobalt oxide (experimental 9.4%, calculated 10.5%) (Fig. 4.9d). In **CP-4.4**, a 5.13% weight loss took place between 126 °C and 148 °C due to the loss of two coordinated aqua ligands (calculated 5.36%). Further weight loss took place at 265 °C to give zinc oxide (experimental 11.38%, calculated 12.11%) (Fig. 4.9e). In **CP-4.5**, a 5.7% weight loss took place between 117 °C and 168 °C due to the loss of two water molecules of the lattice (calculated 5.4%). Weight loss was completed at 312 °C to give zinc oxide (experimental 11.61%, calculated 12.11%) (Fig. 4.9f). The loss of aqua ligands at two stages was only observed in **CP-4.2** (121-184 °C), similar to the water loss from the hydrated ligand

($L_{4.1}$)·H_2O. But in **CPs 4.1**, **4.3**, **4.4**, and **4.5**, the two coordinated aqua ligands were lost in a single step. The thermal loss of aqua ligand from the coordination polymers occurred at higher temperatures than the standard boiling point of water. The loss of aqua ligands in two steps (in **CP-4.2**) occurred due to a change in the coordination sphere to transform to another form of **CPs**. Due to the presence of an aqua ligand per metal site, it probably served as a bridge to crosslink the chains of **CP-4.2** by dehydration. It was reported earlier that aqua-bridged cobalt carboxylate complexes were easily formed, whereas zinc complexes often formed carboxylate complexes with or without coordinated water molecules.[56,57] A stepwise thermal loss of aqua ligands took place from the metal carboxylate complexes due to different hydrogen bond environments. [58,59] Coordinated water and water molecules of crystallization underwent dehydration at distinguishable temperatures in some coordination polymers.[60] Thus, metal ion and hydrogen bonding scaffold contributed to the differences in the dehydration of aqua ligands in our cobalt and zinc coordination polymers **4.1-4.5**.

4.5.4. Solid-state UV-visible and photoluminescence spectroscopy

The ligand **($L_{4.1}$)·H_2O** showed absorption at 291 nm due to n-π* transition. The coloured cobalt(II) **CPs 4.1-4.3** showed absorption in the range of 282-324 nm due to n-π* transition. In the visible region, these three **CPs** showed absorption between 494-498 nm due to $^4T_{2g} \leftarrow {}^4T_{1g}$ transition. On the other hand, the colourless zinc(II) **CPs 4.4** and **4.5** showed two absorbances in the UV region due to n-π* and d-d transitions (Fig. 4.10a, Table 4.7). The solid sample of the **($L_{4.1}$)·H_2O** showed broad emissions at 473 nm, 492 nm, and 530 nm upon excitation at 330 nm due to aggregation-induced emission. The cobalt(II) **CPs 4.1-4.3** were non-emissive due to the paramagnetic nature of the cobalt(II) metal center. However, the zinc(II) **CPs 4.4** and **4.5** showed dual emission 400-510 nm due to metal-to-ligand charge transfer transition, where aggregation affected the emission positions (Fig. 4.10b, Table 4.7). Zinc(II) complexes are well known to show dual emission due to twisted intramolecular charge transfer and metal-to-ligand charge transfer transition[61–63] and in the present case also, such a situation occurred with emission at a shorter and a longer wavelength due to such paths being operative. In **CP-4.5**, the dicarboxylate ancillary ligand, namely fumarate, has a double bond, which was responsible for the more rigidity nature of **CP-4.5** compared to that

in **CP-4.4**, having a flexible ethylene bridging unit in the succinate. Thus, the change in hydrogen bonding caused aggregation resulting in the shift of the emission wavelengths.

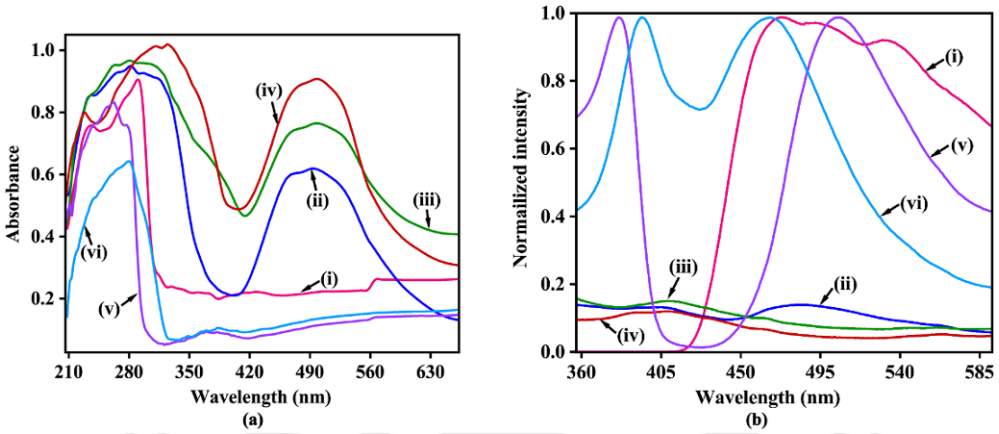

Figure 4.10. (a) UV-visible, and (b) photoluminescence spectra of the solid samples of (i) **($L_{4.1}$)·H_2O**, **CPs** (ii) **4.1**, (iii) **4.2**, (iv) **4.3**, (v) **4.4**, (vi) **4.5** (for all compounds, λ_{ex} = 330 nm)

Table 4.7. absorbance and emission wavelengths of the solid samples of **($L_{4.1}$)·H_2O** and **CPs 4.1-4.5**

Compound	λ_{max} (nm)	λ_{em} (nm) (λ_{ex} = 330 nm)
($L_{4.1}$)·H_2O	291	473, 492, 530
CP-4.1	282, 494	Non-emissive
CP-4.2	282, 498	Non-emissive
CP-4.3	324, 498	Non-emissive
CP-4.4	262, 368	381, 506
CP-4.5	281, 384	394, 467

4.6. Aggregation-induced emission of ligand $L_{4.1}$

The solid sample of **($L_{4.1}$)·H_2O** showed a broad emission in the region 473 nm-530 nm. The large shifts of the emission peak towards higher wavelength were due to aggregation-induced emission.[64] In the DMSO solvent, **$L_{4.1}$** was weakly emissive, showing emission peaks at 373 nm and 396 nm, and it also showed aggregation-induced quenching followed by enhancement upon adding different fractions of water (Fig. 4.11). It was found that with an increasing concentration of water to 60% water, aggregation-induced quenching took place at 373 nm and 396 nm. In contrast, an increase in the concentration above 60% water resulted in emission enhancement at 373 nm and 400 nm. The ^{1}H-NMR titration carried out by adding D_2O to a solution of **$L_{4.1}$** showed that only the chemical shifts of the N-H were affected by

increasing concentration of D_2O. This suggested that the compound did not change its ground state; no structural changes were observed from the titration.

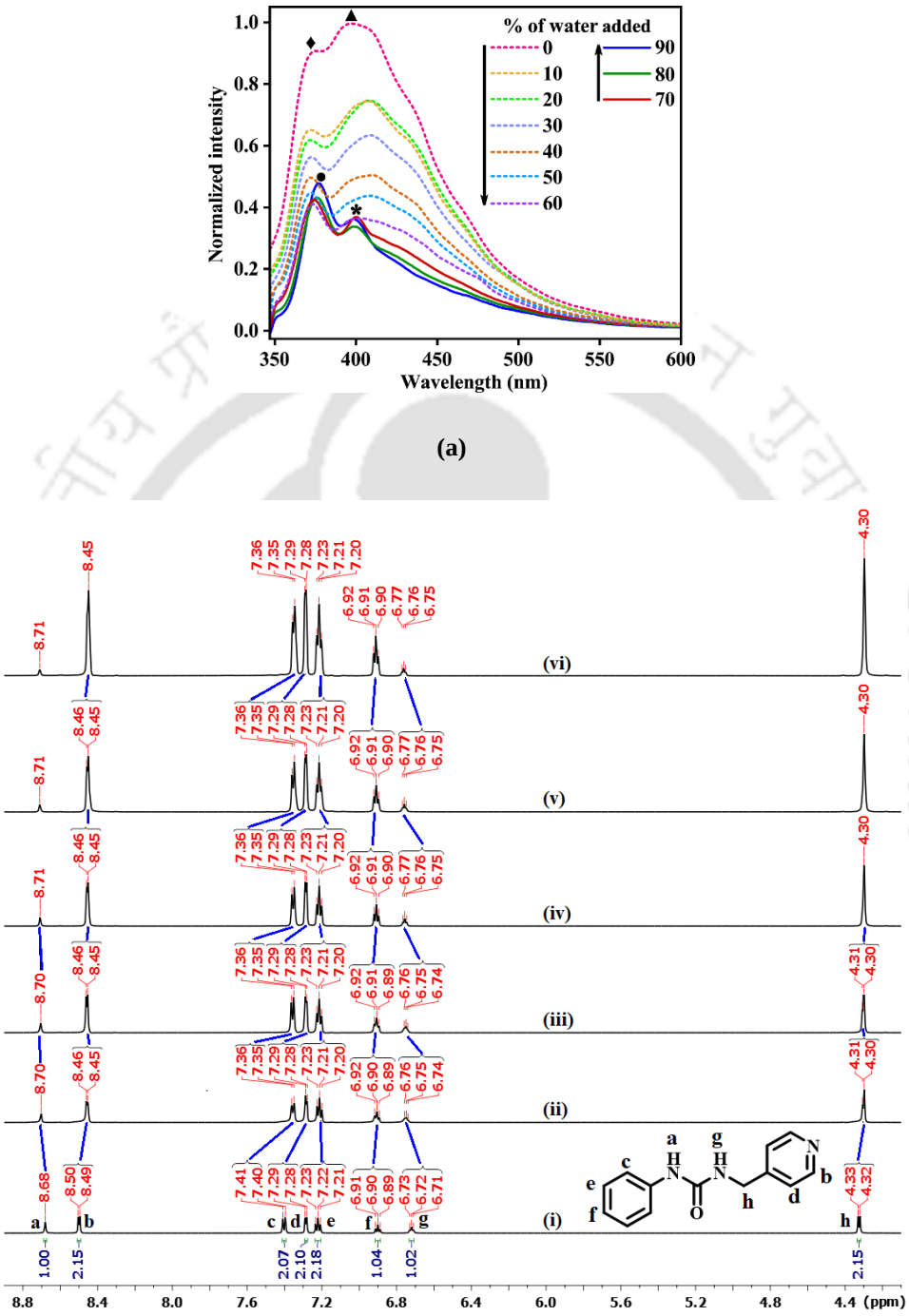

Figure 4.11. (a) Fluorescence emission spectra of **L4.1** (10^{-4} M) in DMSO (λ_{ex} = 330 nm) with the concentration of water varying from 10% to 90% (♦ 373 nm, ▲ 396 nm, ● 377 nm, * 399 nm), and (b) ^{1}H-NMR (600 MHz) spectra of **L4.1** in (i) DMSO-d_6 and with different fractions of D_2O (ii) 10% (iii) 30% (iv) 60% (v) 70% (vi) 90%

4.7. Dye adsorptions by the coordination polymers CPs 4.1-4.6

Organic dyes are toxic colouring agents that are used in various chemical laboratories. Their presence in water and the environment is a concern for human health. So, their adsorption by an insoluble adsorbant and recovery of the adsorbent are being pursued by researchers. In this regard, the porousity and hydrogen bonding abilities of various metal frameworks make them good candidates for dye adsorptions.[65–67] In the present case, all the six coordination polymers **4.1-4.6** were insoluble in water. So, their utility in adsorbing dyes was explored. Four different cationic and anionic dyes, namely methyl orange (MO) (anionic), phenol red (PR) (anionic), rhodamine blue (RhB) (cationic), and methylene blue trihydrate (MBT) (cationic) (Figs. 4.12a-d), were chosen with an expectation that these dyes would bind easily to the -NH sites of $\mathbf{L_{4.1}}$ by hydrogen bonds (Figs. 4.12e-i). A hydrolytic ring opening of PR assisted by a **CP** would yield ring-opened quinone methide form from the bis-phenol form of PR (Figs. 4.12b). PR would have lower binding ability unless it underwent a ring-opening reaction to bind through the sulphonate group, as illustrated in Fig. 4.12f and Fig. 4.12g.

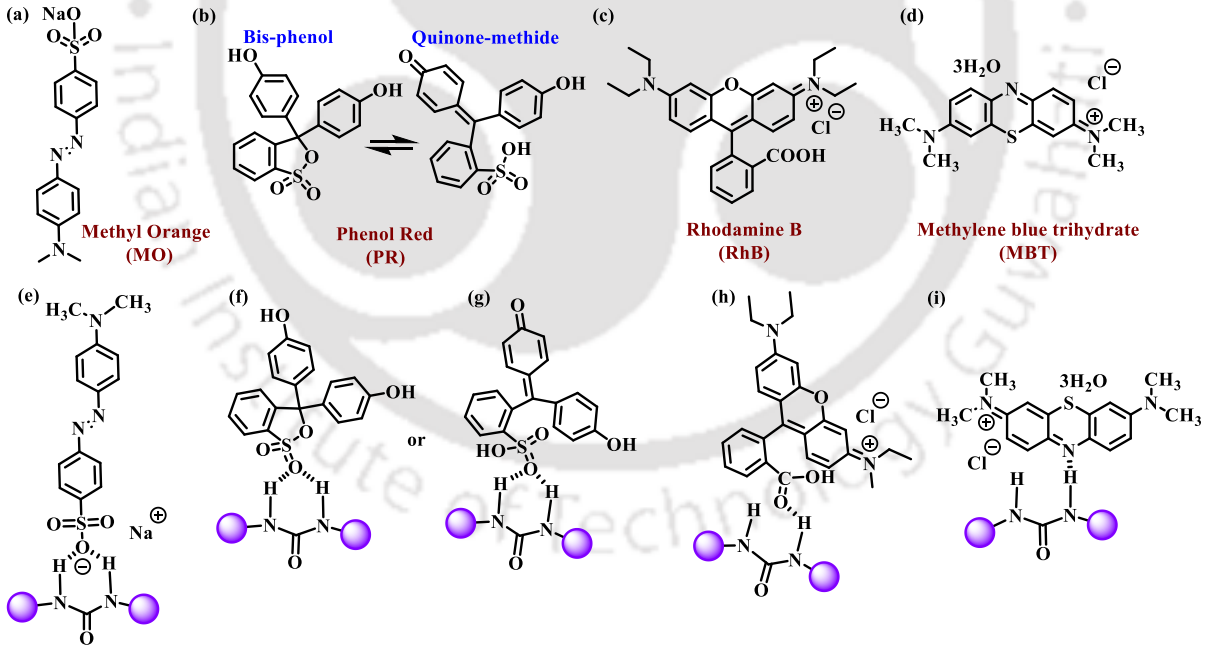

Figure 4.12. Structures of dyes (a) methyl orange, (b) two forms of phenol red, (c) rhodamine blue, (d) methylene blue trihydrate. (e)-(i) Possible hydrogen bonding through the sulphonate group of the two dyes.

The coordination polymers could be used for selective adsorption of dye, which causes decolourisation of the dye. All the **CPs** showed decolourising abilities for MO. The changes

in the adsorption profiles of the four dyes, namely MO, PR, RhB, and MBT, were monitored at 464, 432, 554, and 665 nm, respectively. The spectral changes are shown in Figs. 4.13. The spectra were from the dye samples after treating independently for three hours with respective insoluble **CPs** as suspension. From the plots in Fig. 4.13(a), it was found that **CP-4.3** recognized MO selectively as compared with the other CPs. It was found that 1.986 mg g^{-1} MO per gram of **CP-4.3** was decolourised; in comparison to this, 1.320 mg g^{-1}, 1.369 mg g^{-1}, 0.867 mg g^{-1}, and 0.731 mg g^{-1} of MO (Table 4.8), respectively were decolourised by **CP-4.1**, **CP-4.2**, **CP-4.4**, and **CP-4.5**. Thus, **CPs 4.1**, **4.2**, **4.4**, and **4.5** could not cause decolourisation of MO. In the adsorption of PR dye, **CP-4.2** caused a fraction of the ring-opening reaction of PR, as reflected in the development of a new peak at 560 nm. **CP-4.2**, however, decolourised 0.714 mg g^{-1} of PR. In this case, a small fraction of the PR underwent a ring-opening reaction. **CP-4.1** did not show selectivity in the adsorption of anionic dyes and had comparable adsorptions of both dyes in a similar manner as **CP-4.2**. A set of zinc CPs derived from 1,3,5-benzenetricarboxylic acid and 1,4-bis(4-pyridyl)-2,3-diaza-1,3-butadiene were utilized for cationic dyes,[67] but were ineffective towards adsorption of MO which is an anionic dye. These results indicated that MO adsorption by **CP-4.3** was selective, and the same **CP** was not able to decolourise PR. This occurred because of the higher hydrogen bond formation ability of the oxygen atom bearing a negative charge of the sulphonate group of MO with the urea moiety of the **CPs**. Thus, it provided a means to recognize MO through decolourisation that was affected by the formation of hydrogen bonds with the CPs. We attempted to study competitive adsorption from a mixture of MO and PR but found that an equimolar mixture of MO and PR showed a common UV-visible peak at 443 nm (Fig. 4.15). This deterred us from further studying the competitive adsorption aspect. Among different dyes, MO has been widely studied with other adsorbents, and 100% efficiency in its adsorption was suggested with MIL-100-Fe.[68] The amounts of adsorption of MO by some adsorbents reported in the literature are compared in Table 4.9. The cationic dye RhB was adsorbed the highest by **CP-4.4** with an amount of 2.858 mg g^{-1}. All six **CPs** could not decolourize the cationic dye MBT. In practice, metal-organic frameworks (MOFs) are good adsorbents of dyes. From the comparison in Table 4.9, it is clear that the adsorption observed with the CPs in this study had low intake capability and will not have practical application. Furthermore, the analyses of MOFs studied in the literature were carried out by extrapolating the data collected from studies performed in solutions by using them in suspension or

heterogeneous conditions. In those experiments, the proportions of dye used with respect to the amount of adsorbent were also very low; hence, the practical utility of those claims on the adsorptions also requires attention. The adsorption of MO by **CP-4.6** was ascertained by us and it was found to be 1.309 mg g^{-1}.

Hence, the study of the adsorption ability of the four dyes by the present set of **CPs** helped to understand the observed recognition between the four dyes by the **CPs**. The relative removal efficiencies are shown in Fig. 4.14. Since the amounts adsorbed with respect to the weight percent of **CP** are very small, we would suggest the **CP** decolourising ability to be of a higher priority than the dye removal process to find an application in effective dye removal.

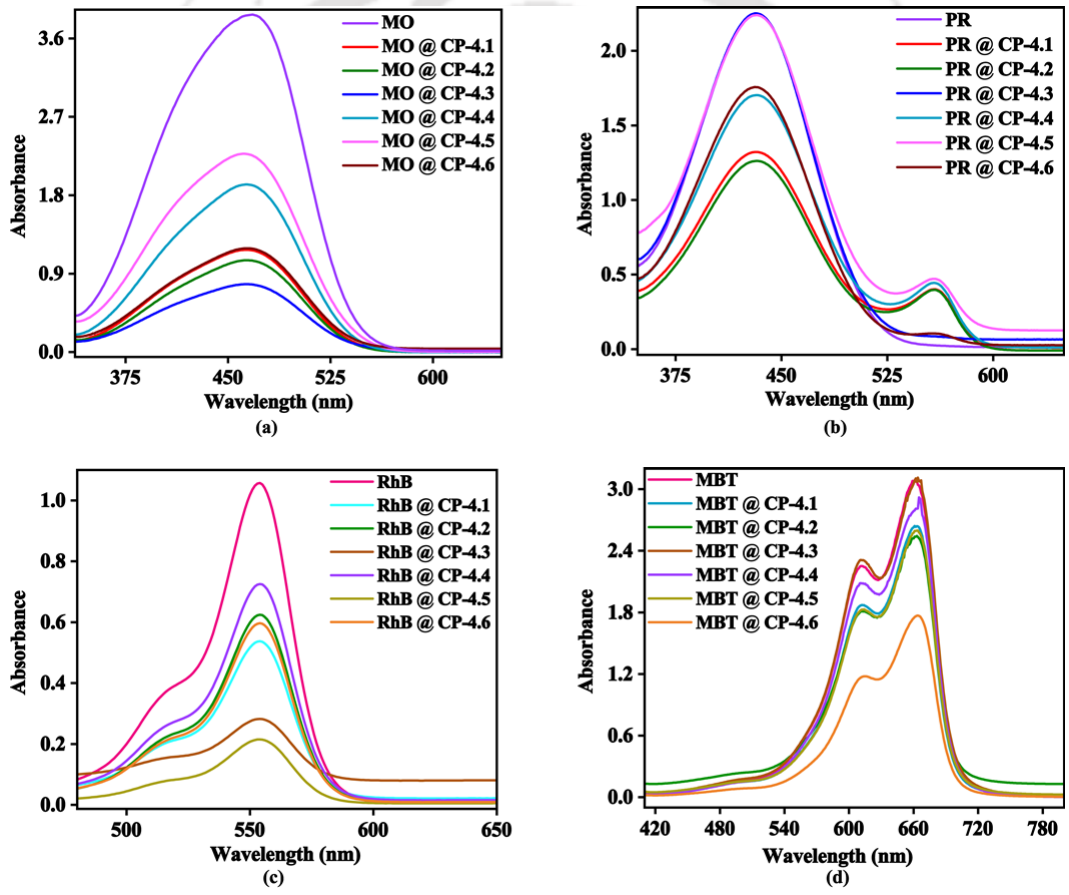

Figure 4.13. UV-visible spectral changes of (a) methyl orange (MO), (b) phenol red (PR), (c) rhodamine blue (RhB), (d) methylene blue trihydrate (MBT) after treating with **CPs 4.1-4.6**

Table 4.8. Amount of dyes adsorbed by **CPs 4.1-4.6**

Coordination polymers	Amount of dye adsorbed, q_e, (mg g^{-1}) and {dye removal (%)}			
	MO	**PR**	**RhB**	**MBT**
4.1	1.320 {48.4}	0.632 {21.4}	1.852{46.4}	0.45 {14.4}
4.2	1.369 {50.2}	**0.714 {24.2}**	1.524 {38.2}	0.58 {18.6}
4.3	**1.986 {72.83}**	0.100 {3.4}	2.698 {67.6}	0.08 {2.5}
4.4	0.867 {31.8}	0.378 {12.8}	1.297 {32.5}	0.16 {5}
4.5	0.731{26.8}	0.194 {6.6}	**2.858 {71.6}**	0.54 {16.6}
4.6	1.309 {48}	0.289 {9.8}	1.573{39.4}	**0.95 {30.4}**

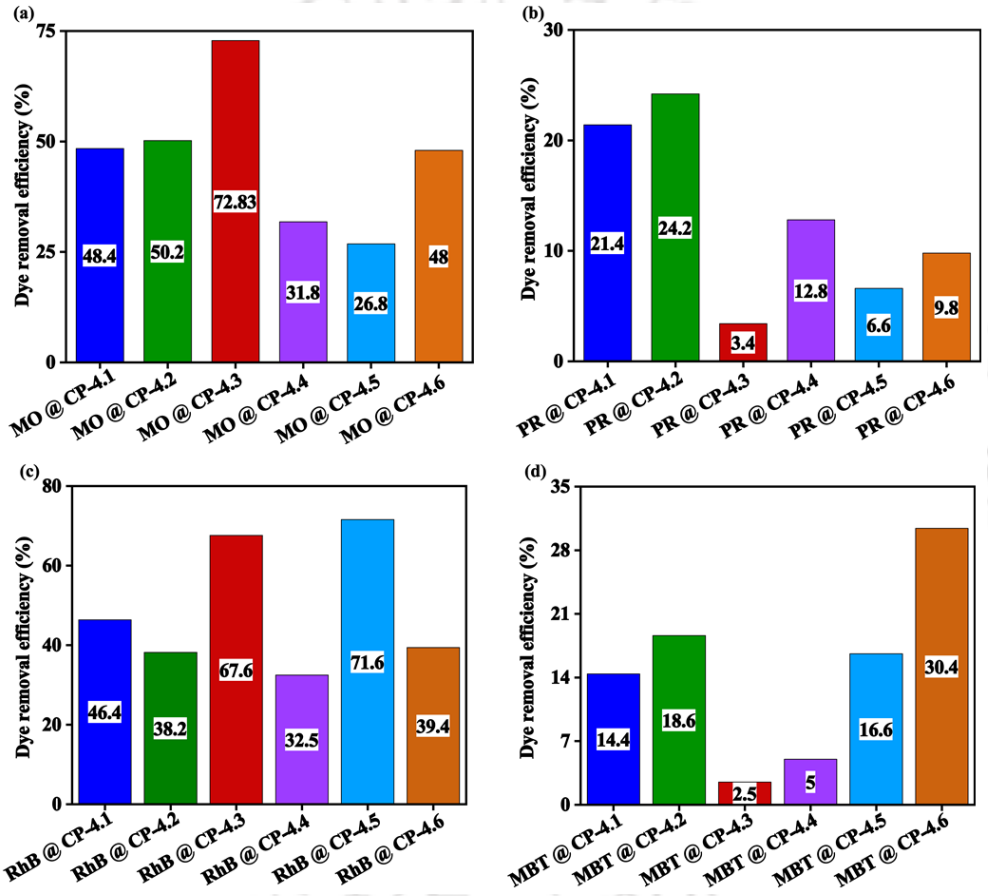

Figure 4.14. Relative removal efficiencies (a) methyl orange (MO), (b) phenol red (PR), (c) rhodamine blue (RhB), (d) methylene blue trihydrate (MBT) after treating with **CPs 4.1-4.6** (the spectra were taken after treatment of CPs with the dye for 3 h)

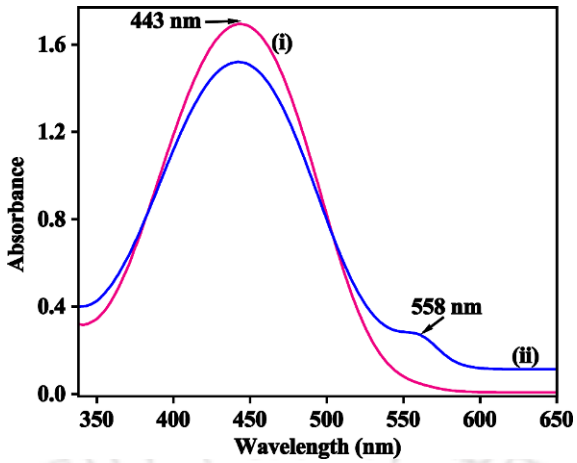

Figure 4.15. A mixture of MO and PR dyes adsorbed after (i) 0 hour, and (ii) 3 hours treatment by **CP-4.3**

Table 4.9. Amounts of methyl orange adsorbed by various adsorbents

Absorbent	**Amount (mg/g)**	**Reference**
Chromium terephthalate MOFs (MIL-101) (MIL = Matérial Institut Lavoisier)	114-194	69
Iron 1,3,5-benzenetricarboxylate MOF (MIL-100-Fe)	1045	68
Chromium 1,3,5-benzenetricarboxylate MOF (MIL-100-Cr)	736	68
Chromium amino functionalised carboxylate MOF (NH_2-MIL-101-Al)	188	70
{[$Zn_2(HL^1)_2(L^2)(H_2O)_2$][$C_2H_5OH)_3$}n ($H3L^1$ = 1,3,5-benzene tricarboxylic acid, L^3 = 1,4-bis(4-pyridyl)-2,3-diaza-1,3-butadiene	0.4	67
{[$Ag(L^3)_2$][BF_4)}$_n$, L^3 = N1,N4-bis((pyridin-3-yl)methyl) .ofumaramide	37.88	71
Melaminium Adipate	2.35	72
{[$Ni_2(L^4)_3$]·Cl·solvent}n HL^4 = 3,5-di(1H-imidazol-1-yl)phenyl)-2H-tetrazole)	285	73
[Co_2L_2(Suc)(H_2O)$_2$]$_n$	1.320	Present work
[Co_2L_2(Fum)(H_2O)$_2$]$_n$	1.369	
[Zn_2L_2(Suc)(H_2O)$_2$]$_n$	0.867	
[Zn_2L_2(Fum)(H_2O)$_2$]$_n$	0.731	

4.8. Conclusion

In this part of our thesis work, we have shown a change in metal ion and carboxylate moieties brings about subtle changes in the weak hydrogen bonding scheme in a series of dicarboxylate **CPs**. The metal ions influenced the fluorescence spectra; in the case of zinc complexes, dual emissions were observed from solid powdered samples. The cobalt

complexes were non-fluorescent due to the paramagnetic effect. The presence of terephthalate bridges rather than succinate or fumarate provided a different self-assembly having urea easily accessible to bind to MO better than to PR, RhB, and MBT. The presence of C–H···π interactions involving the phenyl ring next to urea caused conformational locking to decide the course of self-assembled structures of the **CPs**.

4.9. Experimental section

The detailed synthetic methodologies for the synthesis of the metal complexes are described. Analytical data are provided with each compound. The instrumental details, crystallographic parameters, and method used for dye adsorption study, are provided in Appendix section at the end of this chapter. The following abbreviations are used for identification of spin multiplicities in 1H-NMR spectra: s = singlet, d = doublet, t = triplet, q = quartet, m = multiplet; and for FTIR spectra, following abbreviations were used to identify the absorption bands: s = strong, w = weak, br = broad, m = medium.

Synthesis of 1-phenyl-3-(pyridin-4-ylmethyl)urea ($L_{4.1}$): Phenyl isocyanate (108 µL, 1 mmol) was dissolved in diethyl ether (15 mL). To this solution, 4-aminomethylpyridine (102 µL, 1 mmol) was added dropwise and stirred at room temperature overnight. A white precipitate was formed, which was filtered and dried. Yield: 90%. ESI MS: calculated [M+1] $C_{13}H_{13}N_3O$, 228.1092; found, 228.1194 [M+1]. The white precipitate was dissolved in methanol-water mixture (10 mL, v/v) and the solution was allowed to evaporate at 25 ºC, yielding colourless crystals of **($L_{4.1}$)·H_2O**. 1H NMR (DMSO-d_6, 600 MHz): 8.69 (s, 1H), 8.50 (d, J = 6 Hz, 1H), 7.40 (d, J = 6 Hz, 1H), 7.29 (d, J = 6 Hz, 1H), 7.23 (t, J = 6 Hz, 1H), 6.91 (m, J = 6 Hz, 1H), 6.73 (t, J = 6 Hz, 1H), 4.33 (d, J = 6 Hz, 2H). IR (cm^{-1}): 3427 (s), 3323 (m), 1675 (s), 1599 (s), 1555 (s), 1497 (s), 1440 (s), 1415 (s), 1316 (s), 1236 (m), 808 (s), 744 (m), 688 (s), 631 (w), 579 (s), 471 (s), 454 (s). UV, solid (λ_{max}): 291 nm.

General procedure for the synthesis of coordination polymers CPs 4.1, 4.2, 4.4, and 4.5: A mixture of **$L_{4.1}$** (0.454 g, 2 mmol) and dicarboxylic acid (1 mmol), namely, succinic acid (for **CPs 4.1** and **4.4**), or fumaric acid (for **CPs 4.2** and **4.5**), in methanol (10 mL), was stirred for 30 minutes at room temperature, respectively. To this solution, the corresponding cobalt(II) acetate tetrahydrate (0.249 g, 1 mmol) (for **CPs 4.1** and **4.2**),or zinc(II) acetate

dihydrate (0.220 g, 1 mmol) (for **CPs 4.4** and **4.5**), was added and the reaction mixture was refluxed for one hour. A pink precipitate was formed in the case of cobalt complexes, whereas a dirty white precipitate was formed in the case of zinc complexes. The precipitate obtained was redissolved in DMF–water mixture (1 : 1 v/v, 5 mL). The resulting solution was filtered and kept undisturbed for crystallisation, which yielded crystals of the corresponding **CP**.

$[Co_2(L_{4.1})_2(Suc)(H_2O)_2]_n$ (CP-4.1): Pink needle-like crystals, isolated yield 62.5% based on Co. Elemental analysis (%) calcd: C, 54.09; H, 5.10; N, 12.62; found: C, 53.97; H, 5.27; N, 12.99. IR (cm^{-1}): 3029 (br), 3323 (m), 1634 (s), 1556 (m), 1490 (w), 1444 (s), 1422 (s), 1396 (m), 1313 (s), 1295 (s), 807 (s), 771 (s), 734 (w), 693 (w), 660 (s), 589 (s), 502 (s), 484 (s). UV-visible, solid (λ_{max}): 282 nm, 494 nm.

$[Co_2(L_{4.1})_2(Fum)(H_2O)_2]_n$ (CP-4.2): Pink needle-like crystals, isolated yield 64% based on Co. Elemental analysis (%) calcd: C, 54.25; H, 4.82; N, 12.66; found: C, 53.77; H, 5.07; N, 12.69. IR (cm^{-1}): 3112 (br), 3308 (m), 1635 (s), 1554 (m), 1443 (s), 1422 (s), 1384 (s), 1312 (s), 1294 (s), 800 (s), 770 (s), 734 (w), 711 (w), 672 (s), 590 (s), 500 (s), 485 (s). UV-visible, solid (λ_{max}): 282 nm, 498 nm.

$[Zn_2(L_{4.1})_2(Suc)(H_2O)_2]_n$ (CP-4.4): Colourless plate-like crystals, isolated yield 59% based on zinc. Elemental analysis (%) calcd: C, 53.57; H, 5.06; N, 12.50; found: C, 53.72; H, 5.37; N, 12.78. IR (cm^{-1}): 3052 (br), 3318 (m), 1634 (s), 1554 (m), 1490 (w), 1444 (s), 1422 (s), 1395 (m), 1313 (s), 1294 (s), 807 (s), 771 (s), 735 (w), 661 (s), 588 (s), 502 (s), 483 (s). UV-visible, solid (λ_{max}): 262 nm, 368 nm.

$[Zn_2(L_{4.1})_2(Fum)(H_2O)_2]_n$ (CP-4.5): Colourless block crystals, isolated yield 60% based on Zn. Elemental analysis (%) calcd: C, 53.73; H, 4.77; N, 12.54; found: C, 52.51; H, 5.09; N, 12.93. IR (cm^{-1}): 3075 (br), 3312 (m), 1634 (s), 1554 (m), 1489 (w), 1443 (s), 1422 (s), 1382 (s), 1312 (s), 1293 (s), 1223 (w), 802 (s), 770 (s), 734 (s), 673 (s), 588 (s), 500 (s), 483 (s). UV-visible, solid (λ_{max}): 281 nm, 384 nm.

General procedure for the synthesis of coordination polymers CPs 4.3 and 4.6: To a solution of ligand **$L_{4.1}$** (0.454 g, 2 mmol) in methanol (10 mL), terephthalic acid (166.13 mg, 1 mmol) in DMF (5 mL) was added. The solution was allowed to stir at room temperature for 30 minutes. To this, cobalt(II) acetate tetrahydrate (0.249 g, 1 mmol) (for **CP-4.3**) or zinc(II)

acetate dihydrate (0.220 g, 1 mmol) (for **CP-4.6**), was added and the reaction mixture was refluxed for one hour. A pink (in case of **CP-3**) or white (for **CP-4.6**) precipitate was formed, which was redissolved in DMF-water mixture (1 : 1 v/v, 5 mL). The resulting solution was filtered and kept undisturbed for crystallisation.

$[Co_2(L_{4.1})_2(Ter)(H_2O)_2]_n$ (CP-4.3): Pink block crystals, isolated yield 63% based on Co. Elemental analysis (%) calcd: C, 57.17; H, 4.76; N, 11.77; found: C, 57.25; H, 5.18; N, 11.72. IR (cm^{-1}): 3065 (br), 3278 (m), 1655 (s), 1574 (w), 1550 (w), 1524 (w), 1436 (s), 1424 (s), 1376 (s), 1311 (s), 1271 (m), 1231 (s), 752 (s), 692 (s), 641 (w), 692 (s), 513 (w), 481 (s), 461 (s). UV-visible, solid (λ_{max}): 324 nm, 498 nm.

$[Zn_4(Ter)(H_2O)(DMF)]_n$ (CP-4.6): White block crystals, isolated yield 61.5% based on Zn. Elemental analysis (%) calcd: C, 41.17; H, 4.06; N, 4.36; found: C, 41.13; H, 4.01; N, 4.40. IR (cm^{-1}): 3289 (br), 3053 (w), 2931 (w), 1670(s), 1618 (s), 1504 (s), 1381 (s), 1434 (m), 1102 (s), 889 (m), 824 (s), 747 (s), 545 (s).

4.10. References

1 P. A. Gale, S. E. García-Garrido and J. Garric, *Chem. Soc. Rev.*, 2008, **37**, 151–190.

2 P. D. Beer and P. A. Gale, *Angew. Chemie Int. Ed.*, 2001, **40**, 486–516.

3 Y. Zhou, J. F. Zhang and J. Yoon, *Chem. Rev.*, 2014, **114**, 5511–5571.

4 C. M. G. dos Santos, T. McCabe, G. W. Watson, P. E. Kruger and T. Gunnlaugsson, *J. Org. Chem.*, 2008, **73**, 9235–9244.

5 J. Wu, B. Kwon, W. Liu, E. V Anslyn, P. Wang and J. S. Kim, *Chem. Rev.*, 2015, **115**, 7893–7943.

6 K. Honer, E. Kalfaoglu, C. Pico, J. McCann and J. Baltrusaitis, *ACS Sustain. Chem. Eng.*, 2017, **5**, 8546–8550.

7 K. Honer, C. Pico and J. Baltrusaitis, *ACS Sustain. Chem. Eng.*, 2018, **6**, 4680–4687.

8 L. Mazzei, V. Broll, L. Casali, M. Silva, D. Braga, F. Grepioni, J. Baltrusaitis and S. Ciurli, *ACS Sustain. Chem. Eng.*, 2019, **7**, 13369–13378.

9 A. Karmakar and J. B. Baruah, *Inorg. Chem. Commun.*, 2009, **12**, 140–144.

10 M. Tiliakos, P. Cordopatis, A. Terzis, C. P. Raptopoulou, S. P. Perlepes and E. Manessi-Zoupa, *Polyhedron*, 2001, **20**, 2203–2214.

11 C. Huang, X. Luo, J. Zhai, Y. Chen, D.-M. Chen and B.-X. Zhu, *Polyhedron*, 2019, **165**, 111–115.

12 B. Wu, X. Huang, J. Liang, Y. Liu, X.-J. Yang and H.-M. Hu, *Inorg. Chem. Commun.*, 2007, **10**, 563–566.

13 X. Huang, Z. Yang, X.-J. Yang, Q. Zhao, Y. Xia and B. Wu, *Inorg. Chem. Commun.*, 2010, **13**, 1103–1107.

14 X. Huang, Y. Xia, H. Zhang, Z. Yan, Y. Tang, X.-J. Yang and Biao Wu, *Inorg. Chem. Commun.*, 2008, **11**, 450–453.

15 N. T. X. Lee, J. Hicks, K. J. Wallace and D. R. Turner, *Inorg. Chem.*, 2017, **56**, 12535–12541.

16 L. Roecker, J. Akande, L. N. Elam, I. Gauga, B. W. Helton, M. C. Prewitt, A. M. Sargeson, J. H. Swango, A. C. Willis, T. Xin and J. Xu, *Inorg. Chem.*, 1999, **38**, 1269–1275.

17 J. Zhao, D. Yang, X.-J. Yang and B. Wu, *Coord. Chem. Rev.*, 2019, **378**, 415–444.

18 D. Zhang, L.-K. Hou, Q. Zhang, J.-W. He, H.-J. Feng, F. Würthner, X.-J. Yang and B. Wu, *Chem. – A Eur. J.*, 2020, **26**, 1414–1421.

19 M. N. Hoque, U. Manna and G. Das, *Polyhedron*, 2016, **119**, 307–316.

20 A. Basu and G. Das, *J. Org. Chem.*, 2014, **79**, 2647–2656.

21 D. Kalita, R. Sarma and J. B. Baruah, *CrystEngComm*, 2009, **11**, 803–810.

22 L. S. Shimizu, S. R. Salpage and A. A. Korous, *Acc. Chem. Res.*, 2014, **47**, 2116–2127.

23 L. Applegarth, A. E. Goeta and J. W. Steed, *Chem. Commun.*, 2005, 2405–2406.

24 G. O. Lloyd and J. W. Steed, *Chem. Commun.*, 2014, **50**, 1426–1428.

25 A. J. Sindt, M. D. Smith, P. J. Pellechia and L. S. Shimizu, *Cryst. Growth Des.*, 2018, **18**, 1605–1612.

26 N. Phukan and J. B. Baruah, *CrystEngComm*, 2016, **18**, 7753–7763.

27 A. Tarai and J. B. Baruah, *ACS Omega*, 2017, **2**, 6991–7001.

28 R. Custelcean, B. A. Moyer, V. S. Bryantsev and B. P. Hay, *Cryst. Growth Des.*, 2006, **6**, 555–563.

29 D. Yang, L. K. S. von Krbek, L. Yu, T. K. Ronson, J. D. Thoburn, J. P. Carpenter, J. L. Greenfield, D. J. Howe, B. Wu and J. R. Nitschke, *Angew. Chemie Int. Ed.*, 2021, **60**, 4485–4490.

30 C. Huang, X.-M. Yi, D.-M. Chen and B.-X. Zhu, *Inorganica Chim. Acta*, 2018, **476**, 123–128.

31 S. Banerjee, N. N. Adarsh and P. Dastidar, *Cryst. Growth Des.*, 2012, **12**, 6061–6067.

32 N. N. Adarsh and P. Dastidar, *Cryst. Growth Des.*, 2010, **10**, 483–487.

33 R. Custelcean, P. V Bonnesen, N. C. Duncan, X. Zhang, L. A. Watson, G. Van Berkel, W. B. Parson and B. P. Hay, *J. Am. Chem. Soc.*, 2012, **134**, 8525–8534.

34 Q. Shi, X. Zhou, W. Yuan, X. Su, A. Neniškis, X. Wei, L. Taujenis, G. Snarskis, J. S. Ward, K. Rissanen, J. de Mendoza and E. Orentas, *J. Am. Chem. Soc.*, 2020, **142**, 3658–3670.

35 J. M. Stauber, G. E. Alliger, D. G. Nocera and C. C. Cummins, *Inorg. Chem.*, 2017, **56**, 7615–7619.

36 R. Zhang, Y. Zhao, J. Wang, L. Ji, X.-J. Yang and B. Wu, *Cryst. Growth Des.*, 2014, **14**, 544–551.

37 J. B. Baruah, *J. Chem. Sci.*, 2018, **130**, 56.

38 G. A. Farnum, D. P. Martin, L. K. Sposato, R. M. Supkowski and R. L. LaDuca, *Inorganica Chim. Acta*, 2010, **363**, 250–256.

39 H. F. Clausen, R. D. Poulsen, A. D. Bond, M.-A. S. Chevallier and B. B. Iversen, *J. Solid State Chem.*, 2005, **178**, 3342–3351.

40 G. B. Deacon and R. J. Phillips, *Coord. Chem. Rev.*, 1980, **33**, 227–250.

41 J. B. Baruah, *Comments Inorg. Chem.*, 2009, **30**, 67–88.

42 Y. M. Chumakov, O. Danilescu, O. V Kulikova, P. Bourosh, I. Bulhac and L. Croitor, *CrystEngComm*, 2022, **24**, 4430–4439.

43 R. Brahma and J. B. Baruah, *ACS Omega*, 2020, **5**, 3774–3785.

44 K. Shankar, M. P. Singh and J. B. Baruah, *Inorganica Chim. Acta*, 2018, **469**, 440–446.

45 R.-K. Pan, J.-L. Song, W.-Y. Su and S.-G. Liu, *J. Chem. Crystallogr.*, 2020, **50**, 241–248.

46 S. Konar, E. Zangrando, M. G. B. Drew, J. Ribas and N. Ray Chaudhuri, *Dalt. Trans.*, 2004, 260–266.

47 Z. Shi, S. Feng, Y. Sun and J. Hua, *Inorg. Chem.*, 2001, **40**, 5312–5313.

48 I. M. L. Rosa, A. C. Z. dos Santos, L. A. R. Giusto, C. B. Pinheiro and A. C. Doriguetto, *J. Braz. Chem. Soc.*, 2017, 28, 2073–2083.

49 S. Demir, G. K. Kantar, Y. Topcu and Q. Li, *Transit. Met. Chem.*, 2012, **37**, 257–263.

50 M. Brezovan, V. Kuchtanin, J. Moncol, J. Pavlik, Ľ. Dlháň and P. Segľa, *Chem. Pap.*, 2020, **74**, 3741–

3753.

51 M. Nishio, *Phys. Chem. Chem. Phys.*, 2011, **13**, 13873–13900.

52 J. Bernstein, R. E. Davis, L. Shimoni and N.-L. Chang, *Angew. Chemie Int. Ed. English*, 1995, **34**, 1555–1573.

53 J. K. Nath, A. Mondal, A. K. Powell and J. B. Baruah, *Cryst. Growth Des.*, 2014, **14**, 4735–4748.

54 Y. Marechal and A. Witkowski, *J. Chem. Phys.*, 1968, **48**, 3697–3705.

55 C. F. Macrae, I. Sovago, S. J. Cottrell, P. T. A. Galek, P. McCabe, E. Pidcock, M. Platings, G. P. Shields, J. S. Stevens and Towler, Matthew, Wood, Peter A, *J. Appl. Crystallogr.*, 2020, **53**, 226–235.

56 A. Karmakar and J. B. Baruah, *Polyhedron*, 2008, **27**, 3409–3416.

57 A. Karmakar, R. J. Sarma and J. B. Baruah, *Polyhedron*, 2007, **26**, 1347–1355.

58 N. Barooah, R. J. Sarma, A. S. Batsanov and J. B. Baruah, *Polyhedron*, 2006, **25**, 17–24.

59 G. Guilera and J. W. Steed, *Chem. Commun.*, 1999, 1563–1564.

60 R. Murugavel, D. Krishnamurthy and M. Sathiyendiran, *J. Chem. Soc. Dalt. Trans.*, 2002, 34–39.

61 Z. R. Grabowski, K. Rotkiewicz and W. Rettig, *Chem. Rev.*, 2003, **103**, 3899–4032.

62 P. Khakhlary and J. B. Baruah, *Inorganica Chim. Acta*, 2016, **440**, 53–61.

63 X. Bi and Y. Pang, *J. Phys. Chem. B*, 2016, **120**, 3311–3317.

64 S. Halder, S. Samanta and G. Das, *Analyst*, 2019, **144**, 2696–2703.

65 Z. Hasan and S. H. Jhung, *J. Hazard. Mater.*, 2015, **283**, 329–339.

66 W. S. Y. Ong, R. A. Smaldone and S. C. Dodani, *Chem. Sci.*, 2020, **11**, 7716–7721.

67 Y. Rachuri, S. Subhagan, B. Parmar, K. K. Bisht and E. Suresh, *Dalt. Trans.*, 2018, **47**, 898–908.

68 M. Tong, D. Liu, Q. Yang, S. Devautour-Vinot, G. Maurin and C. Zhong, *J. Mater. Chem. A*, 2013, **1**, 8534–8537.

69 E. Haque, J. E. Lee, I. T. Jang, Y. K. Hwang, J.-S. Chang, J. Jegal and S. H. Jhung, *J. Hazard. Mater.*, 2010, **181**, 535–542.

70 E. Haque, V. Lo, A. I. Minett, A. T. Harris and T. L. Church, *J. Mater. Chem. A*, 2014, **2**, 193–203.

71 K. Nath, K. Maity and K. Biradha, *Cryst. Growth Des.*, 2017, **17**, 4437–4444.

72 J. Johnson, E. Saha, A. Chhetri, E. Suresh and J. Mitra, *ACS Appl. Polym. Mater.*, 2021, **3**, 651–660.

73 S.-Q. Deng, X.-J. Mo, S.-R. Zheng, X. Jin, Y. Gao, S.-L. Cai, J. Fan and W.-G. Zhang, *Inorg. Chem.*, 2019, **58**, 2899–2909.

Appendix- Chapter 4

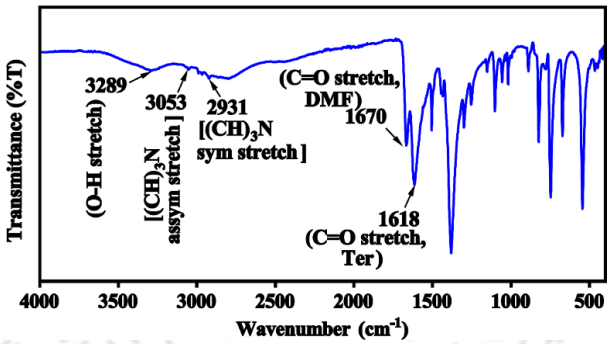

Figure A4.1. FT-IR (ATR) spectrum of **CP-4.6**

Table A2.1. Crystallographic parameters of the ligand **$L_{4.1}$** and coordination polymers **CPs 4.1-4.5**

Parameters	**$L_{4.1}$**	**CP-4.1**	**CP-4.2**	**CP-4.3**	**CP-4.4**	**CP-4.5**
Formula	$C_{13}H_{15}N_3O_2$	$C_{30}H_{34}CoN_6O_8$	$C_{30}H_{32}CoN_6O_8$	$C_{34}H_{34}CoN_6O_8$	$C_{30}H_{34}N_6O_8Zn$	$C_{30}H_{32}N_6O_8Zn$
CCDC	2063021	2063022	2063023	2063024	2063025	2063026
Mol.Wt.	245.28	665.56	663.54	713.60	672.00	669.98
Space group	*Pna*2_1	*Pccn*	*Pccn*	*P*2_1/*n*	*Pccn*	*Pccn*
a(Å)	12.3714(12)	11.653(7)	30.4091(14)	11.4051(14)	11.626(7)	11.700(4)
b(Å)	18.5178(17)	30.448(14)	11.6865(5)	8.0096(10)	30.46(2)	30.466(10)
c (Å)	5.6651(5)	8.960(5)	8.9577(3)	19.454(2)	8.952(4)	8.959(3)
α (°)	90	90	90	90	90	90
β (°)	90	90	90	106.613(3)	90	90
γ (°)	90	90	90	90	90	90
V (Å^3)	1297.8(2)	3179(3)	3183.4(2)	1702.9(4)	3170(3)	3193.4(19)
Density, gcm^{-3}	1.255	1.391	1.385	1.392	1.408	1.394
Abs. coeff., mm^{-1}	0.087	0.598	0.597	0.564	0.833	0.827
F (000)	520	1388	1380	742	1400	1392
Total no. of reflections	3226	4003	2822	4351	2770	3979
Reflections, I > 2σ(I)	2393	3219	2259	3639	2218	3324
Max. θ/°	28.285	28.663	25.043	28.595	25.048	28.343
Ranges (h, k, l)	$-16 \le h \le 16$ $-24 \le k \le 24$ $-7 \le l \le 7$	$-15 \le h \le 15$ $-40 \le k \le 40$ $-12 \le l \le 11$	$-25 \le h \le 36$ $-6 \le k \le 13$ $-9 \le l \le 10$	$-15 \le h \le 15$ $-10 \le k \le 10$ $-26 \le l \le 26$	$13 \le h \le 13$ $-36 \le k \le 36$ $-10 \le l \le 10$	$-15 \le h \le 15$ $-40 \le k \le 40$ $-11 \le l \le 11$
Complete to 2θ (%)	100	99.5	99.9	100	98.4	100
Data/restraints/parameters	3226/1/179	4003/3/218	2822/0/218	4351/0/236	2770/6/206	3979/0/218
GooF (F^2)	1.093	1.021	1.000	1.078	1.045	1.083
R indices [I > 2σ(I)]	0.0641	0.0502	0.0444	0.0310	0.0383	0.0420
wR_2 [I > 2σ(I)]	0.1804	0.2083	0.1370	0.0805	0.1159	0.0873
R indices (all data)	0.0928	0.0678	0.0570	0.0403	0.0556	0.0511
wR_2 (all data)	0.2067	0.2259	0.1477	0.0858	0.1243	0.0909

Crystallographic data: Single-crystal X-ray diffraction data of **CP-4.2** was collected on an Oxford SuperNova diffractometer. The data for **CP-4.3** and **CP-4.5** were collected on a Bruker Nonius SMART APEX CCD diffractometer. The data for **CP-4.1** and **CP-4.4** were collected on Bruker D8 Venture Single Crystal X-Ray diffractometer. CrysAlisPro software was used for analysis of data obtained by Oxford SuperNova diffractometer, whereas SAINT and XPREP were used for the Bruker Nonius SMART APEX CCD diffractometer. Structural refinements were performed in XSHELL, Version 6.3.1 software.[A.1] All non-hydrogen atoms

were refined in anisotropic approximation against F2 of all reflections. Hydrogen atoms were placed at their geometric positions by riding and refined in the isotropic approximation, whereas in CP4, H2C atom was fixed in Olex2 software and refined in the isotropic approximation. Crystallographic parameters are listed in Table A2.1.

Physical measurements: ^{1}H-NMR was recorded in DMSO-d_6 solvent on a Bruker Ascend-600 MHz using TMS as internal standard. ESI-mass spectrum was recorded in High Resolution Mass Spectrometer (Agilent QTOF 6520). Thermogravimetric analyses were performed using a thermal analyzer (SDTQ600) with a simultaneous DTA/TGA system, under nitrogen with a heating rate of 10°C min^{-1}. Powder X-ray diffraction patterns were recorded using a Bruker powder X-ray diffractometer D2 phaser with Cu-Kα radiation (l = 1.54056 Å), 40 kV of operating voltage, and 125 mA of operating current (step size = 0.02 (2 θ), time = 5°/min, Quartz plate XRD (0.5 mm depth) sample holder). Infrared spectroscopy of the solid samples was recorded on a Perkin Elmer Spectrum Two FT-IR spectrometer in the region 4000-400 cm^{-1} by using ATR method. Fluorescence spectra of all solid samples and aggregation induced emission study were measured in Horiba Scientific FluoroMax-4 Spectrofluorometer. UV-visible spectroscopy of the solid samples was measured in Perkin Elmer Lambda 750 UV/Vis spectrometer. Dye adsorption by **CPs** was recorded in Cary 100 UV-Visible spectrophotometer. Elemental analysis of **CPs 4.1-4.5** was recorded in CHNS elemental analyser (Model: Eurovector EA3000).

Dye adsorption study: The coordination polymers **CPs 4.1-4.6** (60 mg each) were respectively added to the separate aqueous solutions of MO, PR, RhB, and MBT (10 mL, 5 × 10^{-5} M) and stirred for 3 hours. Then the solutions were centrifuged for 10 minutes at 7000 rpm (25 °C) to isolate the solid **CPs** from the liquid. The visible spectrum of supernatant solution of each was recorded (Fig. 4.14). The visible spectra of the original aqueous solutions of all the four dyes (10 mL, 5 × 10−5 M) were also recorded. The amount of dye adsorbed (mg g^{-1}) was obtained by the following Equation A4.1[A.2]:

$$Amount\ of\ dye\ adsorbed = (C_i - C_e)V \times \frac{MW}{m} \quad \ldots\ldots\ldots\ldots\ldots \textit{Equation A4.1}$$

where C_i and C_e are the concentrations of each dye (mol L^{-1}) before and after treatment with **CPs**, V is the volume of the solution (in L), MW is the molecular weight of dye and m is the mass of the CP used (in g).

The removal percentage of dye was calculated by the following Equation A4.2:

$$Percentage\ of\ dye\ removed\ from\ solution = \frac{(C_i - C_{e)}}{C_i} \times 100\% \quad \text{.....Equation A4.2}$$

The observed values for the amount of dye adsorbed by each CP and the percentage of dye removal are listed in Table 4.8.

References

A.1. W. Bruker Advanced X-ray Solutions. XSHELL, *Version 6.3.1*; Bruker AXS Inc.: Madison, 2004.

A.2. Y. Rachuri, S. Subhagan, B. Parmar, K. K. Bisht and E. Suresh, *Dalt. Trans.*, 2018, **47**, 898–908.

Chapter 5

Cis and *trans* isomers of cobalt (II) nalidixate complex having 1-(4-chlorophenyl)-3-(pyridin-4-ylmethyl)urea

Helicity is often encountered in biomolecules, and the development of helical structures through non-covalent interactions and self-organization is an important aspect of supramolecular chemistry.[1–3] Helicity is observed in certain metal complexes due to helical or non-helical organic ligand winds around the metal center to provide screwlike arrangements. The metal complexes having helical geometry are inherently chiral and hence are optically active, and they exist in two enantiomeric forms, P and M (P for right-handed, and M for left-handed orientations).[4–6] In coordination chemistry, optical activity was observed in complexes having chiral ligands, a stereoisomer of a metal complex, and also through helical chirality due to self-orientation of the ligands. Optical activity due to a chiral ligand[7] or from a tetrahedral metal complex having non-equivalent ligands is obvious. Optical activity from an octahedral geometry is attained through helical chirality in complex with *cis*-geometry having two bidentate ligands and two other positions occupied by other ligands.[8] To generate supramolecular chirality in metal-organic frameworks, the assembling abilities of small molecules such as bipyridine, melamine, or solvent molecules have been utilized.[9,10] The switching of helicity and optical activity at different solvents is an interesting phenomenon.[11] As discussed in the introduction, urea derivatives, particularly pyridyl urea, play a substantial role in supramolecular chemistry due to the presence of both hydrogen bond donor and acceptor sites. Urea derivatives adopt *syn-syn* and *syn-anti* orientations depending upon their interaction with the anions or guest molecules.[12–17] Both urea-based metal complexes[18–20] and metal-organic frameworks (MOFs)[21–23] are utilized for the selective adsorption of substrates. On the other hand, anions are well known to guide assemblies of various metal cages.[18]

Optically active complexes of chemically inert cobalt(III) ions are well-known.[25,26] The reaction conditions influencing the formation and stability of the diastereomeric ratio of octahedral cobalt(III) complexes are challenging to synthesize and use a specific optical isomer for optical inductions and asymmetric synthesis.[25,27] Due to low ligand field stabilization of cobalt(II) over the cobalt(III), cobalt(II) metal complexes are kinetically labile. So, the synthesis of *cis*- or *trans*-isomer of cobalt(II) complexes is even more

challenging. In the case of the cobalt(III) complexes, in many cases, only one optical isomer is reported in the literature, and information on the other isomer remains unavailable. In certain cases both the *cis*- and *trans*-isomers are obtained as mixtures[28–31] and the isolation of each of those isomers is not easy. Hence, there remains a scope to prepare one of the optical or regio isomers of cobalt(II) in a specific manner. Accordingly, it is worth exploring new routes for synthesizing geometrical isomers of a complex of less toxic metal ions possessing ligands derived from a drug molecule and analyzing their solvent-induced chirality.

In this chapter, we report the synthesis of *cis*- and *trans*-isomers of hexa-coordinated nalidixate complexes having 1-(4-chlorophenyl)-3-(pyridin-4-ylmethyl)urea ligand (**$L_{5.1}$**) as coligand. The complexes having composition type **$[M(Nald)_2(L_{5.1})_2]$**, {where **Nald** = nalidixate, **$L_{5.1}$** = monodentate neutral ligand, M = cobalt(II)} were synthesized. The *cis*-isomer provided an avenue to study the helical chirality generated by the participation of the urea part in hydrogen bonds. **Nald** was chosen as the ligand because it served as a chelating ligand and it is derived from nalidixic acid, which is a drug molecule and also its ability to form bis-chelated complexes.[32]

5.1. Synthesis and characterization of ligand $L_{5.1}$

The ligand **$L_{5.1}$** was synthesized by the reaction of 4-chlorophenyl isocyanate and 4-aminomethylpyridine at room temperature (Scheme 5.1). In ^{1}H-NMR, the characteristic proton peaks of the two -NH groups (designated as, ′a′ and ′d′) appeared at 8.83 and 6.76-6.78 ppm, respectively (Fig. 5.1a). The mass spectrum of **$L_{5.1}$** showed a peak at 262.0761 (Calculated 262.0702), corresponding to [M+1] peak (Fig. 5.1b). Crystallization of compounds **$L_{5.1}$** from a solution in a methanol-acetone solvent mixture (1:1 v/v) yielded the colourless crystals of **$L_{5.1}$**.

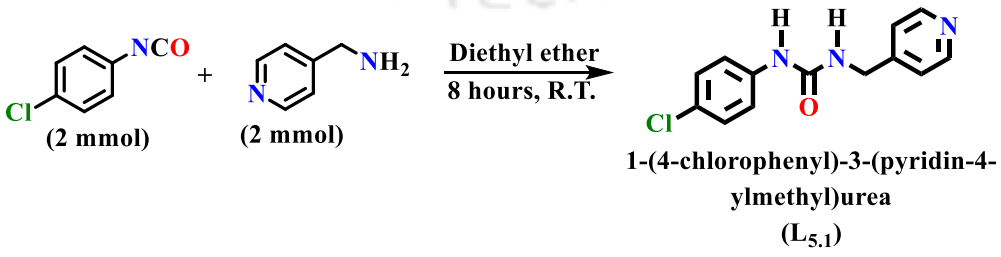

Scheme 5.1. Synthesis of ligand **$L_{5.1}$**

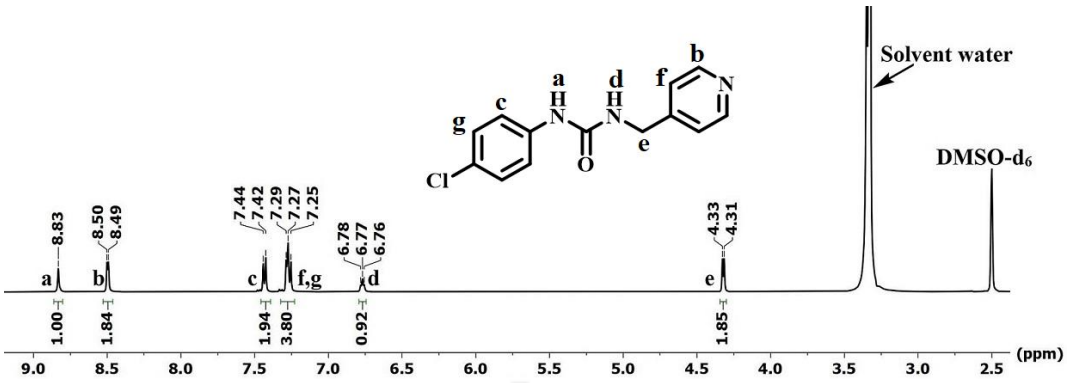

(a)

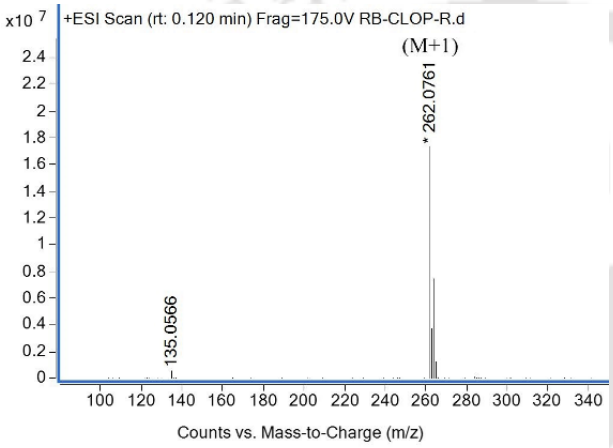

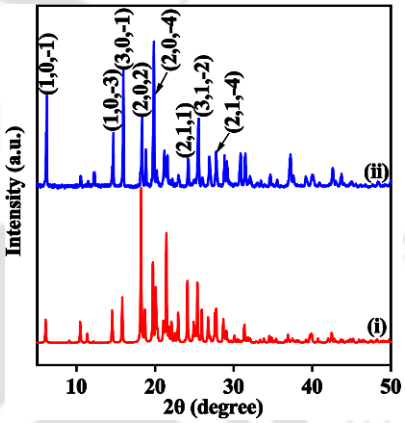

(b) **(c)**

Figure 5.1. (a) ^{1}H-NMR (DMSO-d_6, 500 MHz) spectrum, (b) ESI-Mass spectrum, and (c) Powder X-ray pattern (where (i) and (ii) are simulated and experimental powder X-ray patterns, respectively) of **L5.1**

The crystal structure of **L5.1** was determined by single crystal X-ray diffraction and further characterized by powder X-ray diffraction technique. The crystals of the **L5.1** belonged to the monoclinic crystal system of the *Pn* space group. The phase purity of the compound was analyzed by recording its powder X-ray pattern and comparing it with the simulated X-ray patterns generated from the CIF files by MERCURY software[33] (Fig. 5.1c). The comparison of the Miller indices showed the presence of a single phase. The crystal structure consisted of two symmetry-independent molecules in the unit cell, and each molecule had a *syn-syn* orientation across the 4-chlorophenyl urea part (Fig. 5.2a). The self-assembly involved intermolecular hydrogen bonding between the urea -NH groups and carbonyl oxygen atom, forming a urea α-tape network $R^1_2(6)$ synthon (Fig.

5.2b, Table 5.2). Besides these, the self-assembly of the ligand was guided by C-H···O, C-H···N interactions (Fig. 5.2c). The FTIR spectrum of **L**$_{5.1}$ showed characteristic N-H and C=O stretch at 3296 and 1633 cm$^{-1,}$ respectively (Table 5.3).

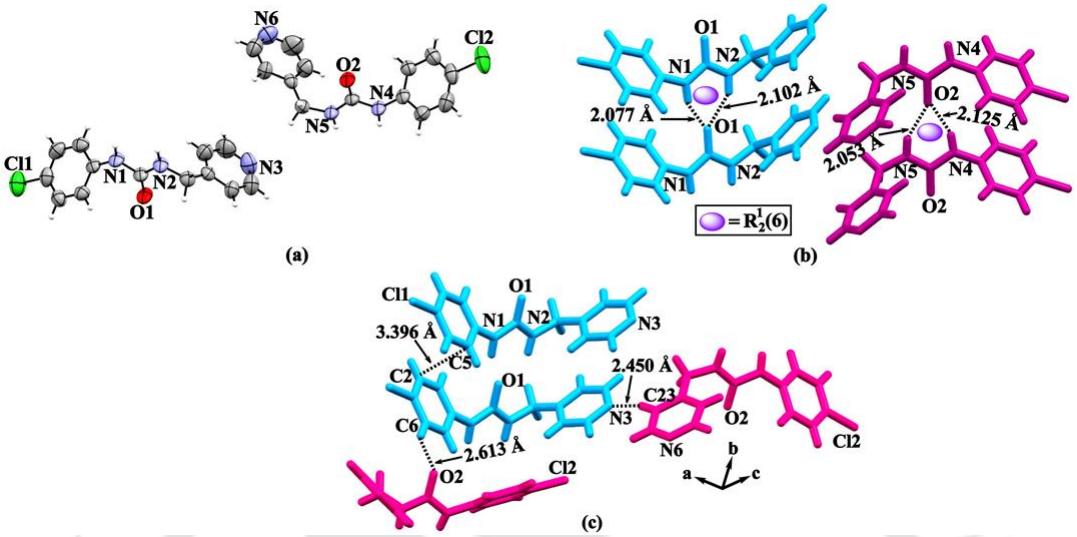

Figure 5.2. (a) Single crystal X-ray structure (50% thermal ellipsoid probability), (b) hydrogen bonds in the symmetry non-equivalent molecules, and (c) C-H···O and C-H···N interactions in **L**$_{5.1}$

5.2. Synthesis and characterization of *cis*-5.1.1 and *trans*-5.2.1

5.2.1. Synthesis of *cis*-5.1.1 and *trans*-5.2.1 from different salts of cobalt(II) ion

Ligand **L**$_{5.1}$ was treated with nalidixic acid (**HNald**) in the presence of various cobalt(II) salts to prepare *cis* and *trans* isomers as a single product or mixture of isomers. From such a reaction, four regio isomers are expected, as illustrated in Fig. 5.3. But only ***cis*-5.1.1** and

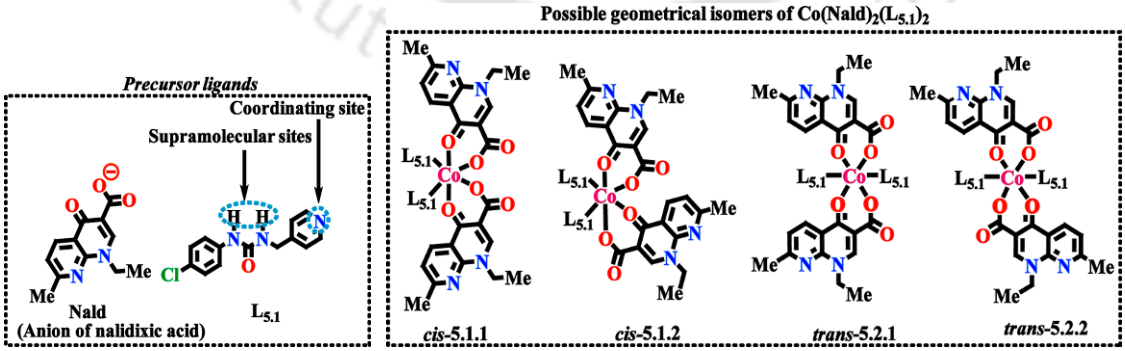

Figure 5.3. (a) The structures of the ligands, (b) The two *cis* isomers and two *trans*-isomers of a cobalt(II) complex with composition **[Co(Nald)$_2$(L$_{5.1}$)$_2$]**

***trans*-5.2.1** isomers were observed in these reactions, and we could not obtain ***cis*-5.1.2** and ***trans*-5.2.2** isomers. The isomers, ***cis*-5.1.1 and *trans*-5.2.1**, of the complex **[Co($L_{5.1}$)$_2$(Nald)$_2$]** as depicted in Scheme 5.2 were synthesized with different cobalt(II) salts in specific conditions. The reaction of nalidixic acid and **$L_{5.1}$** with cobalt(II) chloride hexahydrate (Reaction 5.3) provided only the ***trans*-5.2.1**. Whereas a similar reaction, when carried out for 49 hours at 80 °C using cobalt(II) acetate tetrahydrate (Reaction 5.4), provided a mixture of one of the ***cis*-5.1.1 and *trans*-5.2.1** (ratio 7:2). A similar reaction with cobalt(II) nitrate hexahydrate led to the same ***cis*-5.1.1** or the ***trans*-5.2.1** depending on the reaction conditions. When the reaction of **Nald** and **$L_{5.1}$** with cobalt(II) nitrate hexahydrate was

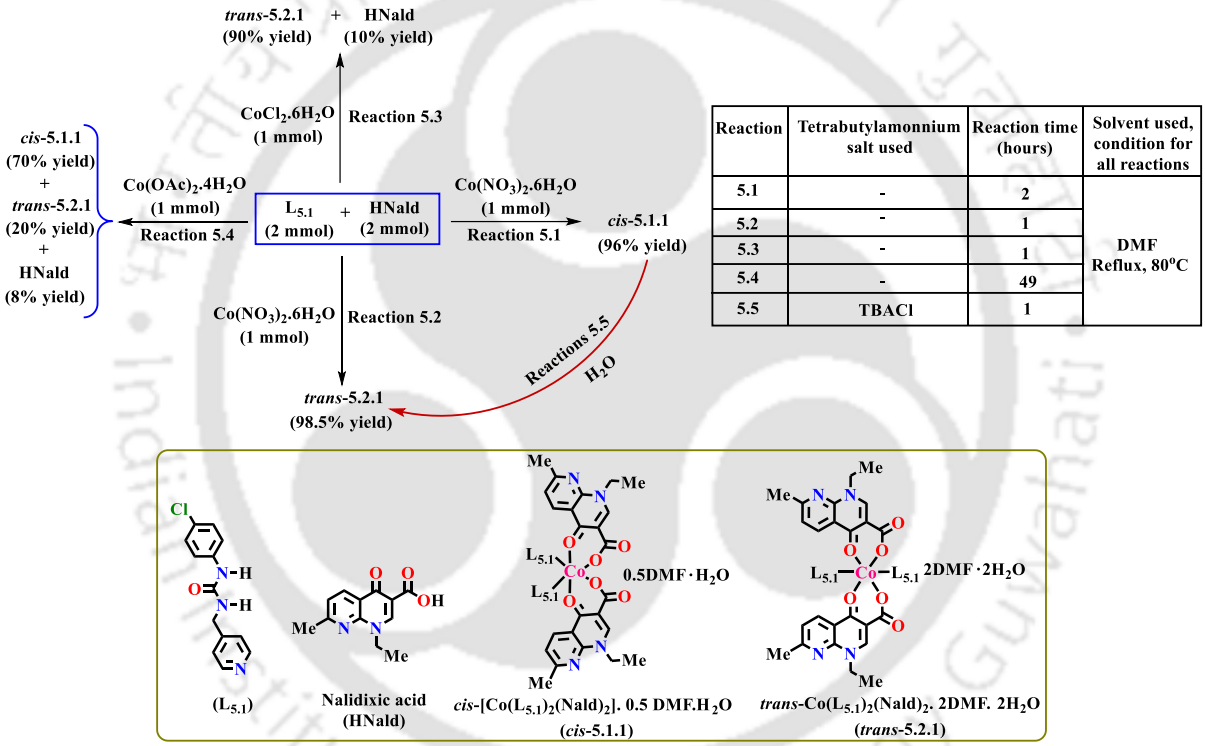

Reaction	Tetrabutylamonnium salt used	Reaction time (hours)	Solvent used, condition for all reactions
5.1	-	2	DMF Reflux, 80°C
5.2	-	1	
5.3	-	1	
5.4	-	49	
5.5	TBACl	1	

Scheme 5.2. Synthesis of *cis*- and *trans*-isomers of cobalt (II) nalidixate complexes of ligand **$L_{5.1}$**

carried out in heating condition for one hour, it provided ***trans*-5.2.1** (Reaction 5.2). The same reaction continued for an additional hour, yielding ***cis*-5.1.1** (Reaction 5.1). This occurred due to the change in the self-assembly caused by the DMF solvent of crystallization. Recent articles from our research group showed that refluxing of the urea derivatives in DMF solvent provided differently solvated assemblies of same compound with DMF.[34,35] ***cis*-5.1.1** and ***trans*-5.2.1** had different amounts of solvent of crystallization; thus, the hydrogen bonding of the DMF solvent must have guided the conversion from ***trans*-5.2.1** (Reaction

5.2) to ***cis*-5.1.1** (Reaction 5.1) where nitrate anion played a role.[36] In general, urea forms bifurcated hydrogen bonds with spherical anions, and with nitrates, it forms planar structure. Hence, the differences in hydrogen bonding modes of urea part must have guided the synthesis. In the case of nitrate anion, initially, ***trans*-5.2.1** was formed through two-point connectivity of bifurcated hydrogen bond (Fig. 5.4a) to form an extended hydrogen-bonded structure. Upon heating, reorganization took place to form three-points connectivity (Fig. 5.4b). These could have been facilitated to bring the urea ligands to the *cis*-geometry (i.e., ***cis*-5.1.1**) by nitrate anion acting as a bridge through three-point connectivity (Fig. 5.4). Hence, *trans*-to-*cis* conversion was possible by using cobalt(II) nitrate as a reactant.

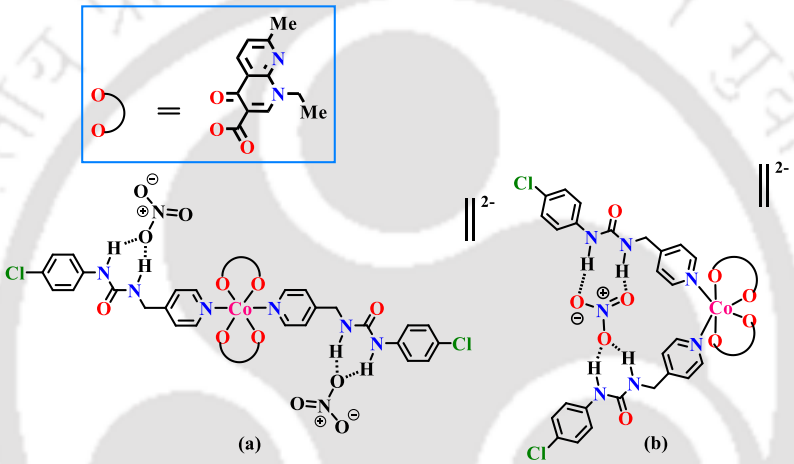

Figure 5.4. Plausible skeletal representation of hydrogen-bonded intermediates during cobalt(II) nitrate assisted (a) ***trans*-5.2.1** formation, which got converted to the intermediate of the (b) ***cis*-5.1.1**

Indeed, we found that ***trans*-5.2.1** was formed from ***cis*-5.1.1** at room temperature in DMF in the presence of tetrabutylammonium chloride in the solution (Reaction 5.5). It may be noted that the ***cis*-5.1.1** was also transformed easily to ***trans*-5.2.1** upon treating it with tetrabutylammonium chloride, which was monitored by UV-visible spectroscopy; this aspect is detailed at a later part of this chapter. Those observations suggested that the spherical ions, namely chloride and bromide, had stabilized the ***trans*-5.2.1** in the solution, leading to its crystallization from the solution. On the other hand, the nitrate ion facilitated the formation of the ***trans*-5.2.1** but also allowed it to transform into ***cis*-5.1.1** upon heating for a longer time.

Since, we obtained the mixture of isomers in the reaction of nalidixic acid with $\mathbf{L}_{5.1}$ and cobalt(II)acetate (Reaction 5.4), it was necessary to ascertain the extent of formation of a particular isomer in the mixture. So, the powder X-ray diffraction

(PXRD) pattern of the crude product was compared with the simulated powder X-ray patterns of **Nald**, ***cis*-5.1.1**, and ***trans*-5.2.1**, which were obtained through recrystallization (discussed in Section 5.2.3). This comparison clearly showed the presence of the starting material **Nald**, ***cis*-5.1.1**, and ***trans*-5.2.1** in the crude mixture.

5.2.2. Structure and self-assemblies of the two isomers of cobalt(II) complex

The isomeric complexes, ***cis*-5.1.1** and ***trans*-5.2.1**, were characterized by X-ray crystallography, and their structures are shown in Fig. 5.5. The *cis*- and the *trans*-geometries in the respective complex around the cobalt(II) ion are reflected in the N-Co-N bond angles. For the *cis*-isomer, N3-Co1-N3´ was 93.02º, whereas for the *trans*-isomer, it was 180.00º. Both the isomers of the complexes have a distorted octahedral geometry. The geometry of the two isomers were also optimised by DFT calculation (Table 5.1). The selected bond angles from the crystal structure and from the DFT optimized structures are listed in the Table 5.1.

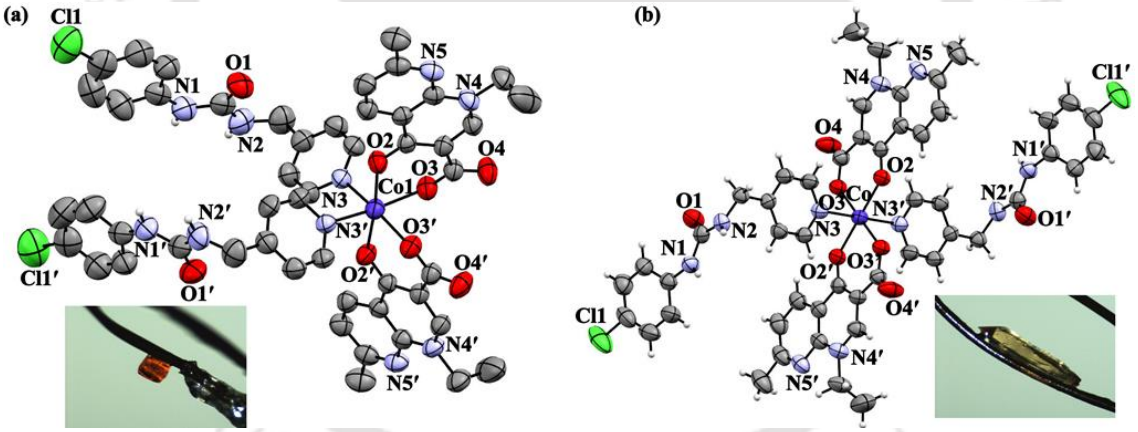

Figure 5.5. Single crystal structure of (a) ***cis*-5.1.1** and (b) ***trans*-5.2.1** (solvent molecules are omitted for clarity) (ORTEP diagram drawn with 50% ellipsoid probability) (inset: respective photograph of the crystals)

Table 5.1. The ligand-cobalt-ligand bond angles of ***cis*-5.1.1** and ***trans*-5.2.1** (the one from the theoretically optimized structure are given inside the bracket).

Complex	**Bond angle (º)**				
	N3-Co1-N3´	**N3-Co1-O2**	**N3-Co1-O3**	**O2-Co1-O3**	**O3-Co1-O3´**
***cis*-5.1.1**	93.02 (92.50)	91.73 (92.65)	92.43 (88.23)	84.75 (84.13)	84.37 (91.90)
***trans*-5.2.1**	180.00 (180.00)	90.15 (90.31)	90.53 (90.18)	87.07 (88.19)	180.00 (180.00)

***cis*-5.1.1** is crystallized in a centrosymmetric *C*2/*c* space group. This isomer is self-assembled through hydrogen bonding between the two -NH groups of **L5.1** with the two independent oxygen atoms of the coordinated and free oxygen atoms of a carboxylate group of another molecule. This resulted in the formation of a hydrogen-bonded cyclic unit with $R^2_2(8)$ graph set notation (Fig. 5.6a). The prominent hydrogen bond parameters are listed in Table 5.2. The assembly also showed C11-$H_{L5.1}$···$N5_{Nald}$ (≈ 2.728Å) intermolecular hydrogen bonds and the π···π stacking interaction (≈ 3.687Å) between two 1,8-naphthyridine units of **Nald** (Fig. 5.6b). These interactions provided a single-stranded helical arrangement along the crystallographic *b*-axis (Fig. 5.6c). Disordered molecules of 0.5 DMF and one water molecule were present in the pores of ***cis*-5.1.1**. We used a solvent mask to reduce the effect of residual electron densities of the highly disordered solvent molecules of 0.5 DMF and one H_2O. 260 electrons were found in a volume of 1212 A^3 in one void per unit cell. The thermogravimetric analysis confirmed the presence of these solvent molecules (Fig. 5.9a).

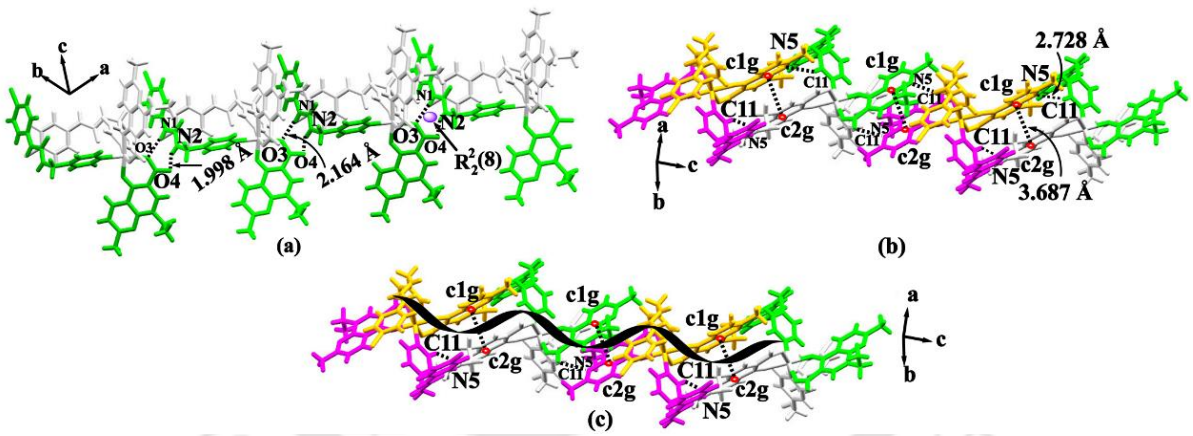

Figure 5.6. (a) Intermolecular hydrogen bonds of -NH groups of **L5.1** and carboxylate groups of **Nald**, (b) π···π stacking interaction and C11-H···N5 hydrogen bond, and (c) single-stranded helical arrangement along crystallographic *b*-axis in ***cis*-5.1.1**

***trans*-5.2.1** crystallized in a monoclinic crystal system, having *C*2/*c* space group. Like ***cis*-5.1.1**, it self-assembled by utilizing the hydrogen bonds of two -NH groups of **L5.1** with the two independent oxygen atoms of coordinated and free oxygen atoms of a carboxylate group of another molecule, giving $R^2_2(8)$ cyclic synthon (Fig. 5.7a, Table 5.2). A DMF molecule is present in the pores of ***trans*-5.2.1** (Fig. 5.7b). We have also used a solvent mask to reduce the effect of residual electron densities of the highly disordered solvent molecules

of one DMF and two H_2O. 444 electrons were found in a volume of 1586 A^3 in one void per unit cell. This is also supported by thermogravimetric analysis (Fig. 5.9b).

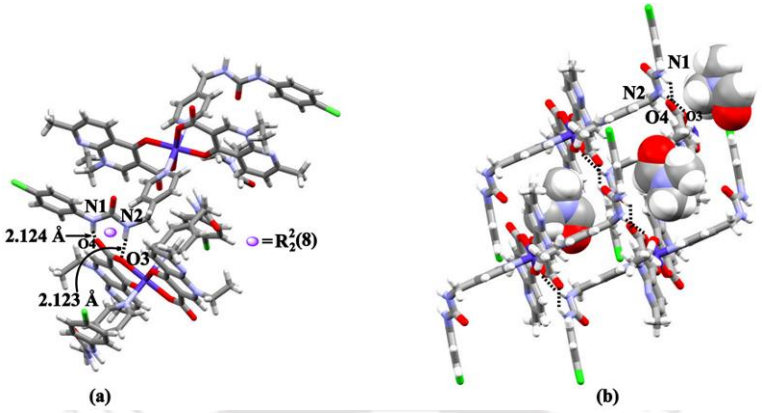

Figure 5.7. (a) Intermolecular hydrogen bonds of -NH groups of **$L_{5.1}$** and carboxylate groups of **Nald**, and (b) a DMF molecule (represented as space-filling model) present inside the pores (along crystallographic *b*-axis) of ***trans*-5.2.1**

Table 5.2. Hydrogen bond parameters of **$L_{5.1}$**, ***cis*-5.1.1**, and ***trans*-5.2.1**

Compound	D-H···A	d_{D-H} (Å)	$d_{H\cdots A}$ (Å)	$d_{D\cdots A}$ (Å)	∠D-H···A (º)
$L_{5.1}$	N(1) -H(1) ···O(1) [x, -1+y, z]	0.86	2.08	2.864(3)	152
	N(2) -H(2) ···O(1) [x, -1+y, z]	0.86	2.10	2.874(4)	149
	N(4) -H(4) ···O(2) [x, 1+y, z]	0.83(4)	2.13(4)	2.883(4)	152(3)
	N(5) -H(5A) ···O(2) [x, 1+y, z]	0.86 (4)	2.05(4)	2.848(4)	153(3)
***cis*-5.1.1**	N(1) -H(1) ···O(3) [1/2+x, 1/2+y,z]	0.86	2.16	3.001(4)	164
	N(2) -H(2) ···O(4) [1/2+x, 1/2+y,z]	0.86	2.00	2.807(5)	156
***trans*-5.2.1**	N(1) -H(1) ···O(4) [1-x, y,1/2-z]	0.86	2.12	2.882(5)	147
	N(2) -H(2) ···O(3) [1-x, y,1/2-z]	0.86	2.12	2.945(4)	160

Thus, the self-assemblies were guided by N-H···O_{Nald} hydrogen bonds in both the isomers, but in ***cis*-5.1.1**, this hydrogen bond contributed significantly to show single-stranded helicity.

5.2.3. Powder X-ray diffraction

The powder X-ray pattern of the crystals of ***cis*-5.1.1** (of Reaction 5.1) (Fig. 5.8a) and ***trans*-5.2.1** (of Reactions 5.2 and 5.3) (Fig. 5.8b) were compared with the respective simulated powder X-ray patterns obtained from the CIF files by using MERCURY software. The matching of the Miller indices of each of the peaks of the experimental pattern with the simulated one showed the phase purity of the respective samples. As

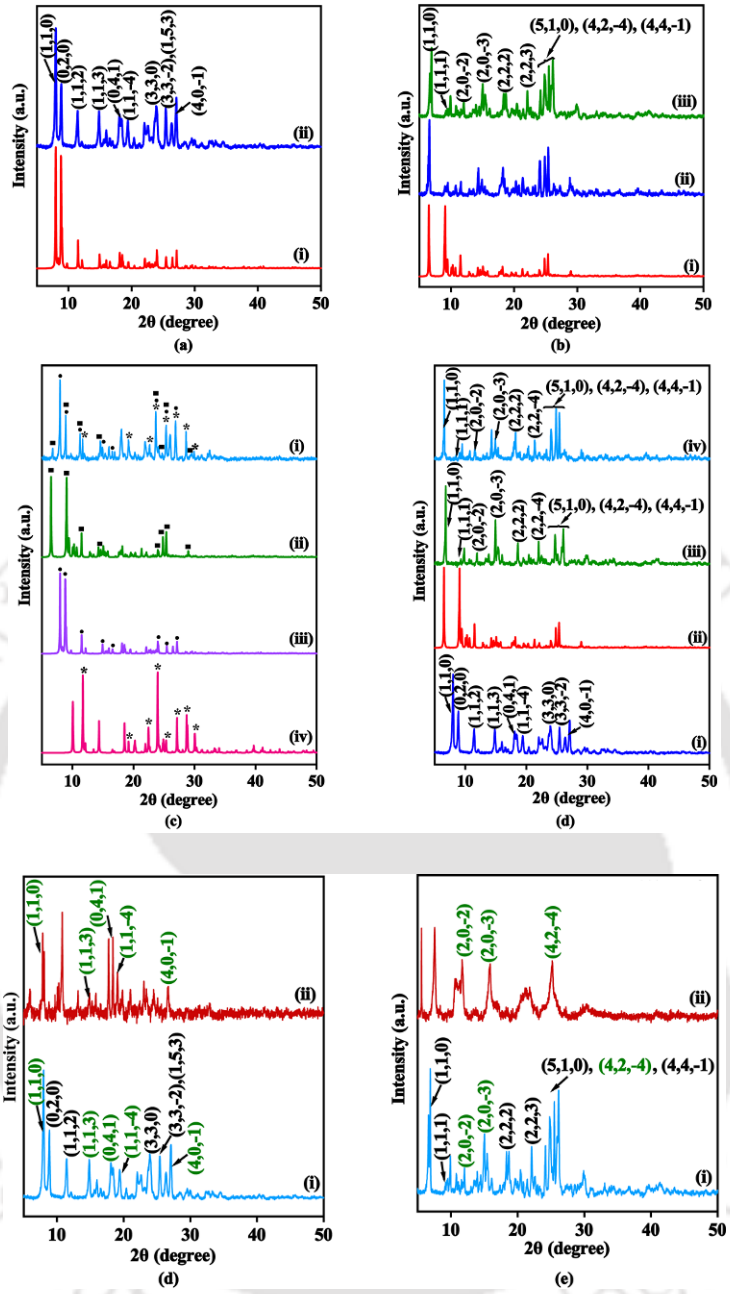

Figure 5.8. Powder X-ray pattern of the isomers (a) ***cis*-5.1.1** (i) simulated, (ii) experimental (Reaction 5.1), (b) ***trans*-5.2.1** (i) simulated, (ii) experimental (Reaction 5.2), (iii) experimental (Reaction 5.3), (c) (i) crude mixture of Reaction 5.4, (ii) ***trans*-5.2.1** simulated, (iii) ***cis*-5.1.1** simulated, (iv) **HNald** simulated, (d) (i) ***cis*-5.1.1** experimental, (ii) ***trans*-5.2.1** simulated, (iii) experimental (Reaction 5.5), (iv) experimental (Reaction 5.6), (e) (i) as-synthesized ***cis*-5.1.1** at room temperature, (ii) ***cis*-5.1.1** after heat treatment at 180°C for seven days, (f) (i) as-synthesized ***trans*-5.2.1** at room temperature, (ii) ***trans*-5.2.1** after heat treatment at 110°C for 14 days.

the crystal morphologies of ***cis*-5.1.1** and ***trans*-5.2.1** were different, it was possible to pick up the compounds from the crude mixture obtained in Reaction 5.4 by hand-

picking method, and then the powder X-ray diffraction of these separated compounds was recorded to confirm their identity. There was a comparable intensity diffraction peak. ***cis*-5.1.1** had diffraction peak for {110} Miller plane at 2θ = 7.926 (Fig. 5.8c), and ***trans*-5.2.1** had such Miller plane {110} peak at 2θ = 6.413 (Fig. 5.8c), and based on these two peaks and comparing their occurrence in the crude mixture in the powder XRD pattern(Fig. 5.8c), we found that the ***cis*-5.1.1** was formed in this case as the major product (about 70:20 ratio approximately in crude mixture). The conversion of ***cis*-5.1.1** into ***trans*-5.2.1** (in Reactions 5.5 and 5.6) was confirmed by the identical peaks and Miller indices of the crude product of this reaction with the simulated pattern of ***trans*-5.2.1** (Fig. 5.8d).

To study the ease of desolvation, both the isomers were independently heated in a laboratory oven at 180°C for seven days (for ***cis*-5.1.1**) and 110°C for fourteen days (for ***trans*-5.2.1**), and both the IR spectra (Figs. 5.11b, 5.11c, 5.11d, and 5.11e, discussed in section 5.3.1.) and powder X-ray diffraction patterns of the samples before and after heat treatment were compared (Figs. 5.8e and 5.8f). The powder X-ray diffraction patterns of ***cis*-5.1.1** (Figs. 5.8e) and ***trans*-5.2.1** (Figs. 5.8f) showed a reduction of peak intensities, indicating a distortion of the crystalline lattice.

5.2.4. Magnetic moment

The magnetic susceptibility (χ_M) of the bulk solid samples of ***cis*-5.1.1** and ***trans*-5.2.1** were measured (at a temperature of 18°C ≈ 291.15K) to check the oxidation state of cobalt ion present in the two isomers of the complex. Diamagnetic correction factors (χ_D) were calculated for both these complexes.[37] The respective magnetic moments (μ_{eff}) were finally calculated by using the Equation 5.1,

$$\mu_{eff} = \sqrt{\frac{3k_B}{N_A\beta^2}(\chi_M - \chi_D)T} \quad \text{……(Equation 5.1)}$$

where N_A is Avogadro's constant, k_B is the Boltzmann constant, and β is the Bohr magneton.

The experimental μ_{eff} value of ***cis*-5.1.1** was 4.49 BM, and for ***trans*-5.2.1**, it was 4.67 BM, and these μ_{eff} values were within the $\mu_{spin\text{-}only}$ range of octahedral cobalt(II) complexes. These confirmed that the cobalt metal center in the respective isomer was in a +2 oxidation state with a high spin d^7 electronic configuration.

5.2.5. Thermogravimetric and differential scanning calorimetry analysis

The thermogravimetric and differential scanning calorimetric (DSC) analysis on the two isomers were performed to study their dehydration and thermal stability. ***cis*-5.1.1** had a weight loss of 1.8% in the temperature range 31°C to 85°C was observed due to the loss of one molecule of water of crystallization (calculated 1.63 %) (Fig. 5.9a). This is

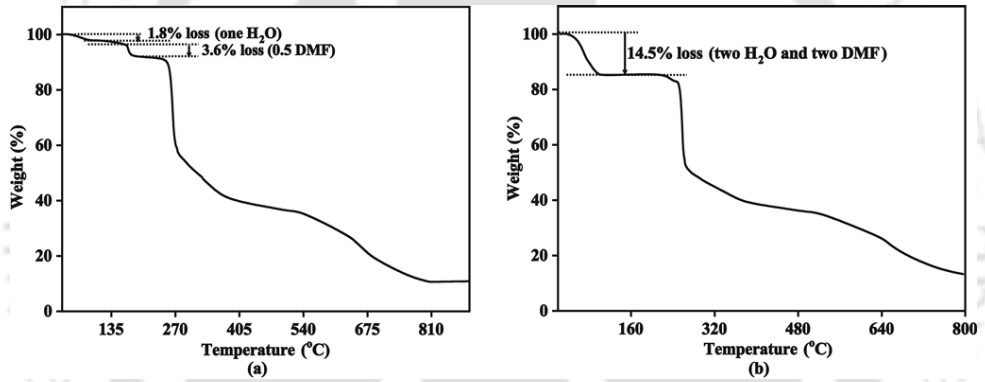

Figure 5.9. Thermograms of (a) ***cis*-5.1.1**, and (b) ***trans*-5.2.1**

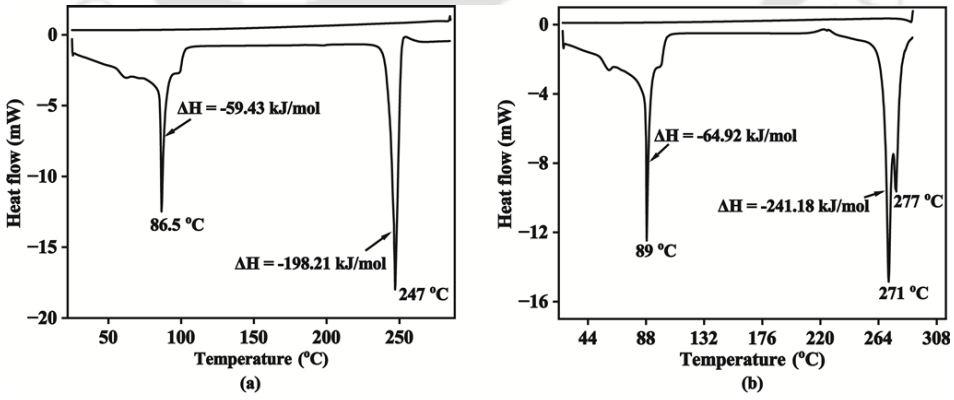

Figure 5.10. DSC curves of (a) ***cis*-5.1.1**, and (b) ***trans*-5.2.1**

also reflected in the differential scanning calorimetry as endothermic peak (Fig. 5.10a). The ***cis*-5.1.1** also showed a second weight loss of 3.6% due to half a molecule

(that is one per two complex) of DMF solvent was observed from 165°C to 179°C (calculated 3.32%). Further weight loss was completed at 638°C yielding cobalt oxide (experimental 7%, calculated 7.17%) (Fig. 5.9a). In the case of ***trans*-5.2.1**, a weight loss of 14.5 % in the temperature range 25°C to 107°C was observed due to the loss of two DMF and two H_2O molecules (calculated loss of two water molecules is 2.77%, and for two DMF molecules is 11.24%). Weight loss was completed at 653°C, yielding cobalt oxide (experimental 5.9%, calculated 6.3%) (Fig. 5.9b). The two complexes had different amounts of solvent of crystallization, and quickly lost the solvent of crystallization molecules. The differential scanning calorimetry showed that the thermal stability of the ***cis*-5.1.1** was lower, as it decomposed by the loss of coordinated ligands beyond 247°C, whereas the *trans*-isomer degraded by losing coordinated ligands from 271°C (Fig. 5.10b).

5.3. Spectroscopic characterization of *cis*-5.1.1 and *trans*-5.2.1

5.3.1. FTIR (ATR) spectroscopy

The IR spectra of the isomers, ***cis*-5.1.1** and ***trans*-5.2.1**, were compared with that of the ligand $\mathbf{L}_{5.1}$ (Fig. 5.11a). The prominent peaks characteristic of the common functional groups are assigned and tabulated in Table 5.3. The ligand $\mathbf{L}_{5.1}$ showed the characteristic N-H and C=O stretching bands at 3296 and 1633 cm^{-1}. There was a slight shift of the N-H stretching band after complexation in ***cis*-5.1.1** (3258 cm^{-1}) and ***trans*-5.2.1** (3248 cm^{-1}). Similarly, the C=O stretching peak appeared in the higher region, 1690 cm^{-1} (for ***cis*-5.1.1**) and 1685 cm^{-1} (for ***trans*-5.2.1**). In ***cis*-5.1.1** and ***trans*-5.2.1**, the asymmetric, symmetric, C=O stretch of the DMF molecule of crystallization appeared in the range of 3038-1660 cm^{-1}. The O-H stretching peak of the water solvent of crystallization appeared at 3428 and 3432 cm^{-1} for ***cis*-5.1.1** and ***trans*-5.2.1**, respectively. To study the ease of desolvation, both the isomers were independently heated in a laboratory oven at 180°C for seven days (for ***cis*-5.1.1**) and 110°C for fourteen days (for ***trans*-5.2.1**), and the IR spectra of the samples before and after heat treatment were compared. In the case of the heat-treated sample of ***cis*-5.1.1**, the IR peaks corresponding to O-H stretch (H_2O molecule) at 3428 cm^{-1}, and the DMF peaks of C-H stretch at 3038 cm^{-1}, 2928 cm^{-1} as well as the

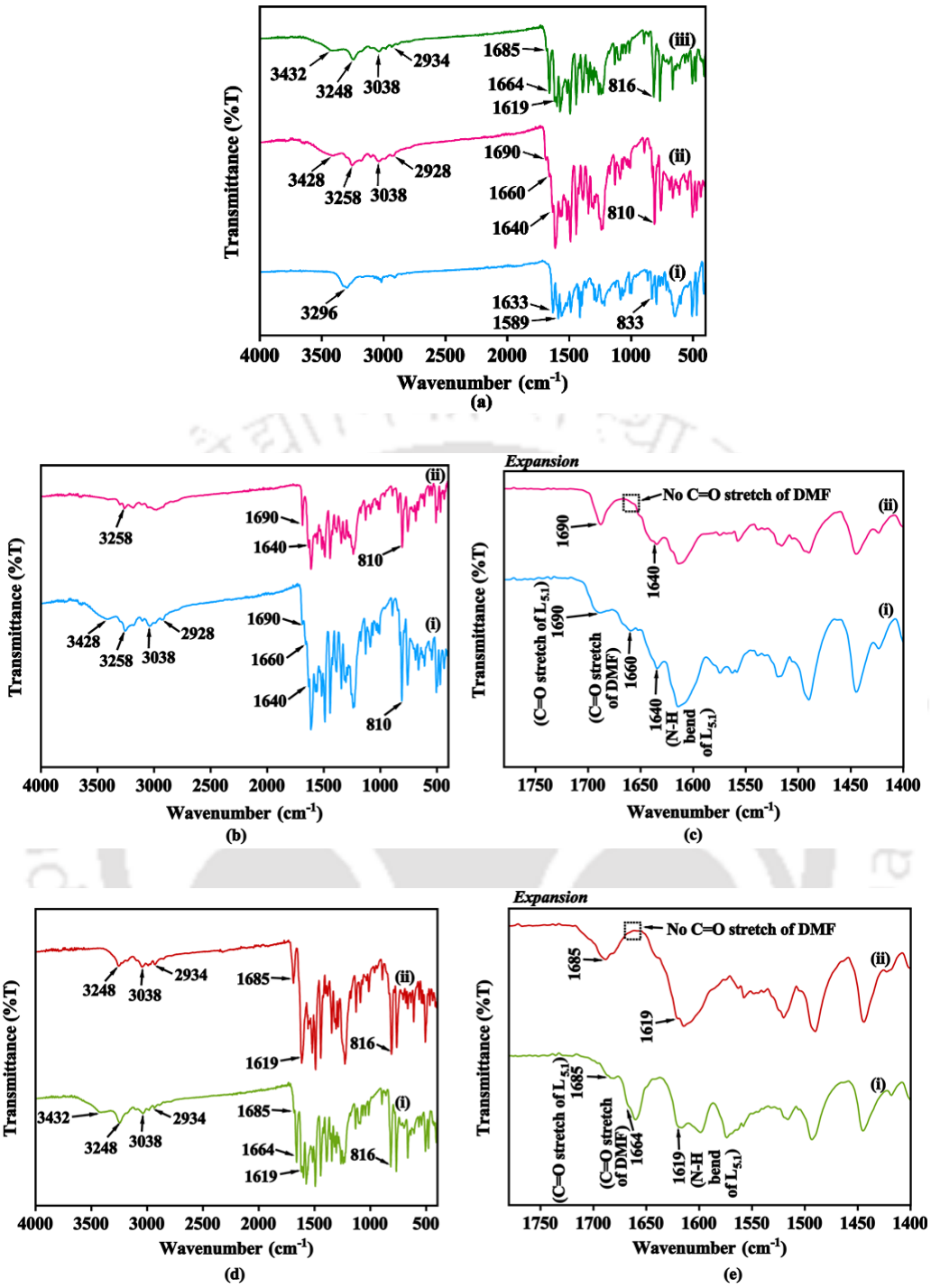

Figure 5.11. FTIR (ATR) spectra of the solid samples of (a) (i) $L_{5.1}$, (ii) ***cis*-5.1.1**, (iii) *trans*-**5.2.1**, (b) and (c) expanded spectra of ***cis*-5.1.1** (i) as-synthesized, (ii) after heating at 180ºC for seven days, (d) and (e) expanded spectra of *trans*-**5.2.1** (i) as-synthesized, (ii) after heating at 110ºC for 14 days

C=O stretch at 1660 cm^{-1} disappeared (Figs. 5.11b and 5.11c). Similarly, the O-H stretch (H_2O molecule) at 3432 cm^{-1} and the C=O stretch of DMF at 1664 cm^{-1} of the ***trans*-5.2.1** were not found in the heat-treated sample (Figs. 5.11d and 5.11e).

Table 5.3. Assignments of IR stretching frequencies of **$L_{5.1}$**, ***cis*-5.1.1**, and ***trans*-5.2.1**

Group	Stretching frequencies (cm^{-1}), appearance		
	$L_{5.1}$	***cis*-5.1.1**	***trans*-5.2.1**
O-H stretching (H_2O)	-	3428 (br)	3432 (br)
N-H stretching	3296 (m)	3258 (m)	3248 (m)
C=O stretching ($L_{5.1}$)	1633 (s)	1690 (m)	1685 (m)
N-H bending	1589 (s)	1640 (m)	1619 (m)
C-N stretching (between carbonyl C and N of N-H group)	1556 (s)	1561 (w)	1570 (s)
C-N stretching (between aromatic C and N of N-H group)	1488 (s)	1490 (s)	1493 (s)
C=N stretching (in pyridyl ring)	1301 (m)	1315 (m)	1307 (m)
C-Cl stretching	833 (s)	810 (s)	816 (s)
(CH_3)N (asymmetric stretch) (DMF)	-	3038 (m)	3038 (m)
(CH_3)N (symmetric stretch) (DMF)	-	2928 (m)	2934 (m)
C=O (DMF)	-	1660 (m)	1664 (s)

5.3.2. ^{1}H-NMR spectroscopy

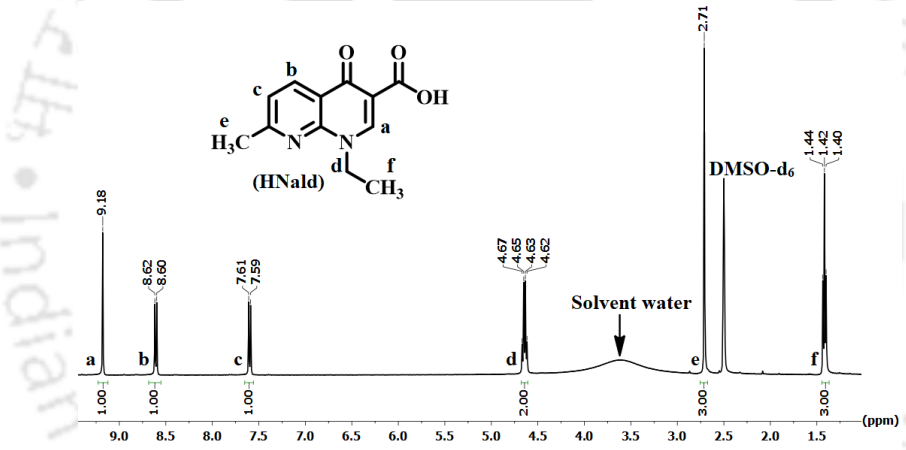

(a)

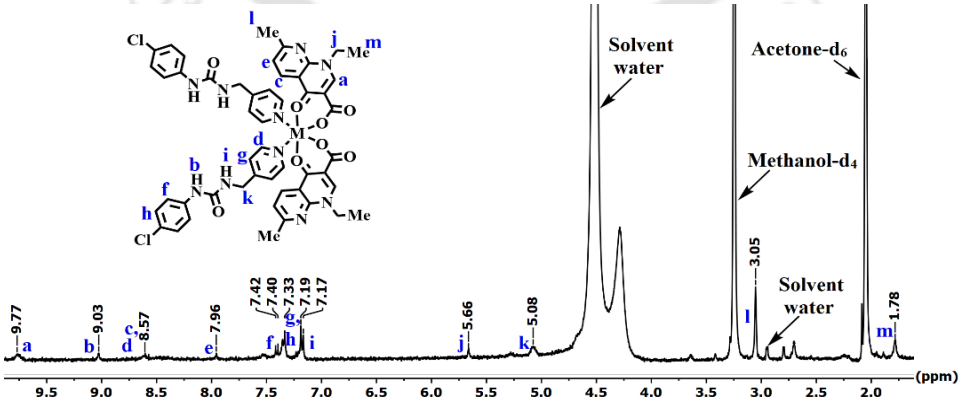

(b)

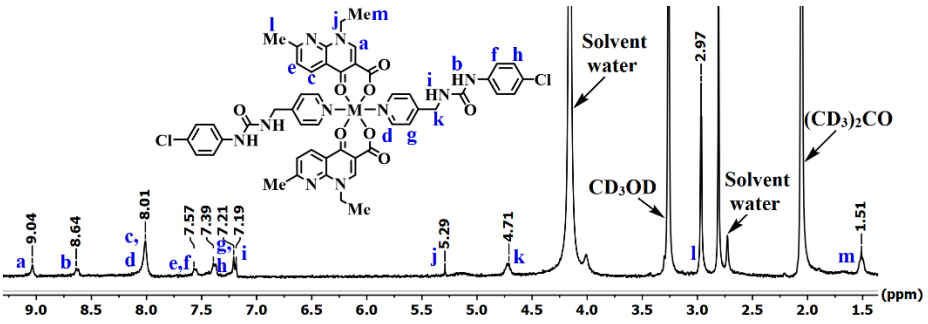

(c)

Figure 5.12. ^{1}H-NMR (400 MHz) spectra of (a) **HNald** in DMSO-d_6, (b) ***cis*-5.1.1**, and (c) ***trans*-5.2.1** in methanol-d_4/acetone-d_6 (1:3 v/v)

Due to the low solubility and paramagnetic effect of the cobalt(II) ion, strong paramagnetic broadening of ^{1}H-NMR signals was observed in ***cis*-5.1.1** and ***trans*-5.2.1**. A slight shift of the two characteristic -NH peaks (designated as ′a′ and ′d′) of $\mathbf{L}_{5.1}$ (8.83, 6.78-6.76 ppm) (Fig. 5.1a) was observed in the two isomeric complexes, that is they appeared (designated as ′b′ and ′i′) at 9.03, 7.19-7.17 ppm for ***cis*-5.1.1**, and 8.64, 7.21-7.19 ppm for ***trans*-5.2.1** (Figs. 5.12b and c). Initially, the protons ′a′, ′b′, and ′c′ on 1,8-naphthyridine ring of **HNald** appeared at 9.18, 8.62-8.60, and 7.61-7.59 ppm, respectively (Fig. 5.12a). After complexation, the protons ′a′ and ′c′ were shifted towards an upfield region to 9.77 and 7.96 ppm, respectively, and ′b′ to 8.57 ppm, in ***cis*-5.1.1** (assigned as ′a′, ′c′, and ′e′). However, in ***trans*-5.2.1**, a downfield shift of all the aromatic protons ′a′, ′b′, and ′c′ of **Nald** were observed at 9.04, 8.01, and 7.57 ppm (labeled as ′a′, ′c′, and ′e′ in ***trans*-5.2.1**).

5.3.3. Solid-state UV-visible spectroscopy

The ligand $\mathbf{L}_{5.1}$ was colourless and showed UV absorbance peaks at 292 and 323 nm (Fig. 5.13a) in its solid state due to π-π^* and n-π^* transitions. The solid sample of the ***cis*-5.1.1** isomer had absorptions at 336 nm, 486 nm, 506 nm, and 546 nm; and ***trans*-5.2.1** showed absorption maxima at 324 nm, 402 nm, 504 nm, and 544 nm, so in the solid state, the UV-visible spectra of the two isomers had very close resemblances (Fig. 5.13a).

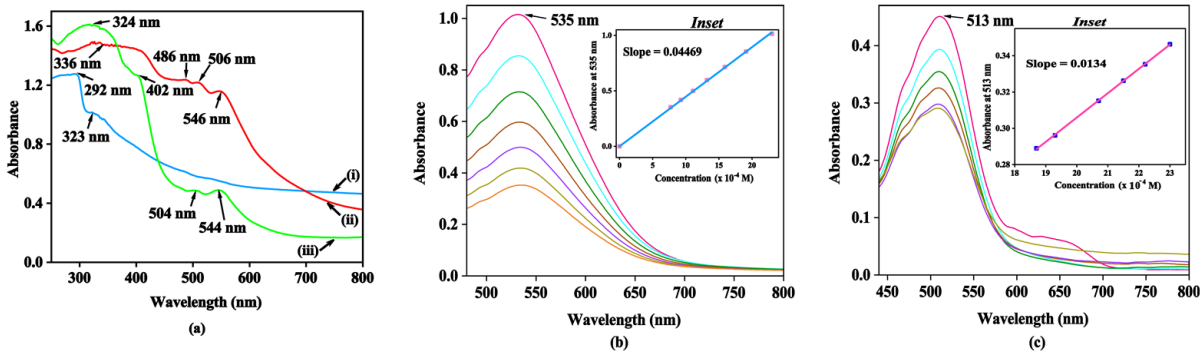

Figure 5.13. (a) UV-visible spectra of the solid samples of (i) $L_{5.1}$, (ii) ***cis*-5.1.1** and (iii) ***trans*-5.2.1**; (b) and (c) are UV-visible spectra of the ***cis*-5.1.1** and ***trans*-5.2.1** respectively at different concentrations in DMF (after every absorption measurement, diluted ten times the initially taken 3ml solution of 23.0×10^{-4} M in DMF maintaining a constant volume in the cuvette) and insets in (b) and (c) are the plots of absorbance versus concentration

5.3.4. UV-visible absorbance in DMF solvent

The concentration-dependent UV-visible spectra of ***cis*-5.1.1** and ***trans*-5.2.1** in DMF were carried out to determine their molar extinction coefficients (Figs. 5.13b and 5.13c). The absorbances in DMF were 535 nm for ***cis*-5.1.1** and 513 nm for ***trans*-5.2.1**. It was found that in DMF, the ***cis*-5.1.1** showed almost a linear dependence of absorbance versus concentration, a clear indication of following the Beer-Lambert law. A linear plot was not observed in the case of the ***trans*-5.2.1** with concentrations. So, in DMF solvent, the molar extinction coefficients of ***cis*-5.1.1** and ***trans*-5.2.1** were 446.9 and 168.9 $Lmol^{-1}cm^{-1}$, respectively.

5.4. *cis*-5.1.1-to-*trans*-5.2.1 conversion study through UV-visible spectroscopy

While preparing ***trans*-5.2.1** using cobalt(II) chloride hexahydrate, a clear blue solution was formed under heating, indicating that a tetracoordinated Co(II) complex was formed. This solution had visible absorptions at 606 nm ($^4T_1(P) \leftarrow {}^4A_2(F)$ transition and 667 nm ($^4T_1(F) \leftarrow {}^4A_2(F)$) (Fig. 5.14.iii). Once milli-Q water was added to this solution, the solution turned pink, the original peaks disappeared, and the solution

showed a new peak at 513 nm (Fig. 5.14.iv). The peak at 513 nm ($^4T_{1g}(P) \leftarrow {}^4T_{1g}(F)$ transition) corresponds to the absorption peak of the *trans*-isomer (inset of Fig. 5.14).

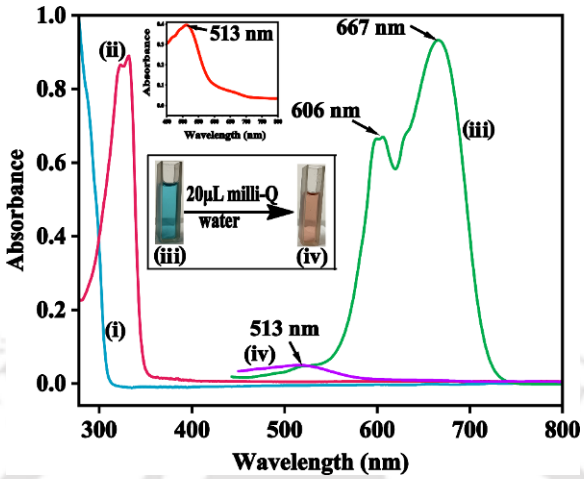

Figure 5.14. UV-visible absorption spectra of (i) **L**$_{5.1}$ (λ_{abs} = 287 nm) (0.06 × 10^{-3} M), (ii) **HNald** (λ_{abs} = 322 nm, 331 nm) (0.06 × 10^{-3} M), and visible absorption spectra of (iii) blue solution formed in reaction of **L**$_{5.1}$, **HNald** with $CoCl_2 \cdot 6H_2O$ (in DMF, 4.84 × 10^{-3} M) upon heating; (iv) The blue solution turning pink after addition of 20µL milli-Q water (λ_{abs} = 513 nm) {inset iii and iv are colour of solution in cuvette and, inset (top) is the visible spectra of the *trans*-isomer (in DMF, 23.0 × 10^{-4} M)

To ascertain the role of halide ions in converting the *cis*-isomer to *trans*-isomer, ***cis*-5.1.1** (23.0 × 10^{-4} M) was titrated with TBAX (20 µL aliquot) (46.0 × 10^{-4} M) (TBA = tetrabutylammonium, X = F, Cl, Br, I) in DMF followed by the addition of 20µL aliquot of milli-Q water. Initially, the ***cis*-5.1.1** had a visible absorbance at 535 nm. This absorption was drastically affected by TBACl, showing a new broad peak at 600 nm. After adding water, this peak was quenched, and the solution showed the absorption of the *trans*-isomer at 513 nm as a broad peak (Fig. 5.15a). Reactions carried out in the presence of chloride ions resulted in an intense blue colour solution, which pointed out to the formation of tetrahedral cobalt(II) species in solution, which could be possible through the temporal release of carbonyl oxygen of **Nald** from the kinetically labile cobalt (II) ion as shown in Fig. 5.15a. Such an intermediate would have formed because the urea part recognized chloride ions and had to avoid steric and electronic repulsions between the chloride-bound ligands. This permitted a four-coordinated tetrahedral cobalt(II) complex, and upon the addition of water, the chloride ions were released from urea, providing ***trans*-5.2.1**. There was no shift of the peak at 535 nm with the other TBAX (X = F, Br, I), but in each case, the absorbance

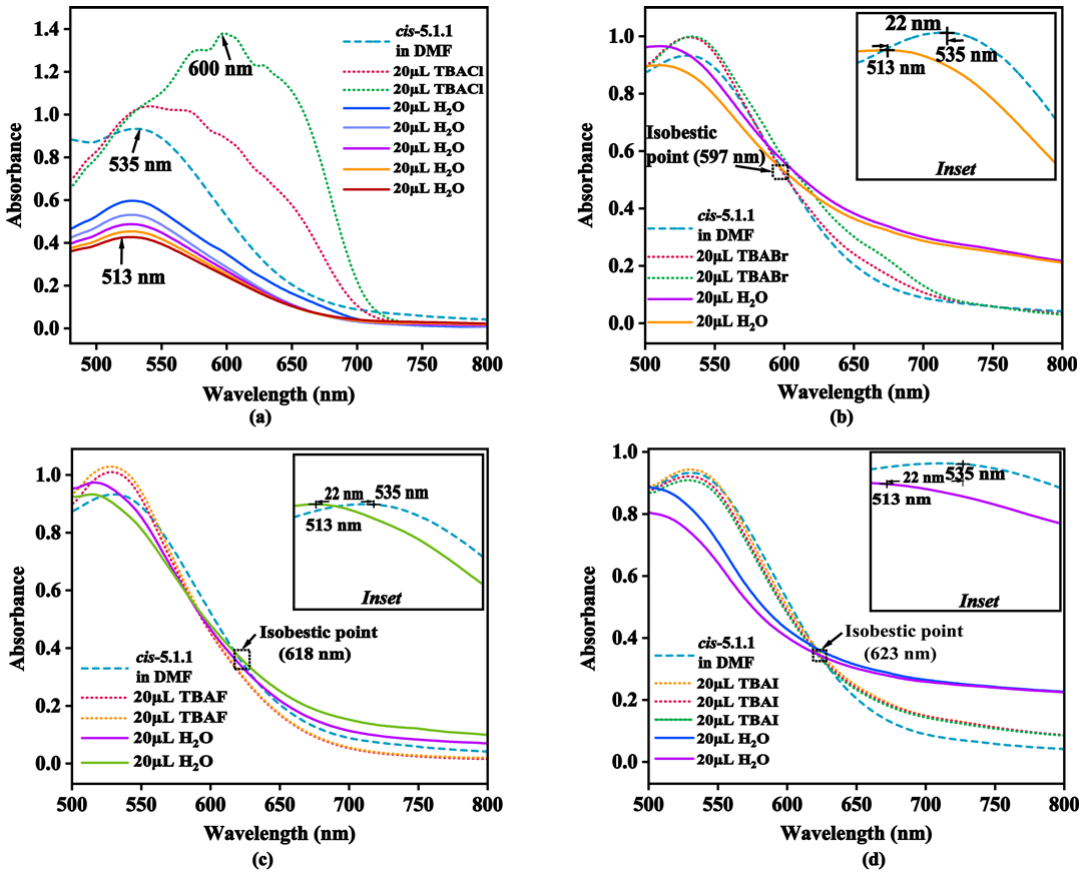

Figure 5.15. Visible absorption spectral titration of ***cis*-5.1.1** in DMF (23.0×10^{-4} M) with 20μL aliquot of TBAX (46×10^{-4} M) followed by 20μL aliquot of water (a) TBACl, (b) TBABr, (c) TBAF, (d) TBAI

of the solution slightly increased initially. The addition of milli-Q water to such a solution showed a blue shift to show a new absorption at 513 nm, corresponding to the absorption of ***trans*-5.2.1**. As the change passed through an isosbestic point at 597 nm in Fig. 5.15b (for TBABr titration), it suggested an intramolecular process involving one conversion. In the case of titration of ***cis*-5.1.1** with TBAF and TBAI, the isosbestic points were observed at 618 nm and 623 nm, respectively (Figs. 5.15c and 5.15d). Different examples of isomeric complexes transform through different twist mechanisms to form one form to another.[38,39] However, the addition of water to the solution of ***cis*-5.1.1** did not change the absorption spectra, except for a decrease in intensity due to dilution. The *cis*- and *trans*-isomers of cobalt (III) inert (non-labile) complexes undergo various twist mechanisms to transform between *cis*- and *trans*-isomers.[40–42] Hence, it can be safely suggested that the halide ions, other than chloride ions, did not break the chelation and keep metal site coordination intact; they preferred to form hydrogen bonds with the urea parts (Fig. 5.16a). Whereas the

chloride ion cleaved each of the chelating bonds (possibly the weakly bound C=O···M bond helped ***cis*-5.1.1** to form a tetrahedral intermediate as reflected in the visible spectral changes shown in Fig. 15a and this intermediate transformed into ***trans*-5.2.1** after water addition to the solution. Hence, the chloride ion-assisted conversion of ***cis*-5.1.1** to ***trans*-5.2.1** was through such a partial dissociative path involving a four-coordinated intermediate (Fig. 5.16b). Recent examples of time-dependent formation[43] of *cis*- and *trans*-isomers of copper(II) have been attributed to the role of water of crystallization. Thus, the nature of conversions was highly dependent on the nature of the central metal ion and their oxidation states.

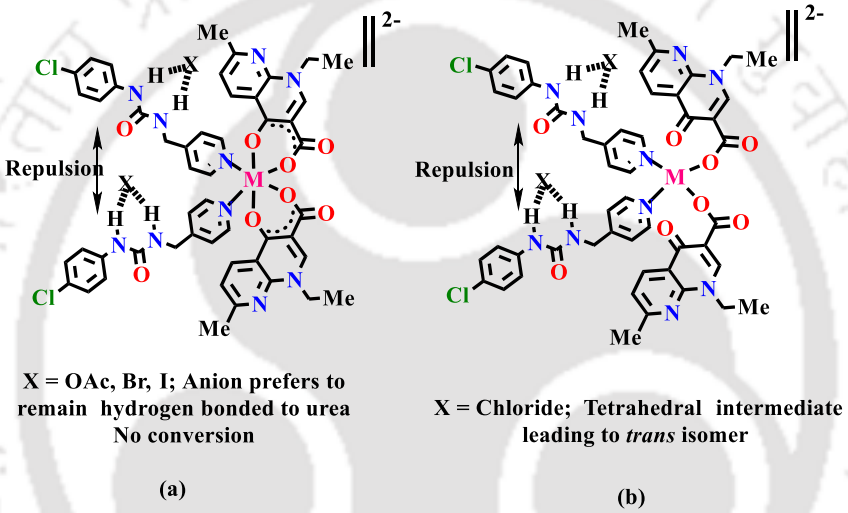

Figure 5.16. Plausible anion bound (a) six-coordinate ***cis*-5.1.1** not converting to ***trans*-5.2.1**; and (b) four-coordinate intermediate in conversion of ***cis*-5.1.1** to ***trans*-5.2.1** assisted by chloride ion

5.5. Comparison of torsion angles of the urea part in ligand $L_{5.1}$ *and* two isomeric complexes

A DFT calculation relating the energy profile of conformation of the urea-containing portion in ligand **$L_{5.1}$**, ***cis*-5.1.1**, ***trans*-5.2.1** by varying the dihedral-angle N1-C7-N2-C8 is shown in Fig. 5.17. The torsion angles of the two independent molecules of the free ligand are N1-C7-N2-C8 [-180.0(3)º] and N4-C20-N5-C21 [+175.8(3)º] (Table 5.4). The urea part of **$L_{5.1}$** in the ***cis*-5.1.1** had the N1-C7-N2-C8 torsion angle -179.1 (4)º, whereas for ***trans*-5.2.1**, it was +164.9 (3)º. Hence, the formation of ***cis*-5.1.1** did

not involve a notable change in the orientation of the urea portion of **$L_{5.1}$**, but a significant amount of orientation change occurred while forming ***trans*-5.2.1**. The evaluation of the bisecting angle between the planes containing N1-C7-N2-C8 and another plane containing the pyridyl ring of each ligand in the coordinated ligands of the ***cis*-5.1.1** and ***trans*-5.2.1** was carried out as illustrated in Fig. 5.18. In free **$L_{5.1}$**, the bisecting angle between these two planes was 85.33º, whereas this angle was 85.10º and 84.04º in the case of ***cis*-5.1.1** and ***trans*-5.2.1**, respectively (Fig. 5.18). The observation of having similar angles in each case suggested that the plane of the pyridyl ring with respect to the urea portion of the ligand remained the same and in complexes. The crystal structure of the free ligand **$L_{5.1}$** had two symmetry-independent molecules, a similar bisecting angle in both the counterparts was also checked, and another molecule of the same unit cell had this angle of 86.54º. These observations have shown that the geometrical features of the urea-based ligands did not change, but the reorganization around the metal ion was facilitated by the anions present in the reaction media. In their respective structures, the two N-H moieties of each urea ligand were projecting in opposite directions, suggesting that in the anion-bound state (Fig. 5.16), those were also projected away, and this maximized their separations in ***trans*-5.2.1**. Hence, the competitive effect to form hydrogen bonds

Table 5.4. List of torsion angles contributing to the geometries of **$L_{5.1}$**

Torsion	**Torsion angle (º)**
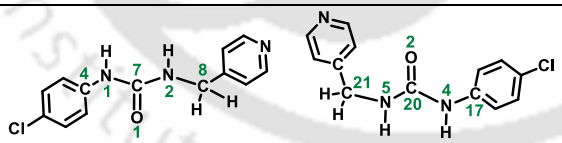	
N1-C7-N2-C8	-180.0(3)
N4-C20-N5-C21	175.8(3)
C4-N1-C7-O1	-0.8(5)
C17-N4-C20-O2	-0.8(5)
C4-N1-C7-N2	178.8(3)
C17-N4-C20-N5	179.8(3)

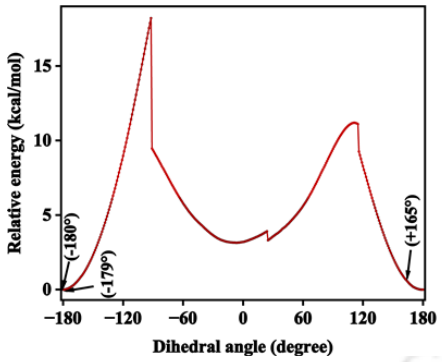

Dihedral angle (°)	Conformer of	Relative Energy (kcal/mol)
-180	(in $L_{5.1}$)	0
-179	(*cis*-5.1.1)	0.005
+165	(*trans*-5.2.1)	0.503

Figure 5.17. Comparison of conformation of the dihedral-angle (N1-C7-N2-C8) in **L**$_{5.1}$, ***cis*-5.1.1**, and ***trans*-5.2.1** from the plot of conformational energy as a function of the torsion angle θ (N1-C7-N2-C8) of **L**$_{5.1}$ obtained from the relaxed scan (calculation was done at B3LYP/6-31G level using the program Gaussian 09W)

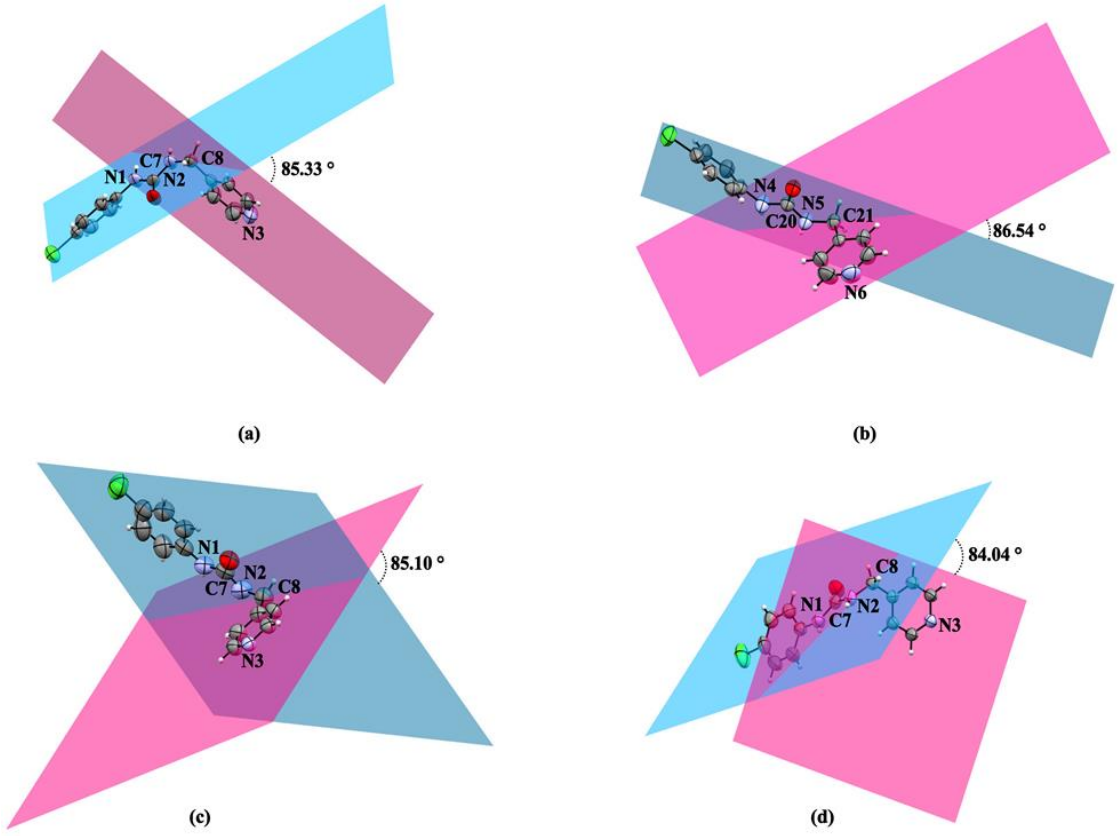

Figure 5.18. Angle of bisection between the plane containing N1-C7-N2-C8 with the plane containing pyridyl ring of (a) **L**$_{5.1}$, (c) ***cis*-5.1.1**, (d) ***trans*-5.2.1**, and (b) is the bisecting angle between the similar plane N4-C20-N5-C21 and pyridyl ring of the symmetry non-equivalent counterpart in the crystal structure of **L**$_{5.1}$

and propensity to overcome the repulsion between the hydrogen-bonded anions to stay as a thermodynamically stable ***trans*-5.2.1** guided the overall ratio of *cis*- and *trans*-isomers in respective reaction conditions.

While forming a metal chelate, **Nald** would utilize the oxygen atoms of carbonyl and carboxylate groups to form a chelate with a metal ion. There are possibilities for two *cis*-isomers and two *trans*-isomers as shown in Fig. 5.3. The isomer ***cis*-5.1.1** had both the carboxylates in the plane containing the nitrogen atoms of $\mathbf{L}_{5.1}$ ligands, whereas ***cis*-5.1.2** had one carbonyl from one **Nald** and one carboxylate of the second **Nald** positioned on the plane containing the $\mathbf{L}_{5.1}$ ligands coordinated to cobalt(II) ion. One of the synthetic options to prepare a specific isomer would be to utilize the directional supramolecular aspects of those hydrogen bonding sites. The free carbonyl groups in ***cis*-5.1.1** were located in close vicinity and projecting in the same direction to make a clear distinction, whereas, in the case of ***cis*-5.1.2**, they were projecting away from each other. The isomers ***trans*-5.2.1** and ***trans*-5.2.2** are based on similar differences in the binding environment as described for the *cis* isomers.
As we did not observe the formation of ***cis*-5.1.2** and ***trans*-5.2.2** (Fig. 5.3) during our study, so, we optimized the geometries of the four isomers by DFT calculation (using B3LYP functional using 6-31G as the basis set) and individual energy was calculated. The energy profiles of the four isomers of the complexes are shown in Fig. 5.19. The calculation showed that the ***trans*-5.2.1** isomer had lower energy than ***cis*-5.1.1** by an energy of 3.55 kcal/mole (Fig. 5.19). It was found that ***trans*-5.2.2** was the most stable form, followed by ***trans*-5.2.1**, and ***cis*-5.1.1** and then ***cis*-5.1.2**. The energy difference between the two *cis*-isomers was 2.21 kcal/mol, whereas the energy difference between ***trans*-5.2.1** isomer and ***cis*-5.1.2** was 3.55 kcal/mol. These energy differences were small, yet the values were significant enough to support the experimental findings on the ***cis*-5.1.1** isomer converting to ***trans*-5.2.1** and the fact of not observing the highest energy isomer (***cis*-5.1.2**).

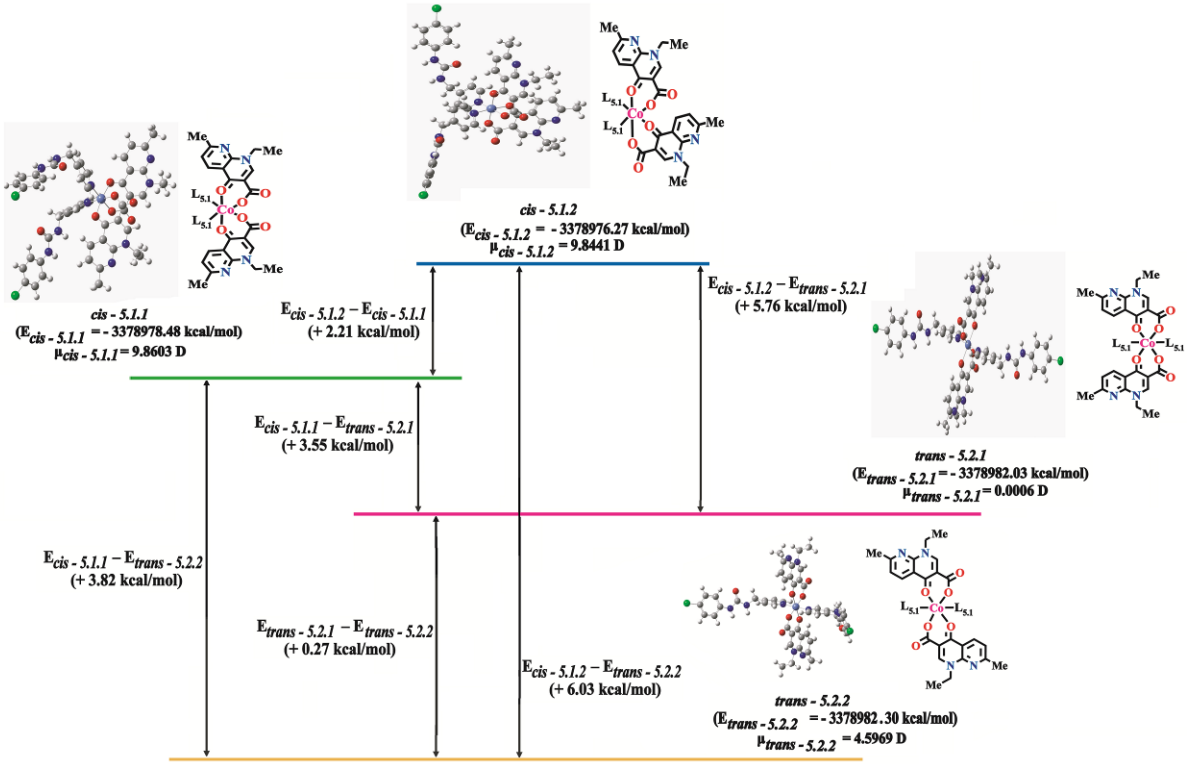

Figure 5.19. Theoretical energies of ***cis*-5.1.1**, ***cis*-5.1.2** (i.e., ***cis*-[Co(L$_{5.1}$)$_2$(Nald)$_2$]** and ***trans*-5.2.1**, ***trans*-5.2.2** {i.e., ***trans*-[Co(L)$_2$(NALD)$_2$]**} (DFT calculation was done with B3LYP functional using 6-31G as the basis set; ball and stick structures are the respective optimized structures of the isomers)

The geometry of the four-coordinated intermediate (Fig. 5.16b) was optimized using B3LYP functional using 6-31G as the basis set. It was found that this intermediate had higher energy than both ***cis*-5.1.1** and ***trans*-5.2.1** by an energy of +14.55 kcal/mol and +18.10 kcal/mol, respectively (Fig. 5.20). The bond length and bond angle parameters of the optimized geometry of the four-coordinated intermediate are shown in Table 5.5.

Table 5.5. Optimized parameters of the four-coordinated intermediate (E = -3378963.93 kcal/mol)

Optimized parameters of the four-coordinated intermediate		
Bond length (Å)	Co1-O3	1.921
	Co1-O61	2.013
	Co1-N5	1.951
	Co1-N63	2.099
Bond angle (°)	O61-Co1-O3	165.55
	O3-Co1-N63	90.79
	N5-Co1-N63	99.46
	N5-Co1-O61	98.12

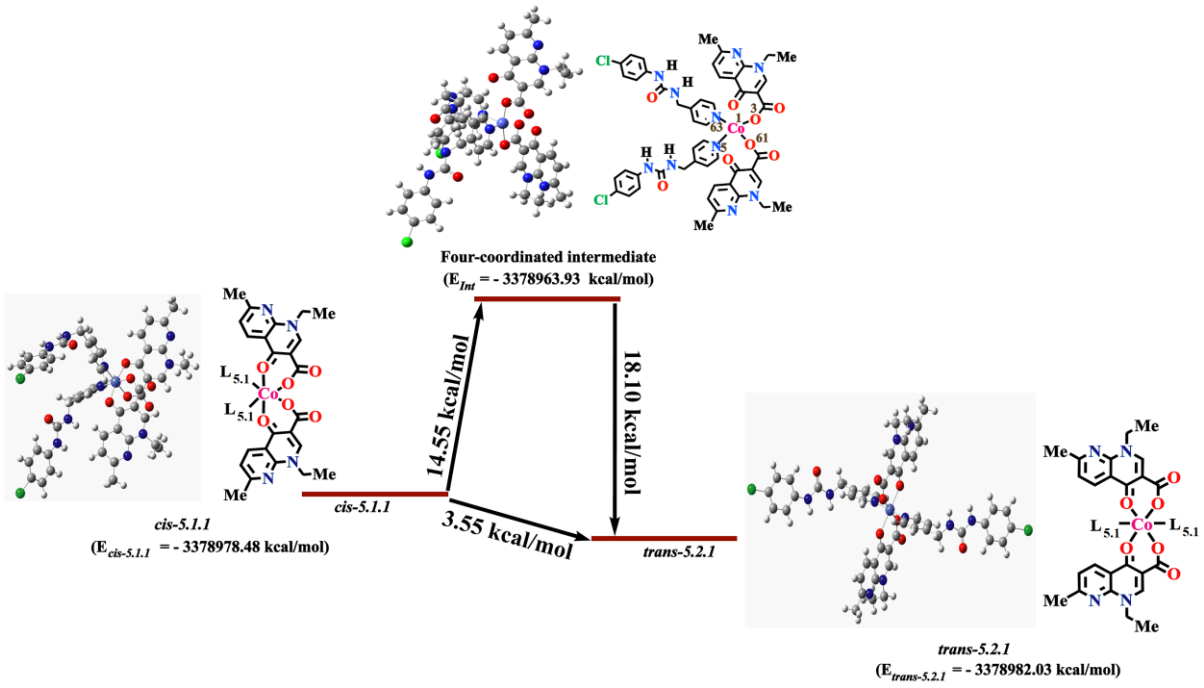

Figure 5.20. Theoretical energies of ***cis*-5.1.1**, four coordinated intermediate, and ***trans*-5.2.1** (DFT calculation was done with B3LYP functional using 6-31G as the basis set; ball and stick structures are the respective optimized structures of the isomers)

5.6. Circular dichroism and optical activity of *cis*-5.1.1

***cis*-5.1.1** was less soluble in common solvents, such as methanol, acetone, tetrahydrofuran (THF) and dichloromethane (DCM), so we prepared independent solutions in three different mixed solvents other than a solution in DMF, and circular dichroism (CD) spectra of ***cis*-5.1.1** were recorded in different solvents; such as, DMF and binary solvent mixtures DCM-acetone (1:3 v/v) THF-DMF (2:1 v/v) methanol-acetone (1:3 v/v). A negative Cotton effect was observed in DCM-acetone (1:3 v/v) and methanol-acetone (1:3 v/v). A positive Cotton effect was observed in both DMF and THF-DMF (2:1 v/v) binary solvent mixture (Fig. 5.21). The specific rotation of each of these solutions was recorded (Table 5.6), and the readings were in accordance with the CD spectral studies. These solvents had preferentially stabilized the P or M form of the single-stranded helical structures to show the positive or negative optical rotations in different solutions. In achiral metalloorganic frameworks, small molecules and solvent-caused Cotton-effect have been reported in the literature; [10,44] our examples are

new ones showing solvent-assisted helical chirality in a non-covalent assembly of a urea-based cobalt(II) complex, ***cis*-5.1.1**, in solution.

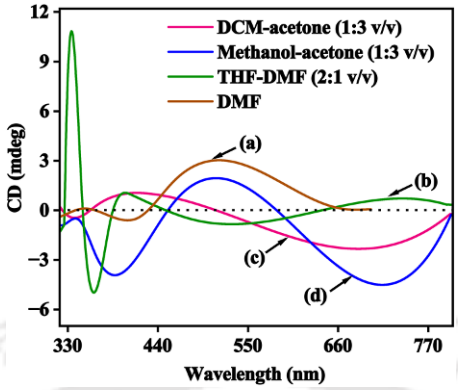

Figure 5.21. Circular dichroism spectra of solutions of the ***cis*-5.1.1** in different solvents, (a) DMF (1.14×10^{-3} M), and in binary solvents, (b) THF-DMF (2:1 v/v), (c) DCM-acetone (1:3 v/v), and (d) methanol-acetone (1:3 v/v); concentration of ***cis*-5.1.1** in binary solvents = 1.5×10^{-2} M (cuvette used: 1mm path-length).

Table 5.6. Specific rotations of the solution of the ***cis*-5.1.1** in different solvents

Solvent	Specific rotation [α] (°) (Temp = 20 °C)
DMF[a]	- 5.88
DCM-acetone (1:3 v/v)[a]	+ 45.00
MeOH-acetone (1:3 v/v)[b]	+ 29.60
THF-DMF (2:1 v/v)[a]	-10.00
a = (0.017 g/100mL) and b = 0.0135 g/100mL	

The achiral metal-organic framework leading to chiral form through aggregation by adding pyridine[44] has been demonstrated in the literature. However, the present systems have shown a racemic mixture of an isomer showing optical activity differently in different solvent systems and solutions in purely a solution study. It is important to note that Guo and coworkers[45] showed achiral polyaniline in different conditions guided by solvent to generate different fractions of helical nano-ribbons. Depending on the fraction of the chiral helical ribbon, the optical activity and the sign of the CD spectra varied. We also had a similar observation, but our studies were in a solvent where solvent caused composition differences in the nature of variable helicity, and accordingly, optical rotations varied with solvents. For this purpose, we have measured the specific rotation of ***cis*-5.1.1** at different concentrations, as well as with different solvent compositions. Both positive and negative values were observed from different compositions (Fig. 5.22, Tables 5.7-5.10). To get better evidence on this aspect, we carried out dynamic light scattering studies to determine the particle sizes in

each case and found that particle sizes were highly dependent on solvent. These studies showed that the aggregates varied diameters from 230-5745 nm (please refer to Z values in the plot Fig. 5.23 and Tables 5.11 and 5.12); hence, the solvents caused fractional variations of the single-stranded helical portions in the aggregates. As the particle sizes of the aggregates in different solvents varied, the extent of helical structure formation and magnitude of helicity of the single-stranded structure were affected. This was due to the change in the hydrogen bond schemes from solvent to solvent, and the root of the helical structures was due to hydrogen bond formation. These changes in the structures resulted in a difference in the optical activity of ***cis*-5.1.1** in different solvent mixtures.

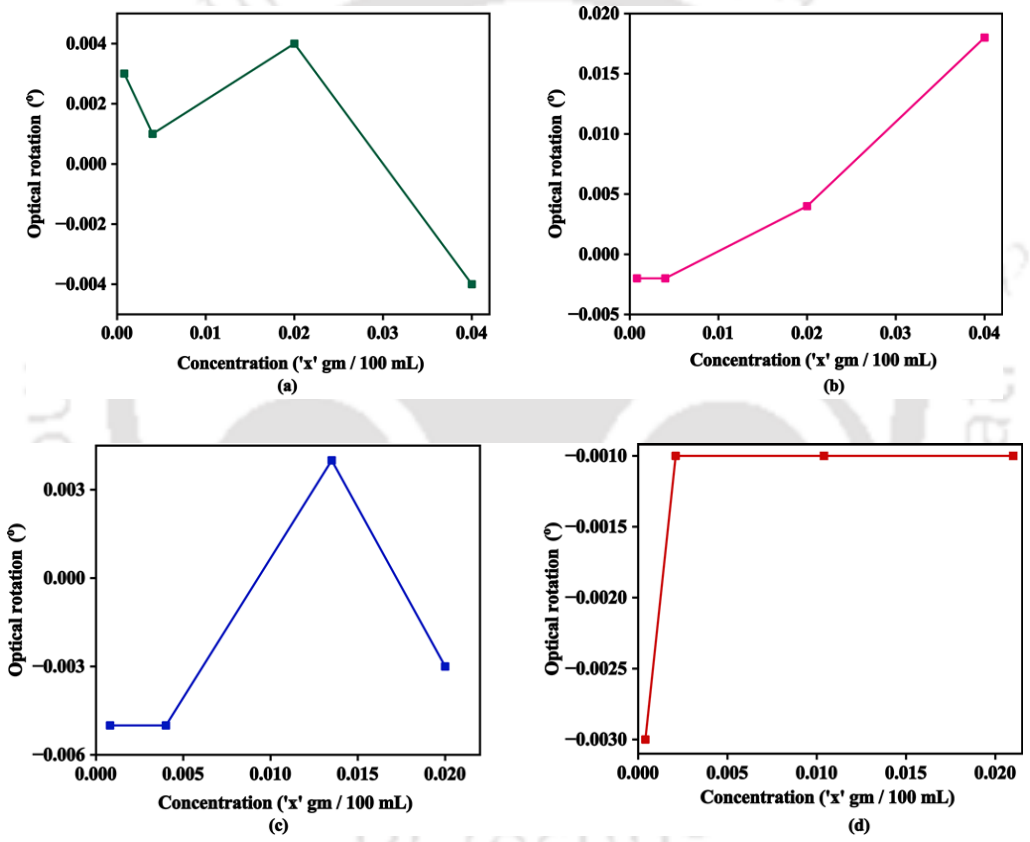

Figure 5.22. Optical rotation versus concentration plot of ***cis*-5.1.1** in binary solvents (a) THF-DMF (2:2 v/v), (b) DCM-acetone (1:3 v/v), (c) methanol-acetone (1:3 v/v), and (d) DMF

Table 5.7. Optical rotation and specific rotation of ***cis*-5.1.1** in THF-DMF (2:1 v/v) at different concentration at T = 25 ºC

Concentration (‘x’ gm/100mL)	Optical rotation (º)	Specific rotation (º)
0.0400	-0.004	-10.000
0.0200	+0.004	+20.001
0.0040	+0.001	+25.001

0.0008	+0.003	+375.019

Table 5.8. Optical rotation and specific rotation of ***cis*-5.1.1** in methanol-acetone (1:3 v/v) at different concentration at T = 25 ºC

Concentration (‘x’ gm/100mL)	Optical rotation (º)	Specific rotation (º)
0.0200	-0.003	-15.001
0.0135	+0.004	+ 29.600
0.0040	-0.005	-125.006
0.0008	-0.005	-625.031

Table 5.9. Optical rotation and specific rotation of ***cis*-5.1.1** in DCM-acetone (1:3 v/v) at different concentration at T = 25 ºC

Concentration (‘x’ gm/100mL)	Optical rotation (º)	Specific rotation (º)
0.0400	+0.018	+ 45.002
0.0200	+0.004	+20.001
0.0040	-0.002	-50.002
0.0008	-0.002	-250.012

Table 5.10. Optical rotation and specific rotation of ***cis*-5.1.1** in DMF at different concentrations at T = 20 ºC

Concentration (‘x’ gm/100mL)	Optical rotation (º)	Specific rotation (º)
0.0004	-0.003	-714.321
0.0021	-0.001	-47.621
0.0104	-0.001	-9.616
0.0210	-0.001	-4.762

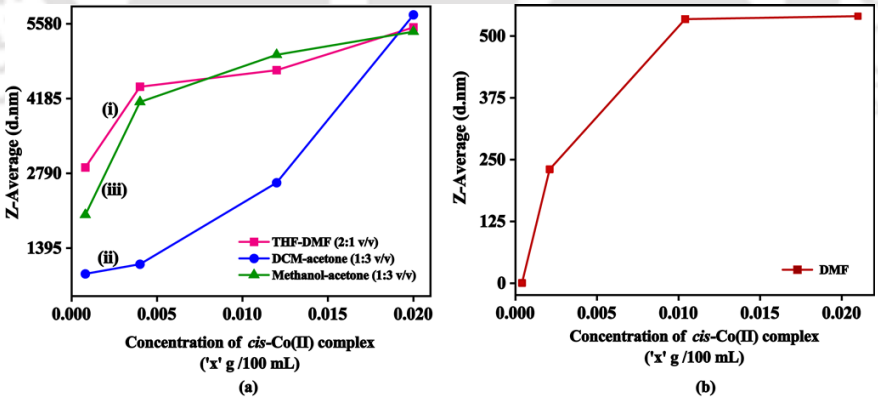

Figure 5.23. Plot representing Z-average versus concentration of ***cis*-5.1.1** at different concentrations in different solvent mixtures (a) (i) THF-DMF (2:1 v/v), (ii) DCM-acetone (1:3 v/v), (iii) methanol-acetone (1:3 v/v), and (b) DMF

Table 5.11. Z-average values of ***cis*-5.1.1** in different solvent mixtures at different concentrations

Solvent mixture	Z-average value (nm) at different concentration (‘x’ g / 100 mL)			
	0.02	**0.012**	**0.004**	**0.0008**
THF-DMF (2:1 v/v)	5514	4716	4406	2901

Methanol-acetone (1:3 v/v)	5434	5002	4122	2016
DCM-acetone (1:3 v/v)	5745	2618	1095	915.3

Table 5.12. Z-average values of ***cis*-5.1.1** in DMF at different concentrations

Concentration of *cis*-5.1.1 in DMF ('x' g / 100 mL)	**Z-average value (nm)**
0.021	540.2
0.0104	534
0.0021	230.4
0.0004	0.3969

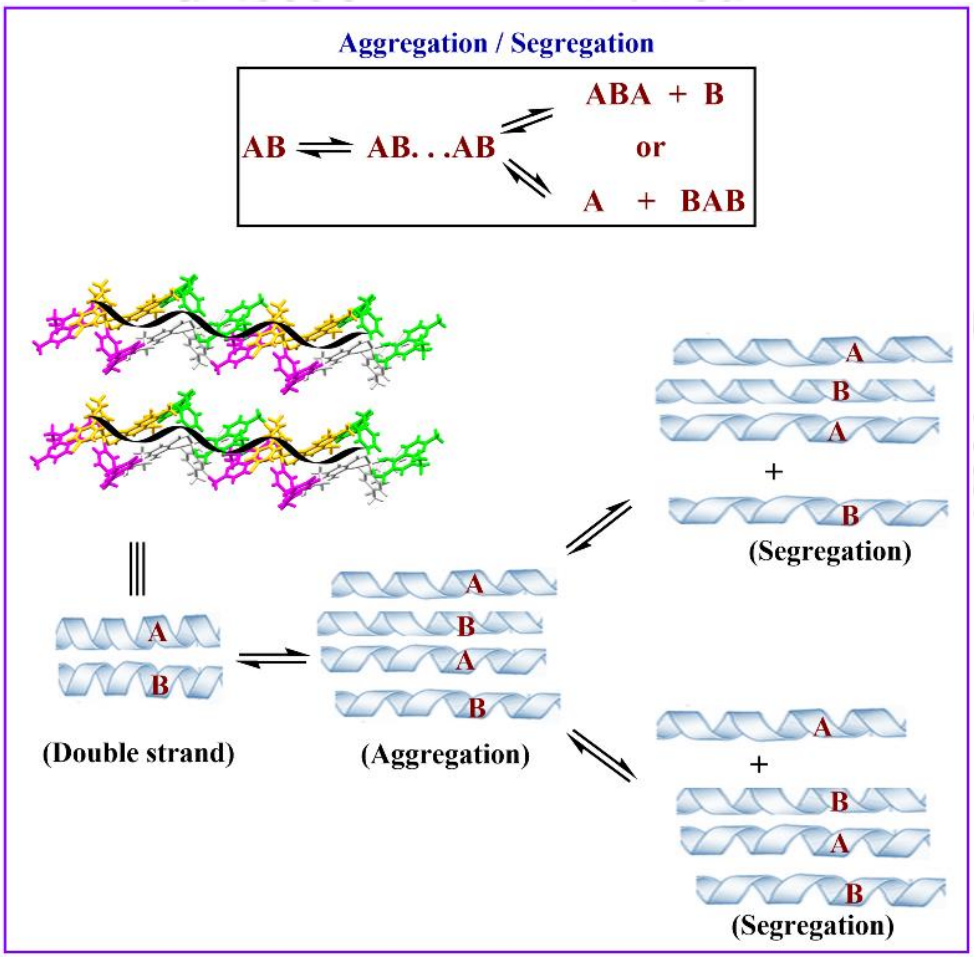

Scheme 5.3. Aggregation and segregation of a racemate of helical assembly

Based on the data obtained from these, the phenomenon is explained in Scheme 5.3. Considering the helical assembly of ***cis*-5.1.1** as AB, it underwent aggregation as well as segregation by different solvents and concentrations (vide Dynamic Light Scattering observations). If a combination provides an odd number of units, then the

weightage of optical rotations of those species will be guided by the optical properties of independent assembled components (BAB or ABA). In the event of a fraction of host molecules being unevenly distributed due to a defect in an assembled unit, that will show a positive or negative specific rotation, and this occurred in the present case to show solvent-dependent optical rotations and circular dichroism. Both positive and negative values were observed from different compositions, as listed in Tables 5.7-5.10. To get better evidence on this aspect, we carried out light scattering studies and determined the particle sizes in each case.

5.7. Conclusion

In this work, we have shown the utility of the effect of anion-guided synthesis by modulating the reaction conditions to prepare geometrical isomers of a cobalt(II) nalidixate complex of a pyridyl urea ligand **$L_{5.1}$**. At first, the preferential anion binding was used at the discretion of the isomers to show that through anion-guided synthesis and by changing the reaction conditions, one can selectively obtain the *cis*- or *trans*-isomer of **$Co(L_{5.1})_2(Nald)_2$** complex. Secondly, the reaction condition-dependent synthesis provided avenues to utilize the same reagents but different conditions to generate specific and desired *cis*- or *trans*-isomer of **$Co(L_{5.1})_2(Nald)_2$** complex through the improvised supramolecular effect of anion recognition. Thirdly, the solvent-induced aggregation induced chirality in the helical *cis*-isomer (***cis*-5.1.1**), which resulted in positive and negative Cotton effects in solution depending upon the solvent. Thus, external achiral solvent-induced helical chirality in self-assembly of the ***cis*-5.1.1** complex bearing achiral precursors **Nald** and **$L_{5.1}$** has been documented. This study will facilitate further investigation of the role of small achiral agents in inducing helical chirality in achiral non-covalent self-assembling systems.

5.8. Experimental section

The detailed synthetic methodologies for the synthesis of the metal complexes are described. Analytical data are provided with each compound. The instrumental details and

crystallographic parameters are provided in Appendix section at the end of this chapter. The following abbreviations are used for identification of spin multiplicities in ^{1}H-NMR spectra: s = singlet, d = doublet, t = triplet, q = quartet, m = multiplet; and for FTIR spectra, following abbreviations were used to identify the absorption bands: s = strong, w = weak, br = broad, m = medium.

Synthesis of 1-(4-chlorophenyl)-3-(pyridin-4-ylmethyl) urea ($L_{5.1}$): To a solution of 4-chlorophenyl isocyanate (307 mg, 2 mmol) in diethylether (15 mL), a mixture of 4-aminomethyl pyridine (203 µL, 2 mmol) and diethylether (5 mL) was added dropwise and was stirred at room temperature for 8 hours a white precipitate of **$L_{5.1}$** was observed in the reaction mixture. The reaction mixture was filtered and residue of **$L_{5.1}$** was collected and dried. Colourless crystals of **$L_{5.1}$** were obtained by slow evaporation of a solution of **$L_{5.1}$** in mixed solvent comprising of methanol-acetone (1:1 v/v). Yield: 92 %. Elemental anal. calculated: C, 59.61; H, 4.59; N, 16.04; found: C, 59.65; H, 4.61; N, 16.07. ^{1}H NMR (DMSO-d_6, 500 MHz): δ 8.83 (s, 1H), 8.50-8.49 (d, *J* = 6Hz, 2H), 7.44-7.42 (d, *J* = 10 Hz, 2H), 7.29-7.25 (m, *J* = 10 Hz, 4H), 6.78-6.76 (t, *J* = 5 Hz, 1H), 4.33-4.31 (d, *J* = 10 Hz, 2H),. ^{13}C NMR (DMSO-d_6, 125 MHz): δ 155.64, 149.96, 139.81, 128.95, 125.18, 122.43, 119.79, 42.29. ESI MS: calculated [M+1] $C_{13}H_{12}ClN_3O$, 262.0702; found, 262.0761 [M+1]. IR (cm^{-1}): 3296 (m), 1633 (s), 1589 (s), 1556 (s), 1488 (s), 1301 (m), 833 (s). UV, solid (λ_{max}): 292 nm.

***cis*-[Co($L_{5.1}$)$_2$(Nald)$_2$]·0.5 DMF·H_2O (*cis*-5.1.1):** To a solution of **$L_{5.1}$** (262 mg, 1mmol) in DMF (10 mL), nalidixic acid (**HNald**) (232 mg, 1mmol) was added and the reaction mixture was stirred for 30 minutes at room temperature. The solution was filtered, cobalt nitrate hexahydrate (146 mg, 0.5 mmol) was added, and the reaction mixture was heated for two hours at 80°C. A clear dark pink solution was formed. The reaction mixture was filtered and the filtrate was allowed to concentrate by evaporation at ambient condition. Pink block crystals of ***cis*-5.1.1** were formed after 24 hours. Yield: 96%. Elemental anal. Calculated: C, 56.21; H, 4.68; N, 13.37; found: C, 56.29; H, 4.69; N, 13.38. IR (cm^{-1}): 3428 (ν_{O-H}, br), 3258 (ν_{N-H}, m), 2928 ($\nu_{C-H[DMF]}$, m), 1690 ($\nu_{C=O}$, m), 1660 ($\nu_{C=O[DMF]}$, m), 1640 ($\nu_{N-H[bend]}$, m), 1561(ν_{C-N}, w), 1490 (ν_{C-N}, s), 1315 (ν_{C-N}, m), 810 (ν_{C-Cl}, s). UV-vis, (solid, λ_{max}): 336 nm, 486 nm, 506 nm, 546 nm.

Visible (DMF, λ_{max}) 535 nm (**ε,** 446.9 $Lmol^{-1}cm^{-1}$). Magnetic moment (18°C): 4.49 BM.

Mixture of *cis*-5.1.1, *trans*-5.2.1, and HNald: When cobalt(II) acetate tetrahydrate (125 mg, 0.5 mmol) was used in place of $Co(NO_3)_2.6H_2O$ and the solution was stirred at 80°C for 49 hours, a yellow suspension was formed. The addition of water (5ml) to the suspension, followed by heating for five minutes, provided a clear pink solution. This solution was filtered and kept for crystallization. After eight days, a mixture of ***cis*-5.1.1** (70% yield) and ***trans*-5.2.1** (20% yield) was formed. The mixture also contained starting material, nalidixic acid (8 %). The crystals of different types of the three compounds found in the mixture of crystals were separated by hand-picking. After the separation, the powder X-ray diffraction pattern of each sample was recorded, which confirmed their identities and phase purity.

***trans*-[Co($L_{5.1}$)$_2$(Nald)$_2$]·2DMF·2H_2O (*trans*-5.2.1):**

***trans*-5.2.1** was prepared following the procedure used for the preparation of ***cis*-5.1.1**, but the heating time was reduced from 2 hours to only one hour. A clear dark pink solution was formed. To this, 0.3 ml of milli-Q water was added, and the solution was filtered and kept for crystallization. Light brown rod-shaped crystals of ***trans*-5.2.1** (yield: 98.5%) were formed the next day.

However, when $CoCl_2.6H_2O$ was used instead of $Co(NO_3)_2·6H_2O$, a clear blue solution was obtained after stirring the reaction mixture at 80 °C for one hour. To the reaction mixture, 5 mL of milli-Q water was added, resulting in a colour change to pink. The pink solution was filtered and concentrated by slow evaporation at room temperature. Light-brown rod-shaped crystals of the ***trans*-5.2.1** (yield: 90%) were formed after 18 days. It was found to be a mixture of crystals, also containing crystals of starting material nalidixic acid (~10%). As the colour of **HNald** and ***trans*-5.2.1** were different, the separation of crystals was done by hand-picking. Elemental anal. (%) calcd: C, 54.45; H, 5.46; N, 13.99; found: C, 54.48; H, 5.497; N, 14.04. IR (cm^{-1}): 3432 (ν_{O-H}, br), 3248 (ν_{N-H}, m), 2934 ($\nu_{C-H[DMF]}$, m), 1685 ($\nu_{C=O,}$ m), 1664 ($\nu_{C=O[DMF],}$ s), 1619 ($\nu_{N-H[bend]}$, m), 1570 (ν_{C-H}, s), 1493 (ν_{C-H}, s), 1307 (ν_{C-N}, m), 816 (ν_{C-Cl}, s). UV-vis,

(solid, λ_{max}): 324 nm, 402 nm, 504 nm, 544 nm. Visible (solution in DMF, λ_{max}) 513 nm (ε, 134.0 $Lmol^{-1}cm^{-1)}$ Magnetic moment (18°C): 4.67 BM.

Conversion of *cis*-5.1.1 into *trans*-5.2.1: *cis*-5.1.1 (0.5 mmol) was dissolved in warm DMF (10 mL). tetrabutylammonium chloride (TBACl) (69.48 mg, 0.25 mmol) was added to this solution, and the reaction mixture was placed over an oil bath (set at 80 °C) for 1 hour, which resulted in the formation of a pink-coloured solution. 2mL of milli-Q water was added to the reaction mixture. The solution was filtered. The filtrate, upon slow evaporation for one week under ordinary conditions at 25°C, yielded light brown-coloured rod-shaped crystals of ***trans*-5.2.1** (yield 92 %).

A similar reaction was performed using TBABr (0.25 mmol) instead of TBACl. A clear wine-red solution was formed after the reaction mixture was stirred for one hour at 80 °C. To this solution, 5 mL of milli-Q water was added and filtered; the filtrate was kept for crystallization. After about 11 days, light-brown rod-shaped crystals of ***trans*-5.2.1** (yield 89 %) were obtained.

Similar reactions were performed by using TBAF and TBAI, respectively. However, we could not obtain suitable crystal or pure products from these reactions.

5.9. References

1 J.-M. Lehn, *Supramolecular chemistry*, Vch, Weinheim New York, 1995, vol. 1.

2 C. Huang, X.-M. Yi, D.-M. Chen and B.-X. Zhu, *Inorganica Chim. Acta*, 2018, **476**, 123–128.

3 S. Khatua, H. Stoeckli-Evans, T. Harada, R. Kuroda and M. Bhattacharjee, *Inorg. Chem.*, 2006, **45**, 9619–9621.

4 C. Piguet, G. Bernardinelli and G. Hopfgartner, *Chem. Rev.*, 1997, **97**, 2005–2062.

5 U. Knof and A. von Zelewsky, *Angew. Chemie Int. Ed.*, 1999, **38**, 302–322.

6 T. Cruchter, M. G. Medvedev, X. Shen, T. Mietke, K. Harms, M. Marsch and E. Meggers, *ACS Catal.*, 2017, **7**, 5151–5162.

7 H. L. Yeung, W. Y. Wong, C. Y. Wong and H. L. Kwong, *Inorg. Chem.*, 2009, **48**, 4108–4117.

8 J. L. Pierre, *Coord. Chem. Rev.*, 1998, **178**–**180**, 1183–1192.

9 D. Wu, K. Zhou, J. Tian, C. Liu, J. Tian, F. Jiang, D. Yuan, J. Zhang, Q. Chen and M. Hong, *Angew. Chemie Int. Ed.*, 2021, **60**, 3087–3094.

10 P. Xing and Y. Zhao, *Acc. Chem. Res.*, 2018, **51**, 2324–2334.

11 S. I. Sakurai, K. Okoshi, J. Kumaki and E. Yashima, *J. Am. Chem. Soc.*, 2006, **128**, 5650–5651.

12 H. L. Stewart, M. Bon, C. Wills, M. P. Martin, L. Z. Wang, E. S. Mackenzie, P. G. Waddell and M. J. Waring, *Bioorg. Med. Chem.*, 2023, **91**, 117387.

13 A. Tarai and J. B. Baruah, *ACS Omega*, 2017, **2**, 6991–7001.

14 M. Matsumura, A. Tanatani, I. Azumaya, H. Masu, D. Hashizume, H. Kagechika, A. Muranaka and M. Uchiyama, *Chem. Commun.*, 2013, **49**, 2290–2292.

15 S. J. Wezenberg and B. L. Feringa, *Org. Lett.*, 2017, **19**, 324–327.

16 V. Amendola, M. Boiocchi, B. Colasson and L. Fabbrizzi, *Inorg. Chem.*, 2006, **45**, 6138–6147.

17 N. T. X. Lee, J. Hicks, K. J. Wallace and D. R. Turner, *Inorg. Chem.*, 2017, **56**, 12535–12541.

18 B. Wu, X. Huang, J. Liang, Y. Liu, X. J. Yang and H. M. Hu, *Inorg. Chem. Commun.*, 2007, **10**, 563–566.

19 Q. Zhao, X. J. Yang, C. Jia and B. Wu, *Inorg. Chem. Commun.*, 2010, **13**, 873–877.

20 R. K. Mohapatra, P. K. Das, M. K. Pradhan, M. M. El-Ajaily, D. Das, H. F. Salem, U. Mahanta, G. Badhei, P. K. Parhi, A. A. Maihub and M. K. E-Zahan, *Comments Inorg. Chem.*, 2019, **39**, 127–187.

21 J. M. Roberts, B. M. Fini, A. A. Sarjeant, O. K. Farha, J. T. Hupp and K. A. Scheidt, *J. Am. Chem. Soc.*, 2012, **134**, 3334–3337.

22 W. Liu, X. Huang, C. Chen, C. Xu, J. Ma, L. Yang, W. Wang, W. Dou and W. Liu, *Chem. - A Eur. J.*, 2019, **25**, 1090–1097.

23 L. Esrafili, A. Morsali, M. L. Hu, A. Azhdari Tehrani, L. Carlucci, P. Mercandelli and D. M. Proserpio, *Inorg. Chem.*, 2020, **59**, 16421–16429.

24 A. B. Grommet, J. B. Hoffman, E. G. Percástegui, J. Mosquera, D. J. Howe, J. L. Bolliger and J. R. Nitschke, *J. Am. Chem. Soc.*, 2018, **140**, 14770–14776.

25 H.-J. Jiang, K. Liu, J. Yu, L. Zhang and L.-Z. Gong, *Angew. Chemie Int. Ed.*, 2017, **56**, 11931–11935.

26 A. Ehnbom, S. K. Ghosh, K. G. Lewis and J. A. Gladysz, *Chem. Soc. Rev.*, 2016, **45**, 6799–6811.

27 M. S. H. Salem and S. Takizawa, *Front. Chem.*, 2022, 10.

28 F. Riblet, G. Novitchi, R. Scopelliti, L. Helm, A. Gulea and A. E. Merbach, *Inorg. Chem.*, 2010, **49**, 4194–4211.

29 C. A. Agambar and K. G. Orrell, *J. Chem. Soc. A Inorganic, Phys. Theor.*, 1969, 897–904.

30 N. C. Jana, X.-H. Qi, P. Brandão, C. Mathonière and A. Panja, *Cryst. Growth Des.*, 2022, **22**, 993–1004.

31 T. Aycan, F. Öztürk, S. Demir, N. Özdemir and H. Paşaoğlu, *J. Mol. Struct.*, 2021, **1225**, 129043.

32 V. André, A. R. F. Da Silva, A. Fernandes, R. Frade, C. Garcia, P. Rijo, A. M. M. Antunes, J. Rocha and M. T. Duarte, *ACS Appl. Bio Mater.*, 2019, **2**, 2347–2354.

33 C. F. Macrae, I. Sovago, S. J. Cottrell, P. T. A. Galek, P. McCabe, E. Pidcock, M. Platings, G. P. Shields, J. S. Stevens and Towler, Matthew, Wood, Peter A, *J. Appl. Crystallogr.*, 2020, **53**, 226–235.

34 J. Nath and J. B. Baruah, *Cryst. Growth Des.*, 2021, **21**, 5325–5341.

35 J. Nath and J. B. Baruah, *CrystEngComm*, 2022, **24**, 3394–3408.

36 R. Brahma and J. B. Baruah, *New J. Chem.*, 2023, 6211–6223.

37 G. A. Bain and J. F. Berry, *J. Chem. Educ.*, 2008, **85**, 532–536.

38 J. G. I. I. Gordon and R. H. Holm, *J. Am. Chem. Soc.*, 1970, **92**, 5319–5332.

39 Q. Gaydon and D. S. Bohle, *Inorg. Chem.*, 2021, **60**, 13567–13577.

40 C. S. J. Springer and R. E. Sievers, *Inorg. Chem.*, 1967, **6**, 852–854.

41 H. S. Rzepa and M. E. Cass, *Inorg. Chem.*, 2007, **46**, 8024–8031.

42 P. Borowski, K. N. Jarzembska, R. Kamiński, K. Durka and D. Schaniel, *Cryst. Growth Des.*, 2023, **23**, 5986–5997.

43 N. Diyali, M. Chettri, A. De, S. J. Panda, C. S. Purohit and B. Biswas, *Giant*, 2023, **15**, 100167.

44 D. Wu, K. Zhou, J. Tian, C. Liu, J. Tian, F. Jiang, D. Yuan, J. Zhang, Q. Chen and M. Hong, *Angew. Chemie - Int. Ed.*, 2021, **60**, 3087–3094.

45 C. Zhou, Y. Ren, J. Han, X. Gong, Z. Wei, J. Xie and R. Guo, *J. Am. Chem. Soc.*, 2018, **140**, 9417–9425.

Appendix- Chapter 5

Materials and physical measurements: All starting materials, including 4-chlorophenyl isocyanate, 4-(aminomethyl)pyridine, nalidixic acid, $Co(NO_3)_2 \cdot 6H_2O$, $CoCl_2 \cdot 6H_2O$, $Co(OAc)_2 \cdot 4H_2O$, and tetrabutylammonium salts of chloride, bromide, fluoride, and iodide, were purchased from Aldrich and Merck and were used without further purification. Infrared spectroscopy of the solid samples was performed with a PerkinElmer Spectrum Two FT-IR spectrophotometer in the region 4000–400 cm^{-1} by using the ATR method. ^{1}H-NMR spectrum was recorded in Bruker Avance Neo 500MHz FT-NMR spectrometer using TMS as an internal standard. The ESI-mass spectrum of $\mathbf{L_{5.1}}$ was recorded on an Agilent QTOF6520 mass spectrometer. Powder X-ray diffraction patterns were recorded using a Bruker powder X-ray diffractometer D2 phaser with Cu-Kα radiation (l = 1.54056 Å), 40 kV of operating voltage, and 125 mA of operating current (step size = 0.02 (2 θ), time = 5º/min, Quartz plate XRD (0.5 mm depth) sample holder). Thermogravimetric analysis was performed on a PerkinElmer thermogravimetric analyzer TGA 4000. UV-visible spectra of the solid samples were measured with PerkinElmer UV WinLab Lambda 950 UV-VIS-NIR spectrophotometer. The UV-visible absorption spectra of different solutions were recorded in PerkinElmer UV/VIS Lamba 365+ spectrophotometer. The morphologies of $\mathbf{L_{5.1}}$ and the two isomers were collected in Field Emission Scanning Electron Microscope (FESEM) with OXFORD windowless EDS, Make: Zeiss, Model: Gemini 300. The magnetic moment of the solid samples of the two complexes was measured in Sherwood Scientific magnetic susceptibility balance.[A.1] The optical and specific rotations of ***cis*-5.1.1** were carried out at 20ºC in different binary solvent mixtures (0.0400 g/100mL) using an Anton Paar MCP 5100 polarimeter equipped with an LED light source (λ = 589 nm) and an optical cell of 100 mm length. The circular dichroism spectra of ***cis*-5.1.1** in different binary solvent mixtures were recorded in Jasco J-1500 and Jasco J-815 CD spectrometers in the range of 320 nm - 700 nm (Concentration of the sample = 1.14×10^{-3} M, at 20ºC). A rectangular quartz cell of 1mm path-length with PTFE stopper was used for CD experiment. The dynamic light scattering (DLS) experiment was performed in Malvern Zetasizer Nano ZS90.

X-ray Data Collection and Structure Refinement: Single crystal X-ray diffraction data were collected on a Bruker D8 Quest X-ray diffractometer using Mo Kα radiation (λ

=0.71093 Å) at 296 K. Multi-scan empirical absorption correction was used. XSHELL (version 6.3.1) and OLEX 2 (version 1.5) program packages were used to solve and refine the structure based on F^2, respectively. The hydrogen atoms were placed in calculated positions and refined isotropically. All non-H atoms were refined with anisotropic thermal parameters. Further details on the refinements are provided in the supporting information.

Certain details on the crystal structure determination:

For CCDC no. 2265811 (***cis*-5.1.1**), we used a solvent mask in Olex 2 (version 1.5) to reduce the effect of residual electron densities of the highly disordered solvent molecules of 0.5 DMF and one H_2O. 260 electrons were found in a volume of 1212 A^3 in one void per unit cell.

CCDC no. 2265812 (***trans*-5.2.1**) has one DMF molecule with disordered O5, C26, and C27 atoms. Attempts were made to use SPLIT SAME for these disordered atoms, but this resulted in a wR_2 value of 19.10% and an increase of shift from 0.000 to 6.476. So, we have not corrected the disordered DMF molecule. This disordered DMF molecule affected the wR_2 value by 21.69%. We have also used a solvent mask in Olex 2 (version 1.5) to reduce the effect of residual electron densities of the highly disordered solvent molecules of one DMF and two H_2O. 444 electrons were found in a volume of 1586 A^3 in one void per unit cell.

Computational method: Geometry optimization of **$L_{5.1}$**, ***cis*-5.1.1**, and ***trans*-5.2.1** was carried out using B3LYP functional[A.2] and 6-31G[A.2] as the basis set in Gaussian 09W software. The conformational energy plot of L was also generated at the B3LYP/6-31G level of theory (relaxed scan) with a step size of 1º (containing 360 points) variation in the dihedral angle (θ) N1-C7-N2-C8.

Table A5.1. Crystallographic parameters of the **$L_{5.1}$**, ***cis*-5.1.1**, and ***trans*-5.2.1**

Parameters	**$L_{5.1}$**	***cis*-5.1.1**	***trans*-5.2.1**
Formula	$C_{13}H_{12}ClN_3O$	$C_{50}H_{46}Cl_2CoN_{10}O_8$	$C_{56}H_{60}Cl_2CoN_{12}O_{10}$
CCDC	2265810	2265811	2265812
Mol. wt.	261.71	1044.80	1190.99
Crystal system, Space group	Monoclinic, *Pn*	Monoclinic, *C2/c*	Monoclinic, *C2/c*
a (Å)	16.854(8)	13.3053(15)	19.691(4)
b (Å)	4.578(2)	20.015(2)	19.736(4)
c (Å)	18.262(9)	21.155(2)	18.462(4)
α (º)	90	90	90
β (º)	112.507(13)	90.540(3)	107.852(6)
γ (º)	90	90	90
V (Å³)	1301.8(11)	5633.4(11)	6829(3)

Density, g cm^{-3}	1.335	1.232	1.158
Abs. coeff., mm^{-1}	0.285	0.456	0.387
F (000)	544	2164	2484
Total no. of reflections	4565	4963	6011
Reflections, I > 2σ(I)	3957	3622	4589
Max θ/ °	24.998	25.000	24.999
Ranges (h, k, l)	-20 ≤ h ≤ 20 -5 ≤ k ≤ 5 -21 ≤ l ≤ 21	-15 ≤ h ≤ 15 -23 ≤ k ≤ 23 -25 ≤ l ≤ 25	-23 ≤ h ≤ 23 -23 ≤ k ≤ 23 -21 ≤ l ≤ 21
Completed to 2θ (%)	99.1	99.9	99.7
Data/restraints/parameters	4565/2/334	4963/0/323	6011/0/371
GooF (F^2)	1.051	1.131	1.123
R indices [I > 2σ(I)]	0.0339	0.0561	0.0636
wR_2 [I > 2σ(I)]	0.0733	0.1499	0.1778
R indices (all data)	0.0433	0.0825	0.0841
wR_2 (all data)	0.0793	0.1897	0.2169

TableA5.2. Metal-ligand bond lengths of ***cis*-5.1.1**, and ***trans*-5.2.1** compared with the bond lengths of the optimized structure given under the bracket.

Complex	**Bond Length (Å)**		
	Co1-N3	**Co1-O2**	**Co1-O3**
***cis*-5.1.1**	2.141 (1.9444)	2.041 (2.2494)	2.119 (1.9365)
***trans*-5.2.1**	2.217 (1.9676)	2.057 (2.1749)	2.047 (1.9474)

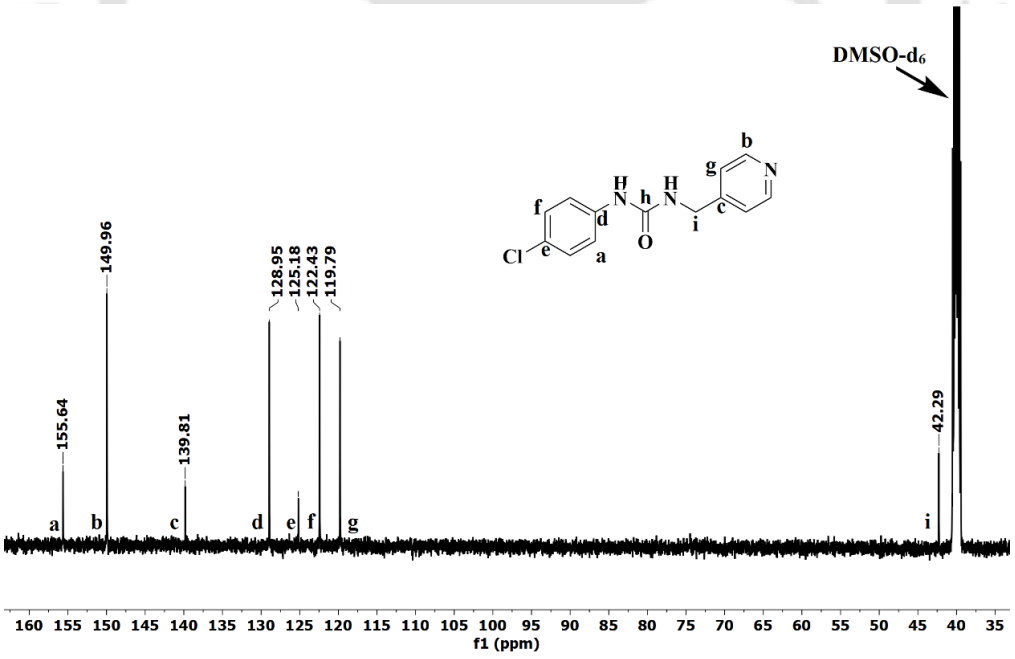

Figure A5.2. ^{13}C-NMR (DMSO-d$_6$, 125 MHz) spectrum of **L$_{5.1}$**

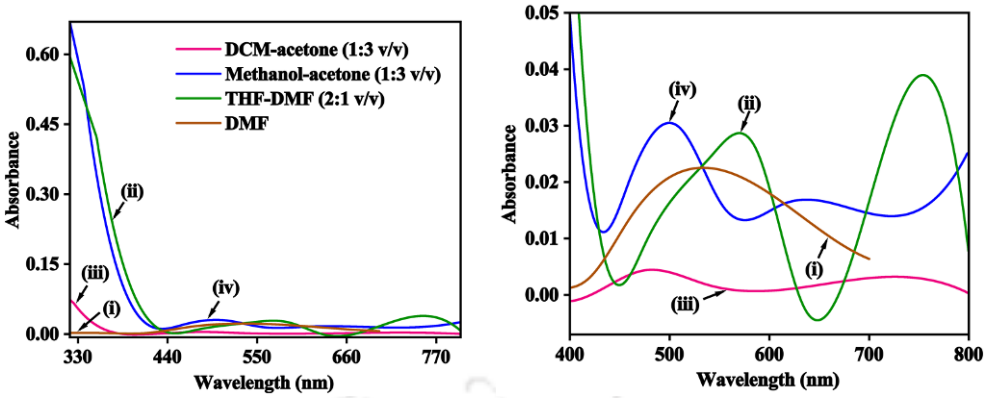

(a) **(b)**

Figure A5.3. (a) UV-visible spectra, and (b) visible spectra of ***cis*-5.1.1** in (i) DMF (1.14×10^{-3} M), and in binary solvents (ii) THF-DMF (2:2 v/v), (iii) DCM-acetone (1:3 v/v), and (iv) methanol-acetone (1:3 v/v); concentration of *cis*-Co(II) complex in binary solvents = 1.5×10^{-2} M (cuvette used: 1mm path-length)

Table A5.3. Coordinates of the optimized structure of $\mathbf{L}_{5.1}$

Center Number	Atomic Number	Atomic Type	Coordinates (Angstroms) X	Y	Z
1	17	0	-11.507042	-0.568516	-2.696048
2	8	0	-5.377584	-2.046222	0.289338
3	7	0	-4.943042	-1.067981	2.331151
4	1	0	-5.190592	-0.358300	3.005113
5	7	0	-6.998085	-0.707680	1.306067
6	1	0	-7.228528	-0.214085	2.157014
7	6	0	-8.021881	-0.716148	0.328620
8	6	0	-1.505724	-0.290423	2.775170
9	1	0	-1.520099	-0.521939	3.835956
10	6	0	-2.490657	-0.800194	1.917847

11	6	0	-7.922291	-1.402719	-0.895358
12	1	0	-7.029846	-1.967743	-1.118875
13	6	0	-5.754858	-1.319831	1.241315
14	6	0	-8.981984	-1.351721	-1.806723
15	1	0	-8.907523	-1.879734	-2.749515
16	7	0	-0.412381	0.840696	0.941975
17	6	0	-0.492782	0.519580	2.252479
18	1	0	0.282118	0.926611	2.892841
19	6	0	-10.249182	0.057748	-0.290191
20	1	0	-11.146916	0.618342	-0.060883
21	6	0	-3.614521	-1.681462	2.437785
22	1	0	-3.655971	-2.609438	1.860852
23	1	0	-3.435069	-1.939180	3.486528
24	6	0	-9.192094	0.010279	0.619443
25	1	0	-9.279351	0.545033	1.561672
26	6	0	-2.408751	-0.470145	0.553316
27	1	0	-3.146679	-0.853062	-0.143207
28	6	0	-10.128443	-0.626172	-1.497167
29	6	0	-1.364882	0.344398	0.114442
30	1	0	-1.272918	0.614778	-0.931687
31	17	0	11.161420	-3.337905	-0.478831
32	8	0	5.533954	0.410693	1.224892
33	7	0	6.000518	-0.254834	-0.963704
34	7	0	4.096633	0.987406	-0.487091
35	6	0	5.232515	0.381194	0.008331

36	6	0	3.154954	1.688720	0.388431
37	1	0	3.578639	1.610176	1.395820
38	1	0	2.184224	1.179453	0.394210
39	6	0	2.955683	3.145109	0.009238
40	6	0	7.208797	-0.965079	-0.786164
41	7	0	2.550317	5.864963	-0.640202
42	6	0	1.668372	3.704786	0.005512
43	1	0	0.808203	3.087997	0.249771
44	6	0	7.839171	-1.128395	0.461840
45	1	0	7.390995	-0.695311	1.343570
46	6	0	1.515257	5.055970	-0.320545
47	1	0	0.531856	5.515211	-0.334205
48	6	0	9.596007	-2.398483	-0.602246
49	6	0	4.034746	3.980288	-0.322078
50	1	0	5.047954	3.592707	-0.333469
51	6	0	7.796905	-1.531776	-1.933599
52	1	0	7.319572	-1.412336	-2.902805
53	6	0	8.990531	-2.249345	-1.847135
54	1	0	9.437193	-2.682207	-2.733742
55	6	0	9.035296	-1.848094	0.546338
56	1	0	9.521328	-1.974173	1.506169
57	6	0	3.788908	5.318932	-0.635587
58	1	0	4.603910	5.988045	-0.892314
59	1	0	3.871875	0.937597	-1.470133
60	1	0	5.667958	-0.215132	-1.916854

Table A5.4. Coordinates of the optimized structure of ***cis*-5.1.1**

Center Number	Atomic Number	Atomic Type	Coordinates (Angstroms) X	Y	Z
1	27	0	1.876461	0.178647	0.512064
2	17	0	-7.353460	-8.550917	-3.016125
3	8	0	2.464271	1.997987	0.182872
4	8	0	3.608393	0.151211	1.971041
5	7	0	1.339076	-1.650314	0.895356
6	8	0	3.976179	3.452038	-0.697166
7	8	0	-1.117739	-6.737798	-0.469881
8	7	0	8.270427	-0.732085	1.147921
9	7	0	7.132432	0.918655	-0.067486
10	6	0	5.936617	-0.262977	1.674291
11	6	0	7.123383	-0.043824	0.936378
12	6	0	4.702506	0.461351	1.367736
13	7	0	-3.060532	-6.766067	0.824937
14	1	0	-3.413496	-6.648851	1.764304
15	6	0	4.822604	1.501361	0.381841
16	7	0	-1.039873	-6.064944	1.734585
17	1	0	-1.552678	-5.752081	2.546046
18	6	0	0.793721	-2.435525	-0.070318
19	1	0	0.615521	-1.947470	-1.017034

20	6	0	0.743828	-4.345363	1.412375
21	6	0	8.301442	-1.666845	2.113176
22	6	0	6.013394	1.664282	-0.286106
23	1	0	6.073306	2.422985	-1.055458
24	6	0	7.163482	-1.947643	2.906615
25	1	0	7.220176	-2.708578	3.677170
26	6	0	3.692413	2.395191	-0.067910
27	6	0	0.483206	-3.773022	0.155822
28	1	0	0.049389	-4.373895	-0.635616
29	6	0	1.607356	-2.194785	2.107447
30	1	0	2.079417	-1.538617	2.825340
31	6	0	5.989064	-1.249531	2.678158
32	1	0	5.088218	-1.439333	3.249287
33	6	0	-1.706589	-6.536640	0.619644
34	6	0	1.321309	-3.527984	2.394304
35	1	0	1.556896	-3.925539	3.376581
36	6	0	-4.021985	-7.189756	-0.122609
37	6	0	8.272107	1.009651	-1.018415
38	1	0	8.272004	2.032675	-1.405305
39	1	0	9.188476	0.845238	-0.451562
40	6	0	0.403406	-5.798594	1.692795
41	1	0	0.810943	-6.436962	0.904462
42	1	0	0.841498	-6.110555	2.646539
43	6	0	9.597307	-2.408539	2.309658
44	1	0	10.361531	-1.997157	1.648027

45	1	0	9.478017	-3.475921	2.083999
46	1	0	9.946134	-2.332529	3.346750
47	6	0	-3.717317	-7.465605	-1.468326
48	1	0	-2.700481	-7.362266	-1.816374
49	6	0	-4.732201	-7.875900	-2.338815
50	1	0	-4.499467	-8.088840	-3.375002
51	6	0	-6.035236	-8.011441	-1.869402
52	6	0	-5.347762	-7.334236	0.328396
53	1	0	-5.594614	-7.122247	1.365485
54	6	0	-6.358424	-7.745879	-0.541290
55	1	0	-7.376384	-7.855330	-0.188418
56	6	0	8.128632	-0.013319	-2.153105
57	1	0	8.263123	-1.028641	-1.768417
58	1	0	8.891484	0.167544	-2.919299
59	1	0	7.136306	0.046513	-2.613282
60	17	0	-10.043817	5.292092	-0.109203
61	8	0	3.050788	-0.517831	-0.861152
62	8	0	0.399071	0.370370	-1.173234
63	7	0	0.658774	0.904665	1.839929
64	8	0	4.355533	-0.152843	-2.688476
65	8	0	-4.664063	2.623611	3.441384
66	7	0	-0.147165	3.818389	-4.488079
67	7	0	1.941987	2.811312	-4.140720
68	6	0	0.046169	2.004949	-2.870041
69	6	0	0.586629	2.885588	-3.836095

70	6	0	0.892256	1.056796	-2.143325
71	7	0	-4.716782	4.830572	2.679828
72	1	0	-4.213737	5.706776	2.689791
73	6	0	2.255332	0.970292	-2.594576
74	7	0	-2.847544	4.003397	3.783705
75	1	0	-2.357408	4.843785	3.512743
76	6	0	1.128964	1.687193	2.841185
77	1	0	2.204358	1.758459	2.908369
78	6	0	-1.116020	2.221874	3.571418
79	6	0	-1.462521	3.912517	-4.226465
80	6	0	2.707216	1.853312	-3.546760
81	1	0	3.747767	1.805588	-3.840522
82	6	0	-2.090144	3.067757	-3.280226
83	1	0	-3.152807	3.169733	-3.089829
84	6	0	3.292797	0.028855	-2.032047
85	6	0	0.271339	2.349761	3.717947
86	1	0	0.690021	2.968995	4.504885
87	6	0	-0.685531	0.765135	1.692227
88	1	0	-1.006098	0.151871	0.861925
89	6	0	-1.331888	2.125301	-2.604580
90	1	0	-1.764689	1.466743	-1.861062
91	6	0	-4.117409	3.745970	3.305645
92	6	0	-1.591784	1.400597	2.533958
93	1	0	-2.658580	1.271621	2.388470
94	6	0	-5.978472	4.876823	2.042218

95	6	0	2.593409	3.866277	-4.960859
96	1	0	3.475518	3.406259	-5.415252
97	1	0	1.895588	4.149197	-5.748859
98	6	0	-2.079763	2.964024	4.480237
99	1	0	-2.813636	2.271686	4.901533
100	1	0	-1.534052	3.430060	5.306982
101	6	0	-2.241602	4.950586	-4.990429
102	1	0	-1.557298	5.573484	-5.569160
103	1	0	-2.822675	5.589622	-4.315009
104	1	0	-2.951431	4.478963	-5.682326
105	6	0	-6.859894	3.781603	1.982316
106	1	0	-6.580843	2.847476	2.446307
107	6	0	-8.088573	3.915308	1.327624
108	1	0	-8.768572	3.073506	1.280814
109	6	0	-8.433787	5.129704	0.742248
110	6	0	-6.350571	6.095128	1.442472
111	1	0	-5.676984	6.947215	1.481738
112	6	0	-7.578009	6.227032	0.791853
113	1	0	-7.858457	7.166969	0.332908
114	6	0	2.979933	5.076082	-4.099754
115	1	0	2.082882	5.601847	-3.759221
116	1	0	3.586266	5.775768	-4.686614
117	1	0	3.547712	4.764418	-3.216095

Table A5.5. Coordinates of the optimized structure of ***trans*-5.2.1**

Center Number	Atomic Number	Atomic Type	Coordinates (Angstroms) X	Y	Z
1	27	0	-0.000025	0.000016	-0.000030
2	17	0	14.205870	-0.579411	-1.525255
3	8	0	-0.793527	-1.919383	0.645412
4	8	0	0.472619	-0.834888	-1.694648
5	8	0	8.014270	-2.360584	1.147026
6	7	0	-0.589364	-5.557075	-1.331672
7	8	0	0.781540	-2.339960	-3.360668
8	7	0	1.756682	-0.489823	0.738447
9	7	0	8.772249	-0.154516	1.056559
10	1	0	8.530925	0.800490	1.281071
11	7	0	-1.584821	-6.656601	0.486518
12	6	0	4.267793	-1.161322	1.800963
13	7	0	6.694968	-0.654313	1.968609
14	1	0	6.582780	0.332285	2.151541
15	6	0	4.119301	-0.823876	0.445544
16	1	0	4.977004	-0.818656	-0.217389
17	6	0	-0.163571	-3.161421	-1.336640
18	6	0	0.401000	-2.043871	-2.195091
19	6	0	-1.202631	-4.253125	0.613424
20	6	0	-0.708800	-3.015771	-0.007519

21	6	0	3.117859	-1.149198	2.603950
22	1	0	3.178687	-1.394565	3.659220
23	6	0	-1.138963	-5.497582	-0.051908
24	6	0	-0.136852	-4.410705	-1.916623
25	1	0	0.276533	-4.490084	-2.915494
26	6	0	10.037657	-0.318939	0.447676
27	6	0	5.614553	-1.549107	2.380284
28	1	0	5.546748	-1.588258	3.475268
29	1	0	5.911843	-2.546694	2.037482
30	6	0	-1.761633	-4.253105	1.906896
31	1	0	-1.817155	-3.308134	2.434981
32	6	0	1.884497	-0.812011	2.049307
33	1	0	0.974893	-0.760038	2.631612
34	6	0	2.861064	-0.497277	-0.052268
35	1	0	2.688698	-0.252379	-1.091313
36	6	0	7.844451	-1.140050	1.373687
37	6	0	-0.532043	-6.847192	-2.067984
38	1	0	0.304499	-6.770027	-2.767653
39	1	0	-0.310467	-7.626973	-1.338817
40	6	0	10.551435	-1.566274	0.046857
41	1	0	9.964359	-2.458689	0.204243
42	6	0	-2.114763	-6.638523	1.723458
43	6	0	-2.217518	-5.437480	2.464300
44	1	0	-2.649810	-5.454412	3.458545
45	6	0	11.814427	-1.636807	-0.549795

46	1	0	12.211063	-2.596129	-0.859077
47	6	0	10.806603	0.842210	0.240243
48	1	0	10.419857	1.810902	0.546045
49	6	0	12.555177	-0.474854	-0.743977
50	6	0	12.066291	0.769671	-0.355625
51	1	0	12.652652	1.666510	-0.512672
52	6	0	-2.592656	-7.951170	2.285215
53	1	0	-3.659895	-7.909842	2.535761
54	1	0	-2.053747	-8.206239	3.206143
55	1	0	-2.433290	-8.746183	1.554787
56	6	0	-1.838235	-7.159763	-2.804955
57	1	0	-2.661605	-7.267432	-2.093310
58	1	0	-1.736637	-8.100621	-3.357671
59	1	0	-2.088356	-6.368769	-3.520290
60	17	0	-14.205735	0.579268	1.525545
61	8	0	0.793477	1.919416	-0.645475
62	8	0	-0.472667	0.834919	1.694587
63	8	0	-8.014217	2.360566	-1.146885
64	7	0	0.589364	5.557098	1.331635
65	8	0	-0.781571	2.339987	3.360615
66	7	0	-1.756731	0.489857	-0.738510
67	7	0	-8.772260	0.154511	-1.056600
68	1	0	-8.530985	-0.800476	-1.281246
69	7	0	1.584827	6.656624	-0.486551
70	6	0	-4.267838	1.161357	-1.801035

71	7	0	-6.695015	0.654337	-1.968715
72	1	0	-6.582852	-0.332250	-2.151717
73	6	0	-4.119351	0.823914	-0.445615
74	1	0	-4.977056	0.818698	0.217316
75	6	0	0.163545	3.161448	1.336589
76	6	0	-0.401036	2.043899	2.195035
77	6	0	1.202610	4.253153	-0.613472
78	6	0	0.708767	3.015801	0.007465
79	6	0	-3.117901	1.149231	-2.604018
80	1	0	-3.178726	1.394597	-3.659289
81	6	0	1.138958	5.497606	0.051868
82	6	0	0.136842	4.410729	1.916580
83	1	0	-0.276539	4.490106	2.915453
84	6	0	-10.037631	0.318903	-0.447631
85	6	0	-5.614597	1.549140	-2.380363
86	1	0	-5.546782	1.588301	-3.475346
87	1	0	-5.911894	2.546721	-2.037549
88	6	0	1.761606	4.253135	-1.906946
89	1	0	1.817115	3.308167	-2.435038
90	6	0	-1.884541	0.812044	-2.049371
91	1	0	-0.974935	0.760069	-2.631673
92	6	0	-2.861116	0.497315	0.052201
93	1	0	-2.688753	0.252418	1.091247
94	6	0	-7.844448	1.140048	-1.373675
95	6	0	0.532059	6.847211	2.067955

96	1	0	-0.304481	6.770049	2.767627
97	1	0	0.310486	7.626998	1.338794
98	6	0	-10.551350	1.566206	-0.046637
99	1	0	-9.964256	2.458622	-0.203948
100	6	0	2.114764	6.638548	-1.723494
101	6	0	2.217502	5.437508	-2.464344
102	1	0	2.649790	5.454442	-3.458592
103	6	0	-11.814310	1.636707	0.550089
104	1	0	-12.210900	2.596005	0.859505
105	6	0	-10.806602	-0.842247	-0.240295
106	1	0	-10.419901	-1.810915	-0.546232
107	6	0	-12.555085	0.474754	0.744170
108	6	0	-12.066257	-0.769740	0.355646
109	1	0	-12.652638	-1.666579	0.512616
110	6	0	2.592672	7.951193	-2.285244
111	1	0	3.659919	7.909865	-2.535756
112	1	0	2.053791	8.206256	-3.206189
113	1	0	2.433284	8.746209	-1.554823
114	6	0	1.838257	7.159765	2.804922
115	1	0	2.661624	7.267432	2.093273
116	1	0	1.736669	8.100621	3.357644
117	1	0	2.088374	6.368766	3.520251

References

A.1. G. A. Bain and J. F. Berry, *J. Chem. Educ.*, 2008, **85**, 532–536.

A.2. N. J. Henson, P. J. Hay and A. Redondo, *Inorg. Chem.*, 1999, **38**, 1618–1626.

Conclusion and Future Perspective

In the second chapter, the structural features of five different zinc(II) complexes prepared from positional isomers of pyridyl amide and nitrobenzoic acid each having differences in coordination geometry and composition have been shown. All these complexes had free amide groups on the coordinated pyridyl based ligands, which were utilized for secondary coordination to provide different hydrogen-bonded architectures. As each reactions were substrate-dependent, energies of the complexes were theoretically optimised to compare the energy of five structures developed by the combinations of the two types of ligands in five different ways. In each combination, the structure with minimum energy had differed from the structure of the isolated complex; this pointed out that the prominence of self-assembling during crystallisation had provided the isolated complexes. These zinc(II) complexes were composed of non-fluorescent ligands, but were AIEgens in both solid and solution states. The wavelength of the emissions in each case commensurated commonly observed metal-to-ligand charge-transfer transitions observed in various zinc(II) complexes.

In the third chapter, the role of non-covalent interactions in the salts of mineral acids were evaluated together with the self-assemblies of the parent pyridyl urea compounds. It was found that the geometries of the urea and thiourea parts of the compounds varied in their salts and attained different assemblies. Due to differences in hydrophobic behaviour of phenyl or naphthyl units and the roles in π-π stacking interactions, the water of crystallization molecules were different in respective salts or prent compound; conversely the water of crystallisation played different roles in the urea compounds having phenyl or naphthyl units as consitutent part. In the hydrated phenyl urea derivative, the water molecule of crystallization prevented the urea tape network formation and acted as a bridge between two urea molecules through hydrogen bonding with the two -NH groups and $N_{pyridyl}$ atom, adopting a puckered geometry of the hydrated compound. However, in the hydrated form of the naphthyl counterpart, hydrogen bonding of the water molecules with the $N_{pyridyl}$ atom resulting in the formation of a chain-like arrangement of the urea molecules and stacking of the naphthyl rings. There was a large difference in the assembling of the perchlorate and nitrate salts of the phenyl thiourea derivative. In its perchlorate salt, the thiourea part had *syn-anti* orientation; but in the nitrate salt, it had a *syn-syn* arrangement of the two -NH groups.

The nitrate salt of the naphthyl urea derivative showed dual fluorescence in the solid state due to combinatory effects of a locally excited (LE) state and twisted intramolecular charge (TICT) transfer, which is a rare observation. The respective composites of perchlorate and nitrate salts of the naphthyl urea derivative mixed with calcium oxide in comparable molarity released their parent compound easily. But, the composites of the salts with excess amounts of calcium oxide had higher stability.

The subtle changes in the hydrogen bonding scheme of dicarboxylate coordination polymers of a pyridyl urea derivative, namely, the one having terephthalate than succinate or fumarate in the coordination polymer provided a different self-assemblies. The C–H···π interactions involving the phenyl ring next to urea causing conformational locking decided the course of self-assembled structures of the coordination polymers. The changes in the supramolecular assembling properties was implicated in the ability to bind methyl-orange dye differently by the individual member of series of the coordination polymers.

Preferential anion binding was used in anion-guided synthesis of *cis*-isomer or the *trans*-isomer of pyridylurea based cobalt(II) nalidixate complex. In *cis*-isomer, the two -NH groups of pyridyl urea ligand hydrogen-bonded with the two independent oxygen atoms of the coordinated and free oxygen atoms of a carboxylate group of the keto-acid ligand. The assembly of the isomers were guided by C-H···N intermolecular hydrogen bonds and the π···π stacking interaction between two 1,8-naphthyridine units of keto acid ligand. These interactions provided a single-stranded helical arrangement to the *cis*-isomer. The solvent-induced aggregation induced helical chirality in the *cis*-isomer which resulted in positive and negative Cotton effects in solution depending upon the solvent.

To summarize, the supramolecular features of pyridyl amide and pyridyl urea compounds provided scopes to reveal new self-assemblies with novel photophysical, host-guest binding, helical chirality properties and enabled to forecast their forth-coming studies in the field of research on urea and thiourea-based supramolecular systems.

List of Publications

1. R. Brahma, M. P. Singh and J. B. Baruah, Stacking among the clips of the poly-aromatic rings of phenazine with hydroxy-aromatics and photophysical properties.

   RSC Adv., 2019, **9**, 33403–33412.

2. R. Brahma and J. B. Baruah, Self-Assemblies of Zinc Complexes for Aggregation-Induced Emission Luminogen Precursors.

   ACS Omega, 2020, **5**, 3774–3785.

3. R. Brahma and J. B. Baruah, Intrinsic Structural Features of Coordination Polymers Make Impact on Dye Selectivity.

   CrystEngComm, 2021, **23**, 3812–3827.

4. K. Mudoi, R. Brahma and J. B. Baruah, Role of a Secondary Building Unit of Copper 2,3-Pyridinedicarboxylate Coordination Polymer in the Interactions with Ionic Dyes.

   Inorg. Chem. Commun., 2022, **144**, 109888.

5. R. Brahma and J. B. Baruah, Assemblies of Salts of Urea and Thiourea Derivatives and Release of Host from Composites with Calcium oxide.

   New J. Chem., 2023, **47**, 6211–6223.

6. S. Verma, R. Brahma, J. B. Baruah, Consequences of Twisting of the Flexible Arms of Imidazole-Derived Urea in Zinc-Dicarboxylate Coordination Polymers.

   CrystEngComm **2024**, *26* (14), 1976–1985.